Study on Climate Extremes and Glacial Lake Outburst Floods

A thesis submitted in partial fulfillment of the requirement

for the award of the degree of

Doctor of Philosophy

By

Uttam Puri Goswami

Department of Civil Engineering

Indian Institute of Technology Guwahati

November 2017

Department of Civil Engineering
Indian Institute of Technology Guwahati
Guwahati-781039, Assam, India

Certificate

It is certified that the work contained in the thesis entitled "**Study on Climate Extremes and Glacial Lake Outburst Floods**" by Uttam Puri Goswami, Roll Number 146104038, a student in the Department of Civil Engineering, Indian Institute of Technology Guwahati for the award of the degree of Doctor of Philosophy has been carried out under our supervision and that this work has not been submitted elsewhere for a degree.

Dr. Manish Kumar Goyal
Assistant Professor
Department of Civil Engineering
Indian Institute of Technology
Guwahati-781039

Date:

Declaration of Authorship

I, Uttam Puri Goswami, declare that this thesis titled '**Study on Climate Extremes and Glacial Lake Outburst Floods**' and the work presented in it has been carried out by me under the supervision of Dr. Manish Kumar Goyal, Department of Civil Engineering, Indian Institute of Technology Guwahati. This work has not been submitted elsewhere for the award of any degree.

Uttam Puri Goswami

Department of Civil Engineering

Indian Institute of Technology

Guwahati-781039

Date:

Acknowledgment

I would like to place on record my deep sense of gratitude and sincere thanks to my thesis Supervisor Dr. Manish Kumar Goyal, Assistant Professor, Department of Civil Engineering, Indian Institute of Technology Guwahati for his invaluable guidance and full hand cooperation throughout the all aspects of this research work. I also admire his patient explanation of the concepts and basic principles.

I am grateful to the Chairman of my Doctoral committee Dr. Sreeja P. and members Dr. Abhishek Kumar and Dr. Sachin Kore for their valuable suggestions and kind support during completion of the research work.

I am grateful to Dr. Bimlesh Kumar, Dr. B. Hazra and Prof. S. M. Narulkar for their valuable suggestions and kind support during completion of the research work.

Particularly I am indebt to my parents Shri N.P. Goswami and Smt. Meera Bai and family members for their blessings and unconditional support for bringing me to such level. Without their faith in me, I would not have been able to carry out this study. Special thanks to Vishal Singh, Shivam, Ashutosh Sharma, Juna, Manas, Bhargava, Srinidhi and Gilbert.

I am thankful to the Indian Institute of Technology Guwahati for providing the magnificent facilities and beautiful atmosphere to carry my research work. I gratefully acknowledge the financial support that was received from the Department of Science and Technology, Govt. of India to carry out the research work.

Abstract

This study is focused on the climate extremes and glacial lake outburst flood over the Teesta River catchment (up to Chugthang), which is a part of Eastern Himalaya. To accomplish this research, Coupled Model Intercomparison Phase 5 (CMIP5), Global Circulation Models (GCMs) with their Representative Concentration Pathways (RCPs) have been used to downscale the daily precipitation, minimum temperature and maximum temperature. A Statistical Downscaling Model (SDSM) has been applied for downscaling. Using SDSM, daily precipitation and temperature time series have been projected for present and 21st century scenarios. Significant upward trend is present in annual precipitation during 2006-2100. The non-monsoon precipitation is also having the significant increasing trend, but monsoon precipitation is showing falling trend. This implies that the precipitation pattern is shifting towards the non-monsoon from monsoon over the study area. The precipitation extremes WD, R10 and R20 are also showing increasing trends. The projected temperature time series are also showing warming trend for both maximum and minimum temperature, except in some of the monsoon months for maximum temperature. The minimum and maximum temperatures are showing warming trends with the rate of $0.015°C/year$ and $0.01°C/year$ in the 21st century, respectively. In case of temperature extremes, the minimum temperature indices are more pronounced than maximum temperature indices in both past and future. Additionally, the precipitation and temperature extremes are used to understand

the joint probabilistic behavior of climate extremes using parametric copula. The result of temperature extremes joint probabilistic behaviour, indicating the change in joint return period of [TN10, TN90] is decreased, this implies that the cool nights would be colder and warm nights would be hotter but other extreme combinations are increased for all scenarios. The joint behaviour of precipitation extremes highlight the decrease in joint return period of [CWD, CDD] for all scenarios, indicating the co-occurrence of floods and droughts are more frequent in same year over the region. In addition, [WD, SDII] is also decreased, implying that the occurrence of flood is more frequent over the region. Whereas, other extreme combinations having no significant changes.

Hydrological modeling and Budyko framework have been carried out to assess the hydrological response and relative contribution of climatic variable on annual runoff changes. For hydrological modeling, MIKE11 NAM model has been used. The MIKE11 NAM model is auto calibrated for nine default parameters. The optimized nine parameters values are used to generate the streamflow for both past and future, where projected annual streamflow have increase for all projected scenarios as compare to historical scenario. From the Budyko framework analysis, the snow-ratio has decreased, but this does not influenced the annual runoff significantly as compared to precipitation. This also implies that, precipitation is less likely to occur as snowfall in future. Precipitation is the major factor that affects the runoff changes with the ranges of 2 to 19% for different scenarios over the region.

The remote sensing satellite applications have used for the glacial lakes mapping over the study area. Then, the potential flood volumes (PFVs) of glacial lakes are estimated using steep lakefront area (SLA) concept. Total 203 glacial lakes having area more than 0.01 km^2 were identified, most of them are situated at the high elevation zone

(>4500 m) and some glacial lakes are found increasing their areal extends. The glacial lake having surface area more than 1 km^2 and maximum PFV is consider for glacial lake outburst flood (GLOF) dynamics using hydrodynamic modeling (MIKE11 HD). The flood routed along the river reach at every chainage point up to Chugthang and found peak discharge could increase up to 4-6 times and depth and velocity increased about 100% during GLOF as compare to no GLOF condition. This huge peak discharge and high velocity with higher water depth can affect the hydropower project (Teesta hydropower project- III) at Chugthang because there is no flat terrain for inundation.

The change in precipitation and temperature and their extremes can alter the water resource systems, consequently, the management plans are needed to sustain the available water resources induced by climate change. In addition, the change in climate variables can amend the glacier environment such as streamflow have increased and snow-ratio has decreased over the region. Furthermore, the precipitation is less likely to occur as snowfall over the catchment and co-occurrence of flood and drought as well as heavy precipitation with high intensity is more frequent in the same year in future. Also, about 90% of glacial lakes are situated above the 4500m altitude. Most of them are increasing their size could increase the frequency of glacier hazards (GLOFs) and causes damages (environmental, social and economical). Further, some lakes are decreasing and some are getting extinct also. Therefore, adaptation measures viz. early flood warning system and mitigation strategies are required in potential glacier shaded areas. The reason behind these decreasing or extinction may be climate change, glacier retreating, loss of connection from the parent glaciers, etc. This study recommends the potential use of the high-altitude glacial lakes as a storage mechanism for the controlled utilization of the melt water.

Contents

List of Figures

List of Tables

List of Abbreviations

ANN	Artificial Neural Network
APN	Asia-Pacific Network
AR	Assessment Report
CDD	Consecutive Dry Days
CMIP3	Coupled Model Intercomparison Project Phase 3
CMIP5	Coupled Model Intercomparison Project Phase 5
CN	Curve Number
CWC	Central Water Commission
CWD	Consecutive Wet Days
DEM	Digital Elevation Model
DN	Digital Number
ESM	Earth System Model
ETCCDI	Expert Team on Climate Change Detection and Indices
FAO	Food and Agriculture Organization
GCM	Global Climate Model
GLOF	Glacial Lake Outburst Flood
HadCM3	Hadley Center Climate Model 3
ICIMOD	International Centre for Integrated Mountain Development

IDWA	Inverse Distance Weighted average
IMD	India Meteorological Department
IPCC	Intergovernmental Panel on Climate Change
ISRO	Indian Space Research Organization
LULC	Land Use Land Cover
MK	Man-Kendall
NAM	Nedbor Afstromnings Model
NASA	National Aeronautics Apace Administration
NCAR	National Center for Atmospheric Research
NCEP	National Centers for Environmental Prediction
NDTI	Normalized Difference Turbidity Index
NDVI	Normalized Difference Vegetation Index
NDWI	Normalized Difference Water Index
NSE	Nash-Sutcliff Efficiency
PRP	Percentage Reduction in Partial Porrelation
RCP	Representative Concentration Pathway
rhs	Relative Humidity
rhsmax	Relative Humidity Maximum
rhsmin	Relative Humidity Minimum
RMSE	Root Mean Square Error
RVM	Relevance Vector Machine
SDII	Simple Daily Intensity Index
SDSM	Statistical Downscaling Model

SP	Super Predictor
SSVM	Smooth Support Vector Machine
SVM	Support Vector Machine
tas	Temperature at Surface
tasmax	Maximum Temperature at Surface
tasmin	Minimum Temperature at Surface
UNEP	United Nations Environment Programme
UNFCCC	United Nations Framework Convention on Climate Change
WD	Wet Day

List of Symbols

Symbols	Description
CO_2	Carbon di-oxide
T_{deb}	Debiased daily time series of temperature
T_{SCEN}	Downscaled temperature scenario
$\bar{T}_{CONT}$	Long term monthly mean of historical model temperature
$\bar{T}_{obs}$	Monthly mean of historical observed temperature
P_{deb}	Debiased daily time series of precipitation
P_{SCEN}	Downscaled precipitation series
$\bar{P}_{obs}$	Monthly mean of historical precipitation
$\bar{P}_{CONT}$	Long term monthly mean of historical model precipitation
T_{o_i}	ith data point of observed temperature
T_{p_i}	ith data point of observed precipitation
$\bar{T}_{o_i}$	Mean of observed variable (temperature/precipitation)
$\bar{T}_{p_i}$	Mean of model variable (temperature/precipitation)
R^2	Coefficient of determination
Q_s	Total surface runoff (mm)
R	Daily rainfall (mm)
S	Retention parameter on combination of soil

Q_{min}	Lower limit of parameter value
Q_{max}	Upper limit of parameter value
U_{max}	Maximum water content in surface storage
L_{max}	Maximum water content in root zone storage
CQOF	Overland flow runoff coefficient
CKIF	Time constant for routing inter-flow
$CK_1.CK_2$	Time constant for routing overland flow
T_{OF}	Root zone threshold value for overland flow
T_{IF}	Root zone threshold value for inter-flow
C_{KBF}	Time constant for routing base flow
T_G	Root zone threshold value for groundwater recharge
km	Kilometer

CHAPTER 1

Introduction

1.1 Background

1.1.1 Climate Change

Climate Change is defined as; "change of climate which is attributed directly or indirectly to human activity that alters the composition of the global atmosphere and which is in addition to natural climate variability observed over comparable time periods suggested by United Nations Framework Convention on Climate Change (UNFCCC) in 1992 (Griggs and Noguer, 2002). The change in the global climate since 20th century, which is mostly recognized by anthropogenic activities, instead of natural climate variability (Sachindra et al., 2014). Additionally, Intergovernmental Panel on Climate Change (IPCC) stated, the recent climate change and rise in the global and continental temperature have had significant impact on physical and biological environmental systems (Chen et al., 2011; Sachindra et al., 2014). Climate change analysis is essential for building resilient mitigation strategies for adaptation. Global Climate Models (GCMs) are an important tool, which are widely utilized in climate research to assess

plausible climate change through scenario analysis. The Coupled Model Intercomparison Project Phase 3 (CMIP3) (Meehl et al., 2007) and Coupled Model Intercomparison Project Phase 5 (CMIP5) (Taylor et al., 2012) have made important contribution towards consistent future projection of changes in climate variables. The CMIP3 and CMIP5 provide coordinated simulations from state-of-the-art GCMs. CMIP5 improves the features of substantial as compared to CMIP3 and used the new emission scenarios named as Representative Concentration Pathways (RCPs) (Taylor et al., 2012). The GCMs are the source of uncertainties, which are associated with computational restrictions to capture physical emissions that pass into the atmospheric concentration due to the lack of appropriate information (sources and sinks) of greenhouses gas emissions and rate of their recycling in the Earth system (Mujumdar and Ghosh, 2008; Crosbie et al., 2010). The climate model's uncertainty is related with unknown atmospheric system e.g. physical and biological condition of atmosphere. Earlier, researched used a single GCM(Mileham et al., 2009; Van Roosmalen et al., 2009; Austin et al., 2010) such as UK researchers have used Hadley Center Climate Model 3 (HadCM3), Australians have used CSIRO and Canadians used CGCM3.1 GCM (Crosbie et al., 2011). but, in order to assess the uncertainty associated with the GCMs, it is important to use multiple GCMs (Crosbie et al., 2011, 2010).

The extreme events such as floods, droughts and heat waves etc. can have significant negative impacts on human society and ecosystem as natural hazards (Easterling et al., 2000; Sheffield et al., 2012; Trenberth et al., 2014). The impact of extreme events are worse in agricultural dominated countries like India and China (Rosegrant and Cline, 2003; Chattopadhyay, 2010). Since the middle of 20th century, the changes in frequency of occurrence of such climate extremes has been altered due to anthropogenic climate

change (Dai, 2011; Lesk et al., 2016) and India is no exception (De et al., 2005). Moreover, IPCC AR5 report (IPCC, 2014), suggested that the composition of CO_2 and other heat-trapping gases have changed significantly in the atmosphere, subsequently the surface temperature could increase robustly. This could possibly increase the likelihood of extreme events in near future. The possible changes in frequency, intensity and duration of extreme events can be assessed with the use of latest CMIP5 GCM dataset (Taylor et al., 2012). Over the years, various extreme indices of precipitation and temperatures with specific physical thresholds have been used as a tool in climate change studies (Manton et al., 2001; Frich et al., 2002; Alexander et al., 2006; Donat et al., 2013). Meanwhile, extreme indices have provided promising local conditions and few physically based indices which are amenable to temperature and precipitation data around the world. The precipitation and temperature extremes are significantly increasing all around the world except some of the regions, where, minimum temperature indices are more pronounced than maximum temperature indices and extreme precipitation is increasing with longer dry spells (Donat et al., 2013; Sillmann et al., 2013a,b).

Analysis of hydrologic extreme events using univariate techniques is well documented (Katz and Brown, 1992; Boo et al., 2006). However, multivariate analysis of such random variables are rarely used (Favre et al., 2004). In general, the hydrological processes are highly stochastic and often exhibits the dependence associated with the other variables. In such situations, univariate techniques may underestimate the risk associated to an event. With this understanding, several researchers focused their attention on multivariate analysis of hydro-meteorological variables (Snyder, 1962; Westra et al., 2007). For multivariate frequency analysis, copulas are becoming important tool due to its flex-

ibility. Thus, copulas are widely used in the different fields such as finance, medicine, hydrological, other civil engineering fields etc. In particular hydrological research, different copulas are employed for analysis such as joint return periods of hydrological events (Salvadori and De Michele, 2004); bivariate flood frequency analysis (Zhang and Singh, 2006); bivariate rainfall frequency distributions (Zhang and Singh, 2007); joint return period of extreme rainfall events (Wang et al. 2010); spatio-temporal pattern of precipitation extremes (Zhang et al., 2012, 2013); flood and drought hazards (Li et al., 2015); probabilistic forecasting of seasonal droughts (Chen et al., 2016) etc. So far, copula has been found an efficient tool in multivariate analysis of different hydrological events. This could improve the existing knowledge of process of various extreme events and provides more information for events prediction.

The major river basins of India such as Ganga, Indus and Brahmaputra, originate from the Himalayan glaciers (India-WRIS, 2012). The Himalayas are an extraordinarily high mountain chain, spanning 2500 km east to west across five countries and encompassing many varied cultures and an extensive diversity of flora and fauna. Himalayan glaciers are the largest sources of major rivers system in Asia, lifeline of more than 1.3 billion people living in the downstream (Bajracharya et al., 2007b). A study carried out jointly by International Centre for Integrated Mountain Development (ICIMOD), United Nations Environment Programme (UNEP), and Asia-Pacific Network for Global Change Research (APN) between 1999 and 2003 documented about 15,000 glaciers and 9000 glacial lakes in Bhutan, Nepal, Pakistan and selected basins of China and India. In India, most of the perennial rivers originate from the Himalayan glaciers. The glaciers are controlled to extra-peninsular region specifically Himalaya within the longitudes $72°E$ to $96°E$ and latitudes $27°N$ to $36°N$. The Indian Himalayan region comprises

about 9,575 glaciers and other permanent ice bodies covering an area of about 40,000 km^2, with an approximate ice volume of 2,000 km^3 (Raina and Srivastava, 2014). The glacier ranges over the entire Himalayas are among the largest and most spectacular in the world (Bajracharya and Mool, 2009). Himalayan glaciers are important for generating hydroelectricity, irrigation, drinking water supply and daily needs of over 10 billion people.

1.1.2 Glacial Lake Outburst Floods

The climate driven activities such as global warming may indeed affect the glacier retreating and snowmelt (Ives et al. 2010) hydrology by imbalancing hydrological processes especially on the Himalayan regions. The Earth's average surface temperature has increased by $0.3°C$ to $0.6°C$ in the last hundred years. Consequently, faster glacier melting is happening. The Himalayan environment is the most symbolic evidence of glacier melting, which is resulting in to the formation of glacial lakes and rise in the risk of GLOF events (Bajracharya et al., 2007a; Shrestha et al., 2010; Mool et al., 2011; Somos-Valenzuela et al., 2015a). Glacial lakes are the mass of water existing in, under, beside and/or in front of glaciers and forming due to glacier activities e.g. melting (Clague and Evans, 2000; Worni et al., 2012; Bannerjee, 2013). The glacial lakes are formed in loose internal composition and lack of engineered spillway (Worni et al., 2013), consequently these are inherently prone to failure. This may pose severe hazards in the terms of high intensity runoff, flash flood and GLOF events to the mountain communities (Watanbe and Rothacher, 1996; Huggel et al., 2002; Shrestha et al., 2010; Anacona et al., 2015a). The glacial lakes are the major sources of serious natural hazards in terms of GLOFs in mountain regions (Shrestha et al., 2010; Anacona et al.,

2015a). GLOFs are the phenomena which can release huge volume of water in short time duration generating high-velocity, high-discharge and deep flow with high erosive and damaging ability (Clague and Evans, 2000; Breien et al., 2008) and is considered as the most essential glacier-related hazard in terms of potential damage (Osti and Egashira, 2009).

The number and size of glacial lakes has increased in different part of the world in last five decades as consequences of glacier retreating (Anacona et al., 2015a). Recently, several outburst have also been reported in Himalayas (Gardelle et al., 2011), tropical Andes and Patagonia (Clague and Evans, 2000). In Patagonia, about 16 glacial lakes have failed and one of them was the largest GLOFs in terms of flood volume reported worldwide (Clague and Evans, 2000; Anacona et al., 2015b). An outburst floods occurred in 1941, resulting killing of 4500 peoples in city of Huaraz, Peru; whereas in 1968 and 1970, an outburst from glacial-dammed lake triggered debris flows and cause huge damages in the village of Saas Balen, Swiss Alps (Ives et al., 2010). A number of GLOF events are recorded in Himalayas in recent past. Recently, GLOF in Kedarnath Uttarakhand, is the most noteworthy event in Indian history till date. From the field information and scientific correspondence, the consecutive two events occurred on 16-17 June 2013, which caused huge destruction in the Kedarnath area of Mandakini River basin (Durga Rao et al., 2014). Furthermore, many GLOF events recorded in last five decades worldwide listed below in Table 1.1.

Table 1.1: GLOF events recorded worldwide in last five decades.

S. No.	**Year**	**Name of Lakes and Country**	**River Basin**	**Reference**
1	1969	Ayaco, Tibet	Arun	Mool et al. 2011
2	1970	Ayaco, Tibet	Arun	Mool et al. 2011
3	1977	Nare, Tibet	DudhKoshi	Mool et al. 2011
4	1977	Engano Lake, Chilean Patagonia	Engano Valley	Anacona et al. 2015
5	1980	Nagma Pokhri, Nepal	Tamor	Mool et al. 2011
6	1981	Zhangzangbo, Tibet	Sun Koshi	Mool et al. 2011
7	1982	Jinco, Tibet	Arun	Mool et al. 2011
8	1985	Dig Tsho, Nepal	DudhKoshi	Mool et al. 2011
9	1991	Chubung, Nepal	TamoKoshi	Mool et al. 2011
10	1998	Tam Pokhari, Nepal	DudhKoshi	Mool et al. 2011
11	1994	Lugge Tsho Lake, Bhutan	Pho Chhu River	Watanbe and Rothacher, 1996
12	1994	British Columbia, Canada	Farrow Creek	Clague and Evans 2000
13	2010	Cordillera Blanca, Peru	Rio Santa	Schneider et al. 2014
14	2013	Chorabari, India	Mandakini River	Durga Rao et al. 2014

The glacial hazards take attention due to risk of loss of life and threats for expensive infrastructures such as hydropower projects, roads buildings etc. The glacier hazards creates the disasters in terms of GLOF such as about 32,000 people have been killed in Peru and hundreds of people have died in the Himalayas in last five decades (Richardson and Reynolds, 2000). In the Sikkim Himalaya, a number of glacial lakes at glacier snout are dammed by loose and friable debris. These glacial lakes are an indirect indicator of retreating of glacier and present hazard to downstream locations (Gardelle et al., 2011; Vuichard and Zimmermann, 1987), but not all glacial lakes are unstable to outburst disastrously. The failure of lake is a function of susceptibility of a dam and triggering events (Richardson and Reynolds, 2000). The geometry, material property and location of a dam are the most responsible factors for moraine stability (Fujita et al., 2009; Worni et al., 2013). The common characteristics of failed lakes worldwide are; should be in contact with retreating glacier and dammed by steep moraine. In Indian Himalaya having less critical glacial lakes as compare to other countries in Hindu Kush Himalaya (e.g. Nepal or Bhutan) (Ives et al., 2010), In Sikkim Himalaya region, no GLOF event has been observed yet but many large and potentially critical lakes exist (Fujita et al., 2013).

1.2 Problem Statement

The Himalayas are the most symbolic evidence to climate change, the Teesta River catchment is the part of North Sikkim Himalaya needs similar attention towards current and future impact of the climate change. The North Sikkim Himalaya, which is mostly covered with snow and glaciers, thus most of the GCM predictors (e.g. pr, prc, tas, rhs, psl etc.), having largest influence on snow glacier hydrology, needed to identify.

Additionally, this area also needs to address the changes in climate extremes, water component, hydrological variables and glacial lakes under the changing climate. Spatio-temporal variation of climate extremes and glacial lakes needs to identify for reduction of hydrological hazards such as floods, droughts and GLOFs etc.

This study shall explore the precipitation and temperature climate extremes induced by climate change; bivariate analysis of climate extremes to understand the joint probability behaviors of extremes; application of remote sensing to identify the glacial lakes and their temporal changes during 1990-2014; hydrological modeling for generation of future scenarios of main water balance components; snow-ratio change and its effects on annual runoff using Budyko framework; hydrodynamic modeling of Teesta River with GLOF dynamics. In recent past, most of the parts of the world have experienced the precipitation and temperature extremes in terms of flood, droughts and heat waves. In order to address the effects of climate extremes at regional scale, the downscaling technique can be used for both past and future scenarios under CMIP5 GCMs. In addition, copulas are used to assess the joint behaviour of climate extremes; hydrological and hydrodynamic modeling used for water balance components and GLOF simulation.

1.3 Research Objectives

The main aim of study is to assess the climate extremes (precipitation and temperature) and glacial lake outburst floods (GLOFs) under the climate change scenarios. To accomplish this research work, the following research objectives were defined as below:

- Downscaling and projection scenarios of precipitation, maximum temperature and minimum temperature of upper Teesta River catchment utilizing CMIP5 GCMs

and their RCP scenarios.

- Bivariate assessment of precipitation and temperature extreme indices using Copula.
- To map the glacial lakes and demarcate their areal extent for hazard assessment over North Sikkim Himalayan glaciers using remote sensing images.
- Runoff assessment of upper Teesta River catchment using hydrological model.
- Long term snow-ratio change and its effects on annual runoff using Budyko framework.
- Glacial lake outburst floods (GLOFs) assessment over the downstream of Teesta River basin utilizing field observation datasets and hydrodynamic model.

1.4 Thesis Outline

- **Chapter 2** represents the detailed literature review of present study. The literature review of present study, emphasized the theme of past and future climate change scenarios, downscaling and future projections, bivariate analysis of climate extremes, application of remote sensing, hydrological modeling, snow-ratio change and its effects on annual runoff using Budylo framework and hydrodynamic modeling. .
- **Chapter 3** presents the detailed description of the study area Teesta river catchment (up to Chugthang), north Sikkim Himalayas and data used. The section describes the hydro-meteorological, geographical, topographical and hydrological characteristic of the study area.

- **Chapter 4** presents the downscaling technique and climate scenarios using latest CMIP5 GCMs (ESM2G, ESM2M and CM3) with their RCPs (RCP2.6, RCP4.5 and RCP8.5). Additionally, the bivariate analysis represents the joint probabilistic behavior of climate extremes. The joint probability behaviour of precipitations temperature extremes is essential to recognize the regional responses of extremes to climate change for glacier melting and water resources management.

- **Chapter 5** describes the generation of water balance component using hydrological model (MIKE11 NAM) and relative contribution of climate variables such as snow-ratio, precipitation and evapotranspiration on annual runoff using Budyko framework.

- **Chapter 6** presents the application of remote sensing to identify the glacial lakes and their vulnerability using defined criteria's. The glacial lake vulnerability is defended by surface area of glacial lakes and potential flood volume (PFV). The PFV is calculated using steep lakefront area (SLA) concept, SLA is the profile of moraine of glacial lake, which represents the approximate inner profile of glacial lake. The PFV is defined as the minimum possible volume of water that could be released if the glacial lake surface lowered to destroy the embankment of glacial lake. Furthermore, the assessment of glacial lake outburst floods (GLOFs) dynamics is carried out at the downstream of Teesta River catchment using field observation dataset and hydrodynamic modeling (MIKE11 HD).

- **Chapter 7** summarizes the major findings and contribution of this research work. The future scope of this research are briefly discussed.

CHAPTER 2

Literature Review

2.1 General

As per the Intergovernmental Panel on Climate Change (IPCC), climate change is likely to affect precipitation and water availability around the globe and Himalaya is no exception (IPCC, 2014). In recent past, number of heavy rainfall events have been recorded over the Himalayan region e.g. Kedarnath, Uttarakhand flash flood in 2013 and Jammu and Kashmir flood in 2014 (Durga Rao et al., 2014; Kumar et al., 2016). Several extreme events such as floods and droughts can have significant negative impacts on the watershed hydrology and ecosystem (Easterling et al., 2000; Trenberth et al., 2014). The frequency of extreme events has been altered due to changes in landuse/landcover pattern and anthropogenic activities all around the world (Dai, 2011) as well as in Himalayan regions (Bolch et al., 2012). India, shows the large spatial variability in rainfall such as north-eastern part receive highest rainfall about 11,690 mm at Mousinram near Cherrapunji, whereas the western parts receive lowest rainfall about 150 mm at Jaisalmer (Kumar et al., 2005).

An assessment of climate extremes induced by climate change and glacier hazards is

essential for appropriate national and local long term development plans. This research work presents the assessment of impact of climate change on hydro-meteorological variables (precipitation and temperature); analysis of water balance components; and glacier hazard in terms of GLOFs over the glaciers in the Teesta River catchment, North Sikkim Himalaya. Therefore, the current study reveals the climate extremes and glacier hazards in terms of glacial lake outburst floods based on the flowing key points:

1. Climate change scenarios and climate extremes
2. Bivariate analysis using Copula
3. Inventory of glacial lakes and parameters
4. Estimation of water balance component
5. Glacier hazards in terms of GLOF

2.2 Climate Change Scenarios and Climate Extremes

The definition of the climate change given by the IPCC , *"Climate change refers to a change in the state of the climate that can be identified by changes in the mean and/or the variability of its properties, and that persists for an extended period, typically decades or longer"* (IPCC, 2014). Climate change analysis is essential for building resilient mitigation strategies for adaptation. The several climatic elements are affecting biological and human systems in different ways. In recent past, several studies reveal that the spatial variability of impact of climate changes; change in global temperature in land and sea and in high and low altitude; change in precipitation patterns in high and low altitude (IPCC, 2007). Additionally, IPCC AR5 report (IPCC, 2014), suggested that the composition of CO_2 and other heat-trapping gases has changed significantly

in the atmosphere, subsequently the surface temperature could increase robustly. On the Indian subcontinent, temperatures are predicted to increase between 3.5 and 5.5° C by 2100 (IPCC, 2007). This could possibly increase the likelihood of extreme events in near future. The changes in frequency and severity of extreme events will have significant impacts on human life and natural systems. The increasing frequency of flood, droughts and heat waves are projected for 21st century and expected to have adverse effects (Thornton et al., 2014). Possible changes in frequency, intensity and duration of extreme events can be assessed by Coupled Model Intercomparison Project Phase 3 (CMIP3) (Meehl et al., 2007) and Coupled Model Intercomparison Project Phase 5 (CMIP5) (Taylor et al., 2012). Many researchers have used these CMIP5 datasets to assess the impact of climate change on precipitation and temperature and their extremes. Over the years, various extreme indices of precipitation and temperatures with specific physical thresholds have been used as a tool in climate change studies (Manton et al., 2001; Frich et al., 2002; Alexander et al., 2006; Klein Tank et al., 2006; Moberg et al., 2006; Donat et al., 2013). Meanwhile, extreme indices have provided promising local conditions and few physically based indices which are amenable to temperature and precipitation data around the world. The precipitation and temperature extremes are significantly increasing all around the world except some of the regions. Where, minimum temperature indices are more pronounced than maximum temperature indices and extreme precipitation is increasing with longer dry spells (Donat et al., 2013; Sillmann et al., 2013a,b).

The CMIP5 was built after the accomplishments of earlier phases of CMIP3. CMIP5 model runs with the considerable changes those are associated with Representative Concentration Pathways (RCPs) to describe future concentration or emission scenarios.

Four RCP scenarios have been formulated which are based on future population growth, technological development and societal responses. RCP provides the estimated radiative forcing values in the 2100 e.g. RCP2.6 is a low scenario in which radiative forcing reaches to peak at the middle of the century and decline to 2.6 W/m^2 by end of the twenty first century. Additionally, there are two intermediate scenarios RCP4.5 and RCP6.0 and a high RCP8.5 scenarios. The radiative forcing in RCP4.5 and RCP6.0 increases and then stable at the end of the century and radiative forcing in RCP8.5 increases throughout the 21st century before reaching the level 8.5 W/m^2 (Taylor et al., 2012). The CMIP5 GCMs are important tool which are widely used in climate studies to assess plausible climate change through different scenario (IPCC, 2014). GCMs are not adequate for climate change assessment at regional or local scale because of their coarse spatial resolution (Wilby et al., 1998). Hence, projection of local climate requires downscaling techniques; the downscaling approaches (dynamic and statistical) have subsequently emerged to satisfy the need to interpolate regional-scale atmospheric predictor variables (Wilby et al., 1998). Recently, many researchers have engaged these methods to downscale number of variables such as: precipitation, mean monthly precipitation, mean annual precipitation, daily precipitation, air temperature (maximum and minimum), extreme temperature, evaporation etc. (Mujumdar and Ghosh, 2008; Mahmood and Babel, 2013; Singh and Goyal, 2016).

Gagnon et al. (2005), simulated the climate data for streamflow modeling using statistical downscaling model (SDSM) in the province of Québec. This study tested the capability of SDSM to derive the local scale climate variables (precipitation and temperature) that can be used as inputs for hydrological modeling for streamflow generation. Results show that the SDSM provides reasonable downscaling data when using predic-

tors representing the observed current climate. The choice of predictors is important for the seasonal variation of streamflow.

Alexander et al. (2006), analyzed the global observed change in daily temperature and precipitation climate extreme during 1951-2003. The temperature extremes showed the widespread significant warming changes, especially for daily minimum temperature extreme indices driven by daily minimum temperature. The result highlights that the significant decrease in annual occurrence of cool nights and a significant increase in annual occurrence of warmer nights over the 70 % of global land. In case of precipitation extremes, it shows the significant increasing but the changes are much less and having the tendency towards the wetter condition throughout the 20th century.

Kang et al. (2007), have used the six multi-model outputs for statistical downscaling predictions of station-scale precipitation in Philippines and Thailand. In this study, the analysis reveals the atmosphere dynamics linkage based on the observed data than model data. The result shows the observed linkage provides a robust basis for predictor selection and its ranges. A movable window is used to select the most sensible area within the range of predictors to avoid spatial shift of predicted field away from observed climate for downscaling.

Donat et al. (2013), have presented 17 temperature and 12 precipitation indices recommended by Expert Team on Climate Change Detection and Indices (ETCCDI) using HadEX2 dataset. The suggested indices are derived from daily maximum and minimum temperature and precipitation observations. The results showed the widespread and significant warming trends related to temperature extremes, especially for minimum temperature indices over the 110 years with strong trends in recent decades. Precipitation indices are showing significant trends but the changes are more spatially

heterogeneous compared with temperature changes. On global scale, there is a tendency towards wetter condition for most of the precipitation indices such as intensity, frequency and duration of precipitation is increased.

Sillmann et al. (2013a), have studied the performance of state-of-the-art global climate models of CMIP5 for simulating the climate extremes defined by ETCCDI and compare with previous phase CMIP3 for present scenarios. The spread amongst CMIP5 models for several temperature indices is reduced compared to CMIP3 models, despite the larger number of models including in CMIP5. The result shows that the CMIP5 models are better to simulate the climate extremes and their trends. There is large variation between reanalysis, which shows the uncertainties to the extremes simulation.

Sillmann et al. (2013b), have studied the performance of state-of-the-art global climate models of CMIP5 for simulating the climate extremes defined by ETCCDI and compare with previous phase CMIP3 for future climate projections. They have analyzed the change in indices at global and regional scale for 21st century as compared to reference period 1981-2000 and found that the minimum temperature extreme indices are more pronounced than maximum temperature indices. Additionally, the precipitation extremes are generally increasing with faster rate than total wet-day precipitation. In the region, Australia, Central America, South Africa and the Mediterranean, the consecutive dry days are increasing with reduction in heavy precipitation days and maximum consecutive 5 day precipitation, which indicates future intensification of dry conditions. Under RCP8.5 scenario, the change in precipitation and temperature extreme indices are more pronounced.

Duhan and Pandey (2015), have compared the three downscaling techniques namely, multiple linear regression (MLR), artificial neural network (ANN), and least square

support vector machine (LS-SVM) for development of models. The result indicates that the LS-SVM models perform slightly better than ANN and MLR models. Than LS-SVM models was used to predict the future temperature time series using Canadian Coupled Global Climate Model 3 (CGCM3) simulation of A2 emission scenario for the period 2001–2100. The projected scenarios are showing the increasing trend for both maximum and minimum temperature. In addition, the minimum temperature will increase with higher rate than maximum temperature.

Zhao et al. (2015), compared two different downscaling, Presim1and Presim2 methods to downscale the CMIP5 GCM outputs in China. The result highlights that the accuracy of Presim1 is much better than Presim2 based on mean absolute error, mean relative error and root mean square error. Presim2 method establishes regression model based on the observed data and has tendency to over and under estimate the real values.

Vu et al. (2015), applied the ANN for rainfall downscaling, which is an established technique with a flexible mathematical structure to identify the complex non-linear relationships between input and output. The principal component analysis (PCA) used to select the best correlated predictors for ANN training. The downscaled precipitation shows the upward trends for rainy season over Bangkok by the end of the 21st century. Also, showed that the strong increase in wet statistical indices in future.

Singh and Goyal (2016) conducted a study on change in climate extremes over the Eastern Himalaya region using CMIP5 GCMs with their RCP scenarios. The large variation in temperature and precipitation rates, intensities and frequencies during 1979-2005, 2006-2030, 2041-2065 and 2076-2100. Also, there is a significant increment in the average annual temperature rate for all climate stations. The diurnal variation of temperature is decreased due to increase in minimum temperature after 2030. A

significant geographical variation was observed in temperature datasets.

Impact of Climate Change on Water Resources

The impact of climate change would be more severe on the terrestrial and fresh water ecosystems over the 21st century under different climate scenarios (IPCC, 2014). The availability of water for agriculture, hydropower projects and human consumption is very less and demands are high, so can no longer be taken for granted. Various factors such as ground water depletion (Gleeson et al., 2012), climate change and population increase (Vorosmarty et al., 2000) and snow and glacier melt (Bolch et al., 2012; Immerzeel and Bierkens, 2012) have been documented as contributors for potential water scarcity.

Vorosmarty et al. (2000), presented a high-resolution geography of water use and availability and analyzed the vulnerability of water resources to climate change, population growth and mitigations. The authors concluded that the major increase in relative demand is much higher and world will face the substantial challenges to water resources and associated water services. Where most of the developing countries will face large increase in relative demands. Furthermore, they have concluded that the future global change in population and economic development will tell us about the relations between water supply and demand to climate change. To secure a more complete picture of future water vulnerabilities, it will be necessary to consider interactions among climate change and variability, land surface and groundwater hydrology, water engineering and human systems, including societal adaptations to water scarcity.

Mujumdar and Ghosh (2008), assess the impact of climate change on water resources by downscaling of GCM. Also, characterize the GCM uncertainty associated

with lack of knowledge about underlying geophysical process and future scenarios. The fuzzy clustering and relevance vector machine (RVM) is applied to project monsoon streamflow from three GCMs with two greenhouse emission scenarios. The result indicates that the reduction in probability of occurrence of extreme high flow events in future. Furthermore, the authors concluded that the reduction in Mahandai stream flow is likely to pose a major challenge for water resources engineers in meeting water demands in future.

Allamano et al. (2009), studied the impact of global warming on flood risks in mountain regions and concluded that the mountain basins are at high risk of frequent occurrence floods in future than past due to global warming. The change in both precipitation and temperature seems to be responsible for temporal trend of discharge over the mountain regions. But in the very high elevated (>2000 m) watersheds are lees influenced by temperature increase; those are almost exempt from the effect of small shift of temperature region because they remain always above the freezing level. They also introduced the assumptions that the flood runoff is directly proportional to liquid precipitation and the related proportionality coefficient is not changing with climate change.

Dai et al. (2009), studied the projection of stream flows and result reveals that the large variation in yearly streamflow for most of the larger rivers, where about one-third of the top 200 rivers (including Congo, Mississippi, Yenisei, Parana, Ganges, Columbia and Niger) show the significant increasing trend during 1948-2004. The inter-annual variation are correlated with El Nino–Southern Oscillation (ENSO) events for discharge in to the Atlantic, Pacific, Indian, and global ocean as a whole. Precipitation is a major driver for the discharge trends and large intra-annual to decadal variations.

Li et al. (2011), conducted a study on effect of temperature change on water discharge, sediment and nutrient loading using soil and water assessment tool (SWAT) modeling and resulted that the relative variation of discharge with temperature was small. Whereas the sediment and nutrient loading showed increasing trend with increasing temperature over the lower Pearl River basin. In addition, the warming can reduce the vegetation cover, resulting intensifies the water and soil loss.

Immerzeel and Bierkens (2012), discussed the impact of climate on Asian water towers. These water towers are the major source for irrigation, hydropower projects and human demands. The Indus River basin is the most vulnerable to change in water availability and strongly dependence on glacier melt and ground water together. Whereas, the Ganges River basin is at an intermediate risk also the increasing projection in precipitation and less dependence on glacier melt. In the Brahmaputra River basin, during monsoon season the river basin is risk in terms of occurrence of extreme rainfall and see-level rise, resulting severe flooding.

Mondal and Mujumdar (2015), assessed the impact of climate change on regional hydrology and water resources systems in terms of water availability, irrigation demands and water quality. Climate change is inherently linked with hydrological processes, and can alter the regional water resources system. For example, change in temperature can change the precipitation pattern resulting change in water availability, evapotranspiration, water demands for vegetation and climate extremes of floods and droughts. This includes the description of methodologies developed to address uncertainty associated with human-induced emission and multiple climate models.

Lutz et al. (2016), analyzed the impact of climate change on the upper Indus hydrology and concluded that the future's water availability is highly uncertain in the

long run, mainly due to the large spread in precipitation projections. The long term water availability, basin-wide pattern and trends of seasonal shifts in water availability are still consistent for different climate scenarios. There is a shift in annual hydrograph attenuation and summer peak flow towards the other seasons. Additionally, the increase in frequency and intensity of hydrological extremes (discharge) are expected for most of the upper Indus basin.

2.3 Bivariate Analysis of Climate Extremes

Change in climate extremes is the one of the most important aspect for global climate change (Easterling et al., 2000). The climate extremes are crucial driver of meteorological and hydrological hazards e.g. floods, drought and heat waves etc. (Li et al., 2015). Previously, analysis of climate extreme events using univariate techniques is well documented (Mearns et al., 1984; Katz and Brown, 1992; Colombo et al., 1999; Boo et al., 2006). Therefore, the many hydrological and meteorological studies require joint probability distributions of climate extremes, to represent the joint behavior of extreme events (Zhang and Singh, 2007). Generally, the hydrological processes are highly stochastic and univariate techniques may underestimate and/or overestimate the risk associated with events. Therefore, several researchers focused on multivariate analysis of hydro-meteorological variables (Snyder, 1962; Grimaldi and Serinaldi, 2006; Renard and Lang, 2007; Westra et al., 2007) to understand the joint behavior of hydro-meteorological events. Yue (2001) used the bivariate extreme value distribution with Gumbel marginal to investigate the joint probability distribution of the annual maximum rainfall intensity and amount. In these studies, the precipitation variables having the same marginal distribution, due to this assumption copula is considered as

an important tool for bivariate analysis of climate extremes. For multivariate frequency analysis, copulas are becoming important tool due to its flexibility and no assumption is needed (Favre et al., 2004). Copulas are widely used in different fields such as finance, medicine, hydrological and other civil engineering etc. (Salvadori and De Michele, 2004; Zhang and Singh, 2006, 2007; Wang et al., 2010; Zhang et al., 2012, 2013; Li et al., 2015; Chen et al., 2016), this could improve the existing knowledge of process of various extreme events and provides more information for events prediction.

Favre et al. (2004) used the multivariate hydrological frequency analysis using copulas. The applied methodology was used for two different problems of hydrology. Firstly, they assessed the combine risk in the framework of frequency analysis using four copulas on peak flow of Peribonka watershed, Quebec Canada. Secondly, joint modeling of peak flow and volume using three copulas in Rimouski River watershed, Quebec Canada.

Zhang and Singh (2006) used the copula methods for bivariate flood frequency analysis in terms of flood peak and volume, and flood volume and duration. The copula is used to calculate the conditional return periods for hydrologic design. The result highlights that the copula-based distributions were found to be in better agreement with plotting position-based frequency estimate than other distributions.

Zhang and Singh (2007) have studied the joint distribution of rainfall frequency distribution using Archimedean Copulas and compared among them. The results suggested that the copula methods need no assumptions for bivariate analysis. They also determined the joint and conditional return periods for rainfall data from the Amite River basin in Louisiana, United States.

Kao and Govindaraju (2010) suggested that the current drought information based on indices do not capture the joint behavior of hydrologic variables. In order to address

this limitation, copula is used to characterize the droughts from multi variables. Further, a joint deficit index (JDI) is defined by using the distribution function of copulas to provide the probability based drought status. This JDI also provides the emerging and prolonged drought status with month-by-month drought in future. In addition, JDI allows the construction of inter variable drought index, where precipitation and streamflow marginal dependence structure is preserved.

Wang et al. (2010) have applied tri-variate copula-based modeling for annual extreme rainfall events based on the 15-min time series precipitation data at 12 station of state of Connecticut. Three characteristics (volume, duration and peak intensity) are modeled using multivariate copula. The weights are assigned using kernel function whose bandwidth is chosen by cross-validation in terms of predictive log-likelihood. The result provides the comprehensive knowledge on design storms and risk assessment in Connecticut.

Zhang et al. (2012) studied the joint probability and changing characteristics (spatio-temporal) precipitation extremes across Xinjiang, Chine using copula. The Kolmogorov –Smirnov (K-S) test was used to select the best marginal distributions and Akaike Information Criterion (AIC) was used to select best fit copula. From the observation, it is observed that the north Xinjiang is wetter then south Xinjiang; more co-occurrence of heavy and weak precipitation extremes over the area of Tianshan Mountains and in eastern part of the Xinjiang, indicating the higher risk of co-occurrence of floods and droughts. Further, after 1980, Xinjiang having the tendency of occurrence of heavy precipitation extremes severely and frequently.

Zhang et al. (2013) evaluated the spatio-temporal pattern of precipitation extremes in Chine using copula for the period of 1960-2005. The result indicates that the

north China having wetting tendency as increasing/decreasing number of consecutive rainy/non-rainy days, whereas drying tendency is observed in Yellow River basin, Huaihe River basin, and Haihe River basin. The intensification of precipitation extremes in south China is reflected as decrease in number of rainy days and increase in number of consecutive dry days, indicating that the south China will be at higher risk of droughts.

Li et al. (2015) presented the future joint probability behavior of precipitation extremes in terms of flood and drought hazards across China. To accomplish this study, five Earth System Models (ESMs) with historical, RCP2.6 and RCP8.5 scenarios from Coupled Model Intercomparison Project Phase 5 (CMIP5) datasets are analyzed to examine future (2021-2050 and 2071-2100) joint probability behaviors of precipitation extremes in China. To understand the joint probability behavior, joint return period based on six precipitation extremes are calculated. Joint return period represents the co-occurrence of extreme heavy and weak precipitation as well as heavy precipitation events in terms of defined extreme combinations. The result showed that there is less co-occurrence of consecutive wet and dry days and more joint extreme heavy precipitation events with various aspects, which indicates that the less risk of co-occurrence of floods and droughts in the same year but higher rick of floods in China in future. While north China may face higher risk of co-occurrence of floods and droughts in same year.

Gomez et al. (2016) have used the seasonal copula for glacier discharge analysis at King George Island, Antarctica. In this study, they have proposed the used time-varying copula to analyze the relation between air temperature and glacier discharge, which is clearly non-constant and non-linear with time. Also they have proposed a methodology to generate missing year hydrological discharge data which were not possible to measure

accurately.

2.4 Inventory of Glacial Lakes and Parameters

2.4.1 Glacial Lake Inventory

As per the International Centre for Integrated Mountain Development (ICIMOD), glacial lakes are defined as the sufficient water mass existing and extending with a free surface in, under, beside and/or in front of a glacier originated by glacier activities such as retreating of glacier (Shrestha et al., 2017). The global climate change is the one of the most key factor for shrinkage and retreat of glaciers all around the world and Himalayan region is no exception. The modified glaciated environment can cause the formation of glacial lakes and expansion of their size (Ives et al., 2010).

In mountain terrain, the glacial lakes are an indicator of vulnerability and glacier change, many of them can become the unstable as their size and volume increases and can create hazards to downstream locations (Gardelle et al., 2011). Worni et al. (2013) studied the glacial lakes inventory in the Indian Himalaya to assess the risk and outburst probability with potential outburst magnitude for three of critical lakes from Jammu and Kashmir, Himachal Pradesh and Sikkim. The glacial lakes situated in Jammu and Kashmir and Himachal Pradesh was found to moderate risk for downstream location, whereas the lake in Sikkim severely threatens the downstream locations. The numbers of new glacial lakes are formed and increased existing one in size over last five decades, many examples have been recorded in the Nepal, Bhutan, China, Tibet, Canada, USA and India (Ives et al., 2010). The lakes located at the glacier snout are mainly dammed moraine, these moraine high tendency to breach, such lakes can cause of flash floods at the downstream areas (Jain et al., 2012). Therefore, systematic

inventory and assessment of glacial lakes is important to reduce the possible glacier hazards in terms of risk of GLOFs. The detailed field and remotely senesced survey of individual lake would be useful to assess the glacial lake parameters and its vulnerability (Richardson and Reynolds, 2000; Fujita et al., 2009). In case of Himalayan region, it is not possible to assess all glacial lake for field investigation, therefore the application of remote sensing would be useful tool to explore the glacial lakes and its vulnerability (Worni et al., 2013).

Fujita et al. (2009) studied the recent change in Imja glacial lake Khumbu region, Nepal Himalaya using remote sensing images and bathymetry. The in situ observation of glacial lakes are required because the insufficient accuracy of remotely sensed datasets. From the field observation it is found that the expansion of a glacial lake in terms of volume has occurred not because of melting of bottom ice under deposited debris, but by the calving of a glacier terminus. The Imja glacial lake is still threaten for downstream peoples and environment in terms of GLOF potential. Monitoring of glacial lake area using remote sensing as well as in situ observations would be useful for anticipate GLOF risk.

Jain et al. (2012) utilized the IRS LISSIII remote sensing data for the years 2004, 2006 and 2008 to map the glacial lakes in Garwhal Himalaya. Total 91 glacial lakes were found in the year 2008 and out of them 45 glacial lakes having surface are more the 0.01 km^2. The area of largest lake is 0.193, 0.199 and 0.203 km^2 in the year 2004, 2006 and 2008, respectively, indicating that the area of lake is increased about 0.01 km^2 from 2004 to 2008. The result shows that the no lake is potentially vulnerable to outburst. Additionally, MIKE11 model is used for assessment of GLOF dynamics, largest lake is selected for GLOF study with 40, 60 and 80m breach widths.

Worni et al. (2013) investigated the first area-wide glacial lake inventory and found 251 glacial lakes >0.01 km^2 in the five states of Indian Himalaya. The three glacial lakes were selected from different geographical and climate regions for detailed risk assessment. The application of remote sensing imageries, field observations and use of dynamic model are applied to evaluate the lake outburst probability, potential outburst magnitude and associated damage from the glacial lake. The glacial lakes analyzed and found Jammu and Kashmir and Himachal Pradesh lakes are present moderate risk for downstream location, whereas Sikkim's lake severely threatens the downstream locations.

Rai and Mishra (2017) presented a study, identification of change in glacial lakes over the Chandra Basin and surrounding of Himachal Pradesh, India, using Landsat multispectral and ASTER-DEM remote sensing datasets. The temporal change detection is done for the years 1989-2013, Landsat TM data for 1989 and 2009, ETM+ data for 2001 and OLI-TIRS data for 2013 were analyzed for glacial lakes and glacier boundaries change detection. The result indicated that about 19% of glacial lakes are increased their size over the region. Furthermore the snow and glacier covered are in the same period is reduced from 1,317.39 to 1,125.59 km^2.

Rounce et al. (2017) studied the identification of hazard and risk associated with glacial lakes in Nepal Himalaya using satellite imagery. Total 131 glacial lakes are identified in Nepal Himalaya in 2015 having surface area more than 0.1 km^2. The glacial lake hazard assessment includes moraine stability, mass entering the lakes and expansion of glacial lake in next 15-30 years. The hazards and impacts on downstream were combined to assess the risk associated with each lakes, where 11 lakes are at very high risk and 31 lakes are at high risk. The potential flood volume was also estimated and

used to prioritize the glacial lakes that are the highest risk, which included Phoksundo Tal, Tsho Rolpa, Chamlang North Tsho, Chamlang South Tsho and Lumding Tsho.

Shrestha et al. (2017) have presented the decadal glacial lake changes in Koshi basin, Central Himalaya using Landsat images for the years 1977, 1990, 200 and 2010. The glacial lake inventory result exhibits that in the year 2010 about 2168 glacial lakes are present with the total area of 127.61 km^2 and average size of 0.06 km^2 over the Koshi basin. Out of these lakes, about 47% were moraine dammed lakes, 34.8% bedrock dammed lakes and 17.7% ice dammed lakes. Over the region, number of glacial lakes and their areal extend increased consistently from 1160 to 2168 and 94.44 to 127.61 km^2, respectively, in last 33 years (1977-2010) with the overall growth rate of 86.9%. Total 42 glacial lakes having area more than 0.2 km^2 are rapidly increasing between 1977 to 2010 over the Koshi basin, which need to be more attention to monitoring in the future and to identify how critical they are in terms of GLOF.

2.4.2 Glacial Lake Outburst Parameters

Applications of remote sensing approaches are most suitable for glacial lake detection, but, they are of limited use for modeling processes (Huggel et al., 2002). There are number of empirical models to complement the remote sensing application results. In case of glacier lake hazards, the volume of glacial lake rather than surface area of glacial lake must be known to estimate the actual potential flood discharge during outburst. There is no possible way to directly estimate this parameter from remote sensing data despite a number of efforts to perform mapping of surface water and depth measurements from satellite imagery. To calculate the glacial lake depths from remote sensing based bathymetric, it requires the establish relationship and large number of

glacial lakes over the poorly known high mountainous regions, due to this reason this approach is not feasible for assessment of glacial lake hazards (Baban, 1993). Therefore, the empirical relationships are more suitable to calculate the glacial lake parameters such as depth, volume and potential discharge. A relationship between lake area and lake volume of the Central Oregon Cascade Range derived as (Cook and Quincey, 2015). The volume of lake is:

$$V = 3.114A = 0.0001685A^2 \tag{2.1}$$

This relationship is used by Mckillop and Clague (2007) for prediction of GLOF hazards in British Columbia. Then, Huggel et al. (2002) developed empirical relations based on glacial lake area and mean depth with bias correction, the suggested equations are:

The mean depth (D) of lake is:

$$D = 0.104A^{0.42} \tag{2.2}$$

The lake volume (V) is calculated as:

$$V = 0.104A^{1.42} \tag{2.3}$$

Also, similar expression was defined by the Canadian Inland Water Directorate for glacier-dammed lakes as:

$$V = 0.035A^{1.5} \tag{2.4}$$

Where, A is the surface area of lake, D is the mean depth of lake and V is the volume of lake. The relations suggested by Huggel et al., 2002 has been used by many

researchers such as Mergili et al. (2011); Huggel et al. (2004); Jain et al. (2012).

Baban (1993) established a bathymetric regression empirical relations and compared and evaluated their performance in mapping with other developed equations. The developed equation is compared with previously developed equations. The comparison of bathymetric map with actual depth map indicates that the each of the algorithms was statistically significant and accurate. Also they have recommended, Benny and Dawson algorithms for further use.

Froehlich (1995) developed new empirical expression for estimating the peak outflow width and time of breach from the breached embankment dam. The following developed relations are:

$$D_m = 55A^{0.25} \tag{2.5}$$

$$B = 0.1803K_0V_w^{0.32}h_w^{0.19} \tag{2.6}$$

$$t_f = 0.00254V_w^{0.53}h_w^{-0.9} \tag{2.7}$$

$$Q_p = 1.77h_w^{2.5} \tag{2.8}$$

D_m = mean depth (m)

A = Area of lake (m^2)

B = Average breach width (m)

V_w = Volume of water stored above breach invert level at failure (m^3)

h_w = Height of breach (m)

K_0 = 1.4 for overtopping and 1.0 for piping

t_f = Failure time in hours

Q_p = Peak outflow (m^3/s)

Huggel et al. (2002) have assessed the glacier hazards in terms of glacial lake outburst using remote sensing and empirical relations in Swiss Alps. The three scale level integrating approach includes remote sensing, existing empirical relationships and validating with observations of recent outburst events is used for critical glacial lakes. Remote sensing includes channel indexing, data fusion, and change detection. And empirical relations are evaluated and compare with available datasets. They have also generated a list of decision criteria, those are essential to evaluate the glacier hazard potential of a glacial lake.

Huggel et al. (2004) assessed the glacial hazards over the Swiss Alps with consideration of glaciological, geomorphological and hydraulic principles together with experience gained from previous events. An approach has been used to assess the maximum event magnitude and probability of occurrence using empirical relationships derived for Swiss Alps and other mountain regions. The probability of occurrence of glacial hazards is difficult, therefore the probability is defined in terms of qualitative and systematic indicators e.g. dam type, geometry and freeboard of glacial lakes.

Mckillop and Clague (2007) have provided s framework for preliminary assessment of glacial lake outburst flood hazards in southwestern British Columbia. This framework include the remote sensing applications and existing empirical relations to estimate the peak discharge, maximum volume, maximum travel distance, maximum area of inundation, and probability. The procedure applied in three case studies and shows the

glacial lake outburst flood hazards varies with major change in glacial lake.

Budhathoki et al. (2010) have developed empirical relations between depth-area and area-volume using statistical models. For development of these relations observed data of lake depth, area and volume are used from different literatures. The areas of Imja glacial lake for different years are estimated using satellite images and prepare the map of lake. Further, documented a list of selection criteria to identify the potential hazards of Imja glacial lake. The developed empirical relations are:

$$V = 0.094A^{1.453} \tag{2.9}$$

and

$$D = 0.94A^{0.453} \tag{2.10}$$

Where, A is the Area of lake, D is the depth of lake and V is the volume of lake.

From the analysis of empirical relations and remote sensing applications, it is found that the Imja glacial lake is at moderate risk of outburst.

Fujita et al. (2013) developed a single index to calculate the potential flood volume (PFV) of glacial lakes over the Himalayan region. The index is based on the depression angle from the lakeshore and steep lakefront area (SLA) concept and validated on five lakes in Nepal, Bhutan and Tibet using remote sensing data before these lakes experienced an outburst flood. The PFV is defined as the maximum volume of floodwater that could be released if the lake surface was lowered sufficiently to destroy the SLA. Than they have calculated the PFVs for more than 2000 Himalayan glacial lakes using ASTER DEMs. This PFV approach allows to identify the potential hazardous lake for further field investigations. PFV is the product of minimum value of Hp or Dm and

surface area of glacial lake (A).

$$PFV = min[H_p \ or \ D_m].A \tag{2.11}$$

Where, Hp is the possible lowering height during glacial lake outburst, A is surface area of glacial lake and Dm is the mean depth of glacial lake.

Babu Govindha Raj et al. (2013) assessed the glacial lake hazards using remote sensing application and also assess the probability of occurrence of lake outburst using moraine-dammed lake outburst probability model developed by Mckillop and Clague (2007). The remote sensing data (CORONA to LISS-III) shows the glacier receded about 1.9 km in between 1962-2006 and formed a moraine-dammed glacial lake at the snout of South Lhonak glacier, Sikkim Himalaya. The formed glacial lake outburst probability is about 42%, peak discharge is estimated using empirical equation.

Cook and Quincey (2015) have used the empirical relationships to estimate the volume of Alpine glacial lakes. The used relationships are based on the notion of lake depth, area and volume, and validated these relationships by evaluating the existing global database of glacial lakes (depth, area and volume). The result exhibits that the relation between lake depth and area are not well correlated but the relation between lake area and volume are well correlated. Additionally, develop a conceptual mode based on the volume of lakes with increasing area.

2.5 Hydrological Modeling

The Himalayan glaciers are the one of the most important sources of water supplies for Indian rivers such as Ganges, Brahmaputra, Indus and Teesta etc. Therefore, the effect of climate change on glaciers as melt water will alter the runoff over the glacierized

catchments (Chen et al., 2017). Thus the knowledge of spatiotemporal distribution of water on the surface, sub-surface and groundwater is most important for sustainable management of water resources and mitigation plans from natural hazards such as flooding (Wang et al., 2011). A hydrological model serves as essential tool for water resources management. A several hydrological models have been developed to understand the various hydrological responses. In the glacierized river catchments, many hydrological models have been used, but there is a lack of focus in the glacier discharge modeling (Chen et al., 2017). Hydrological models are classified as empirical, conceptual and physical based model. Empirical model are based on the empirical equations e.g. unit hydrograph, ANN etc. Conceptual models are also called parametric or grey box model, represents complex, spatially variable, hydrological processes in watershed and mathematical expression e.g. MIKE11 NAM, HBV model and TOPMODEL etc. The physical based model resents all hydrological processes based on the physical governing equations e.g. SWAT and MIKESHE model etc. (Chen et al., 2017).

Impact of climate change on water resources and associated natural and man-made systems have received scientific attention especially at the watershed scale (Mondal and Mujumdar, 2015). A term watershed hydrology, defined as the branch of hydrology that deals with the integration of hydrologic processes at the watershed scale to determine the watershed response in terms of water budget, moisture conditions, environmental flow, overland flow, sub-surface flow and groundwater etc. (Singh and Woolhiser, 2002). The effect of climate change on watershed scale is important because of the physical links between hydrological cycle and climate systems can influence the hydrological components as well as streamflow (Mondal and Mujumdar, 2015). Therefore, hydrological modeling is needed to overcome the issues. The change in climate is expected which

can alter the hydrological processes in the form of high intensity and high volume runoff (Ghosh and Dutta, 2012). Therefore, the accurate predictions of watershed parameters are necessary to assess future changes (Singh and Woolhiser, 2002).

Madsen (2000) formulated an automatic calibration of a conceptual rainfall-runoff model (MIKE11 NAM), where the calibration includes optimization of multiple objectives such as overall water balance, shape of hydrograph, peak discharge and low flows. Significant trade-offs between different objectives are observed and found that there is no single set of parameter is able to optimize all the objectives simultaneously. The optimal parameter sets provides a large variability, resulting in a large range of "equally good" simulated hydrographs. A balanced aggregated objective function is proposed, which gives the compromise solution with equal weights to different objectives.

Shamsudin and Hashim (2002) simulated the rainfall-runoff for Layang River using MIKE11 NAM model. The runoff discharge was simulated for the years 1988-2000 and found peak discharge in 1992 and 1995 with values of 20.94 m^3/s and 18.93 m^3/s, respectively. The performance MIKE11 NAM model was evaluated based on the Efficiency Index (EI) and Root Mean Square Error (RMSE).

Thompson et al. (2004) applied the coupled approach of MIKE SHE and MIKE11 modeling for lowland wet grassland in southeast England. They have developed a procedure to evaluate evaporation from ditches which could not be represented dynamically within MIKE11. The model results are consistent with observed data and replicated the seasonal dynamics of groundwater and ditch water. There are improvements which can bypass the MIKE SHE flow routing to represent more accurately macro-pore flow associated with sol cracking and swelling. Dynamic calculation of evaporation from ditches would enhance the model efficiency to explore alternative water level management and

climate change scenarios.

Abbaspour et al. (2007) have used the SWAT model to simulate the related processes which are affect the water quality, sediment and nutrient loads at a watershed scale. Further, SUFI-2 was used for calibration and uncertainty analysis, which is the interface of SWAT. The uncertainty is calculated at 95% prediction and d-factor performed to assess the goodness of calibration. The d-factor is the ratio of the average distance between the above percentiles and the standard deviation of the corresponding measured variable. They have concluded that SWAT model is feasible for flow and transport simulator.

Wang et al. (2011) have applied the Coupled Routing and Excess STorage model (CREST) to simulate the spatial and temporal variation of land surface and sub-surface water fluxes. The CREST model includes distributed rainfall-runoff generation and cell-to-cell routing, coupled runoff generation and routing; and sub-grid cell variability of soil moisture storage capacity and sub-grid cell routing. The coupled approach of runoff generation and routing allows detailed information of hydrological variables. This research presents the model development and its applicability for Nzoia basin, Lake Victoria Africa.

Ghosh and Dutta (2012) studied the climatic effects on flood characteristics over the Brahmaputra River basin and tributary scale by utilizing macro-scale distributed hydrological model (DHM). The performance of DHM is evaluated based on the prediction of flood characteristics such as peak discharge, flood duration, arrival time of flood wave, timing of the peak flow and number of flood waves. Firstly, the DHM is validated and bias-corrected, than used for projection of flood waves using future-projected meteorological scenario from a regional climate model (RCM). Result indicates that the

there is significant increase in simulated peak discharge and flood duration for both pre-monsoonal and monsoonal seasons, whereas reduction in number of flood waves per season. They have concluded, it is expected that there will be more catastrophic flood under the projected climate change scenarios.

De Paiva et al. (2013) presented a hydrologic and hydrodynamic modeling of the Amazon River basin using MGB-IPH model with remote sensing applications. MGB-IPH is the physical based model which solves all the hydrological processes and a gully 1-D hydrodynamic module used. SRTM digital elevation model is used to extract the flood plain geometry parameters. The result indicates that the model is more sensitive to precipitation forcing and flood plain parameters. Most of the errors occur in westerly region because of poor quality TRMM rainfall dataset in the mountainous areas. They have concluded that the hydrological processes of Amazon governs by terrestrial water storage (TWS) changes about 56%, followed by soil water 27% and ground water 8%. Additionally, floodplains play a major role in flow routing, while backwater effects are also important to delay and attenuate flood waves.

Nayak et al. (2013) demonstrate the potential application of conceptual, data driven and wavelet based computing approach for rainfall-runoff modeling for Malaprabha basin in India. The model performance ware evaluated based on the statistical approaches such as Nash–Sutcliffe efficiency (NSE) coefficient and root mean squared error (RMSE). The results were compared and found that the wavelet based computing approach (wavelet neural network, WNN) performs better than data driven (artificial neural network, ANN) and conceptual (MIKE11 NAM) model in estimating the hydrograph characteristics.

Singh et al. (2013) performed hydrological streamflow modeling in Tungabhadra

River Basin utilizing SWAT model and SWAT CUP (Calibration and Uncertainty Program). The sequential uncertainty domain parameter fitting algorithm (SUFI-2) and generalized likelihood uncertainty equation (GLUE) of SWAT CUP used with multiple sets of parameter and allow to use within the slight limitation of the model structure in boundary conditions and field observations. The performance of SUFI-2 and GLUE was evaluated based on the statistical parameters namely P-factor, R-factor, coefficient of determination R^2 and Nash–Sutcliffe (NS). The result indicates that the observed and simulated discharges are significantly correlated at 95% confidence level (95PPU).

Mishra et al. (2014) performed an experiment to understand the effect of watershed slope on rainfall generated runoff and the runoff curve number (CN) using a field plot in Roorkee India. The field plot is covered with maize and sugarcane, where soil falls in the Hydrological Soil Group C. The result highlights that the generation of largest runoff for plot of 5% slope and CN compared with those the plot of 3% and 1% slope for same rainfall, soil and land use. The slope adjusted CN-valued showing the significant improvement at 5% of slope.

Amir et al. (2015) presented a methodology for flood modeling to assess the impact of climate change in the large river basin (Fitzroy basin) using hydrological and hydrodynamic modeling with Geographic Information System (GIS) applications. They have developed the five flood scenarios to analyze the historical floods with conserving three climate change impacts; upstream sub-catchments flooding, local rainfall fluctuations and sea level rise. The hydrological model used to generate the discharge dataset for different climate scenarios over the Fitzroy basin; then integrate the hydrologic-hydrodynamic model, where outputs of hydrologic model are used as upstream boundaries. Using this approach, the peak flood level, peak flow and flood inundation duration

is identified at Rockhampton city. GIS are used for watershed delineation and cross-section generation.

Wang et al. (2016) analyzed the influence of climate change on discharge characteristics over the alpine valley watershed Xinjiang, China using MIE11 NAM rainfall-runoff model. Further, Bi-Gaussian functions are used to characterize the sensitivity of runoff. The result indicates that there are significant correlations and synchronous variations between runoff and precipitation, evaporation and temperature. Precipitation is the influential factor that effects the runoff than other climate variables. The simulated runoff from MIKE11 NAM model shows the change in annual runoff which is related to initial climate condition. Annual runoff will have the increasing trend if it has a strong sensitivity to the initial meteorological condition. Additionally, the runoff has negative relationship with evaporation, whereas it has a positive relationship with temperature and precipitation.

Chen et al. (2017) have applied hydrological modeling to understand the response of meltwater over the glacierized catchments of central Asia and discussed the limitation of other available models and future challenges and directions. From the analysis, the conclusion was that the main sources of uncertainty in assessing the regional hydrological impacts of climate change are unreliable and incomplete as well as lack of understanding of hydrological regimes over the glacierized catchment of central Asia. The quantification of response of hydrological processes is essential for both climate change scenarios and glacier melting.

2.6 Relative Change and its Impact on Annual Runoff

Climate change and global warming are becoming an immense important issue in the field of hydrology is last few decades (Immerzeel and Bierkens, 2012; Kääb et al., 2012). The intensification of the water cycle at a global scale due to global climate change has led to increase in evaporation and precipitation across the globe. Along with climate change, human interactions have also disturbed the global water cycle by withdrawing groundwater, surface water and changing land cover (Findell et al., 2007). Therefore, water availability assessment is essential for a wide range of applications and is substantially determined by the partitioning of precipitation into evapotranspiration and runoff and climate forcing (Zhang et al., 2004; Immerzeel and Bierkens, 2012; Greve et al., 2015). The hydrological responses of a catchment which are affected by vegetation processes, but the it is difficult to develop models that can be used to make predictions at the catchment scales because the lack of understanding of interaction between the processes and data availability (Zhang et al., 2004). The diminishing water supply and variability in the dynamics of hydrological cycle prove the sensitiveness of river basins in India to climate and LULC change. Therefore it is important to analyze the contribution of climate and anthropogenic activities to changes in runoff generation (Jiang et al., 2015) . To assess the water-energy balance, there are number of global and regional land surface models such as hydrological modeling, statistical methods and Budyko framework, but the Budyko framework is the robust approach to evaluate the water-energy balance (Williams et al., 2012; Xu et al., 2013). The Budyko framework is a simple but effective tool for assess the linkages between land surface and climatic factors to characterize the water and energy cycles at catchment scales (Xu et al., 2013).

This framework has been applied globally because of their simple calculation and inclusion of physical mechanisms (Yang et al., 2007; Williams et al., 2012; Xu et al., 2013; Wang and Tang, 2014; Greve et al., 2015; Jiang et al., 2015; Zhang et al., 2015; Gao et al., 2016).

Zhang et al. (2004) have estimated the annual mean evapotranspiration from a catchment using a rational function approach, where precipitation and potential evapotranspiration play primary role and catchment characteristics such as soil, topography etc. play secondary role. The dryness index is used to estimate the mean annual evapotranspiration, which is the ratio of mean annual potential evapotranspiration to precipitation. Over 470 catchments with long-term precipitation, potential evapotranspiration and runoff were used and found modeled results are similar to observed mean annual evapotranspiration (taken as difference between precipitation and runoff). The result highlights that the dryness index is most significant to determine the mean annual evapotranspiration. Also, suggested that the forested catchment tend to show higher evapotranspiration than grassed catchment, indicating that the catchment characteristics are the sensitive parameter over the regions.

Yang et al. (2007) have presented spatial and temporal variability of annual water-energy balance using Budyko hypothesis over the 108 non-humid catchments of China. They have derived the Fu's formula using Budyko hypothesis and optimized with yearly water balance and calibrated with long term mean water balance. The result shows that this derived equation can be used to predict the inter-annual variability of water balance. Also, have proposed an empirical formula for catchment parameter. This empirical equation can predict both long-term mean and annual actual evapotranspiration and inter-annual variability of runoff accurately. This Fu's equation can also be used for

predicting the annual water balance in ungauged basin. Xu et al. (2013) also have used Fu's equation to quantifying water availability partitioning of precipitation into evapotranspiration and runoff. The universal model was developed to predict water energy using Fu's equation from one form of Budyko framework. This developed model would enhance the capability of Budyko framework for water availability assessment at global scale.

Zhan et al. (2014) quantified the change in annual runoff due to climate change and human activities over the Wei River basin, China. Over the Wei River basin, there is dramatic change in surface runoff over the last 51 years (1958-2008). The climate change and anthropogenic activities are the two main factors for dramatic change (decrease) in surface runoff over the Wei River basin, China. Additionally, they developed an improved climate elasticity method based on the original climate elasticity method and found that the climatic impact contribute 37–40% and human activities contribute 60-63% to the decrease in runoff from original climate elasticity method. The results of the improved climate elasticity method show that the climatic impacts and human activities contribute 22-29% and 71-78% to runoff decrease, respectively. This implies that the improved climate elasticity method has a better mechanism than original methods. Further, Jiang et al. (2015) also analyzed the impact of climate change and human activities on runoff changes using Budyko equations with time-varying parameters. A Budyko-type equation is proposed based on four single-parameters to separate the impact of climate change and human activities on runoff during 1960-2009 in Weihe River. The result indicates that the climate change is the primary driving factor to decrease in runoff over the Weihe River, whereas human activities are secondary factor.

Greve et al. (2015) introduced a probabilistic Budyko framework to estimate this partitioning as a function of the prevailing climatic conditions. They have extended Budyko framework by using specific probabilistic estimate of water availability, which accounts the non-linearity of the underlying phase space. This new approach allows to estimate the predictability of water availability that is related to climatic conditions and catchment characteristics. The result supports the practical experience of low predictability catchment runoff under changing climate.

Zhang et al. (2015) have analyzed the effect of snow-ratio on annual runoff using Budyko framework over the 282 catchments across China. The result shows that the decreasing snow-ratio decreases the annual runoff for a given total precipitation. Using Budyko framework, they developed an empirical equation to evaluate the relationship between snow-ratio and annual runoff based on the water-energy balance. Result indicates that annual runoff in northwestern mountainous and northern high latitude areas are sensitive to snow ratio change. The developed model is capable to easily quantify the effect of possible changes in snow-ratio on water resources and their vulnerability to climate change.

Gao et al. (2016) assessed the impact of climate variability and land used land cover (LULC) change on hydrological responses. The elasticity method was used to quantify the streamflow and runoff coefficient responses to various deriving factor over the 15 catchment of Loess Plateau, China during 1961-2009. The elasticity of streamflow and runoff coefficient in terms of precipitation, potential evapotranspiration and catchment characteristics were analyzed using Budyko framework. The catchment characteristics are main factors to affect the hydrological responses in water-limited and humid region and climatic condition play important role where catchment characteristics had a

greater impact. The LULC and production contribute 64.75% and 41.55% to decrease in streamflow, respectively, while LULC and production contribute 75.68% and 32.06% to decrease in runoff coefficient, respectively. In addition, streamflow and runoff coefficient increase about 64.75% and 41.55% due to decrease in potential evapotranspiration.

2.7 Hydrodynamic Modeling and Glacial Lake Outburst Floods (GLOFs)

Floods are the one of the most disastrous natural event in the world, which can cause huge damage. In India several floods have been experienced, those are flooded from the Himalayan rives during monsoon season (Pramanik et al., 2010). The main causes of flood in India are the low carrying capacity of rives due to poor drainage system, poor flood management practices and sedimentation. Therefore, proper flood management plans are needed to minimize the losses from flood. The hydrodynamic modeling can be an important tool to minimize the losses; as it provides the spatial and temporal variation of flow, water depth, velocity and water level etc. using St. Venant equations (Wang et al., 2000; Gottardi and Venutelli, 2004; Pramanik et al., 2010). Models such as MIKE 11HD, HEC-RAS and LISSFLOD-FP have been categorized as hydraulic models, which use the above numerical methods to compute flow and water level at different grid points along the rivers (Gottardi and Venutelli, 2004; Wang et al., 2006; Pramanik et al., 2010). Recently, the integration of geographical information system (GIS) with hydraulic models (HEC-GeoRAS, MIKE11 GIS and Water RIDE FLOOD) are used for river hydraulic computation (Dutta et al., 2000). The hydraulic models such as MIKE 11, HEC-GeoRAS etc. coupled with GIS, use the extracted river geometry (cross-sections) from digital elevation model (DEM) (Worni et al., 2013). The geometry of

rivers is used in hydraulic models to compute the flow, water level and water depth. In this research work, MIKE11 HD model used for hydrodynamic modeling. MIKE11 HD is 1D fully hydrodynamic model is capable to forecast long term water level, discharge and flood area with their water velocities in large scale as well as small scale river watersheds (Thompson et al., 2004; Jain et al., 2012; Thakur et al., 2016).

The Himalayan regions are largest concentration of glaciers outside the polar region (Bajracharya et al., 2007b). There are numbers of major rivers originate from Himalayas; they provide headwater for these rives, which serves water to one-third of humanity. From the previous studies, it is clearly indicated that the Himalayan glaciers are retreating with an unprecedented rate in recent decades. This causes important change in river discharge and has impact on hydropower, agriculture and drinking purposes. Additionally, the retreating of glaciers is the evidence of glacial lake formation and its growth, which increase the risk of glacial lake outburst floods (GLOFs) (Ives et al., 2010; Somos-Valenzuela et al., 2015b). These glacial lakes are potentially threat for human lives, properties and environment in terms of GLOFs (Watanabe et al., 2009). GLOFs are the phenomena which can release huge volume of water in short time duration generating high-velocity, high-discharge and deep flow with high erosive and damaging ability (Clague and Evans, 2000; Breien et al., 2008) and is considered as the essential glacier-related hazard in terms of potential damage (Osti and Egashira, 2009). Therefore, the assessment of GLOF dynamics at regional scale is needed to prepare the effective flood and water management strategies.

Clague and Evans (2000) reviewed the catastrophic drainage of moraine-dammed lakes in British Columbia and found most of the lakes are formed in high mountains due to glacier retreats. There are many glacial lakes, those are susceptible to outburst be-

cause they are steep sided, having low width-height ratios, poorly sorted sediment and contain ice cores and interstitial ice. The failure of moraine dams generated the damaging floods; the magnitudes of these events are much larger than normal stream flow. Dam characteristics, volume of stored water in dam, failure mechanism and downstream topography are the main controlling factors for peak discharge. 20th century climate warming is also responsible for recent moraine dam failures in mountains throughout the world.

Breien et al. (2008) documented erosion and morphology of a debris flow resulting from a glacial lake outburst floods in Fjaerland, Western Norway in 8 May 2004. During outburst the debris flow increases the flow volume with the range of 25000 to 240000 m^3 before depositing about 3 km from its starting point. Airborne laser scanning (LIDAR) and aerial photograph with field investigation used to describe the flow condition. Erosion and bulking was the noticeable feature over the study region.

Osti and Egashira (2009) evaluated flow behavior of Tam Pokhari glacial lake outburst flood occurred in Mt. Everest region, Nepal using hydrodynamic modeling under rigid and erodible boundary conditions. The calculated hydrograph had a peak flood discharge of 10000 m^3/s, was routed through the Inkhu River. The morphologic changes along the river were also analyzed and the results were compared with satellite images, field observations and recorded data. The result reveals that the GLOF event produced the huge amount of debris; about 440000 m^3 of sediment deposited about 14 km downstream from the lake. The estimated flood peak with debris was found about 30000 m^3/s at 14.4 km from lake, which is about 6 time as compare to observe in rigid boundary condition.

Worni et al. (2012) reconstructed the glacial lake outburst caused by the failure

of the terminal moraine of Ventisquero Negro (Patagonian Andes, Argentina) in May 2009 using flied evidence and dynamic dam break modeling. The result exhibits that the main cause of failure of lake was rise in lake level due to heavy precipitation. The lake volume which is about 10 x 106 m^3 was drained out in 3 hours with the peak discharge of 4100 m^3/s with debris cover.

Jain et al. (2012) presented the glacial hazards in terms of GLOF over the Garwhal Himalaya, India. The remote sensing dataset (IRS LISSIII) and hydrodynamic modeling MIKE11 used to assess the GLOF dynamics. IRS LISSIII data for the years 2004, 2006 and 2008 have been used for glacial lake mapping and found total 91 glacial lake in the year 2008, out of them 45 glacial lakes having area more than 0.01 km^2. The vulnerability of glacial lakes were analyzed and found no lake is vulnerable to outburst. Instead of this, biggest glacial lake (area is about 0.203 km^2) selected for GLOF routing using MIKE11 with 100-year return period flood. The results exhibits the flood peak at the outlet of the catchment is to be 993.74, 1184.0 and 1295.58 cumec due to GLOF only, 3274.74, 3465.0 and 3576.58 cumec due to GLOF and 100-year return period flood together considering breach width of 40, 60 and 80 m, respectively.

Schneider et al. (2014) assessed the impact of glacial lake outburst floods from Lake 5013 Carhuaz, Peru due to an ice avalanches. Also, developed an approach to map the GLOF hazards based on the modeling results and field observations. To model the cascade of mass movement in 2010 RAMMS and IBER numerical models have been used. Different avalanches scenarios have been defined based on the existing guidelines and initial avalanches volumes of 450000, 1000000 and 3000000 m^3.

Durga Rao et al. (2014) studied the Chorabari glacial lake outburst in Kedarnath, India in 2013. The hydrological and hydraulic simulation was carried out over the

Mandakini River to quantify the causes of flash floods and their impact. For lake breach parameters, empirical relations are used which are suggested by Froehlich. Additionally, 10 m spatial resolution CARTO DEM used for flood inundation. The result reveals that, the disaster occurred due to integrated of high intensity rainfall and sudden breaching of lake. Das et al. (2015) also presented a study on GLOF at Kedarnath. Three DEM (CARTO, SRTM and ASTER) were used to determine the physical parameters of lake. The calculated parameter used to estimate the peak discharge in predictive empirical equations. The results showed that at least 149 mm of rainfall in its 291-ha catchment was required to fill up the lake, without considering any losses. During outburst, the lake released about 0.43 x $10^6 m^3$ water with the peak discharge of 1352 cumecs. Due to this event creates disaster in the Kedarnath area with loss of human lives and economy.

Anacona et al. (2015b) reconstructed a moraine-dammed glacial lake outburst in Engano valley, Chilean Patagonia that affected a small village in March 1977, by semi structured interviews, interpretation of satellite images and 2D hydraulic modelling. The result provides the insights of GLOF dynamics and planning issues that led to socioeconomic consequences. The model result shows that the 12-13 x $10^6 m^3$ amount of water released with maximum depth of 1.5 m in Bahina Murta Viejo 26 km away from lake. The flood was lasted for about 10 hour. Before the outburst the lake had common failure characteristics such as lake was in contact with retreating glacier and situated by a narrow-steep moraine.

Vilimek et al. (2015) evaluated the geomorphological impacts of the glacial lake outburst from Lake No. 513 (Peru). The GLOF event occurred due to the volume of ice-rock fall which is about 500000 m^3 from 5450m to 5600 m. the basic landforms and processes (erosion and accumulation) were investigated by field observations during

2010 and 2011. Further, remote sensing dataset (1948, 1962, 1970 and 2010) were used to identify the rate of de-glaciation and found about 1040 m glacier retreated in last 62 years with rate of 17 m/year. HEC-RAS model was used to evaluate the potential to erosion and accumulation and compare with real situations (field investigations) after the GLOF events showed.

Westoby et al. (2015) reconstructed a Dig Tsho glacial lake failure in Nepal using numerical based dam-breach and 2D hydrodynamic modeling. To quantify the predictive uncertainty in model output a generalized likelihood uncertainty estimation (GLUE) framework were used. Multiple breach scenarios were produced using different parameters. Downstream routing of scenario-specific breach hydrographs showed that, there are significant differences in the timing and extent of inundation. A GLUE framework used to prepare the probabilistic maps of inundation extent, depth and hazard, which provides the uncertainty in GLOF hazard assessment.

2.8 Conclusion of Literature Review

From the comprehensive overview of literature review, several studies have reported that the climate change is influencing the global and regional hydrological cycle especially in the Himalayan region, resulting water scarcity in future. The average annual temperature has been increased in 20th century and could be more in next century. Climate extremes are also influencing the available water resources in terms of heavy and low precipitation and glacier retreating. The retreating of glaciers is the symbolic evidence of climate change, due to this number of glacial lakes are forming those are threats for mountain communities. Therefore, the assessment of climate extremes and glacier hazards are essential especially over the Himalayan regions. Based on the

literature review following research questions are arise:

1. How the climate extremes are changing with time and space over the North Sikkim Himalaya?
2. How many glacial lakes are appeared and disappeared in last few decades?
3. Is individual lake increasing/decreasing in North Sikkim area?
4. Does formation of glacial lakes of North Sikkim and their growth due to topographic controlling factors?
5. How many glacial lakes are imposing to glacial lake outburst floods (GLOFs)?
6. How GLOF will affect in downstream of Teesta River catchment?

To answer these questions an overall methodology has been adopted which includes downscaling, glacial lake inventory, hydrological modeling and GLOF dynamics shown in Figure 2.1.

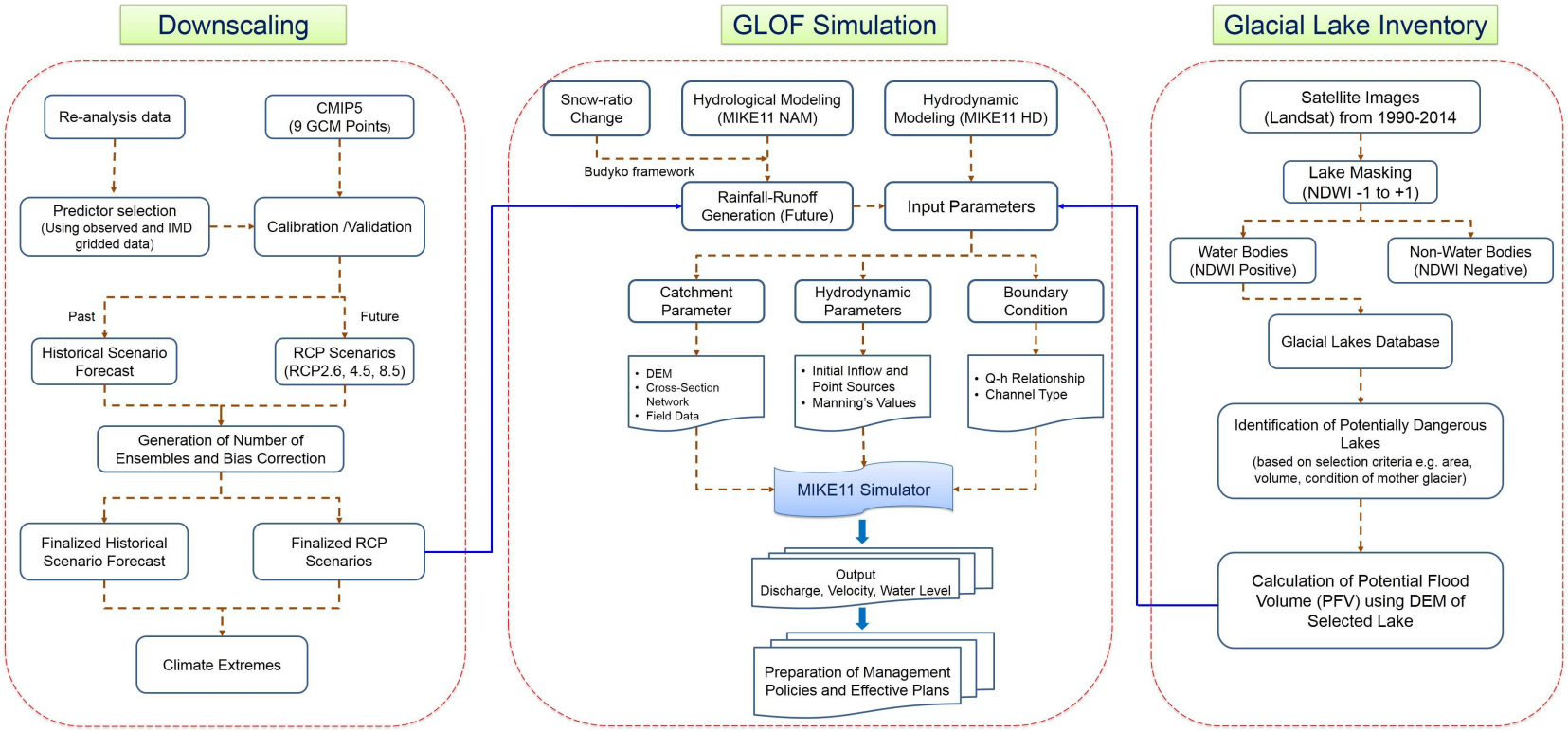

Figure 2.1: Overall methodology framework of the study

CHAPTER 3

Study Area and Data Used

3.1 Study Area – Teesta River and its Major Tributaries

Owing to complex topography of the different parts of sub-Himalayan India, wind circulation pattern and climatic response make it a global discussion issue. In India most major rivers originate from Himalayan glaciers such as Ganga, Brahmaputra, Indus, Sutlej and Teesta etc. Himalayan glaciers are the source of major rivers system in Asia, which serves water to more than 1.3 billion people living in the downstream (Singh and Goyal, 2016; Bajracharya et al., 2007b). Teesta River is also a Himalayan river, which originates from the Tso Lhamo Lake, at 5033 m elevation in the North Sikkim. Pahunri glacier, Khangse glacier and ChhoLhamo lakes are also considered as the sources of Teesta River (Meetei et al., 2007; Singh et al., 2016). The river is formed by two glacier-fed streams Lachen Chhu and Lachung Chhu meeting at Chungthang in North Sikkim. After Chungthang junction, it increases its width with wide loop glowing down to Singhik with elevation drops from 1550 to 750 m. The river flows about 309 km long through the Indian state of Sikkim, joins the Brahmaputra River at Fulchori, Rangpur district, Bangladesh. It is a snow-fed river which receives significant amount of melt

water from glaciers as well as its streamflow runoff depends on the snow cover and glaciers. Over the North Sikkim Himalaya, there are number of valley type glaciers in the Teesta River catchment, among of them Zemu is the largest glacier (Krishna, 2005).

For this study, upper Teesta River catchment (up to Chungthang gauge location), part of north Sikkim Himalaya, Sikkim India, has been considered as study area. Lachung is one of the major tributary of Teesta River also the part of its catchment selected for the study. Chungthang and Lachung are the two gauge stations, which have been taken as outlet of the Teesta and Lachung River, respectively. The Teesta River catchment is located between Latitudes 27°30′ to 28°30′N and Longitudes 87°30′ to 89°30′E in Sikkim Himalaya, Sikkim state of India (Figure 3.1). The study area covers about 2587.4 Km^2. The upper catchment is mostly covered with glacier and snow, while lower catchment covered with forest and hard rocks (Krishna, 2005). The area has predominant steep slopes, varying from 1449 m to 6869 m m.s.l and it has different climatic variability which is characterized by different glacier response. The study are is divided into seven sub-basins (SB), their characteristics are given in Table 3.1.

Table 3.1: Geographic and topographic characteristics of study area at sub-basin scale

Sub-basins	**Lat.**	**Long.**	**Area (km^2)**	**Max. elev (m)**	**Min. elev (m)**
Chopta Valley (SB1)	28.035	88.704	238.46	6652	4714
Thangu (SB2)	27.969	88.556	265.02	6705	3777
Muguthang (SB3)	27.911	88.378	311.76	6868	4382
Lachen (SB4)	27.850	88.272	306.27	6679	3006
Yumthang (SB5)	27.777	88.401	721.8	7392	2612
Lachung (SB6)	27.801	88.802	269.03	6338	2675
Chugthang (SB7)	27.698	88.672	475.06	5442	1495

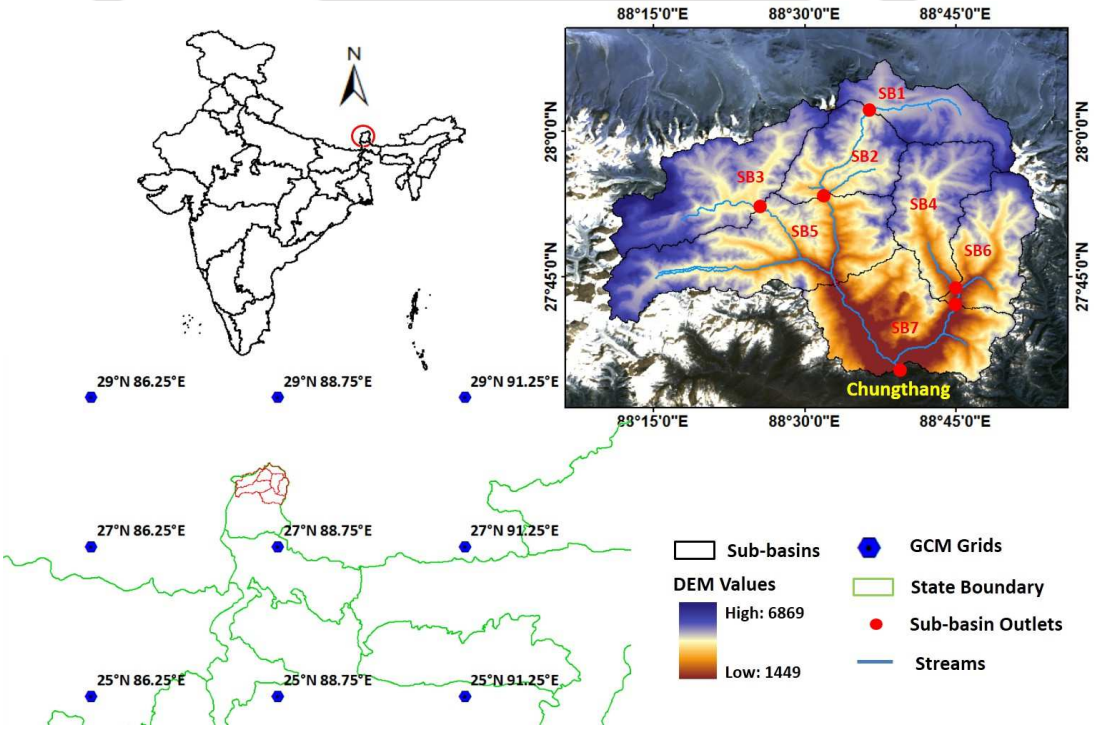

Figure 3.1: Map of study area with GCM grid points over the North Sikkim Himalaya up to Chugthang

Teesta River is a right bank major tributary of Brahmaputra River. The major tributaries of Teesta River are: Rangit River, Talung Chhu River, Rongni Chhu River and Rangpo Chhu River. The largest tributary of Teesta Rivers is Rangit River which originates from Rathong Glacier, West Sikkim and meets at the boarder of Sikkim and West Bengal and its tributaries are Rathong Chhu, Kalej Khola and Rimbi Khola originates from Talung glaciers, West Bengal. At Singhik, Talung Chhu River joins the Teesta River as its tributary which originates from Talung glacier in the Khangchendzonga range. The Rongni Chhu joins at Singtam and Rangpo Chhu River joins at Rangpo. After this Teesta River gradually increases in width and joins major tributary Rangit at the boarder of West Bengal. Then river moves across the Rangpo town where it creates the boundary between West Bengal and Sikkim until it reaches Teesta Bazaar. The major left and right bank tributaries of Teesta river basin are listed in Table 3.2.

Table 3.2: Major left and right bank tributaries of Teesta River

S. No.	**Tributaries**	
	Left-bank tributaries	**Right-bank tributaries**
1.	Lachung Chhu	Rangit River
2.	Chakung Chhu	Rangyong Chhu
3.	Dik Chhu	Zemu Chhu
4.	Rani Khola	
5.	Rangpo Chhu	

3.2 Hydro-meteorological Characteristics of Teesta River Catchment

Sikkim Himalaya is having complex topography, wind circulation and climatic responses. It has various climatic belts such as sub-tropical, temperate and alpine zones from south to north with respect to the altitudinal variation. The meteorological variables such as precipitation and temperature show high variability over the upstream catchment of Teesta River due to its high altitude variations. This area in mainly influenced by south-west monsoon, which normally sets around mid-June and withdraws by end of September. The upstream portion of Teesta River basin where precipitation occurs as snowfall during winter and in the downstream portion, precipitation occurs as rainfall during summer and snowfall during winter. In this study, the upstream portion of Teesta River (up to Chugthang) is considered for research. The average annual precipitation, maximum temperature and minimum temperature are about 2400 mm, 9.76°C and 1.24°C in the catchment, respectively during 1979-2005. The mean monthly precipitation, maximum temperature and minimum temperature over the Teesta River catchment (up to Chugthang) have shown in Figure 3.2. The catchment receives about 75% rainfall during monsoon season and highest in the months of July and August, whereas maximum snowfall receives in the months of February and March. The both maximum and minimum temperatures are highest in the monsoon months (June, July and August) as shown in Figure 3.2. In addition, the mean daily relative humidity is also significantly varying with the ranges of 63.9% to 88.7% over the selected catchment.

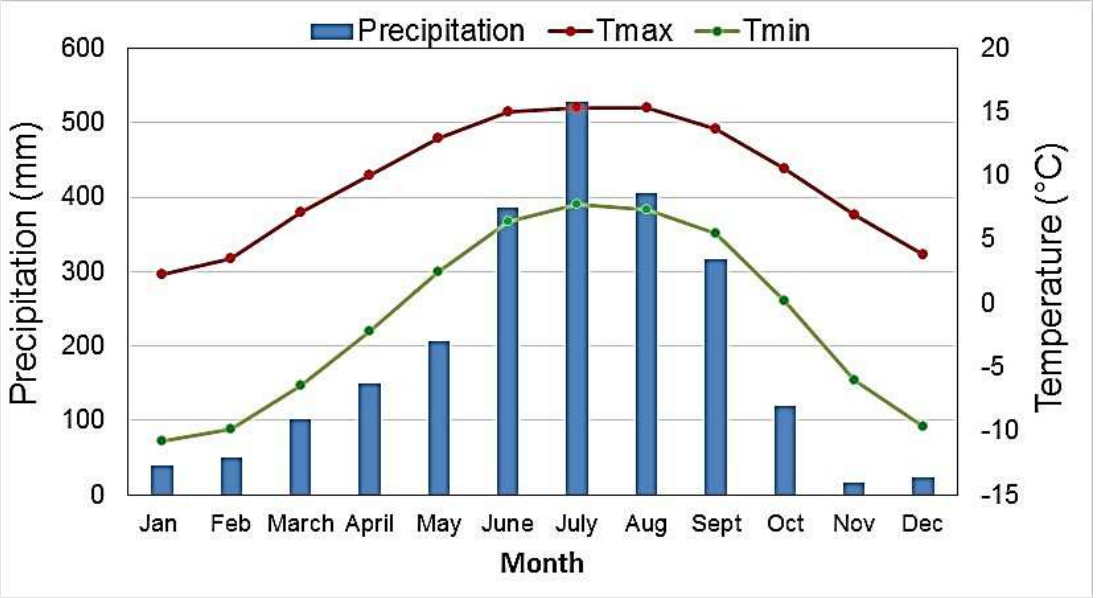

Figure 3.2: Average monthly precipitation and temperature over the selected study area during 1979-2005

3.3 Snow/Glacier Covers over the Teesta River Catchment

To understand the hydrological responses over the glacier/snow faded catchment, the assessment of snow/glacier cover is the important factor. The snow-cover types, glacier characteristics and permanent snowline altitude would be a predominant factor to identify changes in hydrology of such high-mountain catchments (Krishna, 2005). According to the state of environment –Sikkim (2007), the upstream portion of Teesta River is full of permanent snow and glaciers, where 440.24 km^2 are is covered by glaciers and 251.224 km^2 are is covered by snow cover. Krishna (2005), also delineated number of glaciers over the Sikkim Himalaya. Among them Zemu glacier is the largest one followed by Talung, Changsang and others. The Talung has maximum relief which is about 1350m followed by Zemu (1330 m), Tista Kangse (1000 m) and Tongshiong (900 m).

3.4 Geography and Topography of Teesta River Catchment

The upper portion of the catchment area of Teesta River is mostly covered with snow and glaciers and lower portion covered with forest. The Teesta River exhibits large variability in geography such as undulating elevated profile etc. The glacial and periglacial deposition, uneven elevation dissected valleys, undulating plains and floodplains, valley-side slopes and landslide slopes, forest, rich fauna and flora (Singh and Goyal, 2016; Meetei et al., 2007). The Teesta River has formed canyons and narrow valley in Sikkim and highlands with Kalimpong hill. Along the river course, the vegetation cover changes from high elevation zone alpine vegetation to lower elevation zone with tropical deciduous vegetation. It has a rolling to highly hilly topography with maximum elevation of 6869 m and minimum elevation is about 1449 m above mean sea level shown in Figure 3.3.

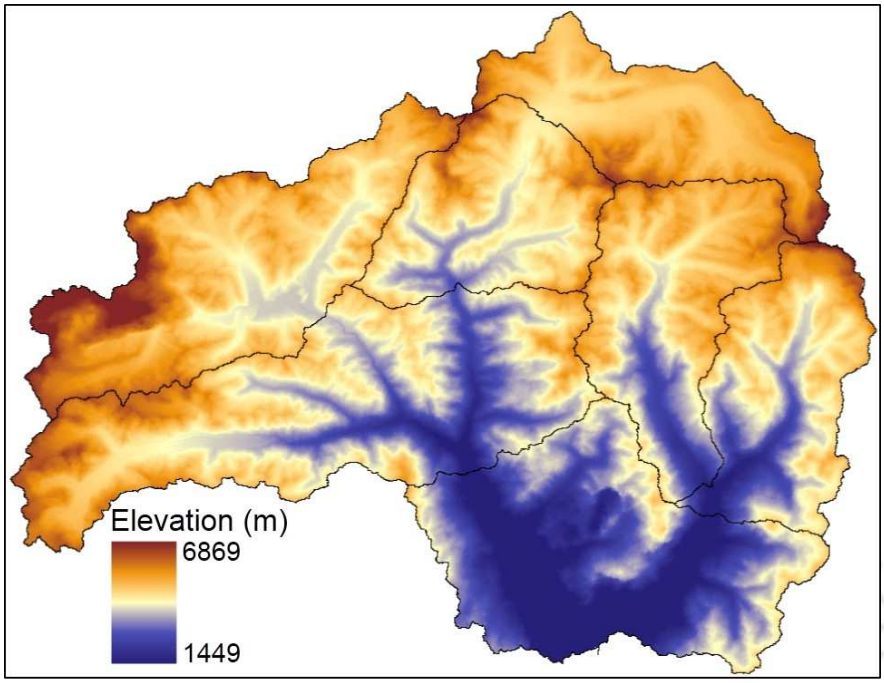

Figure 3.3: Elevation variations over the selected study area.

The landforms in the Teesta river basin is the result of continuous denudation and deposition processes that are constantly modifying the newly formed land forms in the upper reaches existing land forms in the lower reaches. Based upon the geo-morphological ecological and climatic regimes, Teesta basin in Sikkim can be demarcated into five distinct geo-eco-climatic zones such as (2005) (DPR, 2005).

1. Sub-tropic zone up to 1000 m elevation (fluvial processes).

2. Warm temperate zone in between 1000 to 2000 m (fluvial processes).

3. Cold temperate zone in between 2000 to 2500 m (fluvio glacial and fluvial processes).

4. Cold zone between 2500 and 4000 m (peri glacial, fluvial processes).

5. Frigid Zone above 4,000 m (glacial, peri glacial and fluvio glacial processes).

The upper Teesta River basin is characterized by glacial, accumulation of debris, debris avalanches and rock-glaciers. The middle and lower part of the basin is relatively less slope and relatively subdued relief. Teesta and most of its tributaries flow with high velocity and carry boulders and suspended sediment. The flow is turbulent and characterized by high velocities throughout Sikkim.

The Teesta River, north Sikkim Himalaya shows a wide range of soil and vegetation diversity. Figure 3.4 shows the LULC and Soil characteristics of Teesta River (up to Chugthang). The soil map is taken from the Food and Agricultural Organization (FAO) at 1.250000 scale and soil is divided into the three classes shown in Figure 3.4(a). The land used and land cover (LULC) map is prepared from the IRS (Indian Remote Sensing Satellite) LISS III sensor data sets for the period of 2014, it shows eight LULC classes over the region Figure 3.4(b).

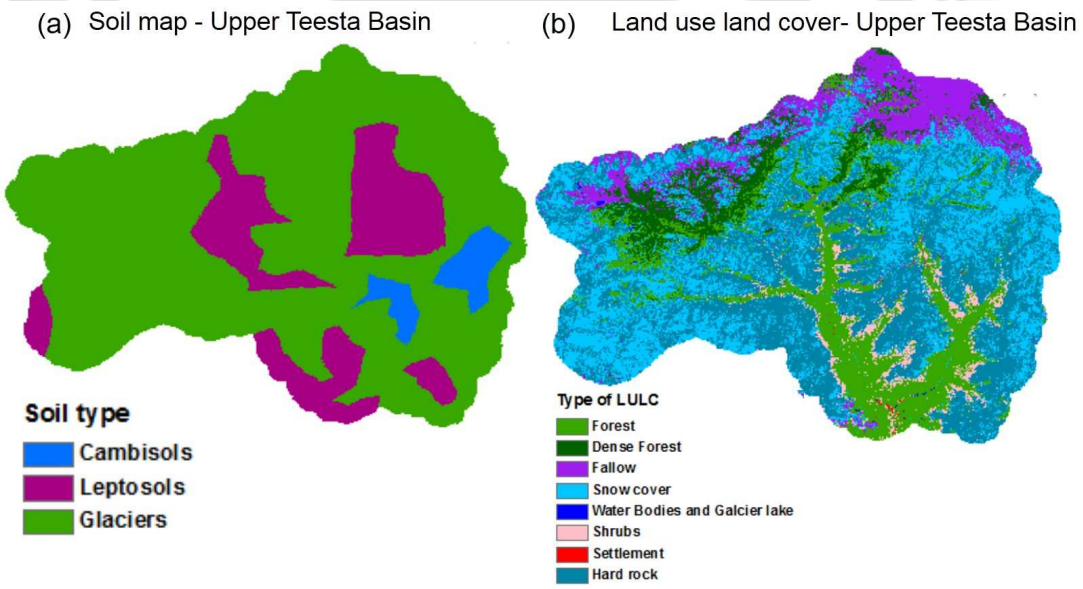

Figure 3.4: (a) Soil map (FAO, 2005) and (b) Land use and land cove (LULC) map of study area.

3.5 Data Used

3.5.1 Observed (1979-2005) Hydro-Meteorological Datasets

A high-resolution daily gridded precipitation ($0.5° \times 0.5°$) and daily gridded temperature ($1° \times 1°$) datasets for the period of 1979 to 2005 (27 years) are available at the Indian Meteorological Department (IMD) and Indian Institute of Tropical Meteorology (IITM) India. This dataset is prepared from quality-controlled observed precipitation/rainfall data from more than 1800 gauges and is increasingly being used in studies on the Indian and Himalayan continents (Subash and Sikka, 2014). Additionally, at Lachung and Chugthang gauge stations, daily observed discharge data sets were collected from Central Water Commission (CWC), India for the years 1991 to 2005 and hence, utilized for the study.

3.5.2 Global Climate Models (GCMs) and their Concentration Scenarios

Coupled Model Inter-comparison Project 5 (CMIP5) models employed by various researchers to downscale various hydro-meteorological variables such as precipitation and temperatures at regional scale (Taylor et al., 2012; Donat et al., 2013; Sillmann et al., 2013b; Singh and Goyal, 2016). The CMIP5 (http://nomads.gfdl.noaa.gov/dods-data/CMIP5/) provides GCM data for various surface and atmospheric variables for different Representative Concentration Pathways (RCPs) scenario. In this study, three CMIP5 models have been taken for analysis namely CM3, ESM2G and ESM2M with three RCPs (RCP2.6, RCP4.5 and RCP8.5). The GCM datasets are at coarser spatial resolution of $2° \times 2.5°$. The RCP represents the radiative forcing values by the end of

the year 2100, where, RCP2.6 is a low emission scenario, represents the radiative forcing would reaches to peak at the middle of the century and decline to 2.6 W/m^2 by end of the twenty first century, RCP4.5 is a moderate emission scenario, the radiative forcing will increase and then stable at the end of the century with 4.5 W/m^2 and radiative forcing in RCP8.5 increases throughout the 21st century before reaching the level 8.5 W/m^2 (Taylor et al., 2012).

Total nine GCM grid points ($2^\circ \times 2.5^\circ$) surrounding by the study area were selected with the most 15 relevant predictors. The GCMs are at coarser resolution, those are not adequate for prediction of climate variables. Thus the downscaling technique (statistical downscaling model, SDSM) is used to downscale the GCM outputs at regional scale (Wilby et al., 2002; Mahmood and Babel, 2013). For downscaling, the observed dataset (1979-2005) used as predictant and National Center for Environmental Prediction (NCEP) and National Center for Atmospheric Research (NCAR) Reanalysis dataset used as controlled scenarios for present time as per the CMIP5 GCMs.

3.5.3 Remote Sensing Dataset

The basic suited material taken for the completion of glacial lake mapping includes different remote sensing images and digital elevation model (DEM). LANDSAT remote sensing images (30 m spatial resolution) for the years 1990, 2000, 2010 and 2014 were used to delineate the glacial lakes and high resolution CARTOSAT DEM with 30 m spatial resolution has been opted from the BHUVAN portal, Indian Space Research Organization (ISRO), India. The DEM is used for better interpretation and calculation of other parameters (e.g. potential flood volume and potential lowering height) of glacial lakes. For clear identification of glacial lakes, satellite images should be cloud free and

least snow cover (Jain et al., 2012). The LANDSAT satellite images area selected for the months such as February and March during accumulation time and October and November during ablation time, less than 10% cloud cover, used for the glacial lakes mapping over the selected study area. The band details of LANDSAT remote sensing datasets are shown in the Table 3.3.

Table 3.3: Band details of LANDSAT remote sensing sensor

Sensors	**Band No.**	**Band Name**	**Band Abbreviation**
LANDSAT 7	Band 1	Blue	B
	Band 2	Green	G
	Band 3	Red	R
	Band 4	Near Infra-Red	NIR
	Band 5	Middle Infra-Red	MIR
	Band 6	Thermal Infra-Red	TIR
	Band 7	Short Wave Infra-Red	SWIR
	Band 8	Panchromatic Band	PB
LANDSAT 8	Band 1	Coastal Aerosol	CA
	Band 2	Blue	B
	Band 3	Green	G
	Band 4	Red	R
	Band 5	Near Infra-Red	NIR
	Band 6	Short Wave Infra-Red 1	SWIR 1
	Band 7	Short Wave Infra-Red 2	SWIR 2
	Band 8	Panchromatic Band	PB
	Band 9	Cirrus	Cirrus
	Band 10	Thermal Infra-Red 1	TIR 1
	Band 11	Thermal Infra-Red 2	TIR 2

CHAPTER 4

Future Projections and Climate Extremes

The CMIP 5 GCMs restricted to direct use of regional impact assessment because of their coarse spatial resolutions and inability to resolve important sub-grid scale features (e.g. clouds and topography) (Wilby et al., 2002). Therefore, the downscaling is the important tool to create a bridge between regional and GCM scale (Mahmood and Babel, 2013).

4.1 Downscaling

Dynamic and statistical downscaling are the two widely used tools to downscale projected scenarios of climate models. The statistical downscaling technique has been used in this study. The statistical downscaling method provides the empirical/statistical relations among the local and global scale variable. This technique is useful for numerical weather prediction and synoptic climatology as well as for climate applications (Mahmood and Babel, 2013). Before applying the downscaling technique, the GCM grid-points have been re-gridded by constructing the combination of GCM grid-points (Table 4.1). The construction of grid-points are based on physical (topographical char-

acteristics such as elevation and land use land cover of area), climatological (climatic variable/factors such as air temperature, relative humidity and wind velocity etc.) and hydrological (rainfall-runoff characteristics) significances. Inverse distance weightage approach, IDWA (Lu and Wong, 2008) was used to re-grid the GCM grid-points for construction of combinations. For example combination 1 is the re-grid point which was constructed with four GCM grid-points (1, 2, 4 and 5) as shown in Table 4.1 and Figure 4.1. Table 4.1 highlights the GCM grid-point locations along with the constructed combinations. Figure 4.1 show examples of how the combinations have been constructed and map of wind circulation.

Firstly, total 14 GCM grid-point combinations are constructed based on the physical, climatological and hydrological significances. Then based on the result analysis, total 7 combinations (shown in Table 4.1) are finalized. The main aim of re-gridding of GCM grid-point or construction of GCM-grid-point combinations is to understand the large area effect on climate variables (precipitation and temperature) over the region. The climate variables (precipitation and temperature) are downscaled at the sub-basin scale, while the results are analyzed at the catchment scale. Sub-basin scale results are not showing significant difference therefore; the results are analyzed at the catchment scale.

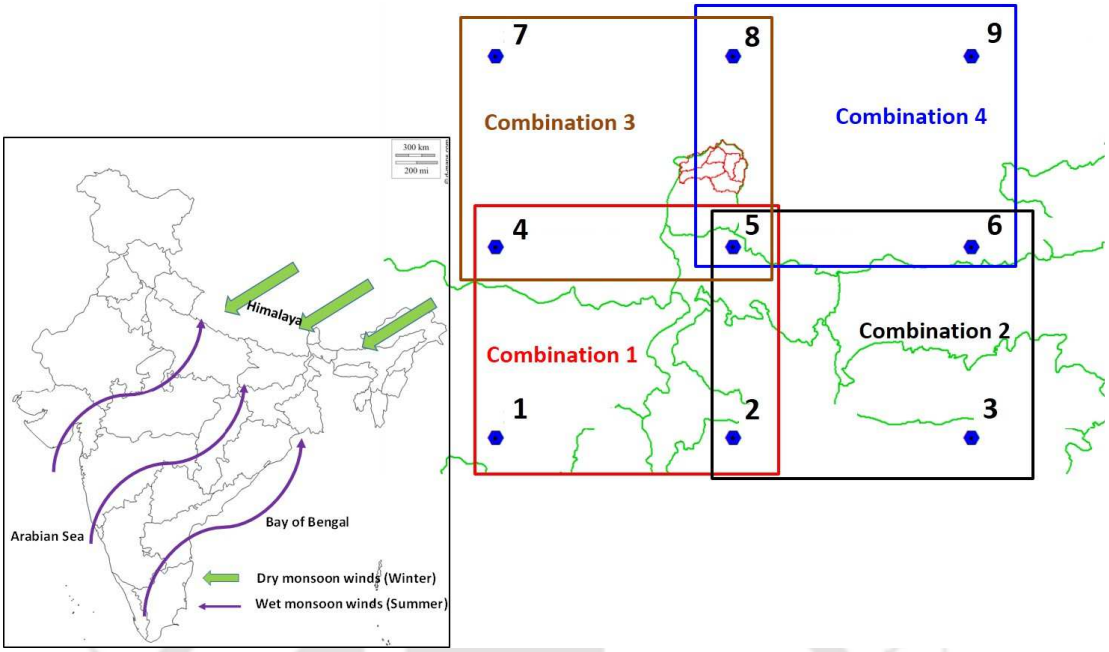

Figure 4.1: Map of wind circulation (left) and examples of constructed GCM-grid point combinations (right).

Table 4.1: GCM grid-point locations and constructed combinations (Cs).

Combinations	**Combination ID**	**Grid point location**
Combination 1	C1	1,2,4,5
Combination 2	C2	2,3,5,6
Combination 3	C3	4,5,7,8
Combination 4	C4	5,6,8,9
Combination 5	C5	1,2,4,5,7,8
Combination 6	C6	2,3,5,6,8,9
Combination 7	C7	4,5,6,7,8,9

Statistical downscaling model (SDSM), which is a combination of stochastic weather generator and multiple linear regressions, and developed by Wilby et al. (2002), was

used to develop statistical relationship between GCMs climatic variables called "Predictors" and the local climatic variable called "Predictands". SDSM can be classified as a conditional weather generator in which regression equations are used to estimate the parameters of daily precipitation and temperature rate and amount, separately, so it is slightly more sophisticated than a straight forward regression model. SDSM performs explained variance analysis, correlation matrix and scatterplot between the predictors and predictands for selection of predominant predictors. Figure 4.2 shows the downscaling steps to downscale GCM outputs. These steps include potential predictor selection using cross-correlation techniques, calibration and validation of developed model using observed datasets, projection of daily incident precipitation based on best calibrated and validated models using CMIP5 datasets, bias correction of projected precipitation.

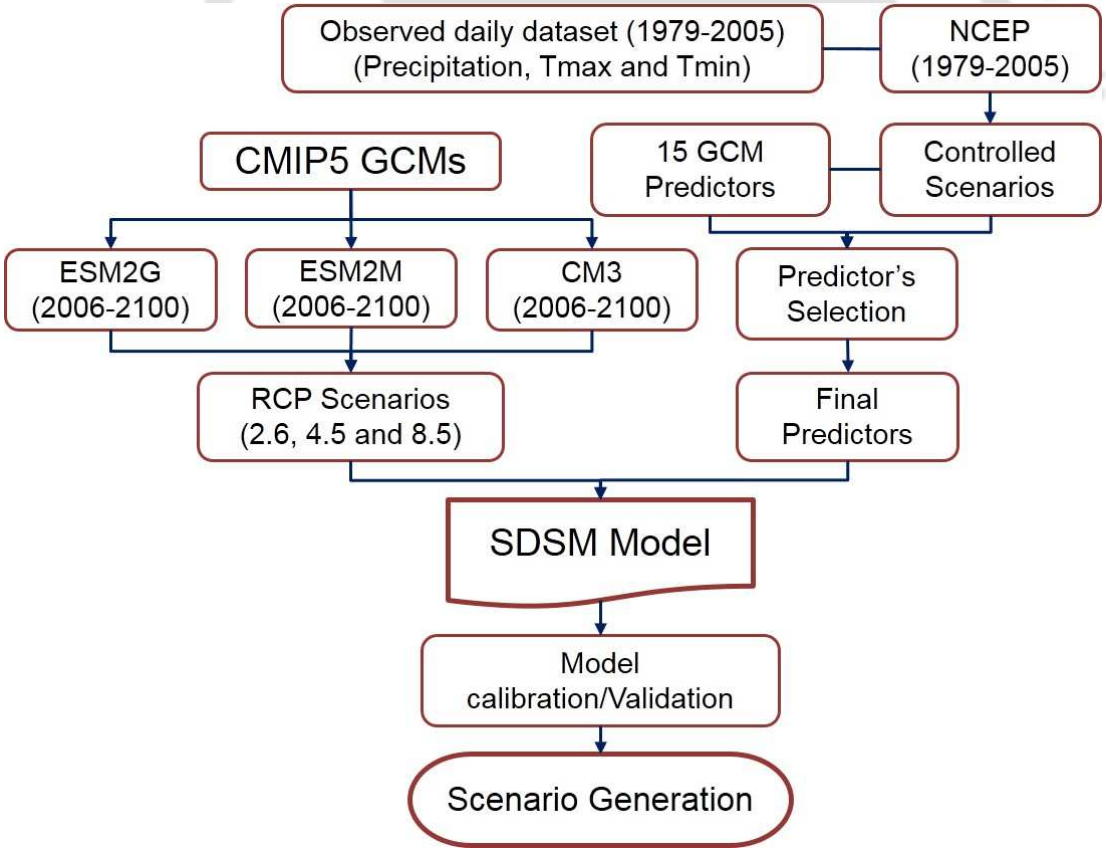

Figure 4.2: Overview of downscaling steps to downscale GCMs.

4.1.1 Predictors Screening

The predictor selection is an important step for establishing regression models between observed and controlled scenario datasets using multi regression analysis. From the generated model negatively correlated predictors has been removed and remaining 15 re-analysis predictors (Table 4.2) were selected to check the best correlation between observed and simulated precipitation. Three main statistical parameters (correlation matrix, partial correlation, and p-value) has been calculated to select the potential predictors for projecting precipitation and temperature (Gagnon et al., 2005). Firstly, correlation matrix is developed between 15 NCEP predictors and predictands and then highest correlated predictor is selected as super predictor (SP). Followed this, the absolute partial correlation coefficient (P.r) is calculated with removing of effect of a set of controlling random variables (SP). Then the other highly correlated predictors are taken out in order to remove any multi-co-linearity. The correlation coefficient up to 0.7 between two predictors is acceptable. Additionally, percentage reduction in an absolute partial correction (PRP) is calculated with absolute correlation for each predictors (Mahmood and Babel, 2013). The PRP is calculated as:

$$PRP = \frac{P.r - R1}{R1} \tag{4.1}$$

Where, PRP is the percentage reduction in partial correlation. P.r is the partial correlation coefficient. R1 is the correlation coefficient between the predictor and predictand. The predictor having minimum PRP is selected as the second most suitable predictor, which shows very less multi-co-linearity with SP. The third, fourth and so on predictors could be selected by repeating the same procedure.

Table 4.2: Re-analysis predictors used for screening process

S. No.	Predictor	Description	Unit
1.	pr	Precipitation flux	Kg.$m^{-2}s^{-1}$
2.	prc	Convective precipitation flux	Kg.$m^{-2}s^{-1}$
3.	tas	Air temperature	°K
4.	tasmax	Daily maximum air temperature	°K
5.	tasmin	Daily minimum air temperature	°K
6.	rhs	Relative humidity at surface	%
7.	rlds	Surface Down-welling longwave flux in air	Wm^{-2}
8.	sfcw	Wind velocity at near surface	ms^{-1}
9.	hfls	Surface upward latent heat flux	Wm^{-2}
10.	vas	Northward wind near surface	ms^{-1}
11.	psl	See pressure level	Pa
12.	hfss	Surface upward sensible heat flux	Wm^{-2}
13.	rsds	Surface Down-welling Shortwave Radiation	Wm^{-2}
14.	uas	Eastward wind near surface	ms^{-1}
15.	rlus	Surface upwelling long wave flux in air	Wm^{-2}

4.1.2 Scenario Generation

A regression model was prepared using observed precipitation and temperature (predictands) with NCEP controlled scenarios during 1979-2005. The dataset divided into two parts for calibration (1979-1995) and for validation (1996-2005). The model per-

formance is evaluated based on the root mean square error (RMSE), Nash-Sutcliff efficiency (NSE) (Nash and Sutcliffe, 1970) , and coefficient of determination (R^2). For the model calibration and parameterization, SDSM is developed on the monthly sub-models. The conditional sub-model is used for maximum and minimum temperature without any transformation and unconditional sub-model for precipitation with fourth root transformations.

Nash-Sutcliff Efficiency

$$NSE = 1 - \frac{\Sigma_{i=1}^{n}(T_{O_i} - T_{P_i})^2}{\Sigma_{i=1}^{n}(T_{O_i} - \overline{T_O})^2} \tag{4.2}$$

Root Mean Square Error

$$RMSE = \sqrt{\frac{\Sigma_{i=1}^{n}(T_{O_i} - T_{P_i})}{n}} \tag{4.3}$$

Coefficient of determination

$$R^2 = \left(\frac{\sum_{i=1}^{n}(T_{O_i} - \overline{T_O})(T_{P_i} - \overline{T_p})}{\left(\sqrt{\sum_{i=1}^{n}(T_{O_i} - \overline{T_O})^2}\right)\left(\sqrt{\sum_{i=1}^{n}(T_{P_i} - \overline{T_P})^2}\right)} \right)^2 \tag{4.4}$$

Where T_{O_i} and T_{P_i} are the i^{th} data point of observed and model generated temperature dataset respectively and $\overline{T_O}$ and $\overline{T_P}$ are the mean of observed and model generated temperature data series respectively. Furthermore, the calibrated and validated models are used for generating the projected scenarios of precipitation and temperature for the period of 2006–2100 for RCP scenarios RCP2.6, RCP4.5 and RCP8.5 using CMIP5 GCM outputs.

4.1.3 Bias Correction

The main drawbacks of CMIP5 GCMs are the biases involved in it, which can lead to insignificant impact assessment. Several methods of bias correction are used by many researchers all around the world for hydro-meteorological variables (Mahmood and Babel, 2013). Thus, the removal of biases from the projected scenarios is important for accurate impact assessment. In this study, following equations are used for precipitation and temperature bias corrections suggested by Mahmood and Babel (2013).

$$T_{deb} = T_{SCEN} - (\overline{T_{CONT}} - \overline{T_{obs}}) \tag{4.5}$$

$$P_{deb} = P_{SCEN} \times \frac{\overline{P_{obs}}}{\overline{P_{CONT}}} \tag{4.6}$$

where T_{deb} and P_{deb} are the de-biased (corrected) daily time series of temperature and precipitation respectively for future periods. SCEN represents the scenario data downscaled by SDSM for future periods (2006-2100), and CONT represents downscaled data by SDSM for the present period (1980-2005). T_{SCEN} and P_{SCEN} are the daily time series of temperature and precipitation generated by SDSM for future periods respectively. T_{CONT} and P_{CONT} are the long term monthly values for temperature and precipitation for the control period simulated by SDSM. T_{obs} and P_{obs} represent the long-term monthly observed values for temperature and precipitation respectively. The bar over P and T shows the long-term average.

4.1.4 Trend Analysis

There are many different ways in which changes in hydro- meteorological series can take place. A change can occur abruptly or gradually (trend) or may take more complex

form. Climate change is often recognized as a progressive trend. There are many approaches that can be used to detect trends and other forms of non-stationarity in hydro-meteorological data (Burn and Hag Elnur, 2002). The trend analysis of hydrologic and meteorological data is one of the important aspects to determine a time dependent variation in the time series. Mann-Kendall and Sen's slope estimator are the two most widely used methods for trend detection.

Mann-Kendall (MK) Trend Test

The non-parametric Mann-Kendall test (Mann, 1945; Kendall, 1948) was applied for detecting the statistically significant or insignificant trend in the time series.The Mann-Kendall test was applied to detect the long term trends in monthly and annual time series of Tmax, Tmin and precipitation. Trends were checked on the 95% confidence interval. Based on this significance level (α), values larger than +1.96 or lower than -1.96, indicated a significantly ($p < 0.05$) increasing or decreasing behavior of the time series, respectively. The Mann-Kendall equations can be described below as The statistics (S) is defined as (Eq. 4.7):

$$S = \Sigma_{i=1}^{N-1} \Sigma_{j=i+1}^{N} sgn(x_j - x_i) \tag{4.7}$$

where N is the number of data points. Assuming $\theta = (x_j - x_i)$, the value of sgn (θ) is computed as follows (Eq. 4.8):

$$sgn(\theta) = \begin{cases} 1 & if \theta > 0 \\ 0 & if \theta = 0 \\ -1 & if \theta < 0 \end{cases} \tag{4.8}$$

This statistics represents the number of positive differences minus the number of negative differences for all the differences considered. For large samples (N >10), the test

is conducted using following Eq. 4.10.

$$E[S] = 0 \tag{4.9}$$

$$\text{var}(S) = \frac{(N(N-1)(2N+5) - \Sigma_{k=1}^{n}(t_k - 1)(2t_k + 5))}{18} \tag{4.10}$$

Where n is the number of tied (zero difference between compared values) groups and t_k the number of data points in the k^{th} tied group. The standard normal deviate (Z-statistics) is then computed as (Eq. 4.11):

$$Z = \begin{cases} \frac{S-1}{\sqrt{var(S)}} & if S > 0 \\ 0 & if S = 0 \\ \frac{(S+1)}{\sqrt{var(S)}} & if \theta < 0 \end{cases} \tag{4.11}$$

If the computed value of $|Z| > Z_{\alpha/2}$, the null hypothesis (H_0) is rejected at alpha (α) level of significance in a two-sided test.

Sen's Slope Method

If a linear trend is present in a time series, then the true slope (change per unit time) can be estimated by using a simple non-parametric procedure developed by Sen (1968)

$$Q_i = \frac{x_j - x_k}{j - k} \tag{4.12}$$

Where x_j and x_k are data values at times j and k (j >k) respectively. The Sen's estimator of slope is the median of these N values of Q_i. A positive value of Q_i indicates an increasing trend and a negative value indicates a decreasing trend in the time series.

4.2 Precipitation Downscaling

The above discussed methodology has been applied on Teesta River catchment. A prepared regression model was used for scenario generation. Firstly, most suitable predictors are selected based on the statistical parameters, those are generated between observed and controlled scenario dataset. For precipitation model, the RMSE, R^2 and NSE values for calibration are 15 to 35 mm, 0.75 to 0.84 and 0.70 to 0.76 for different GCM grid-point combinations and sub-basins. The validation results of RMSE, R^2 and NSE are 18 to 38 mm, 0.71 to 0.78 and 0.70 to 0.75 for different combinations and sub-basins. Based on these statistical parameters, the most predominant predictors are: air temperature (tas) super predictor, daily minimum air temperature (tasmin), convective precipitation flux (prc), daily maximum air temperature (tasmax), relative humidity at surface (rhs) and surface down-welling long-wave flux in air (rlds). After calibration and validation, the developed model is used to project the precipitation scenarios for 21st century time scale for different GCMs and their RCP scenarios. The climate variables (precipitation and temperature) are downscaled at the sub-basin scale, while the results are analyzed at the catchment scale. Sub-basin scale results are not showing significant difference therefore; the results are analyzed at the catchment scale. Figures 4.3, 4.4, 4.5 show the precipitation projections for different scenarios and combinations. The 2nd combination shows the higher projection than other combinations and precipitation is showing significantly steep increasing slope after 2050 for all scenarios and combinations as shown in Figures 4.3, 4.4, 4.5. Additionally, trend detection for different scenarios was analyzed using Mann Kendall and Sen's Slope methods. The result shows the significant increasing trend (at 5% significant level, Z = $\pm$1.96) under

RCP4.5 and RCP8.5 scenarios of three GCMs, whereas under RCP2.6 CM3 also projecting significant increasing trend as shown in Table 4.3. The CM3 model projecting higher range of precipitation as compare to ESM2G and ESM2M model. Table 4.3 indicated the annual precipitation trend (Z- statistics and slope) for GCMs and their RCP scenarios for 2006-2100 time scale.

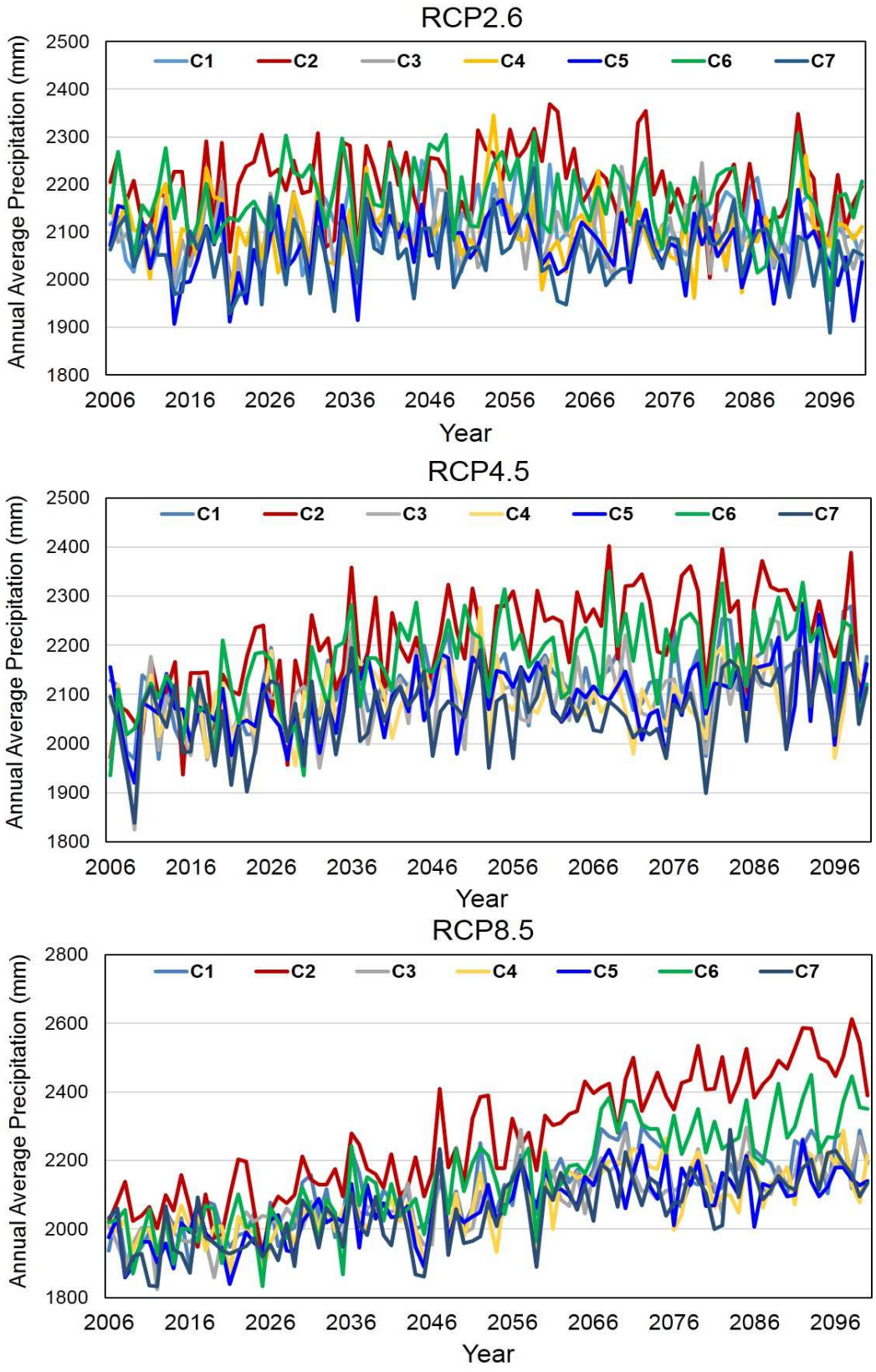

Figure 4.3: Projected annual precipitation for all combinations of ESM2G with RCPs, where Cs' are combinations.

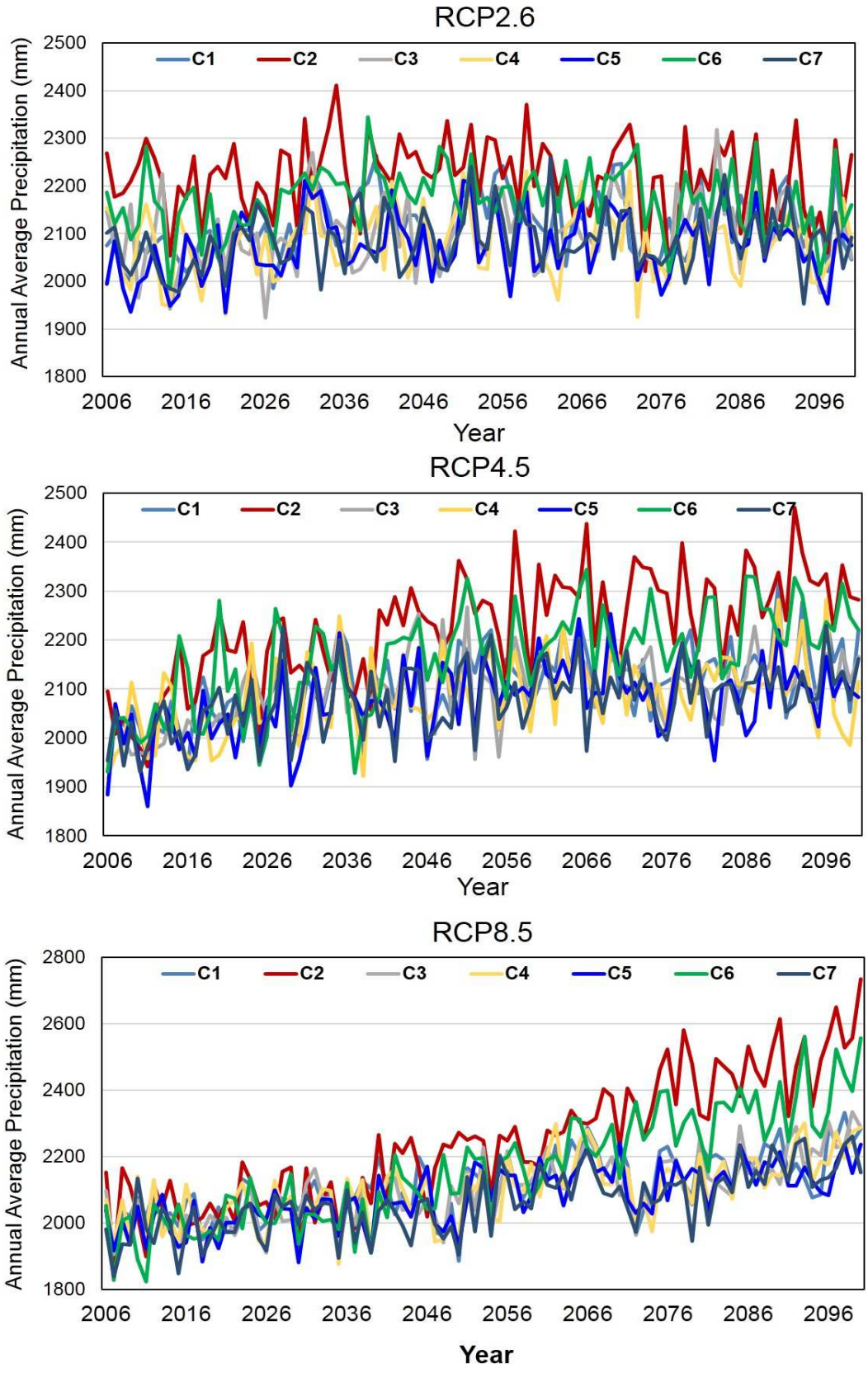

Figure 4.4: Projected annual precipitation for all combinations of ESM2M with RCPs, where Cs' are combinations.

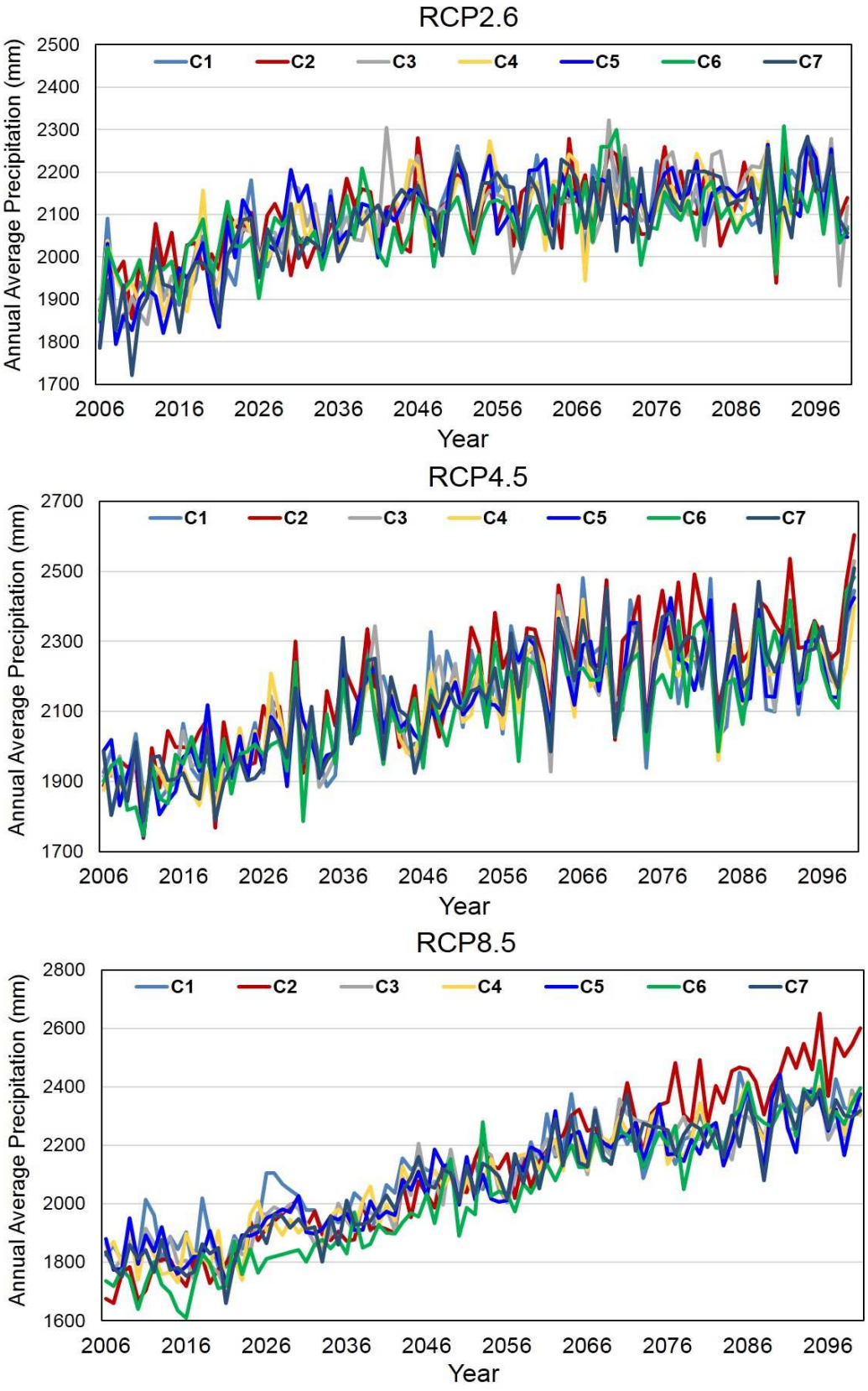

Figure 4.5: Projected annual precipitation for all combinations of CM3 with RCPs, where Cs' are combinations.

Table 4.3: Annual precipitation trend (Z-statistics and slope) for three GCMs with their RCPs over during 2006-2100 at 5% significance level, where Cs' are combinations

ESM2G	Parameter	C1	C2	C3	C4	C5	C6	C7
RCP2.6	Z value	1.41	-0.91	-0.59	-1.04	-0.75	-0.39	-0.21
	Slope	0.37	-0.28	-0.13	-0.27	-0.19	-0.11	-0.04
RCP4.5	Z value	4.93*	6.14*	4.19*	2.80*	3.56*	5.03*	2.43*
	Slope	1.43	2.32	1.17	0.76	0.88	1.60	0.71
RCP8.5	Z value	7.02*	10.32*	7.66*	6.48*	7.12*	9.91*	7.25*
	Slope	2.34	6.20	2.69	2.18	2.20	5.28	2.39
ESM2M	Parameter	C1	C2	C3	C4	C5	C6	C7
RCP2.6	Z value	2.43*	-0.62	1.20	0.44	2.12*	0.23	1.81
	Slope	0.64	-0.21	0.35	0.15	0.53	0.06	0.44
RCP4.5	Z value	5.47*	7.12*	5.01*	3.47*	4.38*	6.26*	4.21*
	Slope	1.54	2.72	1.43	1.18	1.15	2.36	1.16
RCP8.5	Z value	7.93*	10.55*	8.43*	7.02*	7.66*	9.18*	7.49*
	Slope	2.99	5.76	2.64	2.49	2.46	4.39	2.72
ESMCM3	Parameter	C1	C2	C3	C4	C5	C6	C7
RCP2.6	Z value	6.40*	6.18*	7.07*	6.53*	6.33*	5.85*	7.34*
	Slope	2.47	2.04	2.86	2.46	2.57	1.81	2.84
RCP4.5	Z value	7.07*	8.37*	8.12*	8.38*	8.09*	8.07*	8.53*
	Slope	4.10	5.27	4.57	4.29	4.40	4.56	5.02
RCP8.5	Z value	10.49*	12.08*	10.48*	11.09*	10.64*	11.89*	11.01*
	Slope	5.74	9.21	6.12	6.37	6.04	7.75	6.41

Note- * values show the significant increasing (+ve)/decreasing (-ve) trend.

4.2.1 Inter-decadal Variability

The projected precipitation time series are divided into three inter-decadal time scale such as 2021-2047 (20s), 2048-2074 (50s) and 2075-2100 (80s). The precipitation variability for 21st century and inter-decadal (20s, 50s and 80s) are also analyzed and compare with observed precipitation (1979-2005) utilizing box-plots. Figures 4.6, 4.7, 4.8 indicate the box-plot result of GCMs and their RCP scenarios with observed period. A box plot is a graphical interpretation of statistical data based on the minimum, first quartile, median, third quartile and maximum, which provides the information about the distribution such as skewness of dataset. The box-plot result exhibits that the median value of projected precipitation is higher than historical time period for all scenarios except RCP4.5 and RCP8.5 of CM3 model for 2021-2047 (20s). In case of RCP8.5 CM3 during 2021-2047 number of outliers are more, especially for 2nd and 6th combination (Figure 4.8). The variability in precipitation median value is more under RCP8.5 scenario of 80s between the combinations (Figures 4.6, 4.7, 4.8).

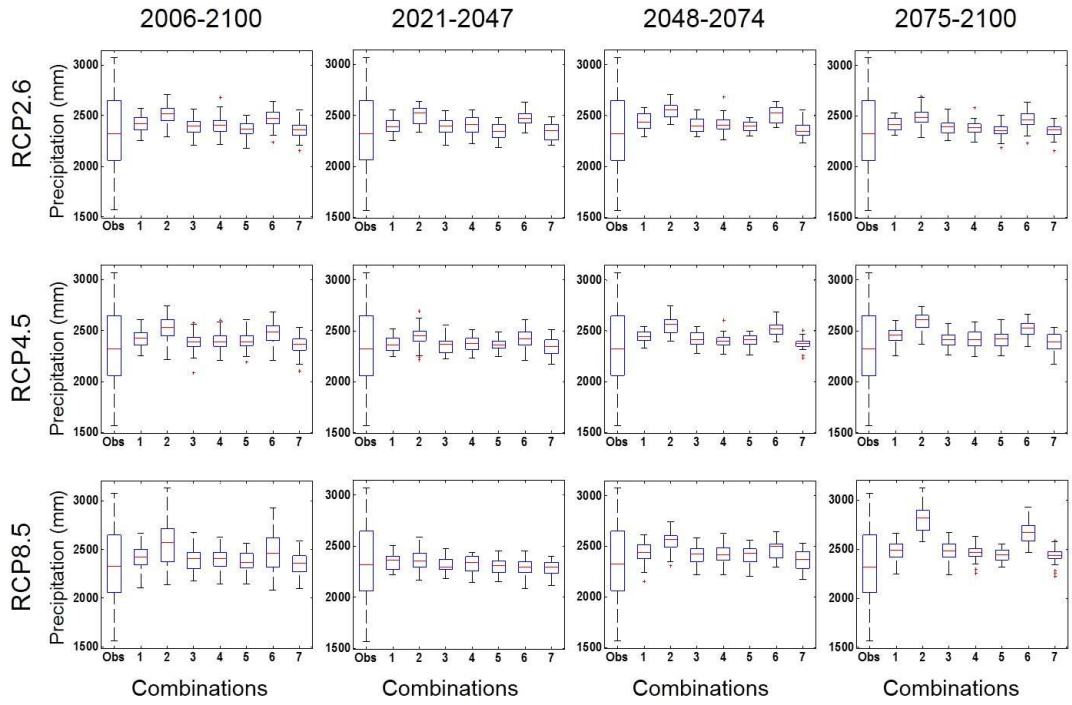

Figure 4.6: Annual variability observed, 21st century and inter-decadal precipitation of ESM2G with their RCP scenarios.

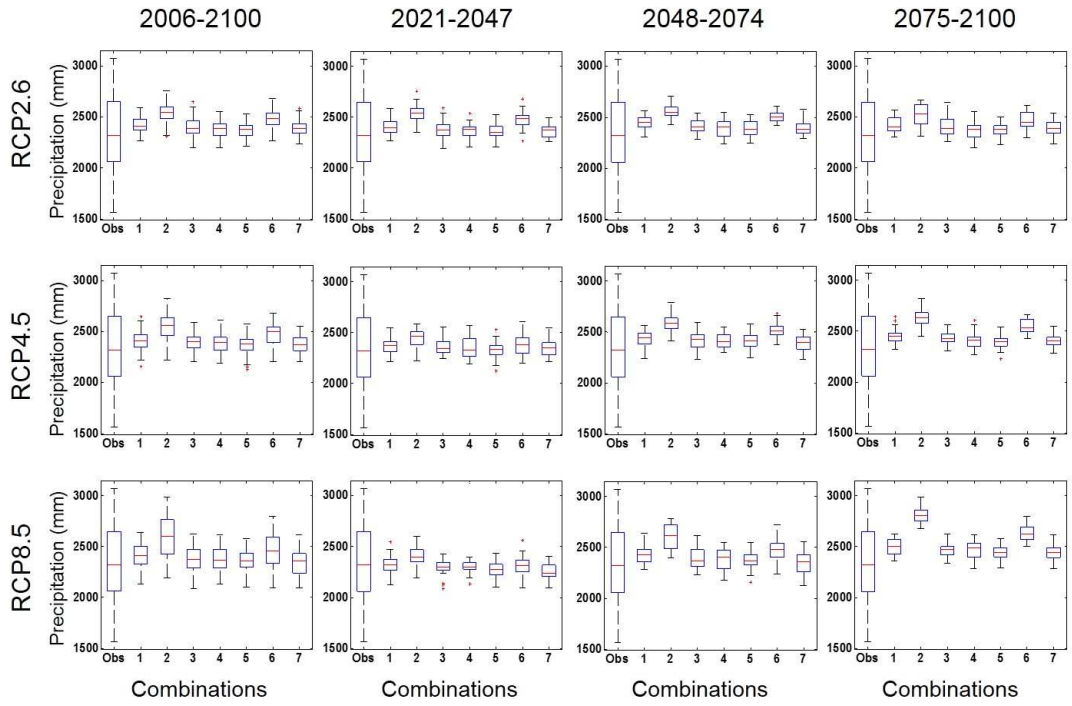

Figure 4.7: Annual variability observed, 21st century and inter-decadal precipitation of ESM2M with their RCP scenarios.

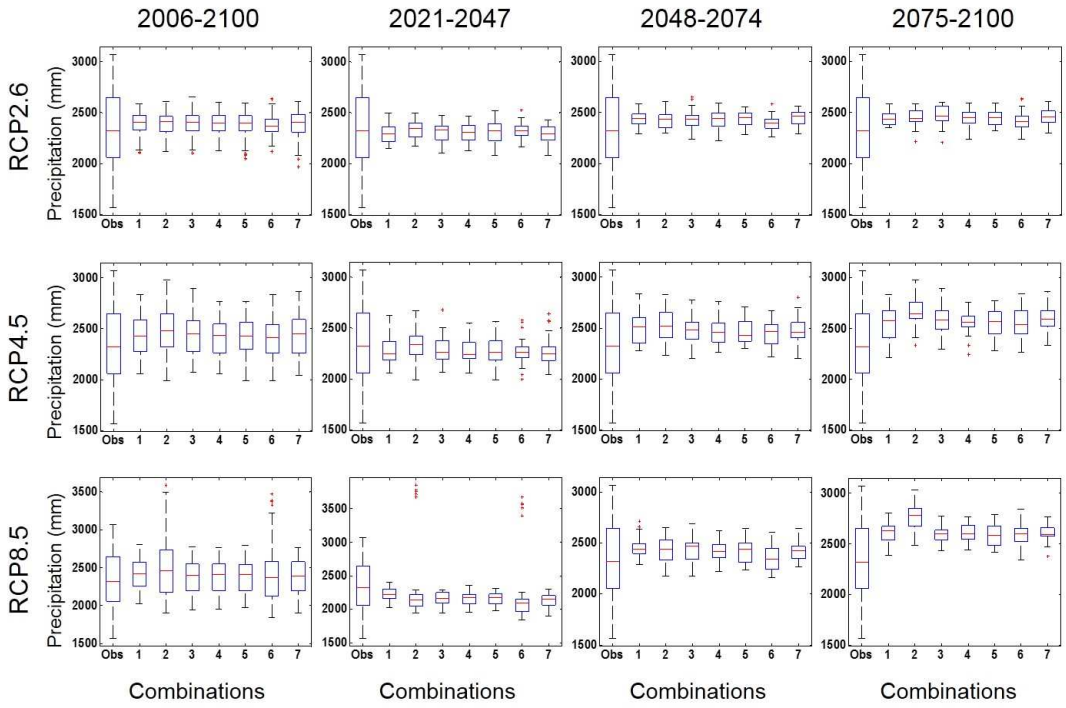

Figure 4.8: Annual variability observed, 21st century and inter-decadal precipitation of CM3 with their RCP scenarios.

4.2.2 Precipitation Extreme Indices

A set of climate extreme indices are selected to obtain insight into the inter-annual variability of precipitation over the region. The selected indices are suggested by the Expert Team on Climate Change Detection and Indices (ETCCDI) (http://etccdi.pacificclimate .org/*list*27*indices*.shtml) (Donat et al., 2013). The precipitation extremes are derived from daily precipitation to evaluate the many aspects of global climate change which include the frequency, intensity and duration of precipitation events. The precipitation extremes make a comparison in the floods and droughts extension. The calculated indices are listed in Table 4.4. The precipitation extreme indices are defined as; wet days (WD), daily intensity (SDII), heavy precipitation days (R10), very heavy precipitation days (R20), very wet day precipitation amount (R95p), extremely wet day precipitation amount (R99p), consecutive wet days (CWD) and consecutive dry days (CDD). In

addition, trends in precipitation extreme indices are assessed using Mann–Kendall test and magnitude of change was estimated from Sen's slopes to predict the rate of change in precipitation and its extremes every year (Burn and Hag Elnur, 2002).

Table 4.4: Definition and description of precipitation indices used in this study

ID	**Descriptive name**	**Indicator Definition**	**Unit**
WD	Wet days	Annual count of days when RR ≥1mm	days
SDII	Simple daily intensity index	Average precipitation on wet days	mm /day
R10	Heavy precipitation days	Annual count of days when RR ≥10mm	days
R20	Very heavy precipitation days	Annual count of days when RR ≥20mm	days
R95p	Very wet day precipitation	Annual total precipitation when RR≥95th percentile on wet days precipitation	mm
R99p	Extremely wet day precipitation	Annual total precipitation when RR ≥99th percentile on wet days precipitation	mm
CWD	Consecutive wet days	Maximum number of consecutive wet days	days
CDD	Consecutive dry days	Maximum number of consecutive dry days	days

The precipitation extremes such as WD, SDII, R10, R20, R95p, R99p, CWD and CDD have been analyzed for different time scale (2006-2100, 2011-2040, 2041-2070 and 2071-2100). The extreme indices are divided into two categories e.g. intensity based

and frequency based indices. The average trend in precipitation indices (frequency based i.e. WD, R10, R20, CWD and CDD) for 21st century time series are shown in Tables 4.5, 4.6 and 4.7 for ESM2G, ESM2M and CM3 models, respectively. Result highlights that wet days (WD), heavy precipitation days (R10) and very heavy precipitation days (R20) are showing significant increasing trend under moderate (RCP4.5) and extreme concentration (RCP8.5) scenarios. CM3 model projecting higher range as well as showing significant increasing trend for all combinations and RCPs. ESM2G and ESM2M model showing similar results, both are showing increasing trend in RCP8.5 and RCP4.5, whereas, no significant trend in RCP2.6. The CWD shows the increasing trend for some of the combinations (Tables 4.5, 4.6 and 4.7), further, CDD are showing no significant trend except some of the combination, where some combinations of CDD are having decreasing trend.

The quantification result shows that the wet days (WDs) are decreased by 2 to 10% during 20s, 50s and 21st century time period, whereas during 80s the WDs are increased about 2% as compare to historical time period (1979-2005) WDs. During historical time period the WDs are about 196 days. The heavy precipitation days (R10) and very heavy precipitation days (R20) are increased for all projected time scale with the range of 16 to 48% and 3 to 50%, respectively as compared to historical period R10 (83 days) and R20 (35 days). In addition, the heavy and weak precipitation in terms of consecutive wet days (CWD) and consecutive dry days (CDD) are decreased for all projected scenarios as compare to historical time period. The CWDs are decreased about 45 to 65% and CDDs are decreased about 28 to 49%, as the historical (1979-2005) average CWD and CDD values are 55 days and 40 days.

Furthermore, the extreme indices such as SDII, R95p and R99p also have been ana-

Table 4.5: Precipitation extreme indices trends (Z-statistics and slope) for ESM2G with different RCPs during 2006-2100 at 5% significance level, where, C's are combination.

Wet days								
Scenarios	**Combination**	**C1**	**C2**	**C3**	**C4**	**C5**	**C6**	**C7**
RCP2.6	Z value	0.2	-0.1	-1.5	-0.9	0.9	1.0	-0.7
	Slope	0.0	0.0	0.0	0.0	0.0	0.0	0.0
RCP4.5	Z value	3.3*	3.1*	2.4*	1.5	2.2*	2.9*	0.9
	Slope	0.1	0.1	0.1	0.1	0.1	0.1	0.0
RCP8.5	Z value	4.0*	6.9*	2.4*	2.0*	1.7	7.1*	2.3*
	Slope	0.1	0.4	0.1	0.1	0.1	0.4	0.1
R10								
RCP2.6	Z value	-1.2	-0.3	-1.5	-0.9	0.2	1.0	-0.9
	Slope	0.0	0.0	0.0	0.0	0.0	0.0	0
RCP4.5	Z value	1.6	3.2*	2.9*	1.5	4.1*	3.3*	0.8
	Slope	0.0	0.1	0.1	0.0	0.1	0.1	0.0
RCP8.5	Z value	4.9*	8.0*	4.2*	3.1*	3.4*	7.1*	3.6*
	Slope	0.2	0.3	0.1	0.1	0.1	0.3	0.1
R20								
RCP2.6	Z value	0.7	-0.5	-1.1	-1.1	-1.7	-0.7	-0.3
	Slope	0.0	0.0	0.0	0.0	0.0	0.0	0.0
RCP4.5	Z value	0.7	1.8	1.7	1.0	2.5*	2.2*	1.2
	Slope	0.0	0.0	0.0	0.0	0.1	0.1	0.0
RCP8.5	Z value	2.2*	7.5*	5.1*	2.5*	3.4*	6.4*	4.0*
	Slope	0.0	0.2	0.1	0.0	0.1	0.2	0.1
CWD								
RCP2.6	Z value	-2.6*	-0.4	0.3	-0.7	-0.4	-0.5	-1.3
	Slope	-0.1	0.0	0.0	0.0	0.0	0.0	0.0
RCP4.5	Z value	-0.5	1.5	0.7	0.3	0.6	1.7	0.1
	Slope	0.0	0.0	0.0	0.0	0.0	0.0	0.0
RCP8.5	Z value	0.6	4.8*	1.5	1.6	1.3	4.0*	2.8*
	Slope	0.0	0.1	0.0	0.0	0.0	0.1	0.1
CDD								
RCP2.6	Z value	0.3	0.3	1.7	0.0	0.3	0.3	1.6
	Slope	0.0	0.0	0.1	0.0	0.0	0.0	0.1
RCP4.5	Z value	0.7	-1.8	0.3	-0.2	-0.2	-2.2*	0.6
	Slope	0.0	-0.1	0.0	0.0	0.0	-0.1	0.0
RCP8.5	Z value	-1.8	0.1	0.6	0.2	-1.3	-0.3	-0.1
	Slope	-0.1	0.0	0.0	0.0	0.0	0.0	0.0

Note- * values show the significant increasing (+ve)/decreasing (-ve) trend.

Table 4.6: Precipitation extreme indices trends (Z-statistics and slope) for ESM2M with different RCPs during 2006-2100 at 5% significance level, where, C's are combination.

Wet days								
	Combination	**C1**	**C2**	**C3**	**C4**	**C5**	**C6**	**C7**
RCP2.6	Z value	1.3	0.3	0.7	1.5	2.0*	1.8	1.1
	Slope	0.1	0.0	0.0	0.1	0.1	0.1	0
RCP4.5	Z value	3.6*	4.8*	3.6*	2.9*	4.4*	4.2*	1.9
	Slope	0.2	0.2	0.1	0.1	0.2	0.2	0.1
RCP8.5	Z value	4.1*	6.1*	4.2*	3.7*	3.9*	5.6*	4.5*
	Slope	0.2	0.3	0.1	0.1	0.1	0.3	0.2
R10								
RCP2.6	Z value	0.3	0.4	1.5	-0.1	1.4	1.1	1.3
	Slope	0.0	0.0	0.0	0.0	0.0	0.0	0.0
RCP4.5	Z value	3.9*	3.8*	1.6	2.2*	3.1*	5.2*	1.8
	Slope	0.1	0.1	0.1	0.1	0.1	0.2	0.1
RCP8.5	Z value	3.6*	7.6*	4.0*	4.3*	4.8*	6.5*	5.9*
	Slope	0.1	0.3	0.1	0.2	0.1	0.2	0.2
R20								
RCP2.6	Z value	-0.6	-0.3	0.1	-0.2	0.6	-0.3	0.4
	Slope	0.0	0.0	0.0	0.0	0.0	0.0	0.0
RCP4.5	Z value	1.4	3.0*	-0.2	2.9*	2.7*	3.8*	1.8
	Slope	0.0	0.1	0.0	0.1	0.1	0.1	0.0
RCP8.5	Z value	3.1*	5.5*	3.2*	2.5*	3.3*	6.7*	5.0*
	Slope	0.1	0.2	0.1	0.1	0.1	0.2	0.1
CWD								
RCP2.6	Z value	-1.7	-1.1	1.1	1.3	-0.9	0.9	-0.5
	Slope	0.0	0.0	0.0	0.0	0.0	0.0	0.0
RCP4.5	Z value	1.5	2.8*	1.0	-0.7	2.6*	3.2*	0.0
	Slope	0.0	0.1	0.0	0.0	0.1	0.1	0.0
RCP8.5	Z value	0.8	3.7*	1.0	2.6*	-0.4	3.8*	2.1*
	Slope	0.0	0.1	0.0	0.1	0.0	0.1	0.0
CDD								
RCP2.6	Z value	-0.9	0.3	0.9	-0.2	0.1	1.0	-0.3
	Slope	0.0	0.0	0.0	0.0	0.0	0.0	0.0
RCP4.5	Z value	-2.2*	0.5	0.2	-1.5	-0.6	0.5	-0.7
	Slope	-0.1	0.0	0.0	-0.1	0.0	0.0	0.0
RCP8.5	Z value	-2.6*	0.5	-1.6	-1.9	-0.2	2.2*	-1.9
	Slope	-0.1	0	-0.1	-0.1	0	0.1	-0.1

Note- * values show the significant increasing (+ve)/decreasing (-ve) trend.

Table 4.7: Precipitation extreme indices trends (Z-statistics and slope) for CM3 with different RCPs during 2006-2100 at 5% significance level, where, C's are combination.

Wet days								
	Combination	**C1**	**C2**	**C3**	**C4**	**C5**	**C6**	**C7**
RCP2.6	Z value	5.3*	3.1*	4.6*	6.8*	5.9*	4.1*	5.7*
	Slope	0.2	0.1	0.2	0.3	0.3	0.2	0.2
RCP4.5	Z value	5.4*	7.9*	7.0*	5.9*	6.5*	5.4*	8.0*
	Slope	0.3	0.5	0.4	0.3	0.4	0.3	0.4
RCP8.5	Z value	7.3*	7.0*	8.1*	8.8*	8.3*	7.4*	9.1*
	Slope	0.4	0.5	0.5	0.6	0.5	0.5	0.5
R10								
RCP2.6	Z value	4.1*	2.7*	4.1*	5.4*	5.7*	3.3*	4.4*
	Slope	0.1	0.1	0.2	0.2	0.2	0.1	0.1
RCP4.5	Z value	6.1*	7.4*	6.3*	5.2*	6.2*	6.0*	7.1*
	Slope	0.3	0.4	0.3	0.2	0.3	0.3	0.3
RCP8.5	Z	7.6*	7.5*	8.6*	9.1*	7.8*	7.7*	8.7*
	Slope	0.3	0.4	0.3	0.4	0.3	0.4	0.4
R20								
RCP2.6	Z value	3.3*	0.9	2.5*	1.7	2.7*	3.3*	2.7*
	Slope	0.1	0.0	0.1	0.0	0.1	0.1	0.0
RCP4.5	Z value	4.4*	7.8*	3.4*	3.7*	3.9*	6.3*	4.8*
	Slope	0.1	0.3	0.1	0.1	0.1	0.2	0.1
RCP8.5	Z value	5.9*	7.0*	4.7*	6.7*	5.1*	7.1*	6.1*
	Slope	0.1	0.3	0.1	0.2	0.1	0.3	0.2
CWD								
RCP2.6	Z value	1.8	1.5	0.2	2.2*	1.0	2.5*	0.3
	Slope	0.0	0.0	0.0	0.0	0.0	0.1	0.0
RCP4.5	Z value	1.8	5.7*	2.1*	2.3*	1.9	2.3*	3.7*
	Slope	0.0	0.3	0.0	0.1	0.0	0.1	0.1
RCP8.5	Z value	4.1*	4.2*	3.4*	2.9*	3.1*	4.1*	3.7*
	Slope	0.1	0.1	0.1	0.1	0.1	0.1	0.1
CDD								
RCP2.6	Z value	0	-0.8	0.1	1.0	-1.4	0.5	-0.2
	Slope	0.0	0.0	0.0	0.0	0.0	0.0	0.0
RCP4.5	Z value	-0.8	0.6	-3.6*	-1.3	-0.8	1.6	-4.3*
	Slope	0.0	0.0	-0.1	0.0	0.0	0.0	-0.1
RCP8.5	Z value	-1.1	-1.3	-0.2	-0.7	-0.9	0.8	0.1
	Slope	0.0	0.0	0.0	0.0	0.0	0.0	0.0

Note- * values show the significant increasing (+ve)/decreasing (-ve) trend.

lyzed and found no significant change except some of the combination of extreme RCP scenario (RCP8.5) in precipitation intensity (SDII). The changes in precipitation intensities for different decadal time series are 1.28 to 2.25 mm/day for 20s, 1.35 to 2.09 mm/day for 50s, 1.65 to 2.87 for 80s and 1.51 to 2.32 for 21st century. The precipitation intensity is increased about 10 to 23% for different scenarios and time scale. These changes are quantified with historical (observed precipitation intensity is about 12.17 mm/day during 1979-2005) time series. Additionally, R95p and R99p have been quantified and found there is slight increase with the range of 0.5 to 17 % and 1 to 16%, respectively.

4.3 Temperature Downscaling

The SDSM is also used to downscale GCM outputs of minimum and maximum temperature over the study area. Firstly, most suitable predictors are selected based on the statistical parameters, those are generated between observed and controlled scenario dataset. For minimum temperature model, the RMSE, R^2 and NSE values for calibration are 0.91 to 0.94 °C, 0.93 to 0.94 and 0.89 to 0.93 for different GCM grid-point combinations. The validation results of RMSE, R^2 and NSE are 0.94 to 1.04 °C, 0.89 to 0.92 and 0.87 to 0.91 for different combinations. In case on maximum temperature, the RMSE, R^2 and NSE values for calibration are 0.86 to 0.91 °C, 0.85 to 0.88 and 0.87 to 0.90 for different GCM grid-point combinations. The validation results of RMSE, R^2 and NSE are 0.89 to 0.98 °C, 0.81 to 0.86 and 0.84 to 0.87 for different combinations. Based on these statistical parameters, the most predominant predictors are: air temperature (tas) super predictor, daily minimum air temperature (tasmin), convective precipitation flux (prc), daily maximum air temperature (tasmax), relative humidity at

surface (rhs) and surface down-welling long-wave flux in air (rlds). After calibration and validation, scenarios have been generated based on the developed SDSM model for both maximum and minimum temperatures. Apart from this, Mann Kendall's Z and Sen's slope, the two most commonly and widely used trend analysis methods are applied. Before applying the Mann-Kendal's and Sen's Slope trend methods, the auto-correlation test were used to check the correlation between time series and found that there is no correlation in any time series. The trend analysis result shows that the minimum temperature has significant rising trend for most of the months (Figure 4.9), whereas maximum temperature shows the no significant trends except July and December months at 5% significant level. Figure 4.9 shows the observed (1979-2005) monthly Z-statistics values of minimum and maximum temperatures with 5% significant level.

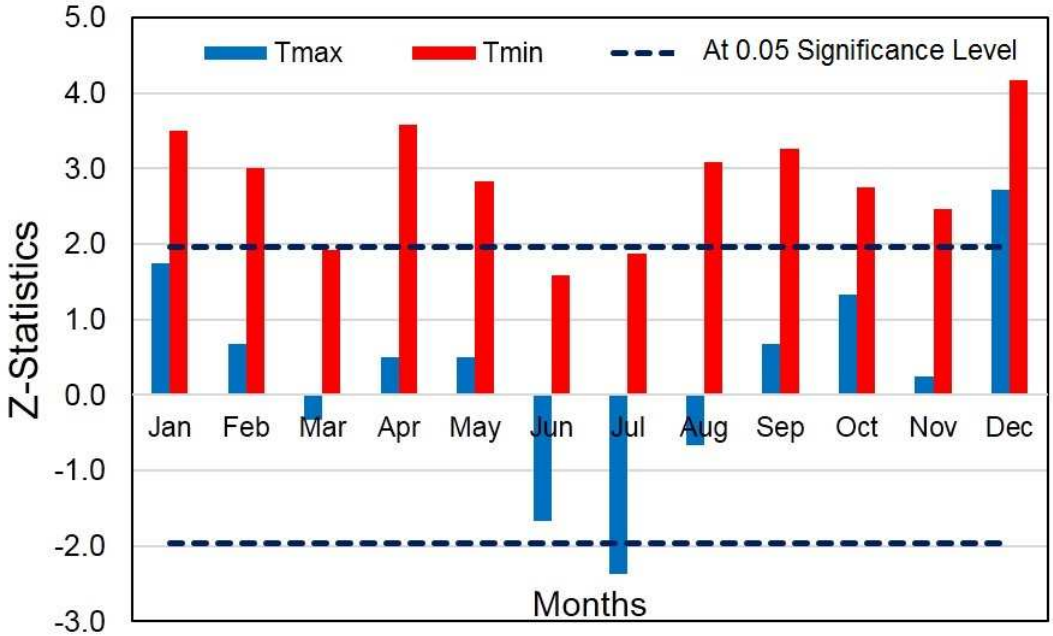

Figure 4.9: Trend analysis results (Z- Statistics) of minimum and maximum temperature for observed time series from 1979-2005.

4.3.1 Minimum Temperature

4.3.1.1 Monthly variability of 21st century data series

The trend analysis methods are also applied on the projected scenarios from CMIP5 GCMs and their scenarios monthly basis. Result indicates the similar pattern as found in observed monthly trend analysis results. The trend analysis result of CMIP5 model and their RCP scenarios exhibits the rising trend in all months for RCP4.5 and RCP8.5 scenarios except some of the combinations (2nd and 6th) of January month. Figures 4.10, 4.11 and 4.12 show the monthly Z-statistics of minimum temperature with threshold of 5% significance level. Under RCP2.6 of CM3 model projecting upward trend for all months except some of the combination of January and February months. The quantification of change in projected temperature ranged from -0.630°C to 0.454°C for monsoon months, -0.863°C to 0.95°C for winter months and -0.756°C to 0.488°C for spring months as compare to historical period. The maximum projected change found in CM3 model in all months except January, September and December months and minimum projected change in ESM2G model for all months and combinations.

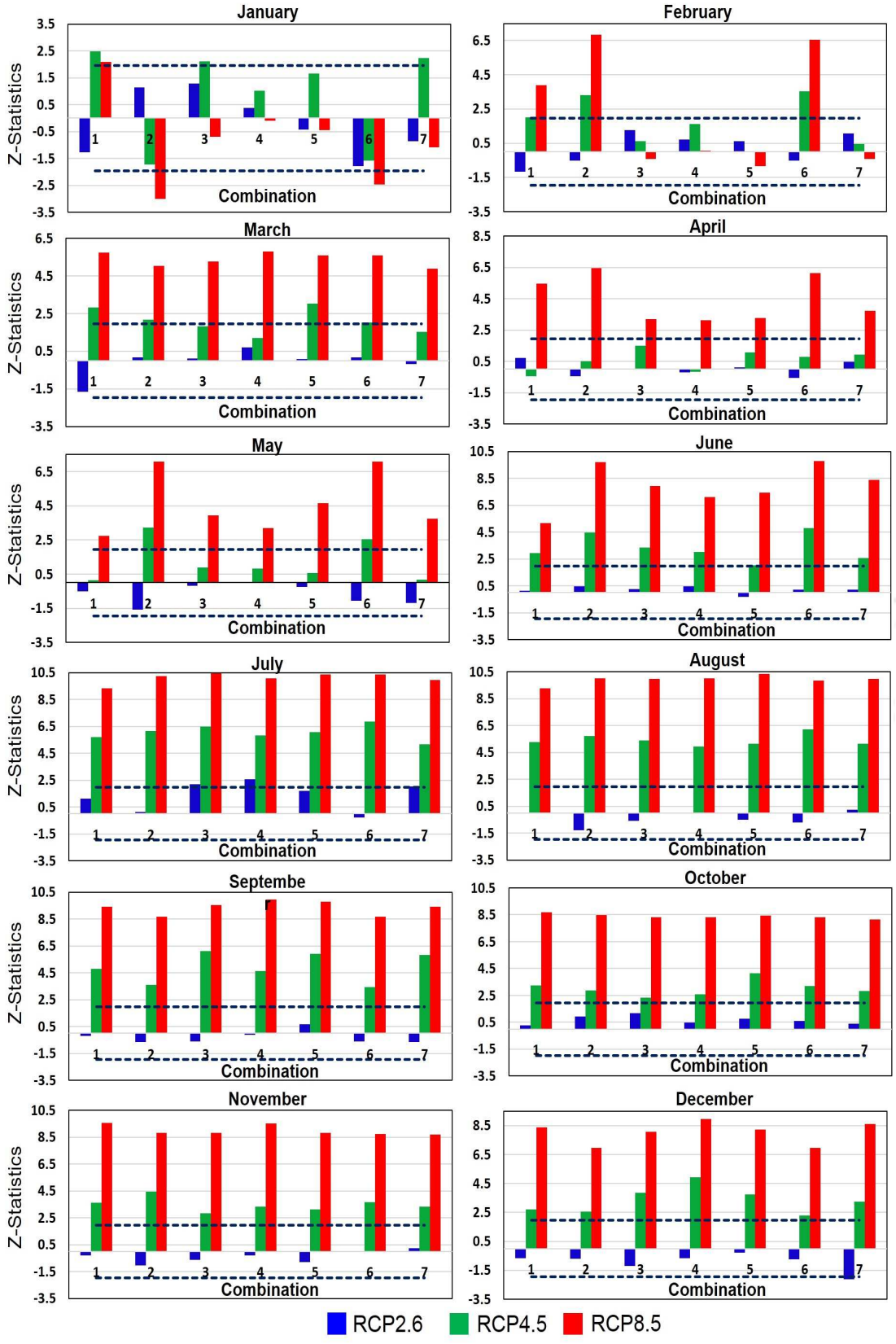

Figure 4.10: Trend analysis results (Z- Statistics) of minimum temperature for ESM2G model with their RCP scenarios during 2006-2100.

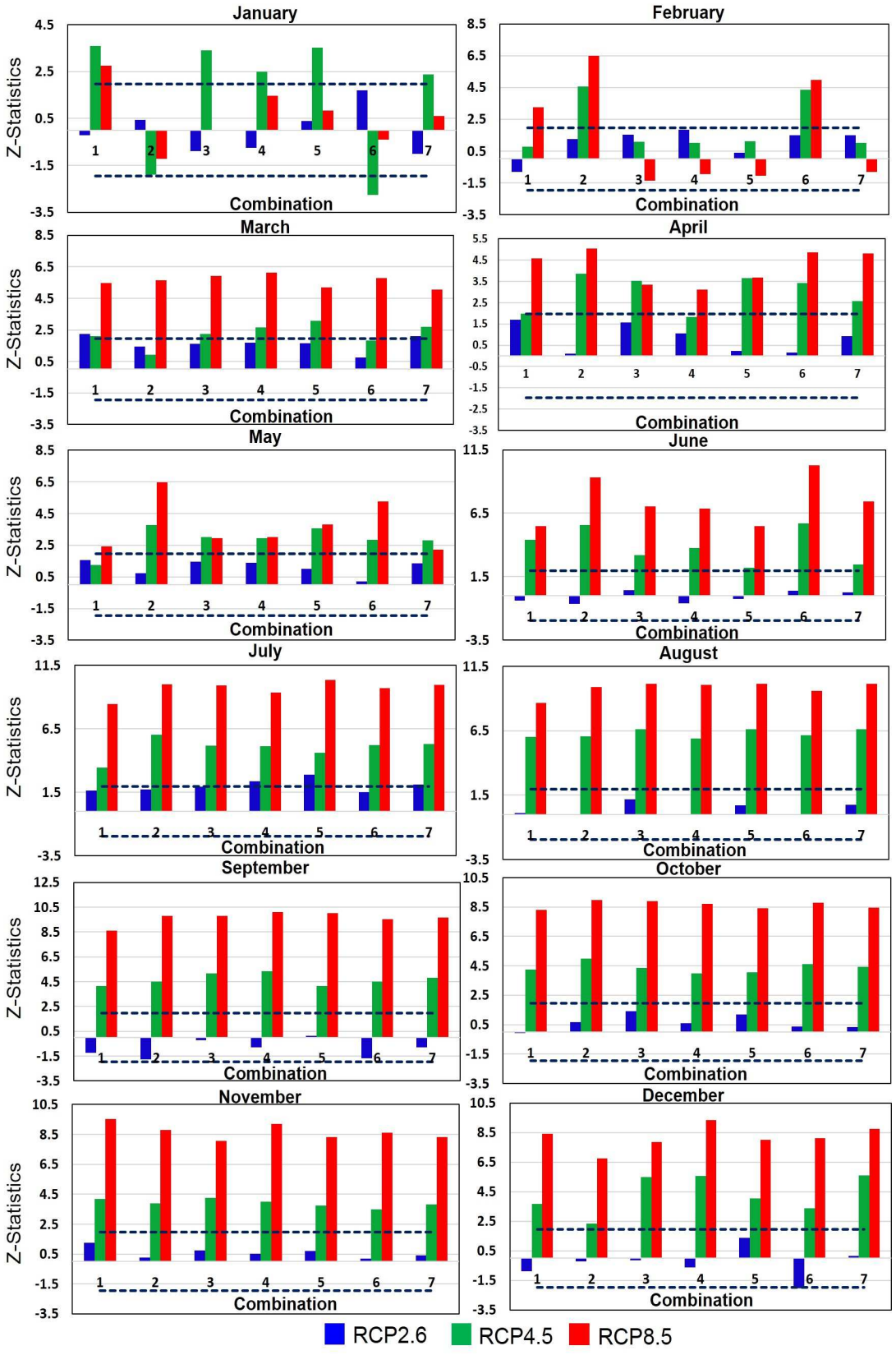

Figure 4.11: Trend analysis results (Z- Statistics) of minimum temperature for ESM2M model with their RCP scenarios during 2006-2100.

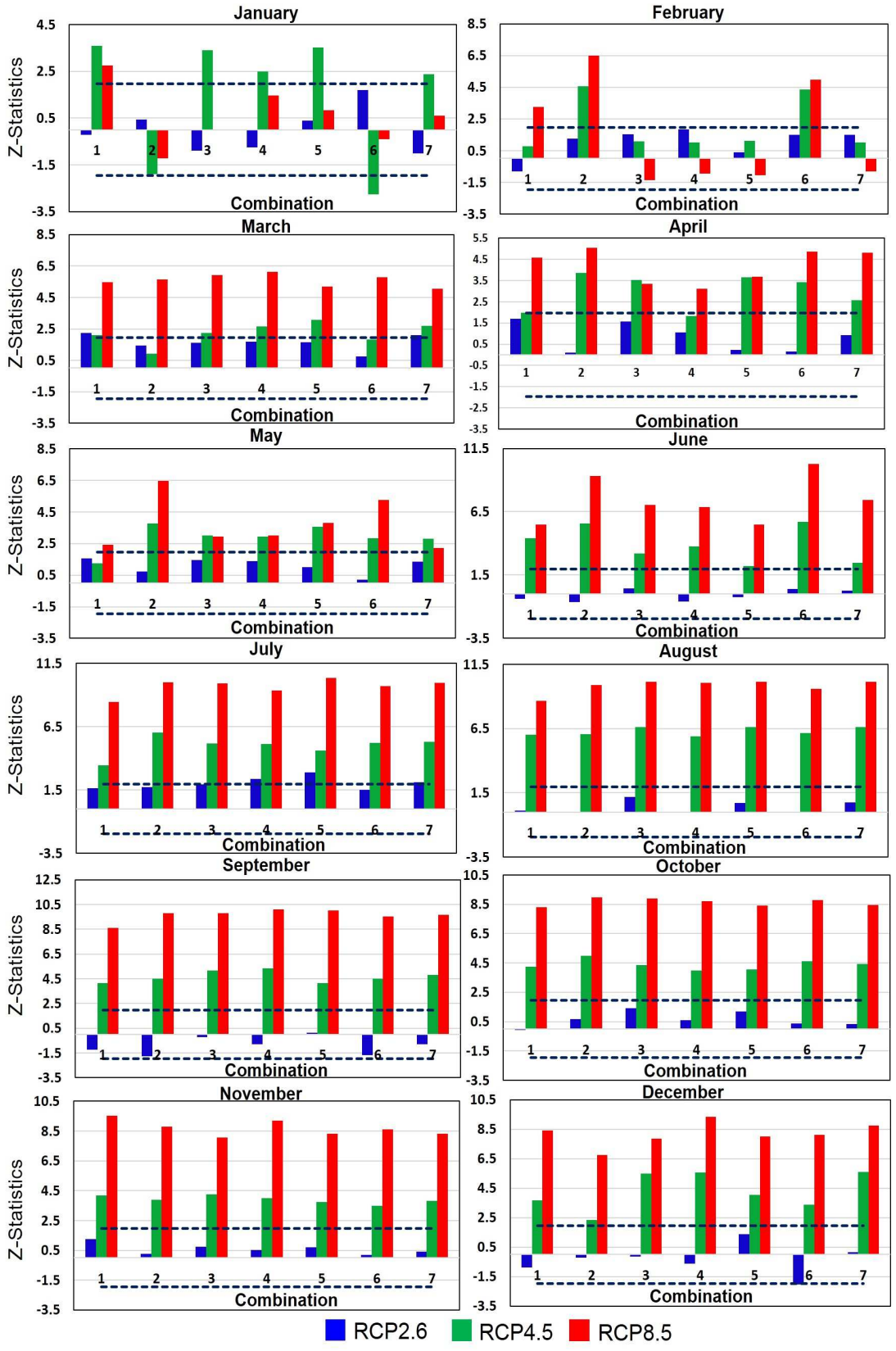

Figure 4.12: Trend analysis results (Z- Statistics) of minimum temperature for CM3 model with their RCP scenarios during 2006-2100.

4.3.1.2 Monthly variability with inter-decadal time series

In this study, monthly variability with inter-decadal such as 2021-2047 (20s), 2048-2074 (50s) and 2075-2100 (80s) time series have also been analyzed and quantified with observed dataset (1979-2005). The results of projected scenarios showing huge variation as compare to observed mean. The projection changes have been obtained with ranges of -0.820°C to 1.169°C during June to September months, during October to February months the range varies from -1.359°C to 1.407°C and during March to May month the range varies from -0.980°C to 0.939°C. Additionally, there are huge variation in median and standard deviation between observed and projected scenarios, especially in the months of July and August. During winter (November, December and January) months the median value has been decreased and during April and May month increased for all combinations as compare to observed median.

4.3.2 Maximum Temperature

4.3.2.1 Monthly variability of 21st century data series

The trend results of projected maximum temperature have also been analyzed for all scenarios as Z-statistics (Mann Kendall) at 5% significant level. The analysis result shows that the maximum temperature is increasing under RCP4.5 and RCP8.5 scenarios of ESM2G model for all months except monsoon months (June to September). Also some of the combination (2nd and 6th) of January month showing decreasing trend and RCP2.6 scenarios having no significant trend for all months as shown in Figure 4.13. In case of ESM2M model similar pattern has been observed but some of the combination such as 2nd, 3rd, 4th and 7th combinations of April months and 5th combination of September month also showing significant increasing Figure 4.14. Further, CM3 model

also showing similar pattern results with significant increasing/decreasing trends for all RCP scenarios, except some of the combination of January, April and September months as shown in Figure 4.15. The projection changes are estimated with observed mean (1979-2005) with the ranges of -0.33°C to 0.52°C for June to September months, during October to February months, range varies from -0.45°C to 0.51°C and during March to May months, range varies from -0.41°Cto 0.48°C. Estimated maximum changes are followed by extreme RCP scenario. The CMIP5 GCMs are showing similar pattern of change but, from the observation it is found that the CM3 model is projecting higher changes than other two models in all combinations.

4.3.2.2 Monthly variability with inter-decadal time series

Same as the minimum temperature we have deliberate inter-decadal (20s, 50s and 80s) time series. The results of RCP scenario of three CMIP5 GCMs have large alteration in projection change as compare to historical mean (1979-2005). The projection change are obtained with ranges of -0.464°C to 0.862°C for June to September months, the ranges from -0.786°C to 0.851°C for October to February months and the ranges from 0.668°C to 0.575°C for March to May months. The quantification result exhibits, the maximum temperature is continuously increasing in the 21st century as well as in inter-decadal time series, similar results already has been predicted by IPCC, AR5 (2014) for the Indian Sub-continent. All projected scenarios are showing similar change pattern except some of the months such as February month highlights the positive changes for ESM2G model, whereas negative change for ESM2M and CM3 models in 20s and 80s. During 50s and 80s having greater positive changes as compare to 20s, which indicates area could be warmer in middle and end of the 21st century. The median value of

maximum temperature is much higher than observed during summer months, while less during winter months.

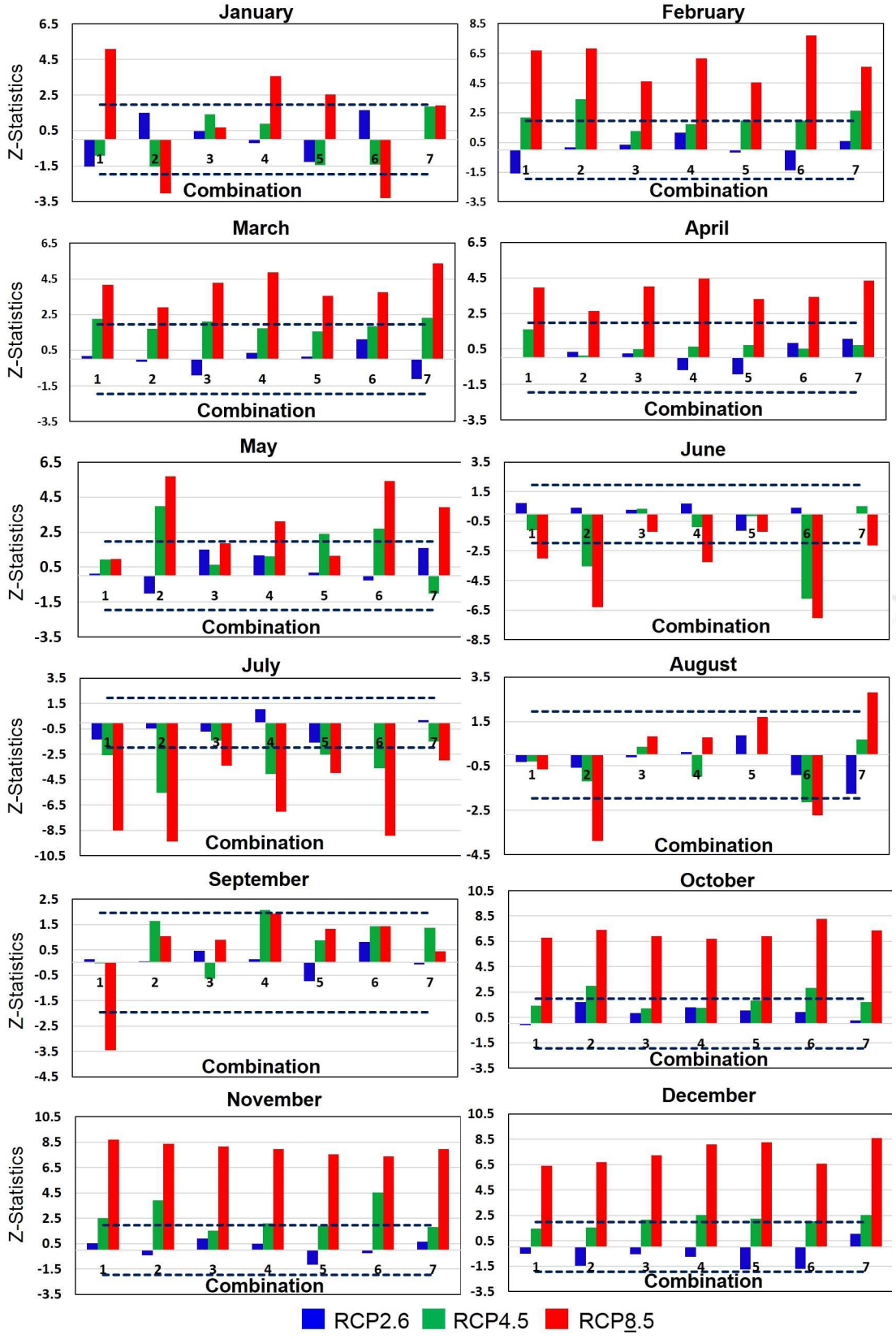

Figure 4.13: Trend analysis results (Z- Statistics) of maximum temperature for ESM2G model with their RCP scenarios during 2006-2100.

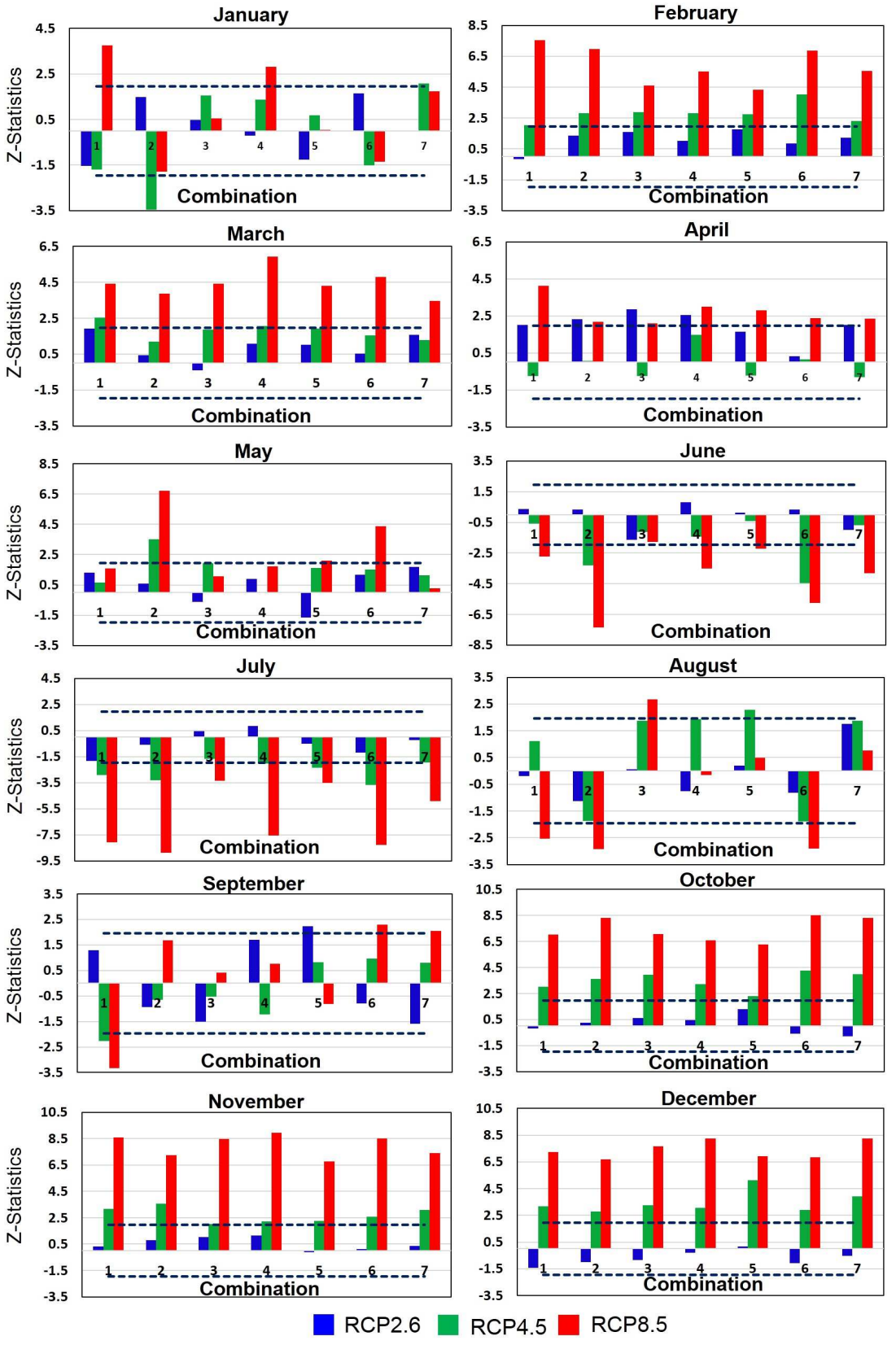

Figure 4.14: Trend analysis results (Z- Statistics) of maximum temperature for ESM2M model with their RCP scenarios during 2006-2100.

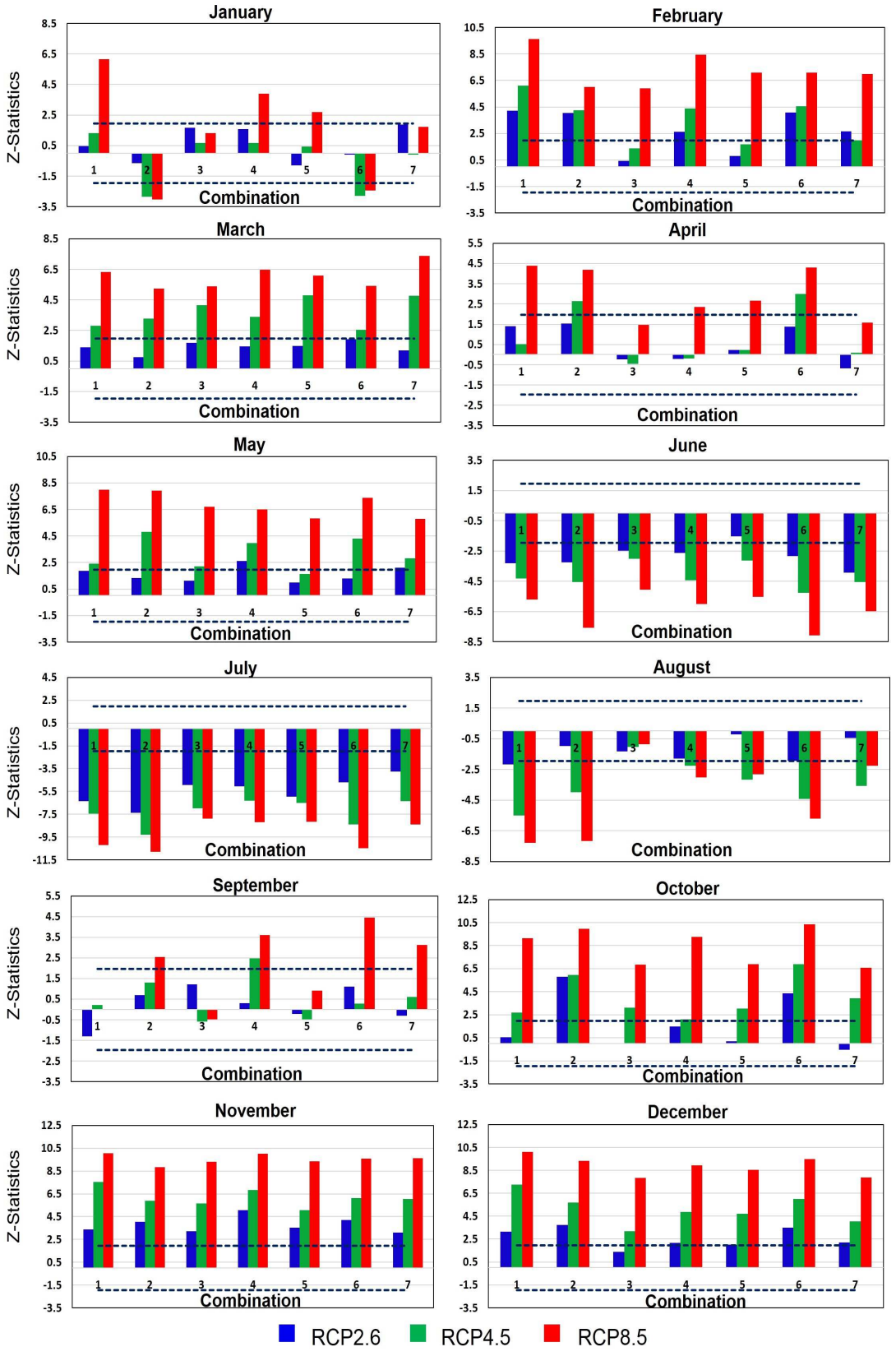

Figure 4.15: Trend analysis results (Z- Statistics) of maximum temperature for CM3 model with their RCP scenarios during 2006-2100.

4.3.3 Temperature Extreme Indices

A set of 10 climate extreme indices are selected to understand the inter-annual variability of maximum and minimum temperature in Sikkim Himalaya. Daily maximum and minimum temperature are used to estimate the all climate extreme indices. The temperature extreme indices are also suggested by the ETCCDI (Donat et al., 2013). The selected extreme indices of temperature make comparison in the warm and cold extensions. The precipitation extreme indices are defined as; max Tmax (TXx), max Tmin (TNx), min Tmax (TXn), min Tmin (TNn), frost days (FD0), ice-days (ID0), cool nights (TN10p), cool days (TX10p), warm nights (TN90p) and warm days (TX90p), and their description and definitions are listed in Table 4.8. Here, out of ten, five indices are derived from daily minimum temperature and remains five are derived from daily maximum temperature. Additionally, trend analysis applied on temperature indices series for each months separately using Mann-Kendall's and Sen's Slope test.

Table 4.8: Definitions of the extreme indices of cold and warm temperature.

ID	**Indicator Name**	**Indicator Definition**	**Unit**
TXx	Max Tmax	Monthly maximum value of daily maximum temp	°C
TNx	Max Tmin	Monthly maximum value of daily minimum temp	°C
TXn	Min Tmax	Monthly minimum value of daily maximum temp	°C
TNn	Min Tmin	Monthly minimum value of daily minimum temp	°C
FD0	Frost days	Annual count when TN(daily minimum)<0°C	Days
ID0	Ice days	Annual count when TX(daily maximum)<0°C	Days
TN10p	Cool nights	Percentage of days when TN<10th percentile	Days
TX10p	Cool days	Percentage of days when TX<10th percentile	Days
TN90p	Warm nights	Percentage of days when TN>90th percentile	Days
TX90p	Warm days	Percentage of days when TX>90th percentile	Days

4.3.3.1 Minimum temperature extreme indices

The extreme minimum temperature indices such as Frost days (FD0), cool nights (TN10p) and warm nights (TN90p) having significant and widespread warming trend. There is large variation in inter-decadal time series as well. The first decade (20s) showing positive change, while second (50s) and third (80s) showing negative projection change as compare to observed (1979-2005) shown in Tables 4.9, 4.10 and 4.11. During 20s, raise in FD0 up to 7.9 days (3.92%) and TN10p 7.3 days (3.54%) but strong reduction in TN90p about 21.3 days (53.99%) for extreme RCP scenario highlighted in bold. Similarly, 50s and 80s having significant decrease in the FD0, TN10p and TN90p. The maximum change during 50s, are -3.8 days for FD0, -2.2 days for TN10p and -

20.1 for TN90p and during 80s, maximum changes are -11.1 days for FD0, 9.7 days for TN10p and -19.2 days for TN90p. During observed time period (1979-2005), the values of minimum temperature extreme indices are FD0 is 192 days, TN10p is 198 days and TN90p is 43 days. Table 4.9, 4.10 and 4.11 highlights the significant changes (increase /decrease) of minimum temperature indices during 21st century and inter-decadal time series as with the baseline period (1979-2005) for CMIP5 GCMs and their RCPs.

The monthly maximum of daily minimum temperature (TNx) and minimum of daily minimum temperature (TNn) are also observed as warmest and coldest temperature of the years. The results highlight that warmest nights (TNx) having positive changes and coldest nights (TNn) having negative changes. The temperature of warmer night (TNx) of the year has increased by 1.41°C and temperature of cooler night (TNn) has decrease by 3.61°C during 2006-2100 with the baseline period of 1979-2005.

Daily minimum temperature extreme indices trend has been analyzed and found FD0 and TN10p are decreasing since 2005. The warmer trends are also found for temperature related to TN90p, whereas a significant increase in TN90p for some of the combinations of extreme emission scenario (RCP8.5). Both warmest nights (TNx) and coldest nights (TNn) have increased for all months except some of the combination such as 2nd and 6th combination for January and February months.

Table 4.9: Significant increase or decrease of minimum temperature extreme indices FD0, TN10p and TN90p for ESM2G model, where Cs' are GCM grid-point combinations.

	FD0 (days) Significant Increase/Decrease							**TN10p (days) Significant Increase/Decrease**							**TN90p (days) Significant Increase/Decrease**						
RCP2.6																					
Time Series	C1	C2	C3	C4	C5	C6	C7	C1	C2	C3	C4	C5	C6	C7	C1	C2	C3	C4	C5	C6	C7
20s	0.6	1.3	0.1	-1.4	-0.1	-1.1	0.9	1.6	3.9	2.2	0.9	0.7	0.0	2.1	-15.2	-13.6	-17.3	-16.0	-18.8	-14.7	-12.0
50s	-3.0	-1.5	-3.0	-2.7	-2.3	-1.5	-3.1	-1.7	0.0	-1.8	-1.8	-1.4	0.0	-1.7	-18.1	-16.2	-17.6	-15.4	-17.1	-17.8	-18.3
80s	-6.9	-5.1	-6.1	-5.8	-6.3	-4.1	-5.7	-4.8	-3.1	-4.7	-3.7	-4.7	-2.8	-4.6	-15.6	-15.6	-17.4	-16.6	-19.2	-16.3	-15.6
21st century	-2.0	-0.4	-1.6	-0.4	-0.5	0.3	-0.3	-0.8	0.8	-0.5	0.6	0.5	1.4	0.3	-17.5	-17.1	-17.7	-17.2	-19.4	-17.5	-18.5
RCP4.5																					
Time Series	C1	C2	C3	C4	C5	C6	C7	C1	C2	C3	C4	C5	C6	C7	C1	C2	C3	C4	C5	C6	C7
20s	2.5	1.6	3.4	0.3	1.9	0.1	2.4	1.6	1.5	2.2	0.8	1.0	0.8	1.4	-17.2	-16.8	-19.4	-18.6	-18.6	-15.1	-15.0
50s	-1.5	-0.7	-2.3	-2.2	-0.7	-2.2	-1.9	-2.2	-1.6	-1.6	-2.1	2.2	0.0	-0.5	-17.1	-17.8	-18.3	-18.1	-16.2	-17.6	-15.4
80s	-5.5	-3.3	-4.9	-6.1	-4.3	-5.3	-5.0	**-9.7**	-6.9	-5.8	-6.7	-5.1	-6.1	-6.3	**-19.4**	-16.3	-15.6	-15.6	-15.6	-17.4	-16.6
21st century	-0.5	0.3	-0.3	-2.0	-0.4	-1.6	-0.4	0.8	1.1	0.8	-0.2	0.9	-0.7	0.4	-19.8	-17.5	-18.5	-17.5	-17.1	-17.7	-17.2
RCP8.5																					
Time Series	C1	C2	C3	C4	C5	C6	C7	C1	C2	C3	C4	C5	C6	C7	C1	C2	C3	C4	C5	C6	C7
20s	-4.1	-3.2	**-4.8**	-4.7	-3.2	-4.7	-4.4	**7.3**	5.1	4.2	2.7	4.8	2.6	4.5	**-20.8**	-18.8	-19.4	-18.6	-18.1	-18.1	-18.0
50s	-8.1	-5.8	-7.4	**-8.6**	-6.9	-7.8	-7.6	2.2	0.0	-0.5	**-2.3**	-1.6	-1.6	-2.1	-16.1	-17.2	-16.8	-17.9	**-20.1**	-18.9	-19.7
80s	-5.1	-8.1	-7.0	**-9.1**	-8.2	-8.7	-8.7	-5.1	-6.1	-6.3	-9.5	-6.9	-5.8	-6.7	-14.9	-15.5	-16.5	-17.6	-17.4	-15.1	-15.2
21st century	1.4	-0.9	-0.6	-2.6	-1.1	**-2.9**	-1.0	1.4	1.2	0.8	**-1.5**	0.4	-0.6	0.0	-17.5	-18.4	-18.4	-19.3	**-20.1**	-18.7	-18.7

Bold values indicates the maximum change.

Table 4.10: Significant increase or decrease of minimum temperature extreme indices FD0, TN10p and TN90p for ESM2M model, where Cs' are GCM grid-point combinations.

	FD0 (days) Significant Increase/Decrease							**TN10p (days) Significant Increase/Decrease**							**TN90p (days) Significant Increase/Decrease**						
RCP2.6																					
Time Series	C1	C2	C3	C4	C5	C6	C7	C1	C2	C3	C4	C5	C6	C7	C1	C2	C3	C4	C5	C6	C7
20s	0.8	0.9	0.1	-1.1	-0.1	-0.9	1.2	1.6	3.9	2.2	0.9	0.7	0.0	2.1	-15.2	-13.6	-17.3	-16.0	-18.8	-14.7	-12.0
50s	-0.7	-2.3	-2.2	-0.7	-2.2	-1.9	-1.5	-1.7	0.0	-1.8	-1.8	-1.4	0.0	-1.7	-18.1	-16.2	-17.6	-15.4	-17.1	-17.8	-18.3
80s	-3.3	-4.9	-6.1	-4.3	-5.3	-5.0	-5.5	-4.8	-3.1	-4.7	-3.7	-4.7	-2.8	-4.6	-15.6	-15.6	-17.4	-16.6	-19.1	-16.3	-15.6
21st century	-0.5	0.3	-0.3	-2.0	-0.4	-1.6	-0.4	-0.8	0.8	-0.5	0.6	0.5	1.4	0.3	-17.5	-17.1	-17.7	-17.2	-19.4	-17.5	-18.5
RCP4.5																					
Time Series	C1	C2	C3	C4	C5	C6	C7	C1	C2	C3	C4	C5	C6	C7	C1	C2	C3	C4	C5	C6	C7
20s	1.8	1.5	2.3	0.6	1.7	0.1	2.3	1.6	1.5	2.2	0.8	1.0	0.8	1.4	-17.2	-16.8	**-19.4**	-18.6	-18.6	-15.1	-15.0
50s	-1.5	-0.7	-2.3	-2.2	-0.7	-2.2	-1.9	-2.2	-1.6	-1.6	-2.1	2.2	0.0	-0.5	-17.1	-17.8	-18.3	-18.1	-16.2	-17.6	-15.4
80s	-5.5	-3.3	-4.9	-6.1	-4.3	-5.3	-5.0	**-9.7**	-6.9	-5.8	-6.7	-5.1	-6.1	-6.3	**-19.2**	-16.3	-15.6	-15.6	-15.6	-17.4	-16.6
21st century	-0.2	0.8	-0.4	-1.8	-0.4	-2.1	-0.1	0.8	1.1	0.8	-0.2	0.9	-0.7	0.4	-19.4	-17.5	-18.5	-17.5	-17.1	-17.7	-17.2
RCP8.5																					
Time Series	C1	C2	C3	C4	C5	C6	C7	C1	C2	C3	C4	C5	C6	C7	C1	C2	C3	C4	C5	C6	C7
20s	-2.1	-4.2	-3.9	-4.8	-3.6	**-5.1**	-2.9	**8.2**	6.1	3.3	2.7	5.1	3.9	4.2	-19.2	-16.2	-14.2	-18.1	-18.1	-17.9	-15.9
50s	-0.5	0.3	-0.3	-2.0	-0.4	**-6.8**	-5.6	2.2	0.0	-0.5	**-2.6**	-1.6	-1.6	-2.1	-16.1	-17.2	-16.8	-17.9	**-20.1**	-18.9	-19.7
80s	-8.2	-8.7	-8.7	-9.1	-7.9	**-9.2**	-8.1	-4.9	-6.1	-6.3	-9.7	-6.9	-5.8	-6.7	-14.9	-15.5	-16.5	-17.6	-17.4	-15.1	-15.2
21st century	1.4	-0.9	-0.6	-2.6	-1.1	**-2.9**	-1.0	1.4	1.2	0.8	**-1.5**	0.4	-0.6	0.0	-17.5	-18.4	-18.4	-19.3	**-20.1**	-18.7	-18.7

Bold values indicates the maximum change.

Table 4.11: Significant increase or decrease of minimum temperature extreme indices FD0, TN10p and TN90p for CM3 model, where Cs' are GCM grid-point combinations.

	FD0 (days) Significant Increase/Decrease							**TN10p (days) Significant Increase/Decrease**							**TN90p (days) Significant Increase/Decrease**						
RCP2.6																					
Time Series	C1	C2	C3	C4	C5	C6	C7	C1	C2	C3	C4	C5	C6	C7	C1	C2	C3	C4	C5	C6	C7
20s	0.5	1.9	0.1	-1.5	-0.3	-2.1	0.7	1.7	3.2	1.3	0.5	0.5	-0.1	2.0	-19.0	-17.6	-17.3	-17.0	-18.0	-17.7	-18.0
50s	-2.5	0.0	-1.7	-3.2	-1.5	-2.3	-1.7	-1.1	1.0	0.3	-2.1	0.0	-0.7	-0.3	-19.7	-16.8	-18.4	-17.4	-15.6	-17.5	-17.8
80s	0.0	-2.0	-1.3	-2.4	-0.2	-2.3	-1.4	1.3	-0.5	0.9	-1.2	1.6	-0.6	-0.7	-18.0	-15.9	-16.7	-16.7	-18.2	-18.0	-16.9
21st century	0.0	0.5	0.0	-2.0	0.2	-1.7	0.2	1.1	1.6	1.5	-0.5	1.3	0.1	1.3	-18.6	-16.9	-18.2	-17.2	-17.4	-18.1	-18.0
RCP4.5																					
Time Series	C1	C2	C3	C4	C5	C6	C7	C1	C2	C3	C4	C5	C6	C7	C1	C2	C3	C4	C5	C6	C7
20s	2.5	1.6	3.4	0.3	1.9	0.1	2.4	3.0	2.9	3.6	0.7	2.4	1.3	2.8	-20.8	-18.8	-19.4	-18.6	-18.1	-18.1	-18.0
50s	-2.3	-1.5	-3.1	-3.0	-1.5	-3.0	-2.7	-1.4	0.0	-1.7	-1.7	0.0	-1.8	-1.8	-17.1	-17.8	-18.3	-18.1	-16.2	-17.6	-15.4
80s	-6.3	-4.1	-5.7	-6.9	-5.1	-6.1	-5.8	-4.7	-2.8	-4.6	-4.8	-3.1	-4.7	-3.7	**-19.2**	-16.3	-15.6	-15.6	-15.6	-17.4	-16.6
21st century	-0.5	0.3	-0.3	-2.0	-0.4	-1.6	-0.4	0.5	1.4	0.3	-0.8	0.8	-0.5	0.6	-19.4	-17.5	-18.5	-17.5	-17.1	-17.7	-17.2
RCP8.5																					
Time Series	C1	C2	C3	C4	C5	C6	C7	C1	C2	C3	C4	C5	C6	C7	C1	C2	C3	C4	C5	C6	C7
20s	7.9*	3.7	3.0	2.2	5.2	1.9	4.0	**7.3**	5.1	4.2	2.7	4.8	2.6	4.5	**-21.3**	-20.4	-19.2	-18.7	-20.0	-20.6	-21.1
50s	1.6	-2.3	-1.8	-3.1	-3.0	**-3.8**	-3.7	2.2	0.0	-0.5	**-2.2**	-1.6	-1.6	-2.1	**-20.1**	-18.9	-19.7	-16.1	-17.2	-16.8	-17.9
80s	-7.1	-8.8	-8.3	**-11.1**	-8.7	-8.6	-8.5	-5.1	-6.1	-6.3	**-9.7**	-6.9	-5.8	-6.7	-17.4	-15.1	-15.2	-14.9	-15.5	-16.5	-17.6
21st century	2.6	-0.5	-0.8	**-2.4**	-0.6	-2.1	-1.0	**2.8**	1.4	0.4	-1.5	0.2	-0.6	0.0	**-20.1**	-18.7	-18.7	-17.5	-18.4	-18.4	-19.3

Bold values indicates the maximum change.

4.3.3.2 Maximum temperature extreme indices

All calculated daily maximum temperature indices showing significant and widespread warming trend. The robust reduction in 'ID0', up to 2.9 days (29.23%) (See Table 4.14) between observed and projected scenarios are found. The average annual frequency of ID0 during the (1979-2005) base periods is by defined about 10 days. Similarly, we found the significant increase in the cool days (TX10p) and maximum increment is about 43% (7.22 days) (Table 4.14) in 20s of RCP8.5. And decrease in the warmer days (TX90p) about 56% (43.71 days) (Table 4.14) in 80s. All extreme changes occurred in extreme emission scenario RCP8.5 for CM3 model. Tables 4.12, 4.13 and 4.14 show the significant increase and decrease (day) of maximum temperature indices during 2006-2100 and inter-decadal time series for CMIP5 GCMs and their RCP scenarios. During the observed time period the maximum temperature extremes indices values are ID0 is 10 days, TX10p is 13 days and TX90p is 80 days. All CMIP5 GCMs showing similar change pattern with different ranges, but the CM3 and their RCPs are projecting higher ranges than other two GCMs and their RCPs, respectively. The changes in indices are noticeable and significant during the 21st century, these changes can alter the regional hydrology and glacier environment. The monthly maximum of daily maximum temperature (TXx) and minimum of daily maximum temperature (TXn) are also apparent as warmest and coldest temperature of the year. Therefore, warmest day (TXx) and coldest day (TXn) have significant changed over North Sikkim, India. The warmer day's temperature of the year has increased about 1.83°C in the month of January and cooler day's temperature has decreased about 4.83°C in the month of December during 2006-2100 with the baseline period of 1979-2005. The trend results of daily maximum temperature indices are evaluated for 21st century and found

ice-days (ID0) and cool days (TX10p) based on daily maximum temperature is shown to have significantly decreased over the 21st century for RCP4.5 and RCP8.5, whereas, warmer days (TX90p) have no significant trend. During monsoon months (June to September) most of the combinations of extreme indices have decreasing trend, while raising trend in the winter months (October to December and February). CM3 CMIP5 model have most significant trend changes as compare to other two models (ESM2G and ESM2M).

Table 4.12: Significant increase or decrease of maximum temperature extreme indices ID0, TX10p, and TX90p for ESM2G model, where Cs' are GCM grid-point combinations.

	ID0 (days) Significant Increase/Decrease							**TX10p (days) Significant Increase/Decrease**							**TX90p (days) Significant Increase/Decrease**						
RCP2.6																					
Time Series	C1	C2	C3	C4	C5	C6	C7	C1	C2	C3	C4	C5	C6	C7	C1	C2	C3	C4	C5	C6	C7
20s	-0.7	-0.5	0.2	-0.8	-0.9	1.2	0.1	3.1	3.2	4.6	2.8	2.4	4.8	2.2	-35.3	-35.1	-39.8	-38.1	-33.2	-36.5	-38.1
50s	-0.6	-0.7	-0.4	-1.2	-0.4	-0.9	0.3	**3.9**	3.4	2.1	2.6	3.1	3.7	2.8	-35.2	-36.8	-39.7	-39.1	-34.2	-34.2	**-40.1**
80s	-1.2	-1.6	0.5	-0.7	-0.4	-1.7	-1.9	**3.6**	2.5	0.8	0.7	0.5	4.2	2.1	-40.1	-35.6	-37.1	-37.9	-35.1	-38.2	-32.1
21st century	-0.8	-0.3	-0.1	-0.2	-0.2	0.4	-0.2	2.8	2.4	3.1	3.8	3.4	4.1	3.7	-36.1	-34.8	-32.6	-34.9	-37.2	-35.4	-36.4
RCP4.5																					
Time Series	C1	C2	C3	C4	C5	C6	C7	C1	C2	C3	C4	C5	C6	C7	C1	C2	C3	C4	C5	C6	C7
20s	-0.3	1.1	-0.5	0.5	-0.8	1.0	0.7	3.5	3.7	3.4	4.1	4.1	4.8	4.3	-38.5	-35.6	-35.9	-37.2	-34.8	-35.9	**-40.1**
50s	-0.7	0.6	-0.2	-0.7	-0.4	-0.9	-0.7	1.5	2.8	2.9	1.8	3.8	1.6	2.5	-38.2	-36.4	-34.2	-37.2	-39.2	-38.1	-39.2
80s	-1.2	-2.1	-1.6	-1.6	0.8	-0.7	0.2	0.9	0.1	2.6	0.8	3.5	2.0	2.9	-40.0	-35.6	-38.2	-36.2	-39.8	-37.9	-36.8
21st century	-0.9	-0.2	0.3	-0.3	0.1	0.1	0.7	2.5	3.2	3.9	2.6	3.4	2.9	2.7	-36.5	-37.5	-37.9	-36.1	-38.2	-35.6	-38.7
RCP8.5																					
Time Series	C1	C2	C3	C4	C5	C6	C7	C1	C2	C3	C4	C5	C6	C7	C1	C2	C3	C4	C5	C6	C7
20s	0.9	0.8	0.9	-0.6	0.1	**1.5**	0.7	5.3	**6.2**	5.6	4.3	3.6	5.9	4.9	-36.8	-38.4	-35.2	-39.8	-37.5	-36.8	-36.4
50s	-0.5	0.4	-0.3	-0.1	-0.6	**1.3**	-1.0	1.8	1.9	2.8	2.5	2.7	3.4	2.8	-38.2	-36.8	-38.7	-34.5	-36.9	-35.2	-36.7
80s	**-2.4**	0.0	-0.9	-1.2	-1.6	-0.8	-1.5	-1.8	0.2	1.5	0.9	0.8	1.0	0.1	**-40.4**	-38.1	-35.9	-36.1	-37.6	-34.6	-36.1
21st century	-0.6	1.2	0.5	-0.1	0.2	**1.9**	0.1	2.9	2.4	3.4	2.9	3.4	**4.8**	4.6	-38.2	-36.4	-36.8	-36.9	-37.5	-38.1	**-39.4**

Bold values indicates the maximum change.

Table 4.13: Significant increase or decrease of maximum temperature extreme indices ID0, TX10p, and TX90p for ESM2M model, where Cs' are GCM grid-point combinations.

	ID0 (days) Significant Increase/Decrease							**TX10p (days) Significant Increase/Decrease**							**TX90p (days) Significant Increase/Decrease**						
RCP2.6																					
Time Series	C1	C2	C3	C4	C5	C6	C7	C1	C2	C3	C4	C5	C6	C7	C1	C2	C3	C4	C5	C6	C7
20s	-0.6	-0.2	0.3	-0.4	-0.9	**1.9**	0.1	2.8	2.9	3.6	2.6	1.9	3.9	2.6	-34.2	-36.8	**-40.1**	-38.2	-35.2	-36.9	-38.1
50s	-0.8	-0.2	-0.9	-1.3	-0.7	-0.9	0.5	3.8	3.4	2.9	2.1	3.8	3.1	2.1	-36.5	-36.4	-39.8	-38.9	-37.2	-34.2	-39.2
80s	-1.6	-1.2	0.5	-1.2	-0.6	-1.2	-1.7	2.9	2.1	0.8	0.7	0.5	**3.8**	2.0	-38.1	-34.6	-36.7	-37.2	-34.2	38.2	-32.5
21st century	-0.2	-0.8	-0.1	-0.2	-0.7	0.1	0.2	2.3	2.1	2.8	2.9	3.1	4.0	2.8	-34.2	-35.1	-38.1	-37.1	-34.5	-35.1	-38.1
RCP4.5																					
Time Series	C1	C2	C3	C4	C5	C6	C7	C1	C2	C3	C4	C5	C6	C7	C1	C2	C3	C4	C5	C6	C7
20s	-0.7	0.3	-0.2	0.5	-0.8	1.4	0.6	2.6	2.7	3.1	3.8	2.6	4.2	4.1	-36.2	-34.2	-36.8	-36.2	-34.5	-36.9	-40.8
50s	-0.9	0.6	-0.1	-0.8	-0.2	-0.7	-0.3	1.2	2.9	3.1	3.8	**4.1**	2.9	3.7	-35.2	-36.2	-36.8	-34.2	37.1	-38.1	-34.1
80s	-1.2	-1.8	-1.2	-1.6	0.6	-0.9	0.6	0.7	0.4	2.4	1.2	2.4	2.1	2.0	-36.1	-34.2	-35.8	-36.7	-39.8	-34.6	-35.8
21st century	-0.4	-0.8	0.4	-0.2	0.5	0.4	0.9	1.3	2.9	2.7	2.9	3.1	2.9	2.9	-35.2	-37.1	-38.1	-34.2	-38.2	-34.2	**-38.7**
RCP8.5																					
Time Series	C1	C2	C3	C4	C5	C6	C7	C1	C2	C3	C4	C5	C6	C7	C1	C2	C3	C4	C5	C6	C7
20s	1.1	0.7	0.6	-0.4	0.1	1.6	0.8	6.1	5.9	5.7	4.9	**6.2**	5.7	4.9	-38.2	-34.2	-35.6	-39.8	-37.2	-34.5	-35.9
50s	-0.8	0.6	-0.4	-0.1	-0.9	**1.8**	-0.9	1.6	1.8	2.9	3.1	3.2	3.6	2.9	-35.8	-36.4	-34.6	-35.9	**-40.8**	-37.9	-36.4
80s	**-2.7**	0.0	-1.1	-1.2	-1.6	-0.7	-1.2	1.2	0.8	1.2	0.9	1.6	1.4	0.6	**-40.2**	-35.6	-37.5	-34.8	-36.9	-35.8	-34.5
21st century	-0.5	1.1	0.8	-0.2	0.2	**1.4**	0.1	2.8	2.4	3.1	3.0	3.5	**4.2**	4.6	-35.8	-36.4	-37.4	36.4	-35.9	-34.8	-36.7

Bold values indicates the maximum change.

Table 4.14: Significant increase or decrease of maximum temperature extreme indices ID0, TX10p, and TX90p for CM3 model, where Cs' are GCM grid-point combinations.

	ID0 (days) Significant Increase/Decrease							**TX10p (days) Significant Increase/Decrease**							**TX90p (days) Significant Increase/Decrease**						
RCP2.6																					
Time Series	C1	C2	C3	C4	C5	C6	C7	C1	C2	C3	C4	C5	C6	C7	C1	C2	C3	C4	C5	C6	C7
20s	-0.9	-0.3	0.4	-0.4	-0.7	1.6	0.4	2.9	3.7	4.1	3.0	3.0	5.1	4.4	-38.6	-36.8	**-42.5**	-39.1	-34.5	-40.1	-39.6
50s	-0.3	0.3	-0.6	-0.1	0.0	-0.2	-1.0	3.2	4.0	2.9	3.4	3.2	3.7	2.7	-38.3	-36.8	**-40.8**	-39.5	-39.7	-37.8	-40.1
80s	-0.5	-0.8	-0.5	-0.8	-0.9	0.2	-0.8	2.1	2.1	3.1	2.7	2.1	4.2	2.6	-39.7	-37.0	-38.0	-37.2	-39.8	-38.5	-37.4
21st century	-0.5	-0.2	-0.3	-0.2	-0.2	0.5	-0.2	3.0	3.2	3.3	3.4	3.3	4.4	3.6	-38.9	-36.5	**-40.0**	-38.1	-37.8	-38.8	-38.9
RCP4.5																					
Time Series	C1	C2	C3	C4	C5	C6	C7	C1	C2	C3	C4	C5	C6	C7	C1	C2	C3	C4	C5	C6	C7
20s	-0.2	0.9	-0.5	0.4	-0.2	1.0	0.6	4.7	4.7	3.9	4.9	4.0	5.0	4.0	-38.1	-39.4	-37.6	-35.4	-38.2	-37.8	-41.1
50s	-0.9	0.3	-0.6	-0.7	-0.4	-1.2	-0.4	2.6	3.1	3.4	2.1	**3.9**	1.7	3.2	-40.8	-38.1	-37.0	-38.0	-38.3	-40.3	-38.3
80s	-1.7	-1.9	-1.2	-1.6	0.5	-0.7	-0.4	0.7	0.5	2.5	0.8	**3.6**	2.1	2.4	-41.2	-39.4	-39.2	-36.8	-40.8	-35.9	-35.4
21st century	-0.5	-0.2	-0.7	-0.3	0.1	0.1	0.0	3.1	3.2	3.6	3.4	4.2	3.6	3.3	-39.7	-38.1	-38.0	-36.9	-38.6	-37.7	-38.0
RCP8.5																					
Time Series	C1	C2	C3	C4	C5	C6	C7	C1	C2	C3	C4	C5	C6	C7	C1	C2	C3	C4	C5	C6	C7
20s	1.4	**1.6**	0.7	-0.1	0.1	1.3	0.8	7.1	**7.2**	5.8	4.1	4.5	6.9	5.4	-37.3	-39.2	-39.0	-38.8	-37.0	-39.4	-39.0
50s	-0.7	0.4	-0.4	-0.1	-0.7	**1.8**	-1.1	2.4	2.7	3.2	2.7	2.7	3.8	2.5	-39.1	-40.7	-40.3	-36.4	-37.1	-39.5	-37.2
80s	**-2.9**	0.0	-1.0	-1.0	-1.5	-0.4	-1.5	-1.1	0.2	1.1	0.5	-0.8	1.0	0.6	**-43.7**	-38.7	-37.3	-40.4	-39.1	-33.1	-39.3
21st century	-0.3	1.0	0.1	-0.2	-0.4	**1.3**	-0.1	4.0	4.2	4.2	3.3	3.0	**4.9**	3.8	-39.2	-38.8	-38.8	-38.0	-38.1	-37.1	-38.5

Bold values indicates the maximum change.

4.4 Joint Probabilistic Behavior of Extreme Indices

India is a developing country with exposure to threats of floods, droughts and warming trends, especially in Himalayan region causing change in hydrology, glacier melting and formation of glacial lakes which makes these areas more vulnerable. The joint probability behaviour of precipitation and temperature extremes are essential to recognize the regional responses of climate change for glacier melting and water resources management with flood and drought controls. As the hydro-meteorological variables are stochastic in nature and analysis of these variables are well documented using univariate techniques (Katz and Brown, 1992). In such situations, univariate techniques may underestimate the risk associated with an event. However, multivariate analysis of such random variables are essential (Favre et al., 2004). With this understanding, several researchers focused their attention on multivariate analysis of hydro-meteorological variables(Grimaldi and Serinaldi, 2006). Figure 4.16 shows the motivational flow chart of multivariate analysis of climate extremes using copula because of its flexibility.

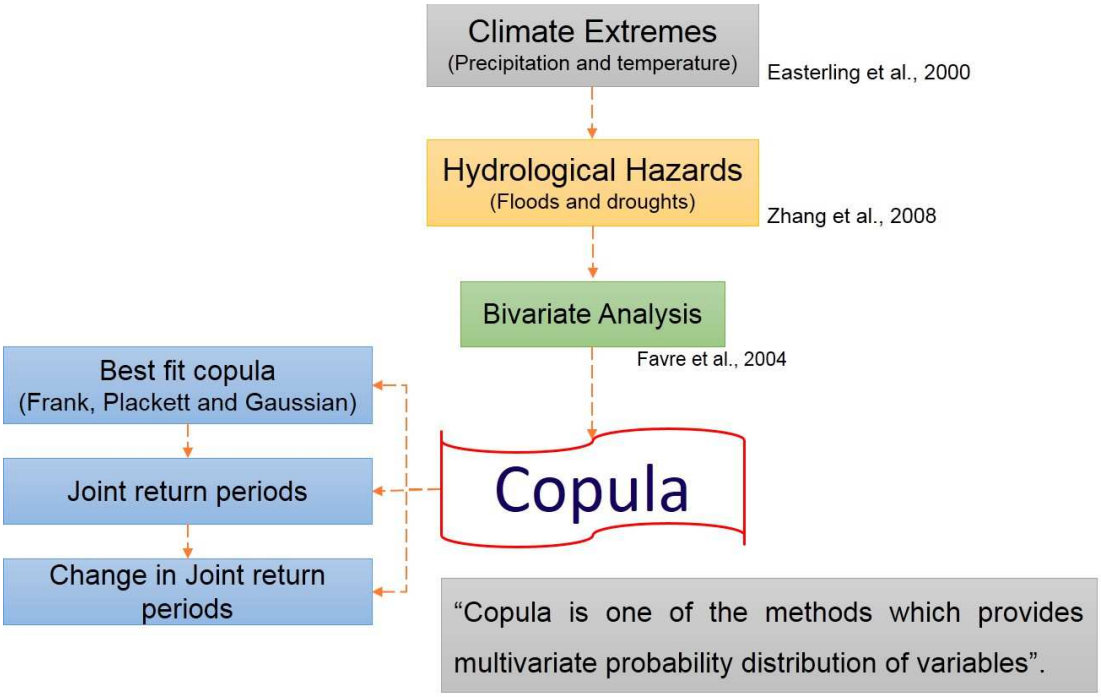

Figure 4.16: Motivational flow chart of bivariate analysis of climate extremes

This study focuses about historical and future joint probability of precipitation and temperature extremes over the North Sikkim Himalaya for understanding the response of change in joint probabilistic behavior of climate extremes during 2021-2100 based on copula and CMIP5 GCMs. To explore the possible spatio-temporal changes in climate extremes, firstly downscale the precipitation and temperature dataset and calculate their extreme indices. Then, joint return period of these extremes were analyzed during 1979-2005 to understand the variation of temperature extremes in North Sikkim. Finally, joint probability and changes in joint return period of projected extreme indices were investigated using copula.

From the extreme indices analysis, it is found that the first combination (GCM grid-point combination) is the most significant combination, which shows the significant impact over the study region. Due to this reason, first combination (GCM grid-point combination) is selected to carry out the further work to demonstrate the joint probabilistic

behavior of extreme indices over the study area. Figure 4.17 shows the methodology steps of bivariate analysis of observed and downscaled extreme indices using copula.

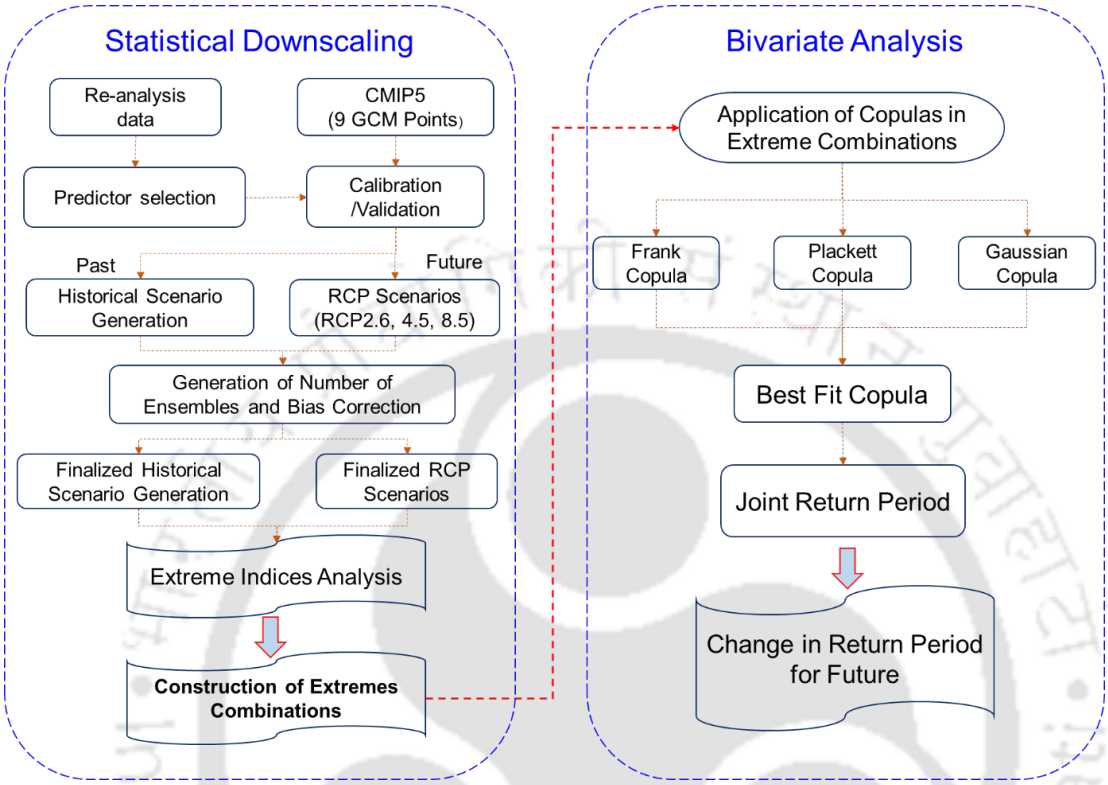

Figure 4.17: Methodology steps of bivariate analysis of extreme indices using copula.

4.4.1 Bivariate Analysis of Extreme Indices

In this study, the historical events are described by the joint behaviour of strongly dependent random variables, despite fact the univariate may lead to either over or underestimation of risk associated of these events. In order to estimate the plausible risk of events, the exceedance probability of extreme events need to characterize the joint behaviour of the specific events (Salvadori and De Michele, 2004). Yue (2001) discussed the physical concept of marginal cumulative distribution (CDF) and return period of the event in the context of bivariate nature. Let $F_{X,Y}(x,y)$=P($X \leq x, Y \leq y$) be a joint probability function of pair of random variables (X,Y) and (x,y) is any event,

then the joint return period of an event (x,y) is represented by $T_{X,Y}$ (x,y) can be written as:

$$T_{X,Y}(x,y) = \frac{1}{(1 - F_X(x) - F_Y(y) + F_{X,Y}(x,y))} \tag{4.13}$$

Let $x_{T'}$ and $y_{T'}$ are the T' year value of x and y, computed from the historical record (1979-2005), then the joint return period, $T_{\{X>x_{T'},Y>y_{T'}\}}$ is denoted by $T_{T'_{X,Y}}$. For example, $T_{10\{TN_{10},TN_{90}\}}$ represents the joint return period of TN_{10} and TN_{90} exceed their 10-year values, as computed from the historical record of (1979-2005). The projected changes in joint return period of during 2021-2100 under three RCP scenarios of three GCM's as mentioned in the earlier sections with respect to historical record (1979-2005) is defined using the (%) change in rate and computed as follows: (Li et al., 2015).

$$\text{Changing rate} = \frac{T_{T'\{X,Y\}f} - T_{T'\{X,Y\}h}}{T_{T'\{X,Y\}h}} \times 100 \tag{4.14}$$

Here, $T_{T'\{X,Y\}f}$ represents the $T_{T'\{X,Y\}}$ of time period (2021-2100) under the adopted three RCP scenarios of three GCM's, and $T_{T'\{X,Y\}h}$ represents $T_{T'\{X,Y\}}$ of historical record (1979-2005).

4.4.2 Copula

Copula is one of the methods which provides multivariate probability distribution of strongly correlated variables (Salvadori and De Michele, 2004; Genest and Favre, 2007). In practice, copula enables the multivariate distributions to the data by fitting the marginal and the dependence between them individually. According to Skalr theorem (Sklar, 1959), every joint distribution can be written as a copula and its univariate marginal. Let $(X_{11}, X_{21}, X_{31}, \ldots,)...(X_{d1}, X_{d2}, ...X_{dN})$ be the observations drawn from a multivariate dataset $X(X_1, X_2, \ldots..X_d)^T$. where d represents number of vari-

ables and N represents number of observations. Let $u_i = F_x(x_i,)i = 1,\ldots,n$ be the marginal cumulative distribution function′s ($CDF′s$) and F_X (X) be the multivariate distribution of $X_i i = 1,2,\ldots,n$.

Thus the multivariate distribution $F_X(X)$ can be expressed as its marginal and the corresponding dependence function C, as:

$$F_X(X) = C_x\{u_1, u_2, \ldots..u_n; \theta\} \qquad X \in R^d \tag{4.15}$$

Where, $C_X : [0,1]^d \rightarrow [0,1]$ is called d-dimensional copula, with corresponding parameter θ. Further details about theoretical background of copula theory and characteristics of various copulas can be found in (Nelson, 2006).

Frank Copula (Archimedean family)

$$C(u_1, u_2; \theta) = -\frac{1}{\theta}\ln\left[1 + \frac{(e^{-\theta_{u1})} - 1)(e^{-\theta_{u2}} - 1)}{e^{-\theta} - 1}\right] \tag{4.16}$$

Where range of θ is$(-\infty, \infty)$.

Plackett Copula

$$C(u_1, u_2; \theta) = \frac{S - \sqrt{(S^2 - 4u_1u_2\theta(\theta - 1)}}{2(\theta - 1)} \tag{4.17}$$

Where $S = 1 + (\theta - 1)(u_1 + u_2)$ and range of θ is(0,∞).

Gaussian Copula (Elliptical family)

$$C(u_1, u_2; \theta) = \Phi_\theta[\Phi^{-1}(u_1), \Phi^{-1}(u_2)] \tag{4.18}$$

Where range of θ is(-1,1).

Note: Φ^{-1} is the inverse standard normal distribution function and Φ_θ is the bivariate standard normal distribution function with Pearson linear correlation coefficient θ.

The above described copulas belong to the different families such as Frank copula belongs to Archimedean family, Plackett copula belongs to Plackett family and Gaussian copula belongs to Elliptical family. These copulas are suitable for both positively and negatively correlated variables. Some of the copulas from same family are only appropriate for positive/negative correlated variables e.g. Gumbel Houggard and Cook–Johnson copula families are only appropriate for the positively correlated variables (Zhang et al., 2007). Due to this reason, in this study three copulas from different families have been chosen.

To verify the bivariate structural equality of dependence the statistical distances are calculated and found that the bivariate structures are changing for different scenarios. This indicates, the non-parametric approach also can be a tool to analyze the bivariate dependence (Grimaldi et al., 2016). The statistical distances are the distance between probability distributions (Marti et al., 2016). Here, we have used the Wasserstein (W_2), Fisher-Rao and related divergences distance. The major difference is Fisher-Rao geometry has negative curvature while Wasserstein geometry is flat and non-negative curvature. The statistical Distances (Wasserstein, Fisher-Rao and related divergences) and their formulas are listed below (Table 4.15):

Table 4.15: Statistical distances and their formulas

Statistical Distances	**Formulas** **D[N(0,$\sum_1$),N(0,$\sum_2$)]**
Fisher-Rao	$\sqrt{\frac{1}{2}\sum_{i=1}^{n}(log\lambda_i)^2}$
KL(Σ1||Σ2)	$\frac{1}{2}\left(log\left\|\frac{\sum_2}{\sum_1}\right\| - n + tr(\sum_2^{-1}\sum_1)\right)$
Jeffreys	KL($\sum_1 \,\|\|\, \sum_2$)+ KL($\sum_2 \,\|\|\, \sum_1$)
Bhattacharyya	$\frac{1}{2}log\frac{\|\sum\|}{\sqrt{\|\sum_1\|\|\sum_2\|}}$
Wasserstein (W_2)	$\sqrt{tr(\sum_1+\sum_2-2\sqrt{\sum_1^{1/2}\sum_2\sum_1^{1/2}})}$

where, λ_i is eigenvalues of $\sum_1^{-1}\sum_2; \sum = \frac{\sum_1+\sum_2}{2}$

But the non-parametric approach also has some serious scaling issues (Marti et al., 2016) and selection of smoothing parameter which may lead to the poor description of dependence structures. In order to avoid these drawbacks, parametric copulas are used for climatic variables.

4.4.3 Bivariate Analysis of Precipitation Extremes

The precipitation extremes are calculated (discussed in section 4.2.2) and assess the joint probabilistic behavior of different extreme combinations such as [CWD, CDD], [R20, SDII], [SDII, R95p], [R95p, R99p], [WD, SDII], [CDD, SDII] and [R20, R95p]. Extreme combinations are constructed based on the physical significances and Kendall's correlations. The combination [CWD, CDD] presents the co-occurrence of consecutive wet days and dry days in the same year, which signifies the co- occurrence of floods and droughts in same year; [R20, SDII] denotes the joint extreme precipitation as very heavy precipitation days and precipitation intensity; [SDII, R95p] represents the joint

extreme precipitation events in terms of precipitation intensity and amount of very wet days precipitation; [R95p, R99p] represents the joint extreme precipitation in terms of very and extreme wet days precipitation amount; [WD, SDII] represents the joint rainy days and precipitation intensity; [CDD, SDII] represents the joint consecutive dry days and precipitation intensity; [R20, R95p] represents the joint extreme precipitation events in terms of very wet days and very wet days precipitation. The joint probability and joint return period of extreme combinations have been analyzed using different copulas.

The bivariate relationship and Kendall coefficient between extremes are calculated (Table 4.16. The Kendall coefficient shows that if the value of one variable is high/low, so there is a chance that the value of another variable would be high/low (Genest and Favre, 2007). The Kendall's coefficient is calculated using equation 4.19.

$$\text{Kendall's Tau}(\tau) = \frac{(\text{number of concordant pairs}) - (\text{number of discordant pairs})}{n(n-1)/2)} \tag{4.19}$$

The [CWD, CDD] and [WD, SDII] have insignificant relations under all scenarios. [R20, SDII] and [R95p, R99p] have significant positive correlation almost for all scenarios and their Kendall's coefficient values are larger than 0.5 for all case except [R20, SDII] of CM3 RCP2.6 scenario. Also, [SDII, R95p] [CDD, SDII] and [R20, R95p] are highly correlated having Kendall's coefficient more than 0.3 for the historical period, while less significant in projected scenarios (Table 4.16). The Kendall's coefficients of projected scenarios are relatively less than observed scenario. This indicates that uncertainty exists in bivariate relationships of precipitation extremes. With this consideration, further study has been carried out.

Table 4.16: The Kendall coefficients τ between precipitation extremes for observed and projected (2021–2100) scenarios.

Extremes	**Observed**	**ESM2G**			**ESM2M**			**CM3**		
		RCP2.6	RCP4.5	RCP8.5	RCP2.6	RCP4.5	RCP8.5	RCP2.6	RCP4.5	RCP8.5
[CWD, CDD]	-0.17	-0.09	0.02	0.07	0.12	0.03	0.01	-0.12	-0.06	-0.03
[R20, SDII]	0.7	0.5	0.57	0.58	0.51	0.54	0.57	0.43	0.51	0.51
[SDII, R95p]	0.43	0.08	0.18	0.03	0.16	0.11	0.19	0.14	0.21	0.17
[R95p, R99p]	0.7	0.67	0.67	0.75	0.7	0.65	0.67	0.67	0.67	0.64
[WD, SDII]	-0.48	-0.04	-0.17	-0.01	-0.23	-0.1	0.01	-0.18	0.02	0.03
[CDD, SDII]	0.3	0.02	-0.1	-0.08	0.11	0.04	-0.01	0.12	0.15	0.06
[R20, R95p]	0.46	0.12	0.19	0.06	0.13	0.03	0.23	0.26	0.34	0.02

Additionally, the marginal distribution of univariate precipitation extremes are also analyzed for 5-year (T5), 10-year (T10) and 20-year (T20) return periods. The comparison of T5, T10 and T20 precipitation extremes between observed and projected scenarios are analyzed. The values of R10 and SDII for T5, T10 and T20 return periods are slightly increased, whereas other variables such as WD, CWD and CDD are decreased in projected scenarios with respect to observed scenario. This implies that the intensity and very heavy precipitation (10) days become stronger, while heavy (WD and CWD) precipitation and weak (CDD) precipitation becomes less in future.

The Kendall's coefficients (τ) and marginal distributions are changed under projected scenarios, consequently, the joint distribution of extreme combinations may also change in future accordingly. To estimate the change in joint distribution, firstly best-fitted copula is selected from different copula families. The best-fit copula selected among Frank (Archimedean), Plackett and Gaussian (Elliptical) based on the minimum of Akaike Information Criterion (AIC) (Akaike, 1974) and Bayesian Information Criterion (BIC) (Li et al., 2015) values. Then joint distribution is estimated using Kendall coefficients (τ), marginal distribution and best fit Copula. The joint distribution of CWD and CDD of historical and projected scenarios are same, but the discrepancy in joint CDF is relatively high when CWD and CDD values are large. The joint return period of [R95p, R99p] and [R20, R95p] are quite similar, but projected scenarios are having higher joint CDF values when corresponding extreme values are large. The AIC and BIC values are calculated as:

$$\mathrm{AIC} = 2(k) - 2\ln(L) \tag{4.20}$$

$$\mathrm{BIC} = 2\ln(L) - 2\ln(N) \tag{4.21}$$

where, k is the number of parameters, L is the maximized value of the likelihood function and N is the sample size. The statistical distances (non-parametric) are used to verify structural dependency, which illustrates that how the distances behave between Gaussian copulas using the following three bivariate Gaussian copulas 2M-RCP2.6, 2M-RCP4.5 and observed scenarios for [R95p, R99p] and [WD, SDII] extreme combinations. The result indicates that 2M-RCP2.6 and 2M-RCP4.5 are closer than 2M-RCP4.5 and observed (Table 4.17). Here, it is surprising that since the strongly positive correlated (2M-RCP4.5 and Observed) are showing higher distance than less correlated scenario. The analytical formulas of statistical distances with its values are listed in Table 4.17.

Table 4.17: Statistical distances of bivariate [R95p, R99p] and [WD, SDII] Gaussian copula

Statistical Distances	**Distances for [R95p, R99p]**		**Distances for [WD, SDII]**	
	D(2M_RCP2.6, 2M_RCP4.5)	**D(2M_RCP4.5, Observed)**	**D(2M_RCP2.6, 2M_RCP4.5)**	**D(2M_RCP4.5, Observed)**
Fisher-Rao	0.1125	0.2122	0.0271	0.411
KL($\Sigma 1 \| \Sigma 2$)	0.0067	0.025	0.0004	0.094
Jeffreys	0.0127	0.046	0.0007	0.172
Bhattacharyya	0.0016	0.006	0.0001	0.0209
Wasserstein (W_2)	0.0402	0.067	0.0191	0.272

4.4.3.1 Joint distribution and joint return-periods of observed (1979-2005) precipitation extreme combinations

The spatial distributions of joint return periods during 1979-2005 are investigated to understand the historical behavior of joint return periods over the study area (Figure 4.18). Here, the joint return periods were analyzed based on the 5, 10 and 20-year marginal values and found that the 5-year values of joint return periods are better estimated than 10 and 20-year values. The T5 [CWD, CDD] is ranging from 33-58 years which indicates that the CWD and CDD exceed their 5-year values and may occur every 33 to 58 years in the same year (Figure 4.18). In the upper part (sub-basins (SB) 1, 2 and 3) of the region, T5 [CWD, CDD] is relatively high which shows the less probability of co-occurrence of flood and droughts. In case of T10 [CWD, CDD] and T20 [CWD, CDD] the value is much higher than T5 [CWD, CDD] which is about more than 150 years, which illustrates that the co-occurrence of floods and droughts in the same year is unlikely.

Moreover, the T5 [R20, SDII] is quite low, ranging from 7 to 9 years, indicates that the R20 and SDII may exceed their 5-year values in every 7 to 9 year (Figure 4.18). For T10 [R20, SDII] and T20 [R20, SDII] the ranges from 17 to 25 years and 59 to 89 years, respectively (Figure 4.18). Similarly, joint return periods of [SDII, R95p] range from 11 to 16 years, 30 to 50 years and 96 to 242 years for 5, 10 and 20-year values, respectively (Figure 4.18). This shows the occurrence of very heavy precipitation with high intensity, may increase the chances of floods.

In Figure 4.18, T5 [CDD, SDII] is ranging from 12 to 17 years which indicates that when CDD exceed its 5-year values, SDII may also exceed its 5-year value and vice versa. This implies that the occurrence of drought with high intensity of precipitation

in every 12-17 years.

Additionally, the T5 [R20, R95p], is ranging from 9 to 14 years, T10 [R20, R95p], is ranging from 23 to 44 years and T20 [R20, R95p] is ranging from 60 to 190 years with similar spatial pattern (Figure 4.18).

Based on the analysis, the spatial distributions of change in joint return periods for extreme combinations are different, whereas it is similar for 5, 10 and 20-year marginal values. The result of most of the extreme combinations shows the considerable risk of flood over the region.

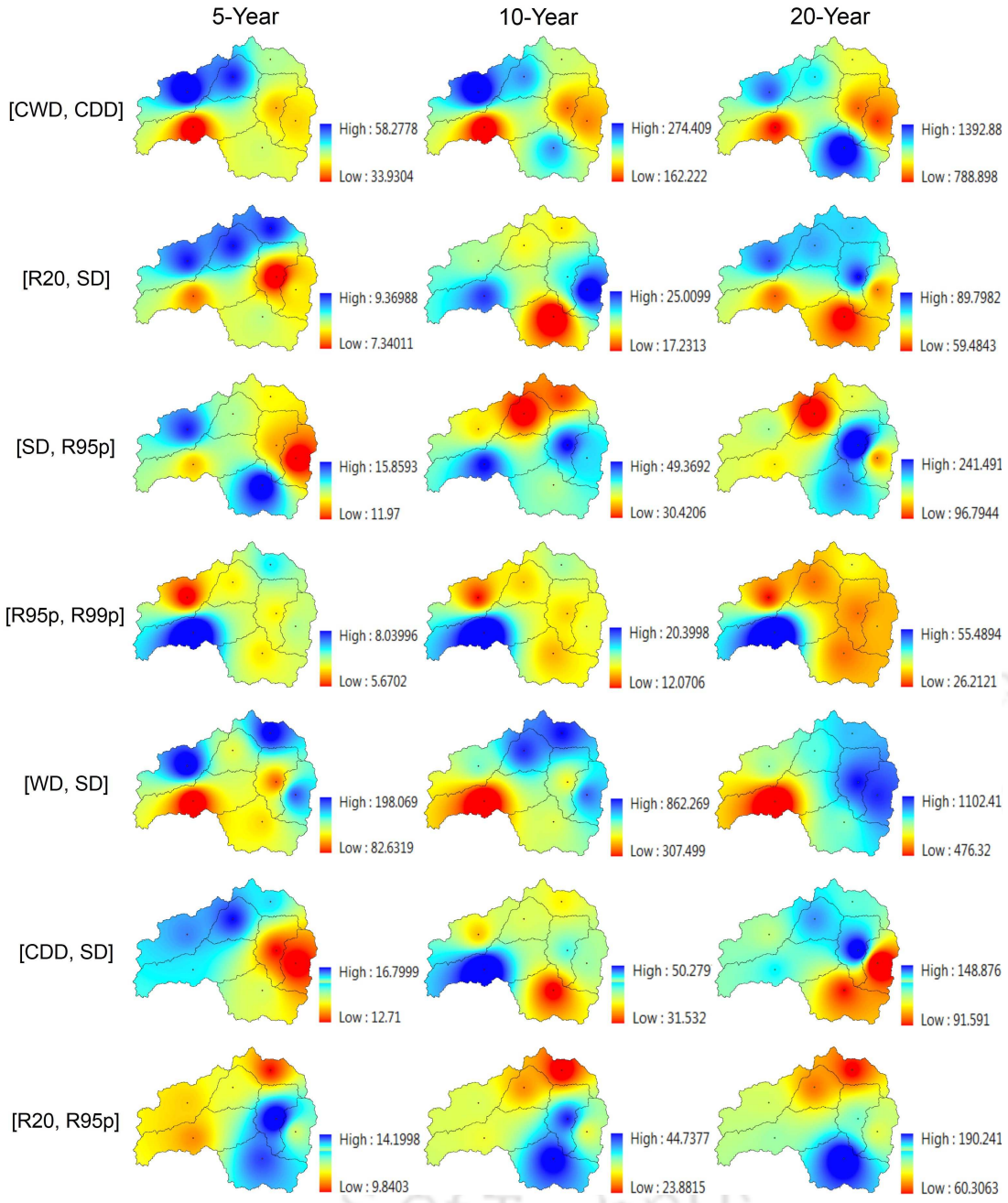

Figure 4.18: Spatial distribution of observed joint return periods (T5, T10 and T20) for precipitation extremes during 1979-2005.

4.4.3.2 The change in joint return period of precipitation extremes during 2021-2100

The change in joint behavior of precipitation extremes is represented as change in joint return periods during 2021-2100 from historical 1979-2005. The spatial patterns of change in joint return period are quite similar for GCM scenarios with different ranges. Figures 4.19 to 4.27 show the spatial variation of change in joint return periods of precipitation extremes for 5, 10 and 20-year marginal during 2021-2100 with the base line period of 1979-2005.

The 5-year change in joint return periods of precipitation extremes are shown in Figures 4.19, 4.20 and 4.21 for different CMIP5 GCMs and their RCPs. The T5 [CWD, CDD] is decreasing by 6 to 50% under RCP2.6, 23 to 55% under RCP4.5 and 14 to 70% under ESM2G RCP8.5 scenarios (Figure 4.19). The co-occurrence of heavy and weak precipitation exceeding their 5-year values in the same year decreased up to 70% under different scenarios. This implies that, in future, the co-occurrence of floods and droughts are more frequent in the same year. The spatial pattern is different for RCP2.6 as compare to RCP4.5 and RCP8.5. For example, the maximum % change found in SB3 under RCP4.5 and RCP8.5, whereas under RCP2.6 the minimum % changes observed in the same SB (Figure 4.19). Similarly, T5 [WD, SDII] is decreased by 80 to 100% under different RCPs (Figure 4.19), representing that once the wet days exceeds its 5-year values, precipitation intensity would also exceed its 5-year values in same year frequently. Consequently, in future, the region may face more occurrence of large precipitation with high intensity especially in upper part of the region (SB1, 2 and 3). The T5 [R20, SDII] is increased up to 70% for all scenarios and SBs, except SB2 of RCP2.6 and SB2, SB3 and SB5 of RCP8.5 (Figure 4.19). T5 [SDII, R95p] is also increased

by 28 to 115% for RCP2.6, 38 to 126% for RCP4.5 and 19 to 168% for RCP8.5, but in the SB5 under RCP8.5 decreased by 2% (Figure 4.19). Similarly, T5 [R95p, R99p] is also increased over the region except in SB5. These results indicate that once the extremes (R20, SDII and R95p) exceed its 5-year values, it is less probability that the other extreme (SDII, R95p and R99p) will also exceed its 5-year values in same year, respectively. The T5 [CDD, SDII] and T5 [R20, R95p] are also increased for all scenarios, implying that, less probability of occurrence of floods over the region. Similarly, Figures 4.20 and 4.21 show the 5-year change in joint return periods for ESM2M and CM3 model, respectively with different ranges of change.

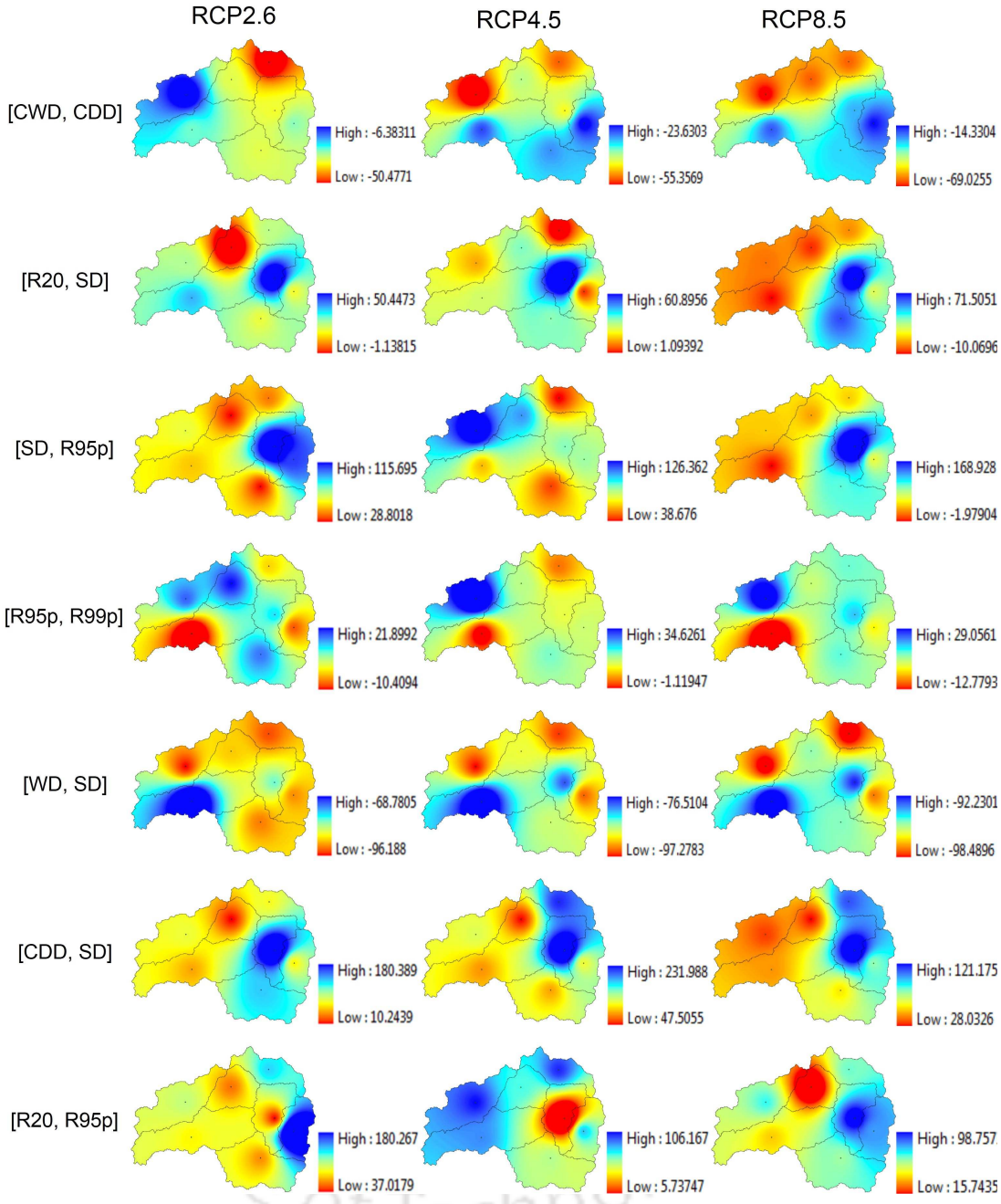

Figure 4.19: The spatial distribution of changing rates (%) of T5 of precipitation extreme combinations during 2021–2100 under ESM2G with their RCP scenarios.

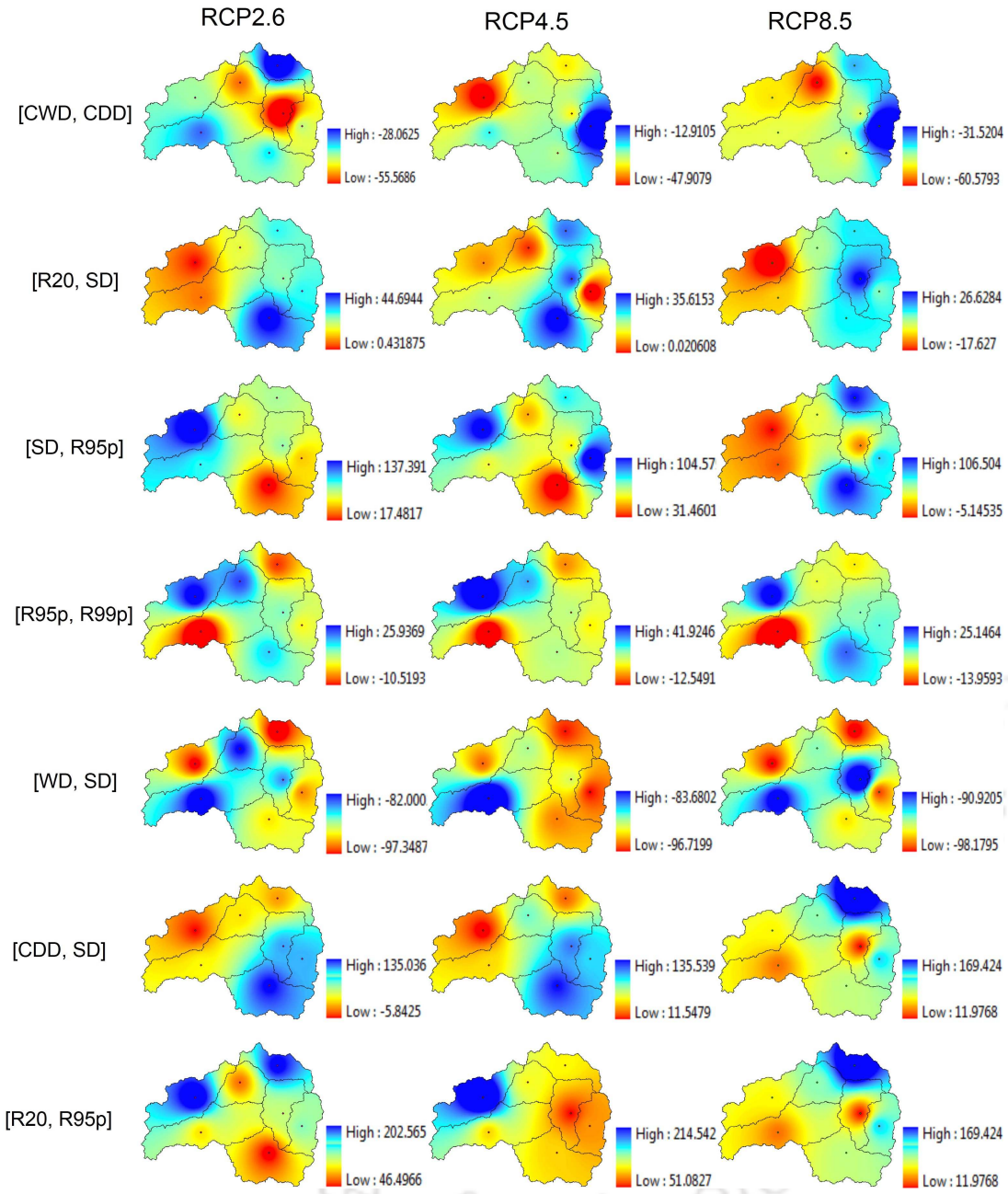

Figure 4.20: The spatial distribution of changing rates (%) of T5 of precipitation extreme combinations during 2021–2100 under ESM2M with their RCP scenarios.

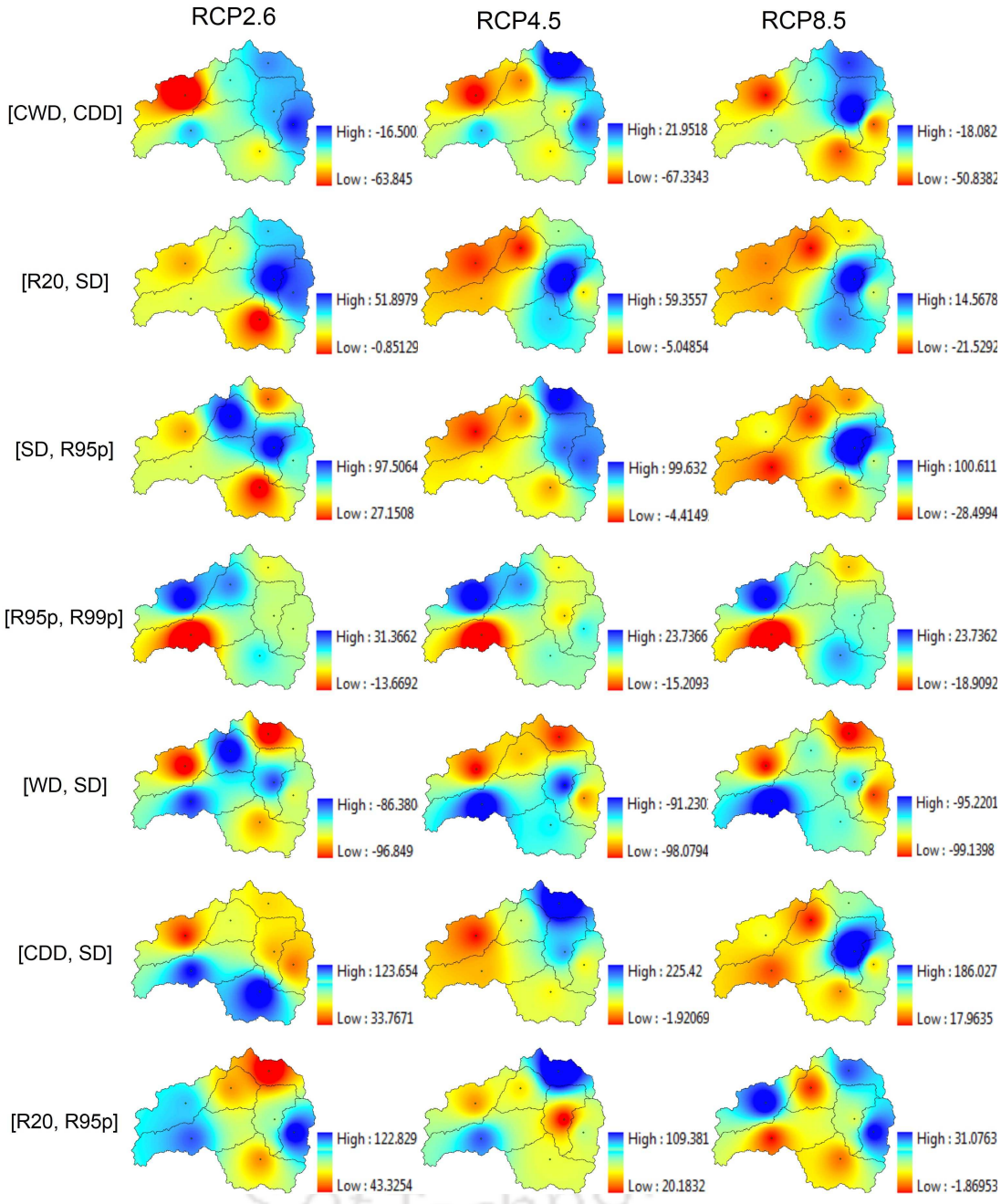

Figure 4.21: The spatial distribution of changing rates (%) of T5 of precipitation extreme combinations during 2021–2100 under CM3 with their RCP scenarios.

In addition, 10-year and 20-year change in joint return period have also been analyzed and found that spatial pattern of 10-year change in joint return periods are similar as 5-year joint return periods, whereas for 20-year, some of the extreme combination are spatially different. Figures 4.22, 4.23 and 4.24 show the 10-year and Figures 4.25, 4.26

and 4.27 show the 20-year change in joint return periods for ESM2G, ESM2M and CM3 models and their RCP scenarios, respectively. For example, T5 [R20, SDII] and T10 [R20, SDII] are showing increasing percentage change except some of the sub-basins, while T20 [R20, SDII] showing decreasing percentage change in most of the SBs. Similar pattern observed in [SDII, R95p], [CDD, SDII] and [R20, R95p]. The result exhibits that the co-occurrence of some the extreme combinations for 20-year would be more frequent as compare to 5 and 10-year.

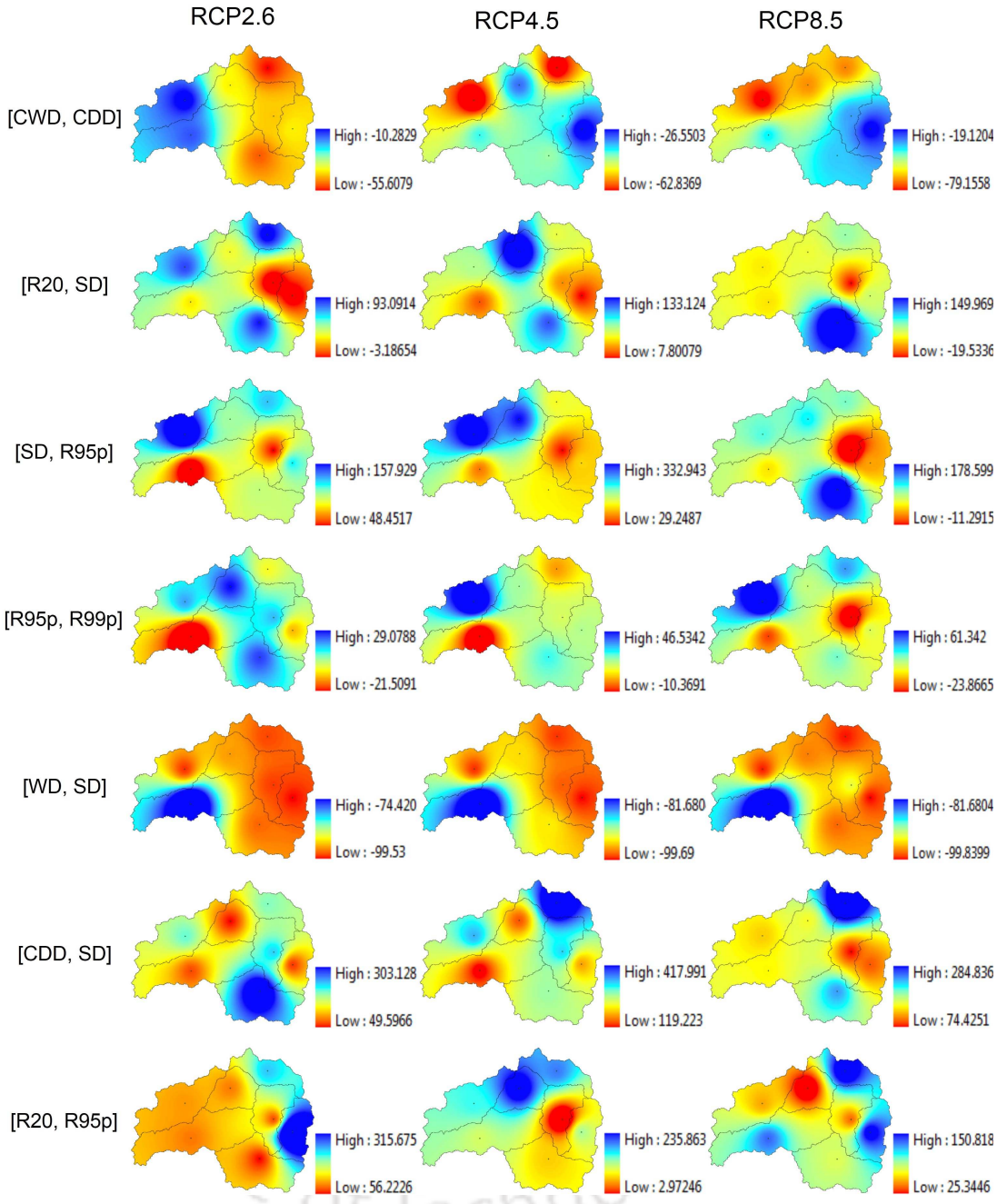

Figure 4.22: The spatial distribution of changing rates (%) of T10 of precipitation extreme combinations during 2021–2100 under ESM2G with their RCP scenarios.

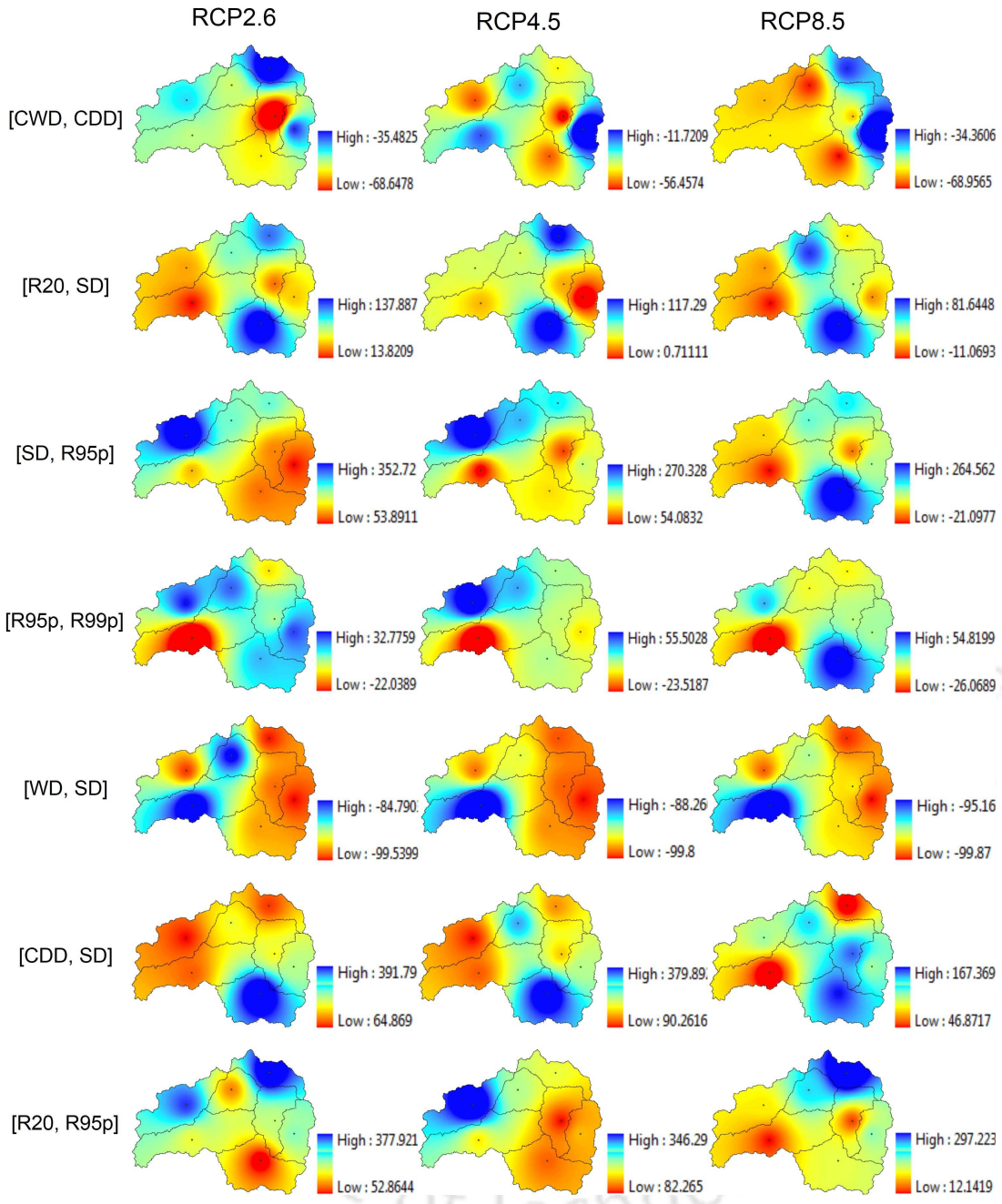

Figure 4.23: The spatial distribution of changing rates (%) of T10 of precipitation extreme combinations during 2021–2100 under ESM2M with their RCP scenarios.

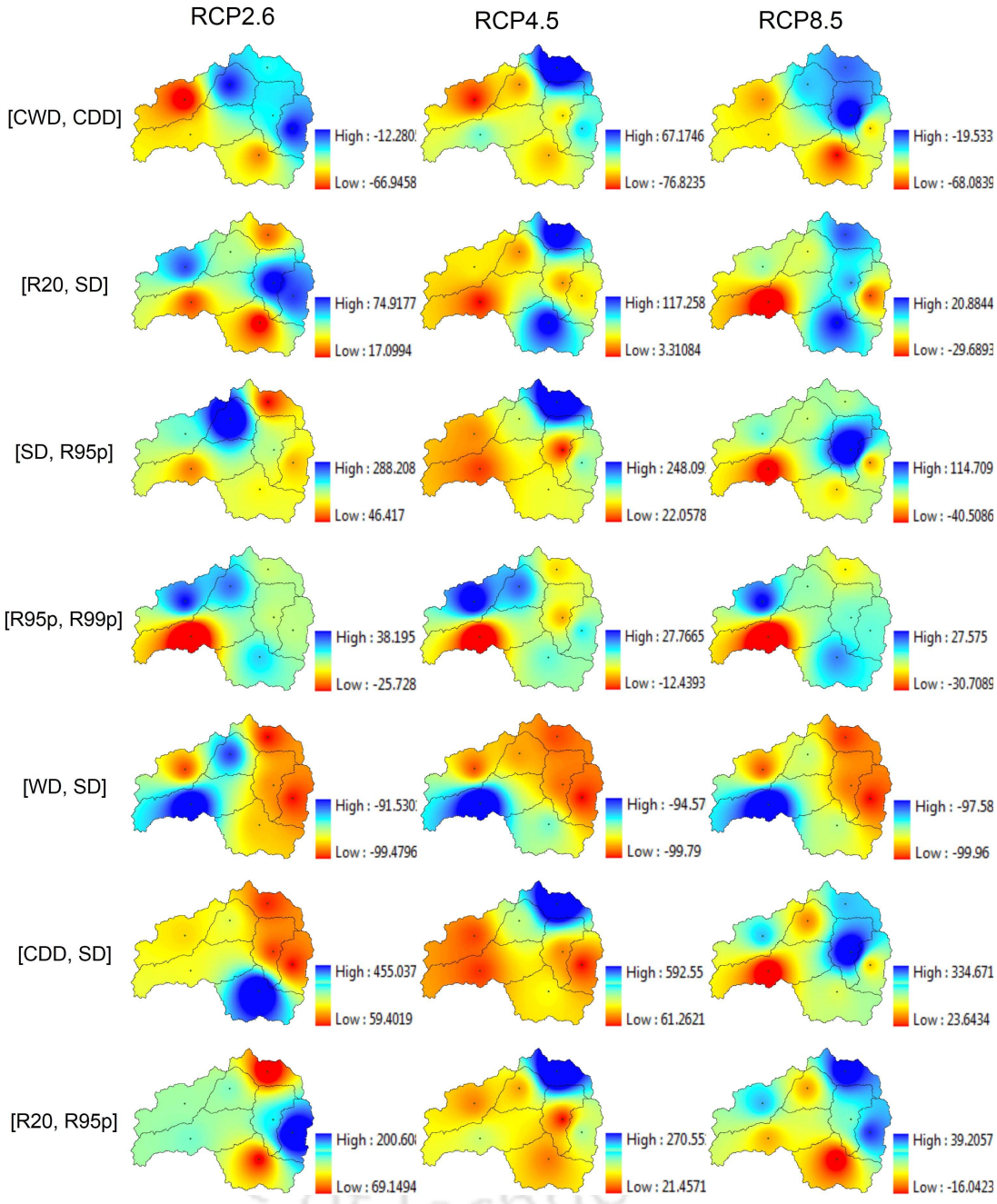

Figure 4.24: The spatial distribution of changing rates (%) of T10 of precipitation extreme combinations during 2021–2100 under CM3 with their RCP scenarios.

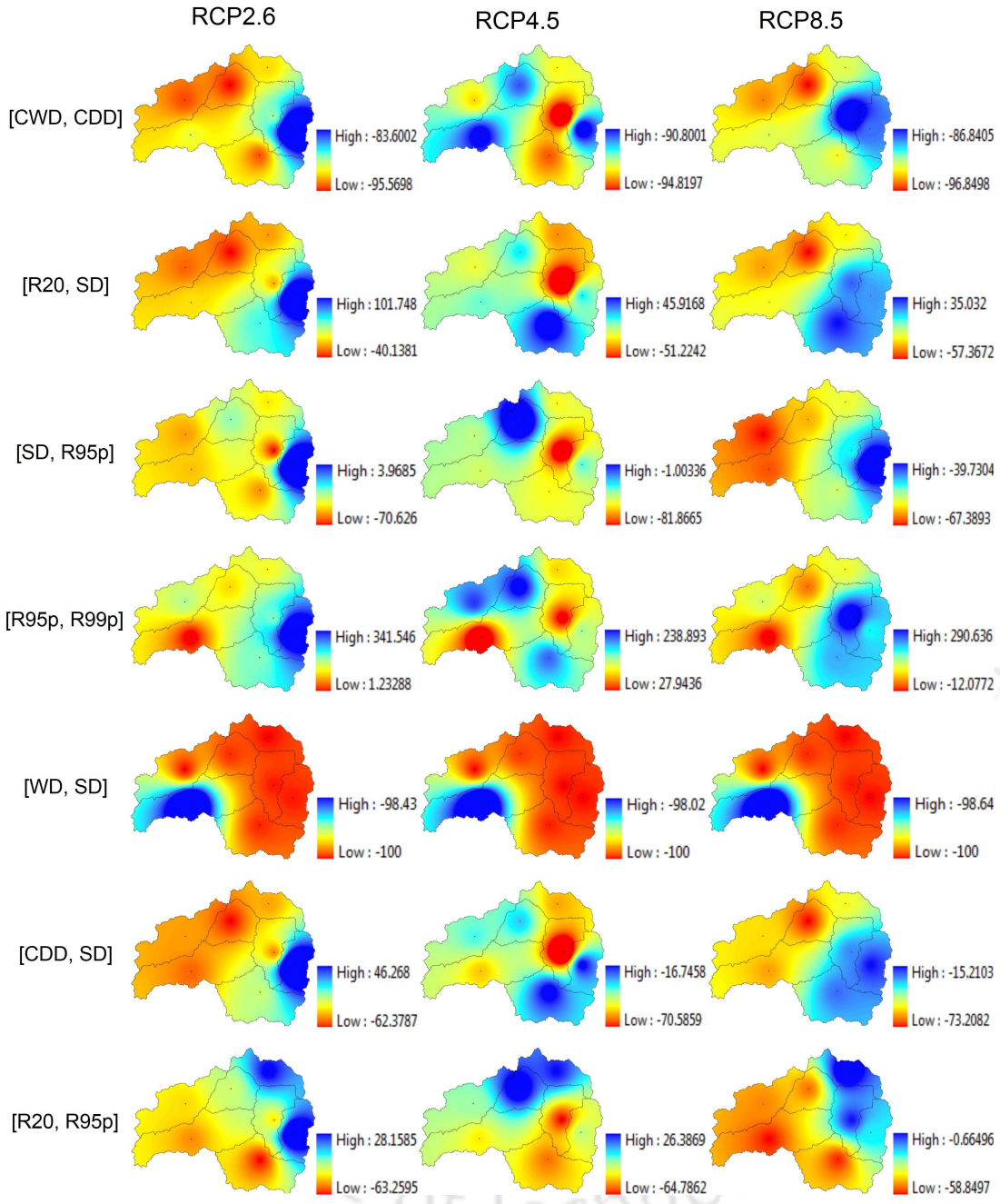

Figure 4.25: The spatial distribution of changing rates (%) of T20 of precipitation extreme combinations during 2021–2100 under ESM2G with their RCP scenarios.

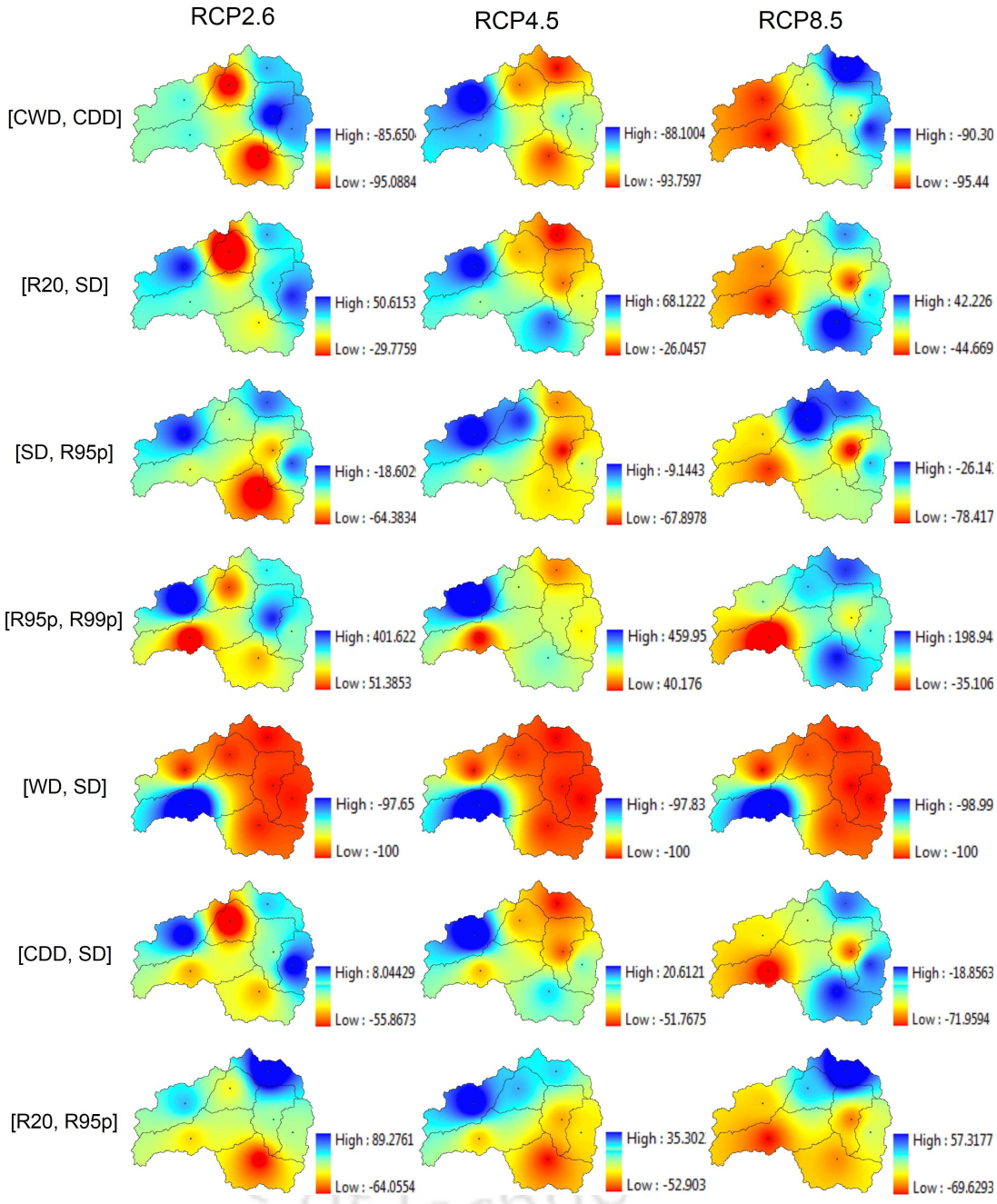

Figure 4.26: The spatial distribution of changing rates (%) of T20 of precipitation extreme combinations during 2021–2100 under ESM2M with their RCP scenarios.

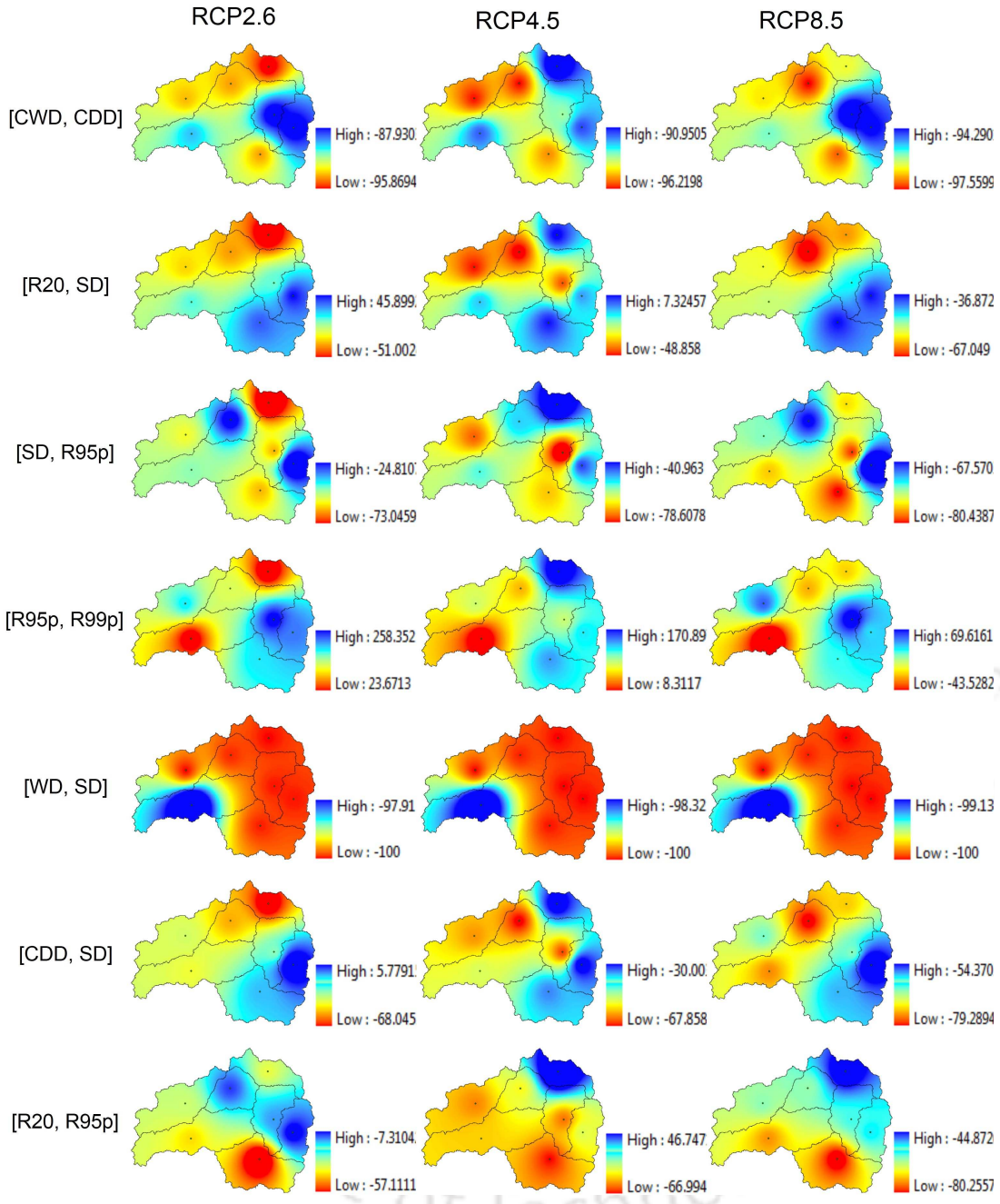

Figure 4.27: The spatial distribution of changing rates (%) of T20 of precipitation extreme combinations during 2021–2100 under CM3 with their RCP scenarios.

4.4.4 Bivariate Analysis of Temperature Extremes

The joint probability behaviour of temperature extremes is essential to recognize the regional responses of warming extremes to climate change for glacier melting and water

resources management. In this study, the joint probability behavior of different combinations of above indices studied, the combinations are [TX90, TN90], [TN10, TN90], [TX10, TN10], [ID0, FD0], [TX10, FD0], [TN10, FD0] and [ID0, TX10]. The combination of extremes have been constructed based on the physical significances such as [TX90, TN90] represents the co-occurrence of extreme warm days and nights within the same year. This may implies the warming trend which can cause the glacier melting, formation of glacial lakes and change in water resources. Similarly the other extreme combinations have been constructed with physical significances and Kendall's coefficient (positively and negatively correlated both). Total seven combinations are constructed in which some are strongly positive correlative and some are negative correlated. Other extreme combination such as [TN10, TN90] represents a joint cool nights and warm nights; the [TX10, TN10] represents a joint cool nights and days; the [ID0, FD0] denotes a joint extreme cold days and nights, [TX10, FD0] represents a joint cold days with extreme cold nights, [TN10, FD0] denotes the joint cool nights with extreme cold nights and [ID0, TX10] represents the joint ice days with cool days. This study illustrates that how the two extremes occurred in the same year and spatiotemporal joint behavior of temperature extremes over the region using a methodology shown in Figure 4.17.

The extreme indices are calculated based on daily temperatures. Then joint distribution and joint return period are assessed for observed (1979-2005) and projected (2021-2100) scenarios. The bivariate relationship and Kendall coefficient between considered extreme indices combination such as [TX90, TN90] under observed (1979-2005) and projected (2021-2100) are investigated (Table 4.18). [TN10, TN90] have insignificant relationships under historical and projected scenarios. TN10 is highly correlated

with FD0 and ID0 is highly correlated with TX10 and their Kendall coefficient values are larger than 0.50 and are significant in all scenarios.

Table 4.18: The Kendall coefficients τ between temperature extremes for observed and projected (2021–2100) scenarios.

Extremes	**Observed**	**ESM2G**			**ESM2M**			**CM3**		
		RCP2.6	RCP4.5	RCP8.5	RCP2.6	RCP4.5	RCP8.5	RCP2.6	RCP4.5	RCP8.5
[TX90, TN90]	0.199	-0.043	-0.065	-0.024	0.111	0.101	0.168	-0.172	-0.016	-0.092
[TN10, TN90]	-0.315	-0.035	-0.16	-0.274	-0.059	-0.157	-0.292	-0.027	-0.199	-0.442
[TX10, TN10]	0.216	0.041	0.1	0.363	0.061	0.303	0.477	0.136	0.358	0.585
[ID0, FD0]	0.162	-0.004	0.034	0.199	-0.053	0.213	0.292	0.166	0.201	0.437
[TX10, FD0]	0.276	0.05	0.116	0.391	0.046	0.29	0.489	0.149	0.341	0.573
[TN10, FD0]	0.893	0.799	0.835	0.902	0.809	0.828	0.899	0.848	0.888	0.928
[ID0, TX10]	0.761	0.624	0.646	0.697	0.624	0.604	0.657	0.727	0.632	0.722

The marginal distribution of univariate temperature extreme indices also analyzed for 5-year (T5) and 10-year (T10) return periods. The comparison of T5 and T10 temperature extremes between observed and projected scenarios are analyzed. The return period (T5 and T10) of discrete variables (FD0 and TN10) are slightly increased in projected scenarios, while return period of remaining variables decrease for both T5 and T10 return periods when compared to the observed. In case of bivariate analysis of temperature extremes, 5 and 10 years return periods are selected because, as return periods increase the uncertainties and biases are large, so it is less confident to interpreting the change in climate extremes (Li et al., 2015), also similar results obtained in bivariate analysis of precipitation extreme case, which is discussed in above section. The Kendall coefficients (τ) and marginal distribution with their joint distribution are analyzed and selected the best fit copula to estimate the joint distribution (for methodology see section 4.4.3). Additionally, the statistical distances are calculated to analyze the structural dependency and distances between two precipitation extremes are shown in Table 4.19.

Table 4.19: Statistical distances of bivariate [ID0, TX10] and [FD0, TN10] Gaussian copulas.

Statistical Distances	**Distances for [ID0, TX10]**		**Distances for [FD0, TN10]**	
	D(2M_RCP2.6, 2M_RCP4.5)	**D(2M_RCP4.5, Observed)**	**D(2M_RCP2.6, 2M_RCP4.5)**	**D(2M_RCP4.5, Observed)**
Fisher-Rao	0.246	0.513	0.458	0.786
KL($\Sigma 1 \| \Sigma 2$)	0.031	0.168	0.131	0.463
Jeffreys	0.056	0.274	0.217	0.684
Bhattacharyya	0.007	0.032	0.026	0.074
Wasserstein (W_2)	0.132	0.219	0.169	0.183

4.4.4.1 Joint distribution and joint return-periods of observed (1979-2005) temperature extreme combinations

Spatial distribution of joint return periods over the North Sikkim during 1979–2005 are studied to understand the past behavior of joint return periods shown in Figure 4.28. The joint return periods of each sub-basins are estimated and interpolated using inverse distance weighted (IDW) technique across region. The 5-year joint return period of [TX90, TN90] is ranging from 12 to 19 years, indicates that the warming event TX90 (warmer days) and TN90 (warmer nights) exceed their T5 values in one year, which may occur every 12 to 19 year in most part of the study region (Figure 4.28). These results indicates that the occurrence of warmer days and nights in the same year. The upper (sub-basin 1) and lower (sub-basin 7) part of the Teesta River, the joint return period of T5 [TX90, TN90] is relatively less, which suggesting that the occurrence warmer days and nights are in higher probability. The 10-year joint return period of [TX90, TN90] is ranging from 35 to 65 year over the region. The occurrence of warmer days and nights over the sub-basin 7 are in high probability as compare to other sub-basins (Figure 4.28).

In Figure 4.28, T5 [TN10, TN90] mainly ranging from 45 to 87 years which indicates the cool nights and warm nights may exceed their 5-year values in the same year. The co-occurrence of cool nights and warm nights in same years in the sub-basin 7 is in low probability. While, in T10 [TN10, TN90] ranging from 257-894 years which are much higher, implying that it's almost impossible to occur over the sub-basin 1. The T5 [TX10, TN10], T5 [ID0, FD0] and T5 [TX10, FD0] over the region are quite low, and ranging from 9 to 15, 9 to 20 and 9 to 14 years, respectively. The co-occurrence of these events in sub-basin 7 (about 9 years) are in high probability in same year. Similarly,

the T10 [TX10, TN10], T10 [ID0, FD0] and T10 [TX10, FD0] are ranging from 21 to 54, 22 to 85 and 20 to 51 years, respectively, and having low probability (Figure 4.28). The 5-year joint return period of [TN10, FD0] is ranges from 5 to 6 years and of [ID0, FD0] is from 5 to 7 years (Figure 4.28). This results indicating that the over the area having high probability to occur cool nights and frost days in same year. Same as the 10-year joint return period is ranges from 12 to 14 years and 12 to 17 years for [TN10, FD0] and [ID0, FD0], respectively (Figure 4.28).

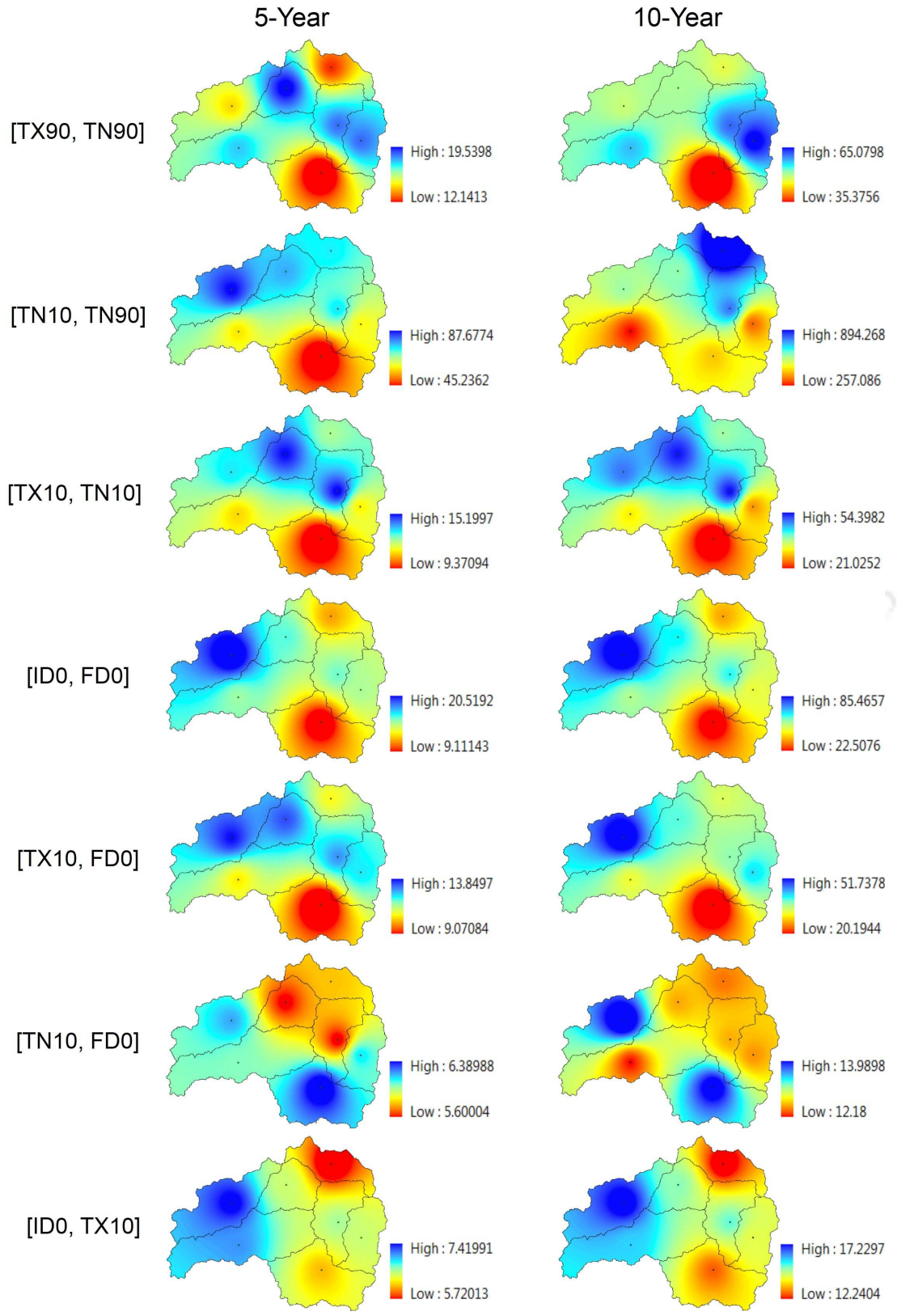

Figure 4.28: The spatial distribution of observed Joint return period (T5 and T10) for temperature extremes during 1979-2005.

4.4.4.2 The change in joint return period of temperature extremes during 2021-2100

The spatial and temporal changes in joint behaviors of temperature extremes can be represented by the spatio-temporal change in joint return period of same. The spatial patterns of change in joint return period are quite similar for GCM scenarios with different ranges. The variations in change in return period for projected temperature extremes from historical duration (1979-2005) are estimated. Figures 4.29 to 4.34 show the spatial variation of change in joint return periods of temperature extremes for 5 and 10-year marginal during 2021-2100 with the base line period of 1979-2005.

The 5-year change in return period of [TX90, TN90], [TX10, TN10], [ID0, FD0], [TX10, FD0], [TN10, FD0] and [ID0, TX10] for all scenarios are increasing over the whole study area, which are representing that the co-occurrences of extremes exceeding their 5-year values in the same year decrease shown in Figure 4.29. T5 [TN10, TN90] in the majority of scenarios decreasing, indicates that the co-occurrences of cool nights and warmer nights exceeding their 5-year values in same year increase (Figure 4.29, 4.30 and 4.31). T5 [TX90, TN90] is increase with the ranges of 42 to 117%, 28 to 150% and 52 to 138% for RCP2.6, RCP4.5 and RCP8.5 of ESM2G model. The increasing percentage change in return period of 5-year, indicating the decrease in co-occurrence of warmer days and nights exceeding their 5-year values in the same year during 2021-2100. Similar patterns are found under ESM2M and CM3 scenarios during 2021-2100, but RCP scenarios of CM3 projecting much higher range of percentage change in return period than ESM2G and ESM2M models shown in Figure 4.31. Figures 4.30 and 4.31 show the percentage change in return period for ESM2M and CM3 with their RCP scenarios, respectively. Highest percentage change obtained in the high elevated zones under the RCP2.6 and

RCP8.5, whereas in RCP4.5 lowest percentage change in same.

During 2021-2100, T5 [TN10, TN90] is decrease in all RCP scenarios with the range of 26 to 95%, 30 to 95 and 19 to 95% for ESM2G RCP2.6, RCP4.5 and RCP8.5 scenarios, respectively. This implies that the occurrence of cool and warmer nights exceeds their 5-year values increase (Figure 4.29). The change in T5 [TN10, TN90] under ESM2M and CM3 RCPs are almost same with different percentage changes. Under the RCP8.5 of CM3, change in T5 [TN10, TN90] in sub-basins 5 and 6 is increased by 2 and 7%, respectively (Figure 4.31). The percentage change in T5 [TX10, TN10] is increased by 54 to 159% for RCP2.6, 61 to 167% for RCP4.5 and 19 to 103% for RCP8.5 of ESM2G (Figure 4.29). Similar pattern have been observed in RCP scenarios of ESM2M and CM3, but RCP8.5 of CM3 is decreased over the region except sub-basins 5 and 7 shown in Figure 4.31. This implies that the chance of occurrence of cool days and nights is increased over the whole region in same year except sub-basins 5 and 7 under the CM3 RCP8.5 scenario.

Similarly, The 5-year percentage change in return period of [ID0, FD0], [TX10, FD0], [TN10, FD0] and [ID0, TX10] are increased for almost all RCP scenarios. This suggests that the occurrence of ice and frost days, cool and frost days, cool nights and frost days and ice and cool days are decrease in same year. Under the CM3 RCP8.5 scenario, 5-year change in return period of [ID0, FD0] in sub-basins 4 and 6, of [TX10, FD0] in sub-basins 3, 4 and 6 and of [TN10, FD0] in sub-basin 6 are decrease.

The percentage change in 10-year return period of [TX90, TN90], [TN10, TN90], [TX10, TN10], [ID0, FD0], [TX10, FD0], [TN10, FD0] and [ID0, TX10] during projected scenarios are showing similar spatial pattern as 5-year percentage change in return period. The spatial distribution of changing rate (%) of 10-year during 2021-2100 for ESM2G,

ESM2M and CM3 models with their RCP scenarios as shown in Figures 4.31, 4.32 and 4.33, respectively. The 10-year percentage change in return period shows the enormous percentage increase for seventh sub-basin for T10 [TX10, TN10], T10 [ID0, FD0], T10 [TX10, FD0], indicates that the co-occurrence of cool days and nights, ice and frost days and cool and frost days exceeding their 10-year value decrease in same year.

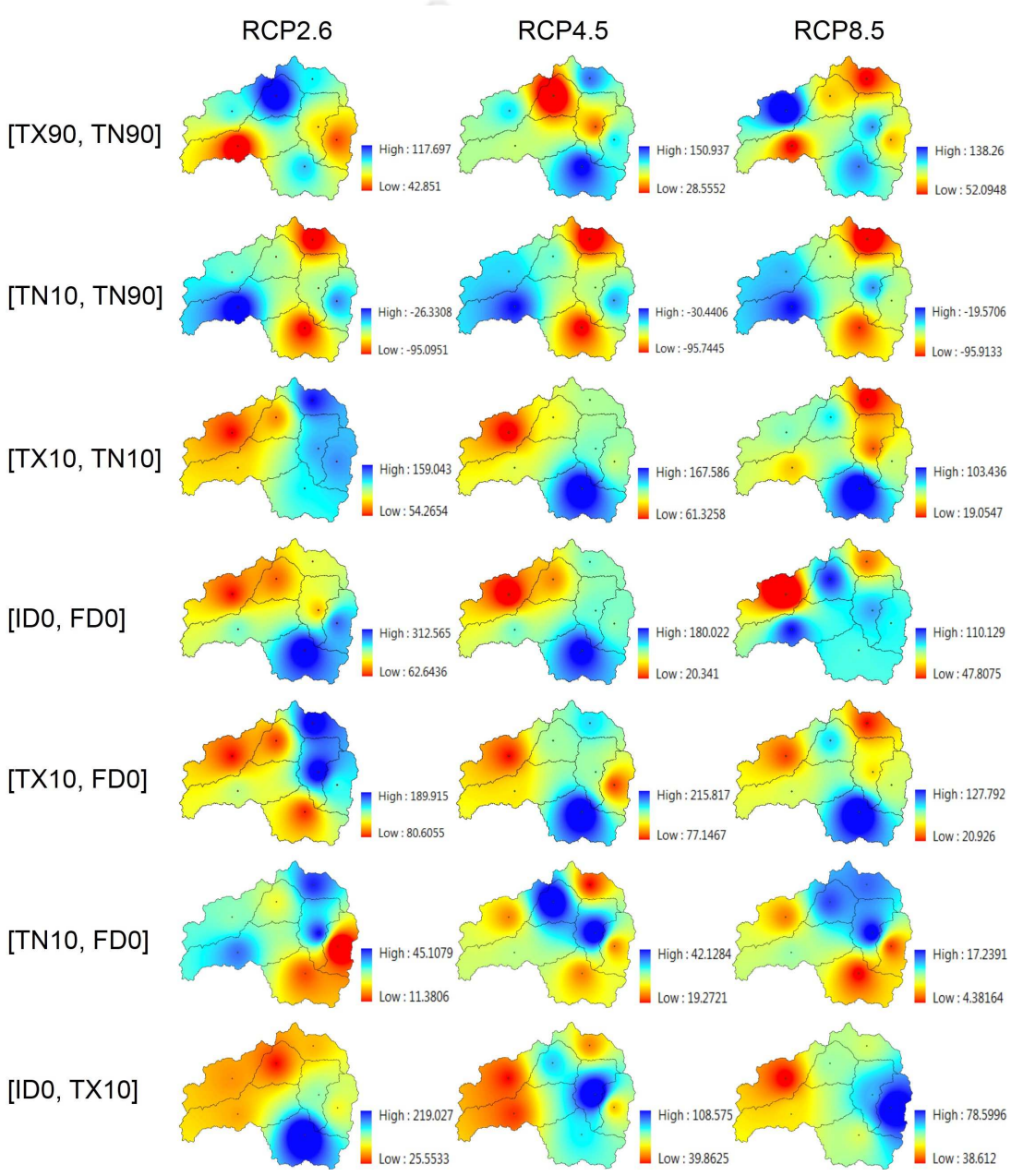

Figure 4.29: The spatial distribution of changing rates (%) of T5 of temperature extreme combinations during 2021–2100 under ESM2G with their RCPs.

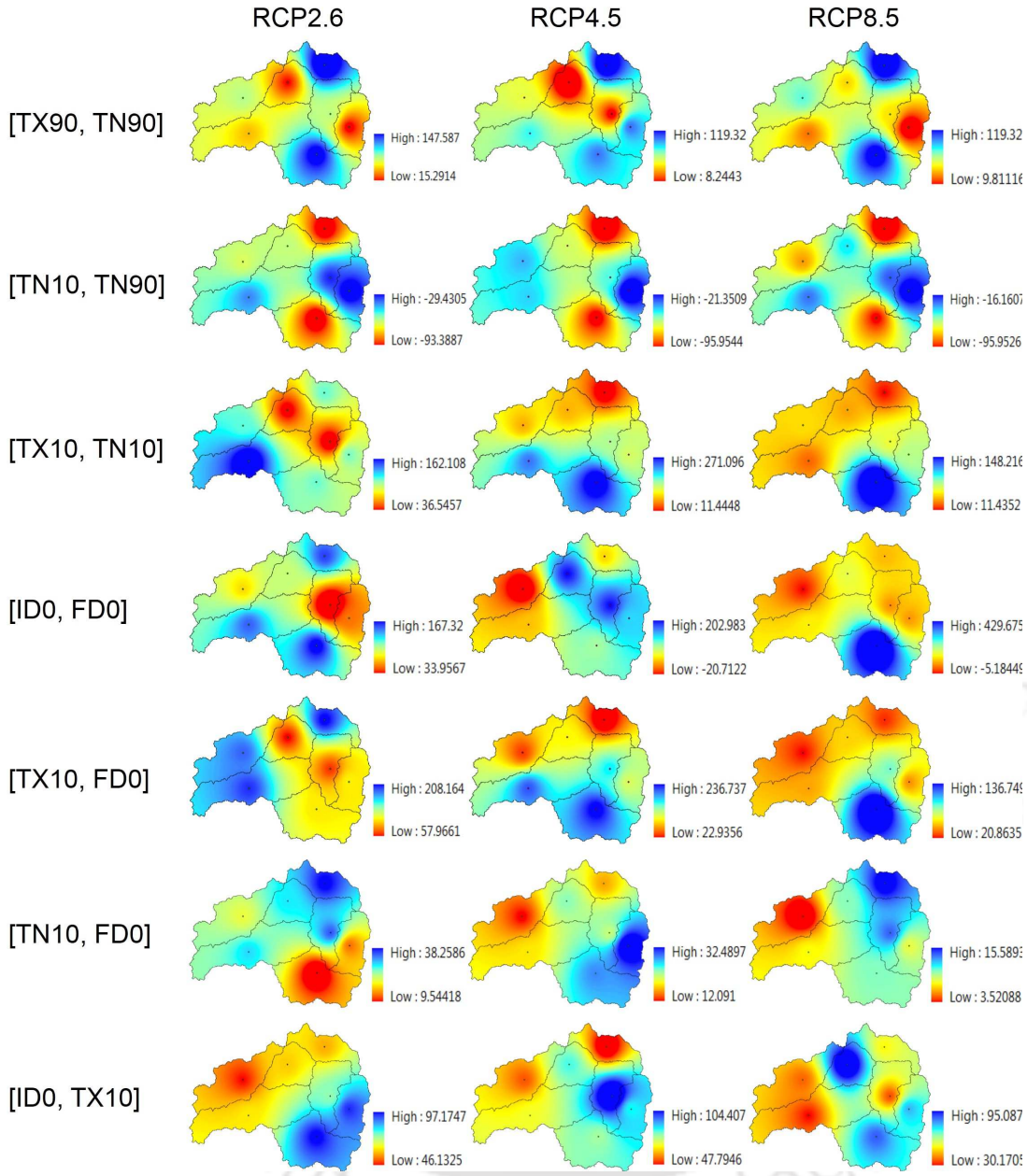

Figure 4.30: The spatial distribution of changing rates (%) of T5 of temperature extreme combinations during 2021–2100 under ESM2M with their RCPs.

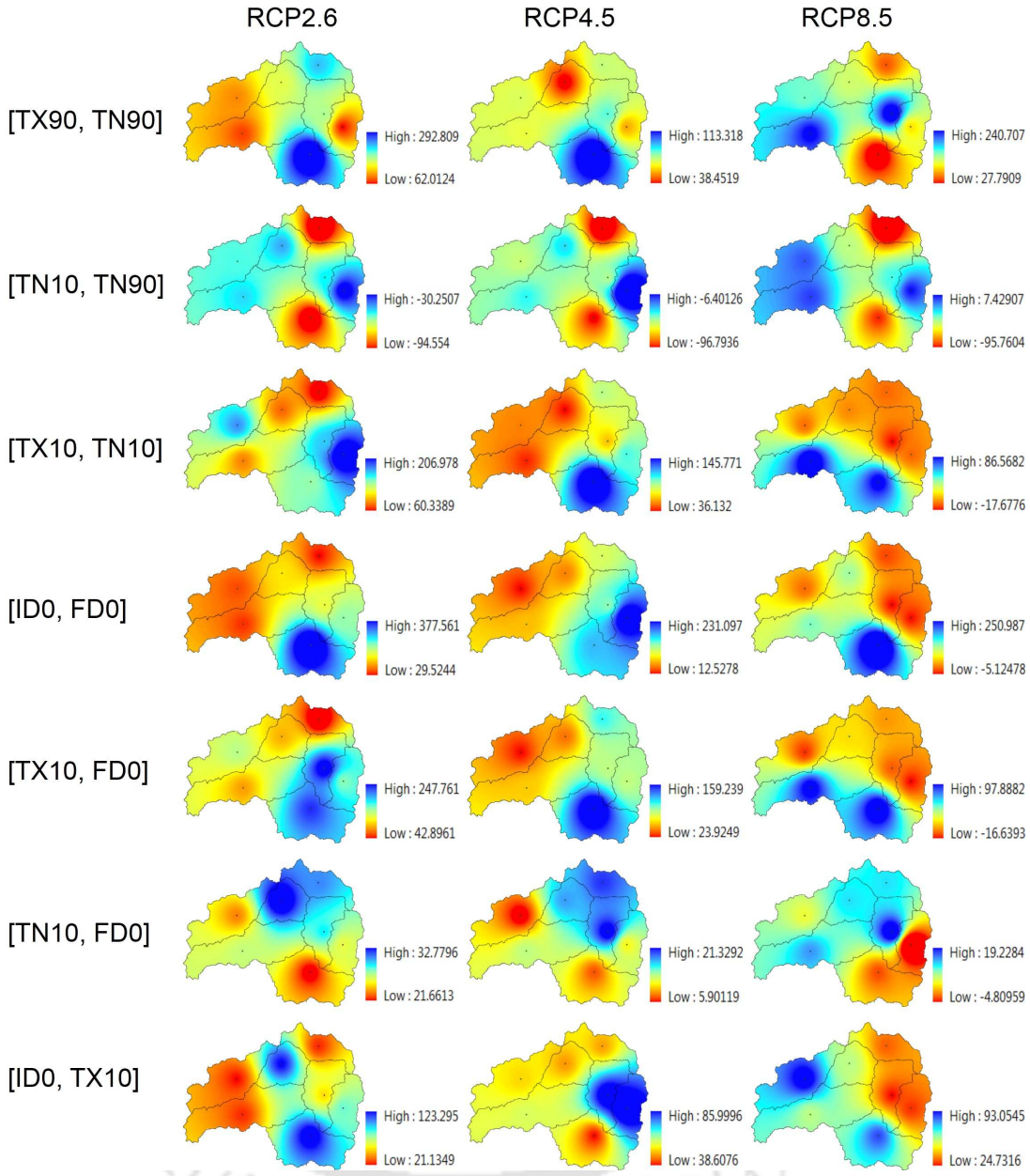

Figure 4.31: The spatial distribution of changing rates (%) of T5 of temperature extreme combinations during 2021–2100 under CM3 with their RCPs.

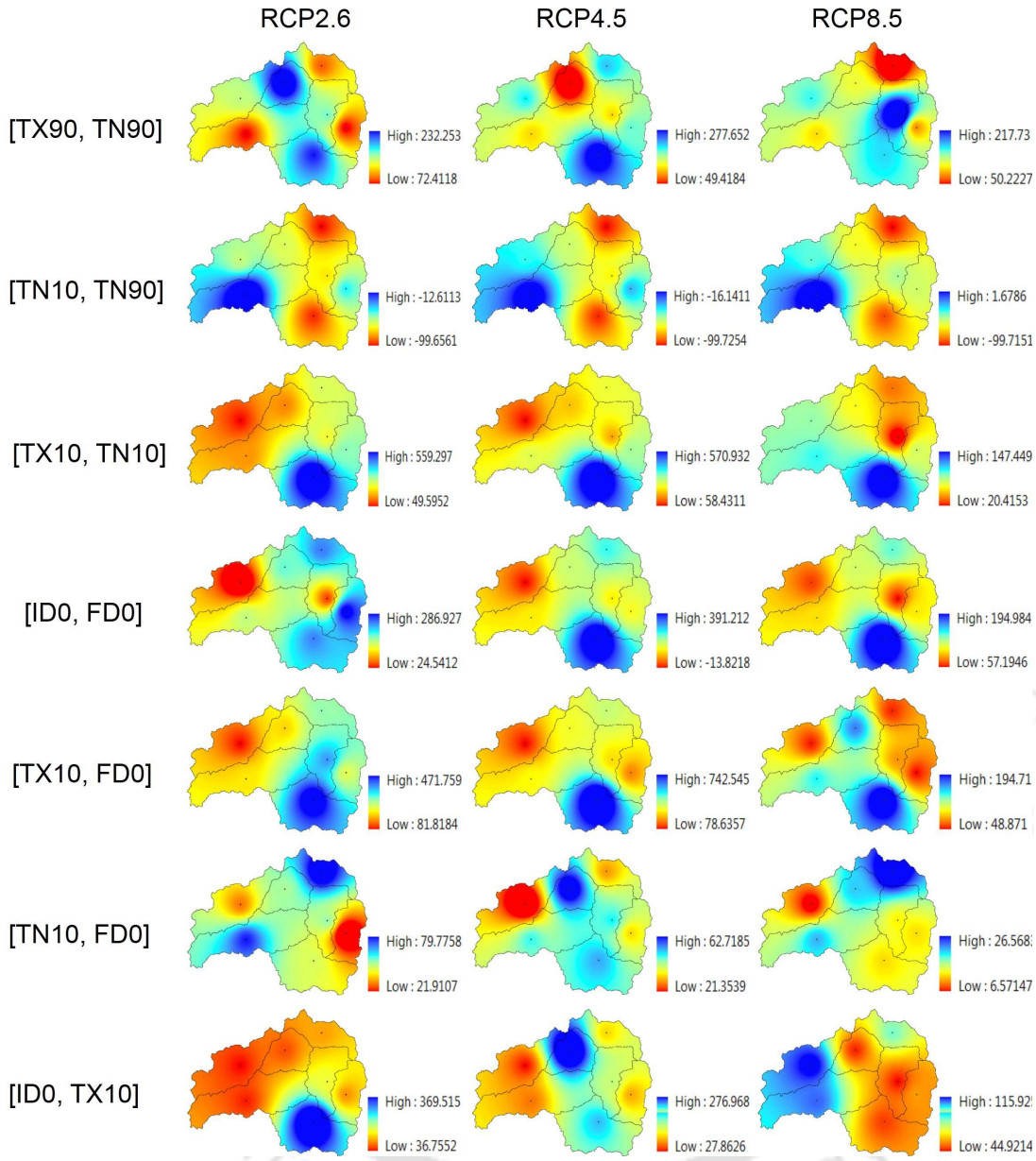

Figure 4.32: The spatial distribution of changing rates (%) of T10 of temperature extreme combinations during 2021–2100 under ESM2G with their RCPs.

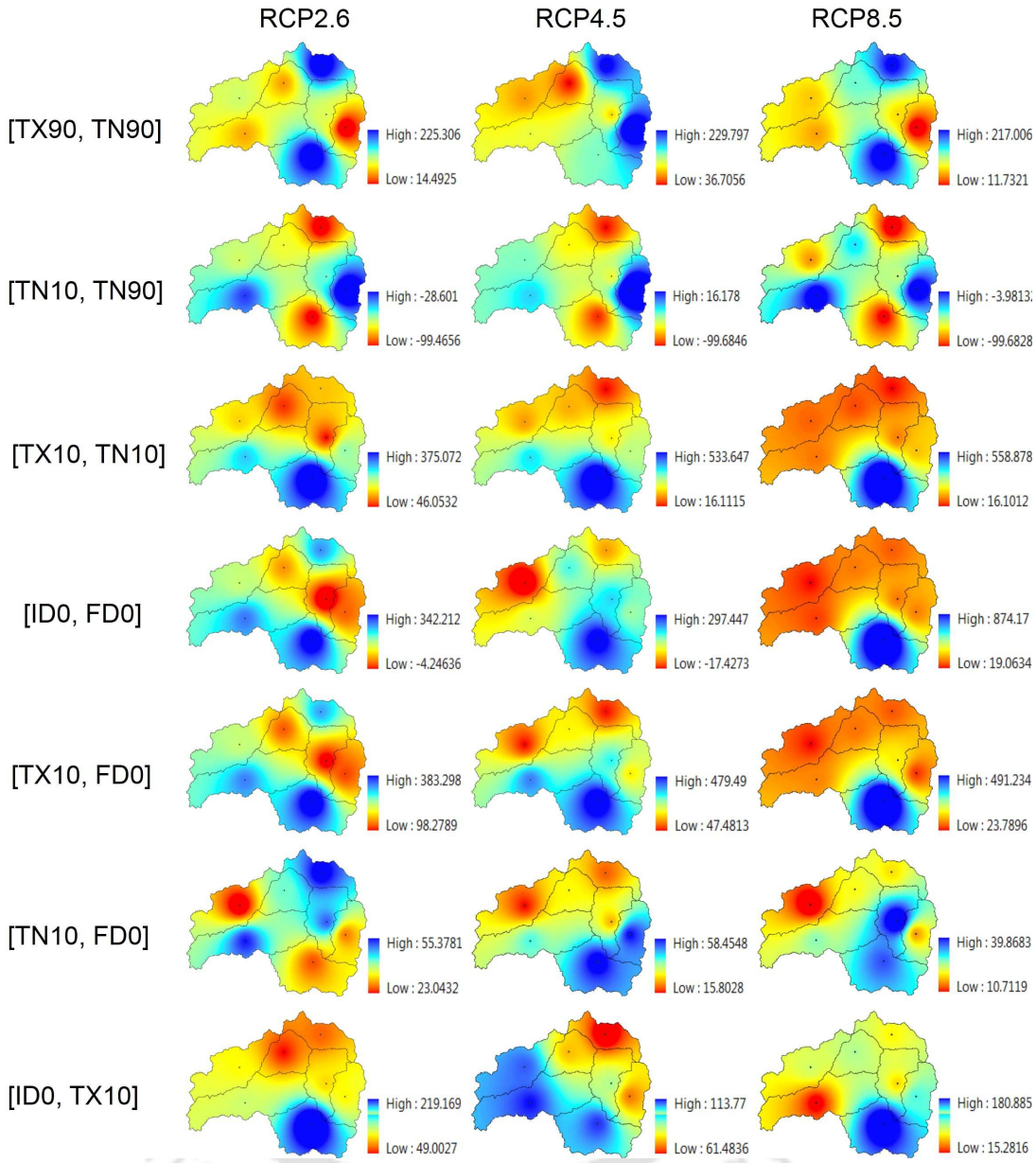

Figure 4.33: The spatial distribution of changing rates (%) of T10 of temperature extreme combinations during 2021–2100 under ESM2M with their RCPs.

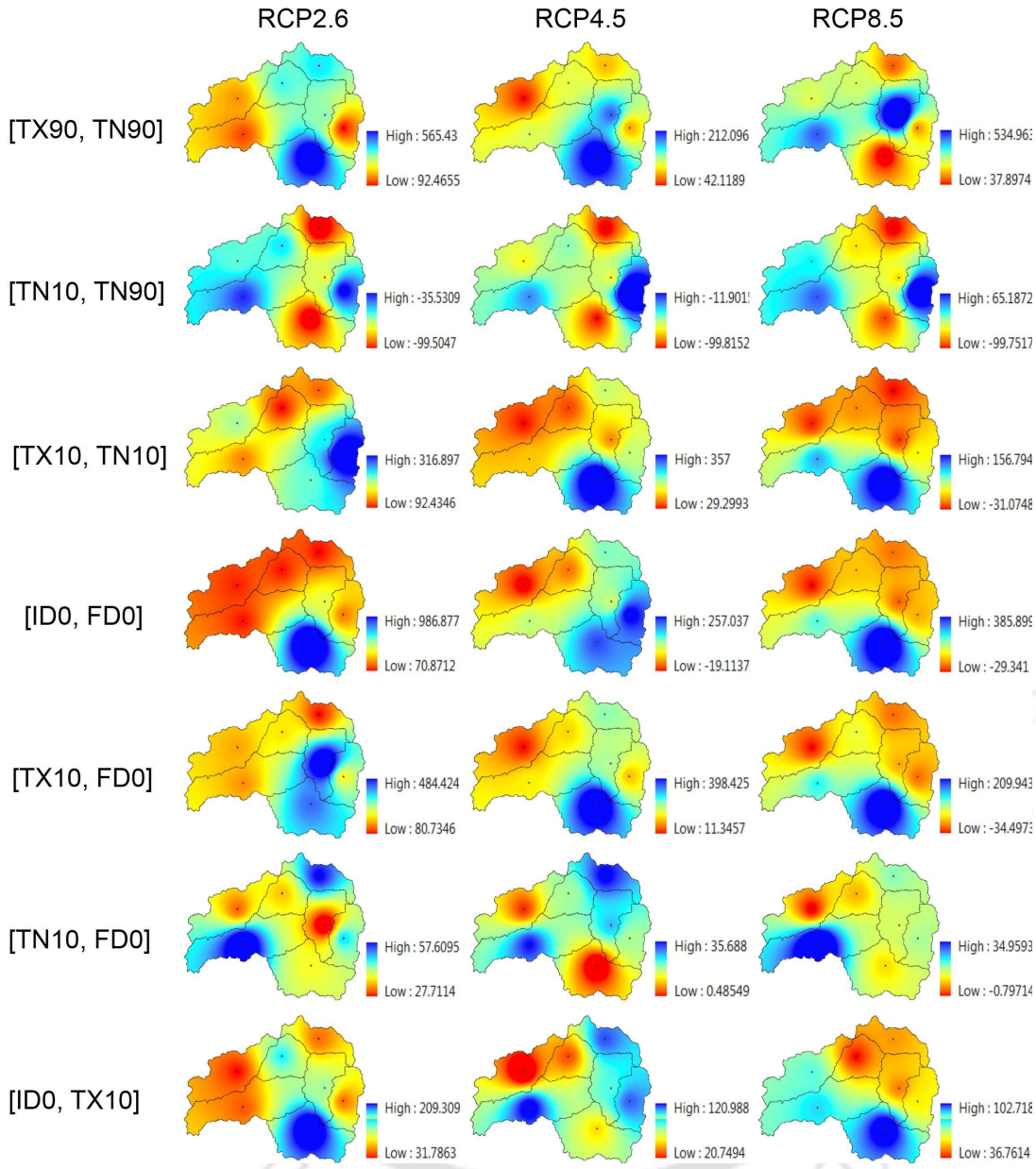

Figure 4.34: The spatial distribution of changing rates (%) of T10 of temperature extreme combinations during 2021–2100 under CM3 with their RCPs.

4.5 Summary and Conclusions

This chapter presets the assessment of climate extremes over the upper Teesta River basin induced by climate change. To accomplish this research work, firstly, the impact of climate change was analyzed by predicting the meteorological variables (precipita-

tion and temperature) using CMIP5 GCMs with their RCP scenarios. Then the joint probabilistic behaviors of climate extremes were investigated using parametric copula. The projected precipitation and temperatures with its extremes are increasing over the Teesta River basin. The heavy and very heavy precipitation days are increased, while number of wet days and CWD are decreased with less dry spell (CDD). The joint return periods of precipitation extreme combinations [CWD, CDD] and [WD, SD] are decreased, indicating that the co-occurrence of floods and droughts as well as floods is more frequent in the same year in future. Additionally, the minimum temperature indices are more pronounced than maximum temperature indices. The joint return period temperature extremes are increased during 2021-2100 except [TN10, TN90]. This implies that the co-occurrence of temperature extreme combination [TN10, TN90] in terms of cool nights and warmer nights are more frequent in the same year in future and other extreme combinations are less frequent over the region.

In all cases, the 2nd combination (GCM grid-point combination) is the more effective combinations than other combination, which shows the significant results as compare to other combinations. This implies that the effects of wind circulation from Bay of Bengal are more predominant over the Sikkim Himalayan environment.

CHAPTER 5

Hydrological Modeling and Relative Contribution

5.1 General

In this chapter, initially hydrological modeling has been presented. The MIKE11 rainfall-runoff edition Nedbor Afstromnings Model (NAM) has been used as hydrological model to assess the main water balance components over the hilly catchment of Teesta River. Hydrologic modeling for the watershed is important for analysis of the hydrological processes of flood forecasting and water resources management (Shamsudin and Hashim, 2002). For the hilly catchment, the distributed hydrological models are not appropriate because of lack of hydrological and hydro-meteorological dataset (Wang et al., 2016). Therefore, a lumped and conceptual model would we useful for rainfall-runoff simulation. This model was originally developed by the Department of Hydrodynamics and Water Resources of the Technical University of Denmark. The hydrological model (MIKE11 NAM) is a lumped conceptual rainfall-runoff model used to simulates the overland flow and base flow to describe the hydrological cycle of watershed using a set of mathematical equations (Shamsudin and Hashim, 2002; De Paiva et al., 2013). Due to being a lumped model, this considers each catchment as a unit,

therefore the average values of parameters are consider for entire catchment. The simulated water balance components are the function of four different soil moisture stages namely; surface zone storage, root zone storage, ground water storage and snow melt storage. Snowmelt storage is only used where catchment area comes under glacier-faded zone (Wang et al., 2016). Some of the model parameters can be evaluated based on the physical catchment dataset, but the final product must be evaluated by calibration with observed hydrological time series (Madsen, 2000). The projected water balance components have been estimated for the time period of 2006-2100 based on the projected precipitation and temperature dataset using CMIP5 GCMs and their RCP scenarios. Global observations have verified that the considerable changes of catchment hydrological regimes are influenced by integrated consequences of climate variability and land use/cover changes induced by human interactions (Gao et al., 2016; Wu et al., 2017). Vorosmarty et al. (2000) have analyzed that the demand of water resources has rapidly increased with population growth, whereas global and local water resources have simultaneously decreased. Thus, the spatial and temporal variability of hydrological cycle is the one of the most key controlling factor to assess the water balance variability (Yang et al., 2007). The diminishing water supply and variability in the dynamics of hydrological cycle prove the sensitiveness of river basins in India to climate and LULC change. Therefore it is important to analyze the contribution of climate and anthropogenic activities to changes in runoff generation (Jiang et al., 2015). There are number of global and regional land surface models to assess the water balance such as hydrological modeling, statistical methods and Budyko framework. Among of them the Budyko framework is the robust approach to evaluate the water-energy balance, which links the land surface and climatic factors to characterize the water cycles at catch-

ment scales (Williams et al., 2012; Xu et al., 2013). Therefore, the Budyko framework is used to assess the relative contribution of climatic factors (precipitation, snow-ratio and evapotranspiration) to runoff changes for different scenarios.

5.2 Hydrological Modeling – MIKE11 NAM

The hydrological model (MIKE11 NAM) a deterministic, lumped and conceptual rainfall-runoff model, simulating the overland flow, interflow and base flow component of catchment runoff as function of soil moisture in four storages. Model includes a number of optional extensions, including an advanced snow-melt routing and a separate description of hydrology within the irrigated areas. The physical processes involved for runoff simulation in the MIKE11 NAM model, the structure of model is shown in Figure 5.1. The model considers each catchment as single unit, thus the variable and parameters are taken as average value for entire catchment. It has a set of linked mathematical relationship to understand the performance of the different zones of the hydrological cycle. The simulation of model is done with four different soil moisture functions namely; surface zone storage, root zone storage, ground water storage and snowmelt storage. Snowmelt storage is only used where snowmelt contributes considerably to runoff of catchment area (Wang et al., 2016). The other three storages such as surface zone storage shows vegetation and near surface soil, root zone storage represents the moisture in root zone above which overland flow is generated and ground water storage represents moisture in root zone above which groundwater is generated.

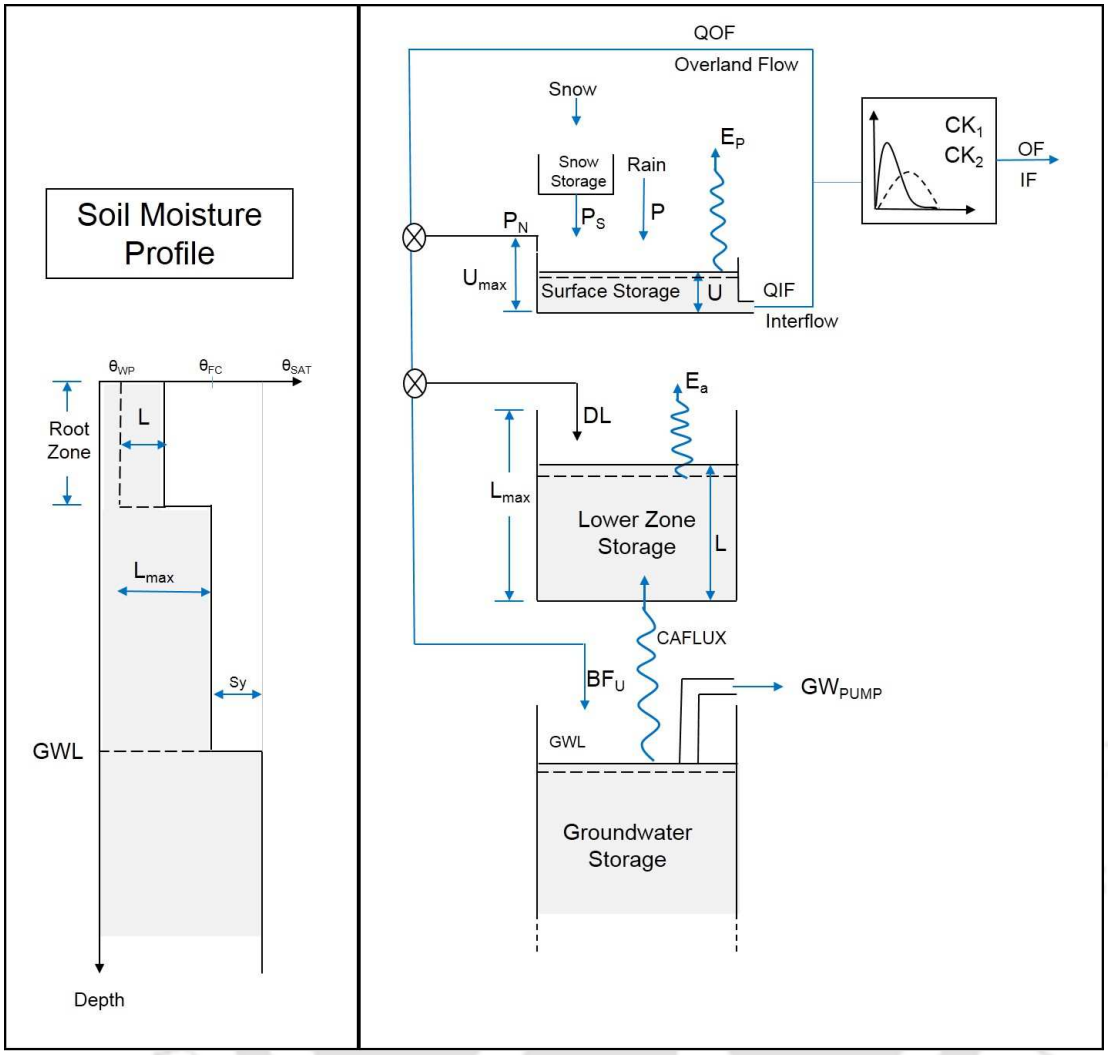

Figure 5.1: Structure of MIKE11 NAM Model

5.2.1 Model Development

MIKE 11 NAM model was applied to the Teesta River catchment (up to Chugthang), for calibration of model precipitation, potential evaporation and mean temperature datasets were used. During calibration total nine parameters are auto calibrated and obtained optimum values. These optimized parameters are used to estimate the runoff within the catchment. NAM considers (as default) nine parameters automatically, accounting the surface zone storage, root zone storage and ground water storage. Additionally, nine parameters are auto calibrated and these parameters are listed below as

suggested by DHI (DHI, 2009).

1. **Maximum water content in surface storage** (Umax), represents the cumulative total wate content of the interception storage (on vegetation) and upper soil layers storage.

2. **Maximum water content in root zone storage** (Lmax), indicates the maximum soil moisture content in the root zone, available for transpiration in vegetation.

3. **Overland flow runoff coefficient** (CQOF), determines the division of excess rainfall between overland flow and infiltration.

4. **Time constant for routing interflow**(CKIF), determines the amount of interflow, decreases with higher time constants.

5. **Time constants for routing overland flow** (CK_1, CK_2), represents the shape of the hydrograph peaks. The routing is done by two-linear series reservoirs for same time constant (CK_1, CK_2). Where, high sharp peaks are obtained at shorter time constant and low peak at longer time constant.

6. **Root zone threshold value for overland flow** (TOF), determines the relative moisture content in root zone (L/Lmax) above which overland flow generated. The impact of TOF can be realize during rainy season, where an increase in parameter values will delay the start of runoff.

7. **Root zone threshold value for overland flow** (TIF), determines the relative moisture content in root zone (L/Lmax) above which overland flow generated.

8. **Time constant for routing base flow**(CKBF), this constant can be determine

from the hydrograph recession during dry season. The shape of the measured recession changes to a slower recession after some time is rarely.

9. **Root zone threshold value for groundwater recharge**, (TG), determines the relative moisture content in root zone (L/Lmax) above which ground water recharge generated. There is less recharge to the groundwater with increase in TG values.

Further defaults ranges of these nine parameters (DHI, 2009) are shown in Table 5.1, which shows the parameter upper and lower range with their units.

Table 5.1: Default parameters ranges of MIKE11 NAM Model

S. No.	Parameters	Lower Range	Upper Range	Unit
1.	U_{max}	10	20	mm
2.	L_{max}	100	300	mm
3.	C_{QOF}	0.1	1.0	-
4.	C_{KIF}	200	1000	hours
5.	CK_1, CK_2	10	50	hours
6.	T_{OF}	0	0.99	-
7.	T_{IF}	0	0.99	-
8.	C_{KBF}	1000	4000	hours
9.	T_G	0	0.99	-

5.2.2 Basic Component of MIKE11 NAM Model

To represent the various phases of hydrological cycle, the component of NAM model represented in terms of mathematically functions as follow:

1. **Evaporation:** The demands of evaporation (Ea) are fulfilled from the surface capacity at the potential rate. The moisture content (U) in surface capacity is rarely less as compare to requirements, and the remaining moisture is extracted back by the lower zone at an actual rate Ea, where Ea is potential evapotranspiration and it varies with relative soil moisture as:

$$\begin{cases} \text{L} & \text{U} \geq E \\ \text{U+L}/(L_{max}\ \text{(E-U)} & \text{otherwise} \end{cases} \tag{5.1}$$

2. **Overland Flow:** At certain limit when the surface storage spills (U $>U_{max}$), the excess water flow as overland flow and also infiltrate. Overland flow (QOF) is the part of net rainfall, which is corresponds to the net rainfall (Pn) and relative soil moisture content (L/L_{max}) at the lower zone storage. This happens only when the saturated fraction of the lower zone exceeds threshold value.

$$\begin{cases} C_{QOF}P_n[\text{L}/L_{max}\text{ -TOF}] & \text{L}/L_{max} > \text{TOF} \\ 0 & \text{otherwise} \end{cases} \tag{5.2}$$

3. **Interflow:** Interflow QIF is directly related to U and relative lower zone soil moisture. The QIF occurs when lower zone saturation fraction exceeds the threshold value. The interflow is available water to upper zone storage to keep it interflow.

$$\begin{cases} C_{QIF}[(\text{L}/L_{max}\text{-TIF})/(1\text{-TIF})] & \text{L}/L_{max} > \text{TIF} \\ 0 & \text{otherwise} \end{cases} \tag{5.3}$$

4. **Interflow and Overland Flow Routing:**The interflow is directly related to two linear reservoirs for same time constant CK12. This is also based on the same idea with variable time constant. The time constants (CK) are modified as

mathematical equation, which holds a linear response of nearly surface flow and kinematic response of above surface flow.

$$\begin{cases} CK_{12} & \text{OF} > OF_{min} \\ CK_{12}[\text{OF}/OF_{min}]^{-\beta} & \text{otherwise} \end{cases} \tag{5.4}$$

Where, OF is overland flow (mm/hr) and β =0.4.

5. **Groundwater Recharge:** The groundwater recharge depends upon the soil moisture content in the root zone storage. It is related to the infiltrating to the lower zone, it occurs when the saturated fraction exceeds the threshold value.

$$\begin{cases} \text{I}[\text{L}/L_{max}\text{-TG}/(1\text{-TG})] & \text{L}/L_{max} > \text{TG} \\ 0 & \text{otherwise} \end{cases} \tag{5.5}$$

In the present study, calibration was carried out using in-built calibration function to set the model parameters. The evaluation of model performance is done based on the root-mean-square error (RMSE) between the observed and forecasted values and Efficiency index as suggested by (Nash and Sutcliffe 1970).

$$RMSE = \sqrt{\frac{\sum_{t=1}^{n}(Q_t^o - Q_t^s)^2}{n}} \tag{5.6}$$

$$Efficiency\ Index(EI) = 1 - \frac{\sum_{t=1}^{n}(Q_t^o - Q_t^s)^2}{\sum_{t=1}^{n}(Q_t^o - \overline{Q^o})^2} \tag{5.7}$$

The ranges of nine default parameters are used to calibrate the model, than calibrated model generates the optimized values of default parameters based on the RMSE and EI as shown in Table 5.2. Further, calibrated model used to generate the historical stream flow during 1991 to 2005 as shown in Figure 5.2. From the Table 5.2, it

is observed that the maximum water content in surface storage (U_{max}) within the top few centimeter which is 18.9 mm and the lower zone representing the maximum water content in root zone storage (L_{max}) is 286 mm. The time series is divided into two part for calibration (1991-2000) and validation (2001-2005), the calibration and validation results are shown in Figure 5.2. The calibration and validation result shows at daily time scale.

Table 5.2: Optimized parameters using auto-calibration in MIKE11 NAM model

S. No.	**Parameters**	**Unit**	**Optimized value**
1.	U_{max}	mm	18.9
2.	L_{max}	mm	286
3.	C_{QOF}	-	0.721
4.	$_{CKIF}$	hours	839.8
5.	CK_1, CK_2	hours	25.8
6.	T_{OF}	-	0.309
7.	T_{IF}	-	0.199
8.	C_{KBF}	hours	11648
9.	T_G	-	0.437

After auto calibration, the optimized parameters are used to simulate the projected streamflow for the time period of 2006-2100. The different projected GCM grid-point combination's precipitation and temperature datasets are used to project stream flow over the Teesta River catchment. The projected stream flow shows the significant increase during 2006-2100 for all projected scenarios (Figures 5.3-5.9). Figures 5.3 to

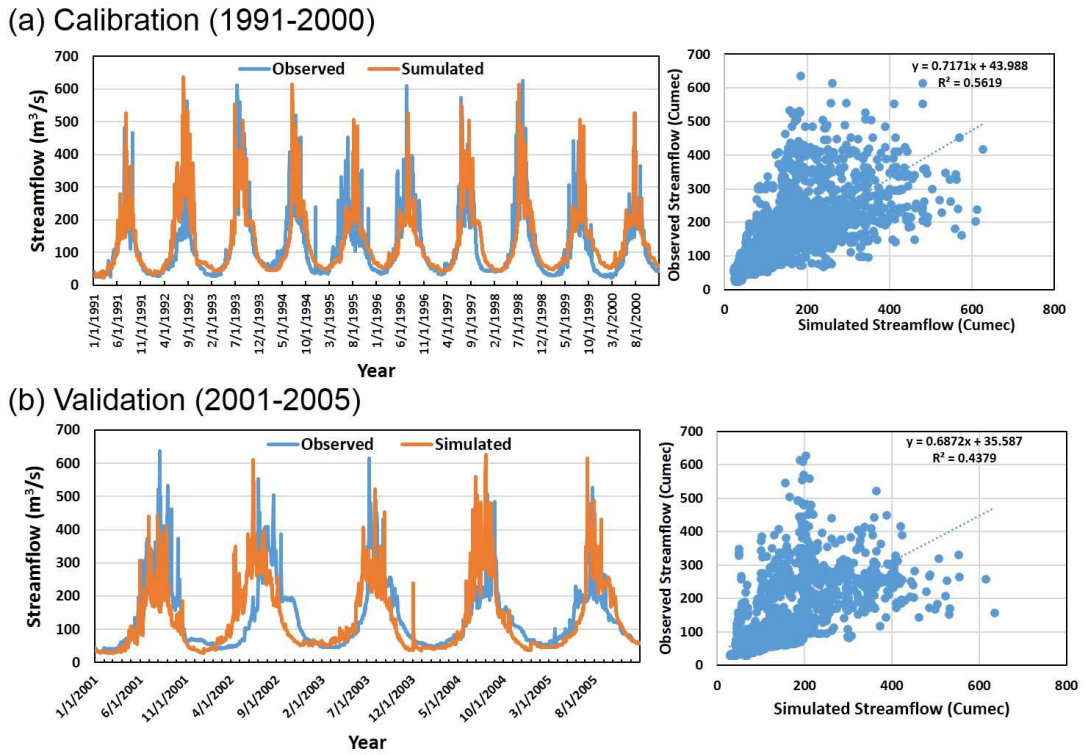

Figure 5.2: Calibration and validation results of MIKE11 NAM model.

5.9 represent the annual streamflow for the duration of 2006-2100 for different GCM scenarios and combinations. The projected streamflow have increased in the 21st century with the range of 8.51 to 22.63 m^3/s for RCP 2.6 scenario, 9.25 to 21.85$m^3/s$for RCP4.5 scenarios and 6.16 to 27.01m^3/s for RCP8.5 scenarios as compare to reference base period of 1991-2005. The average observed annual streamflow during 1991-2005 at Chugthang gauge station is about 132.36 m^3/s. The result shows that the maximum increase in streamflow is about 20.41% and minimum increase is about 4.64%. The maximum change was found in the 2nd combination and minimum change was found in the 6th combinations of RCP 8.5 scenarios.

Form the analysis it is found that the after 2050s the projected streamflow have increased rapidly. The quantification results of during 2006-2050, the streamflow have increased except combinations (2nd, 3rd, 4th, 5th, 6th and 7th) of ESM2M under RCP8.5

scenario with reference to historical period (1991-2005). Whereas, during 2051-2100, all the scenarios and combinations showed the increase in stream flow. The change during 2006-2050, ranged from 4.42 to 23.17 m^3/s for RCP2.6, 3.73 to 16.11 m^3/s for RCP4.5 and -10.12 to 14.03 m^3/s for RCP8.5 scenario. Further, the ranges of streamflow during 2051-2100 are 8.59 to 22.14 m^3/s, 10.47 to 30.88 m^3/s and 13.08 to 38.70 m^3/s for RCP2.6, RCP4.5 and RCP8.5 scenario. These changes are obtained from the difference among historical (1991-2005) and projected scenarios.

Additionally, the streamflow changes have been calculated for the projected streamflow scenarios to check the change in magnitude. The projected time series is divided into two inter-decadal time series viz. 2006-2050 and 2051-2100. The change in stream flow during between these inter-decal times steps have shown in Table 5.3. The result clearly indicates that the projected stream flow after 2050s (2051-2100) would have higher magnitude than before 2050s (2006-2050) except some of the combinations (2nd, 4th and 6th) as shown in Table 5.3. The ESM2M model result projecting higher range as compare to other two models for all RCP scenarios.

Table 5.3: Change in Streamflow amount at Chungthang between two intra-decades (2006-2050) and (2051-2100) for CMIP5 GCMs and their RCPs, where C's are combination.

Scenario		**Combination**						
		C1	**C2**	**C3**	**C4**	**C5**	**C6**	**C7**
ESM2G	RCP2.6	1.35	-1.03	2.38	1.07	2.51	0.04	2.28
	RCP4.5	6.71	11.62	5.11	4.46	5.66	10.06	4.27
	RCP8.5	12.52	24.66	10.99	10.26	10.60	18.78	10.96
ESM2M	RCP2.6	10.12	7.94	10.28	10.12	11.16	7.58	12.32
	RCP4.5	17.54	23.35	19.05	17.59	18.55	18.77	21.77
	RCP8.5	22.43	37.51	26.87	26.19	24.71	30.92	26.98
CM3	RCP2.6	0.50	0.83	0.03	-0.62	0.18	-1.21	0.16
	RCP4.5	4.92	10.05	5.29	2.26	3.82	6.48	2.59
	RCP8.5	10.15	25.23	11.00	9.04	9.49	22.30	9.50

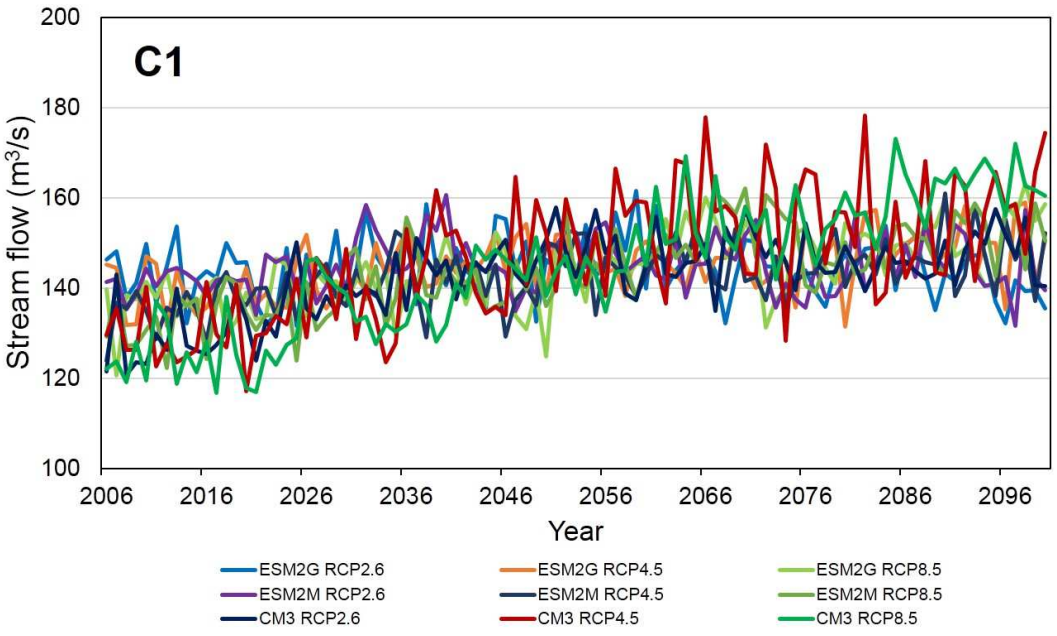

Figure 5.3: Projected streamflow of all scenarios for first GCM grid-point combination (C1) at Chugthang.

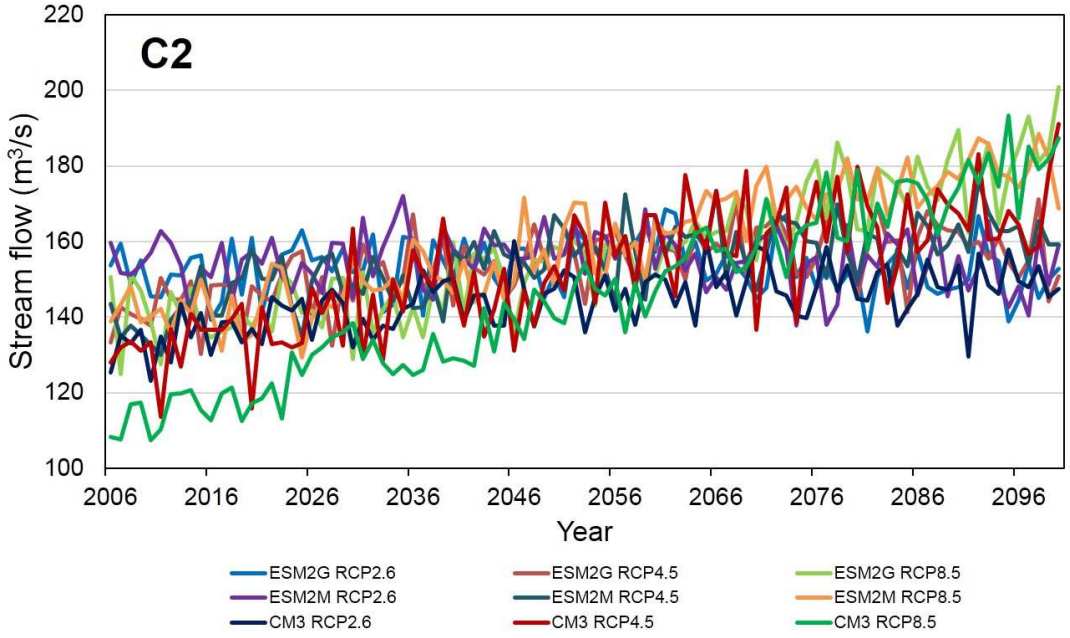

Figure 5.4: Projected streamflow of all scenarios for second GCM grid-point combination (C2) at Chugthang.

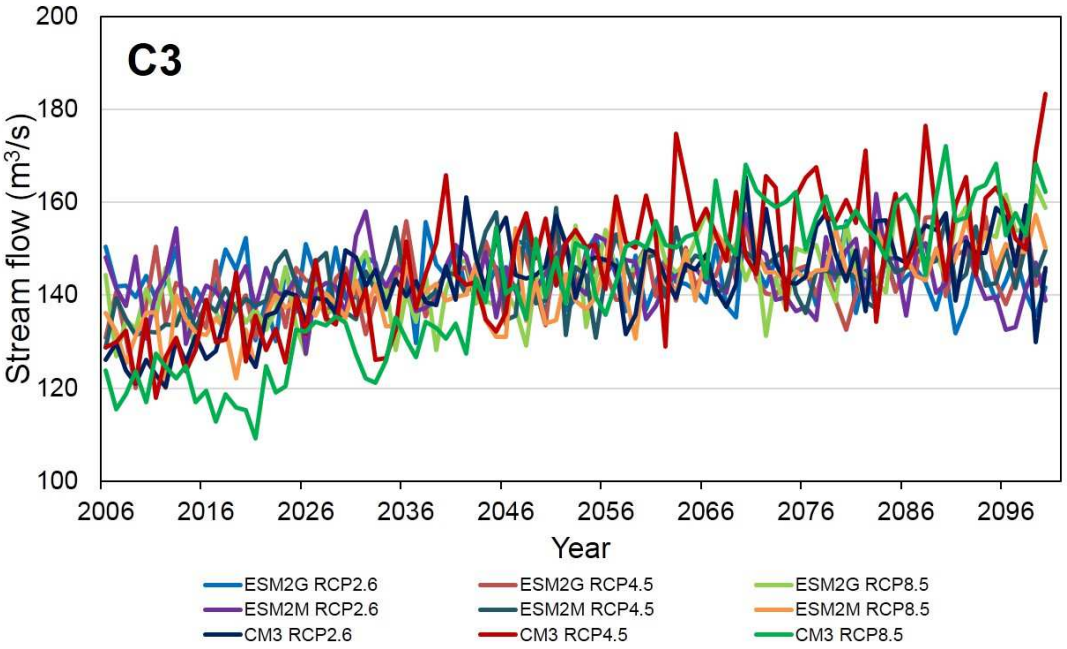

Figure 5.5: Projected streamflow of all scenarios for third GCM grid-point combination (C3) at Chugthang.

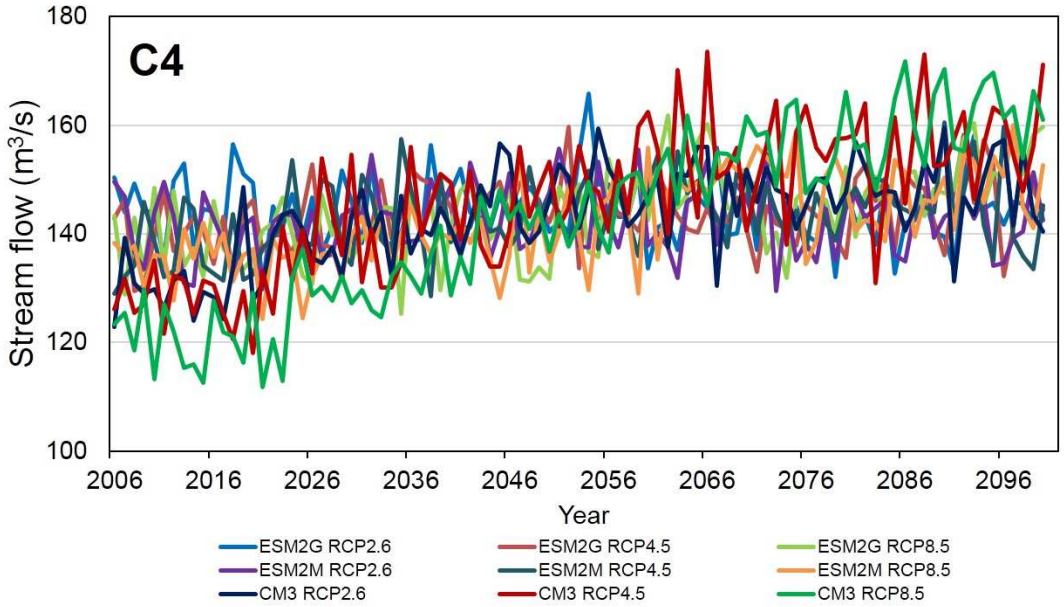

Figure 5.6: Projected streamflow of all scenarios for fourth GCM grid-point combination (C4) at Chugthang.

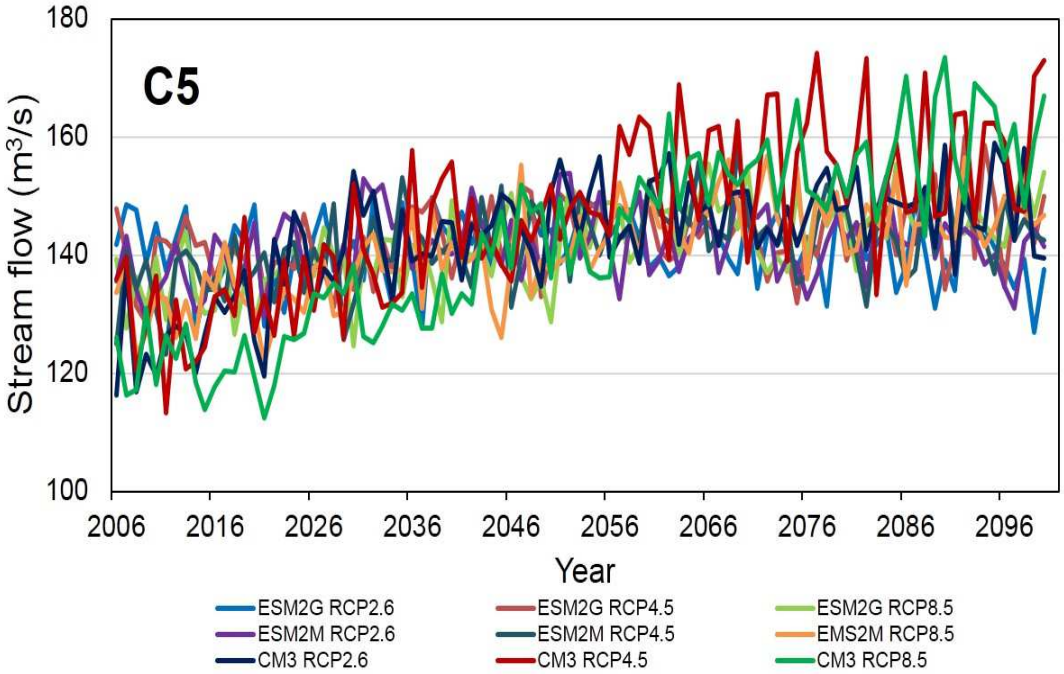

Figure 5.7: Projected streamflow of all scenarios for fifth GCM grid-point combination (C5) at Chugthang.

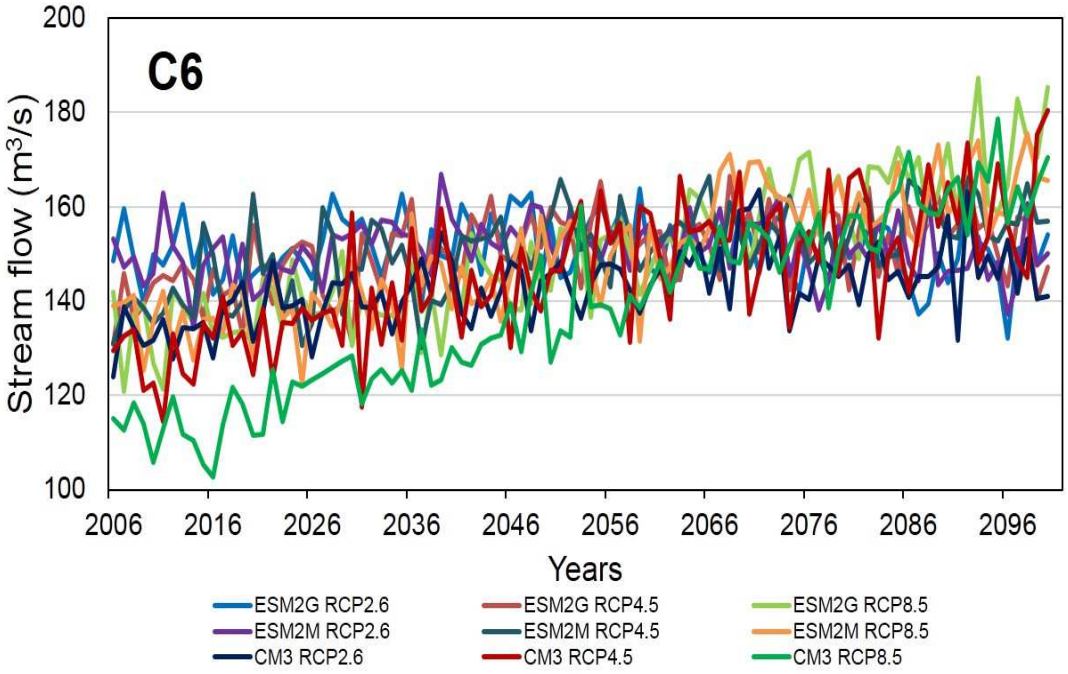

Figure 5.8: Projected streamflow of all scenarios for sixth GCM grid-point combination (C6) at Chugthang.

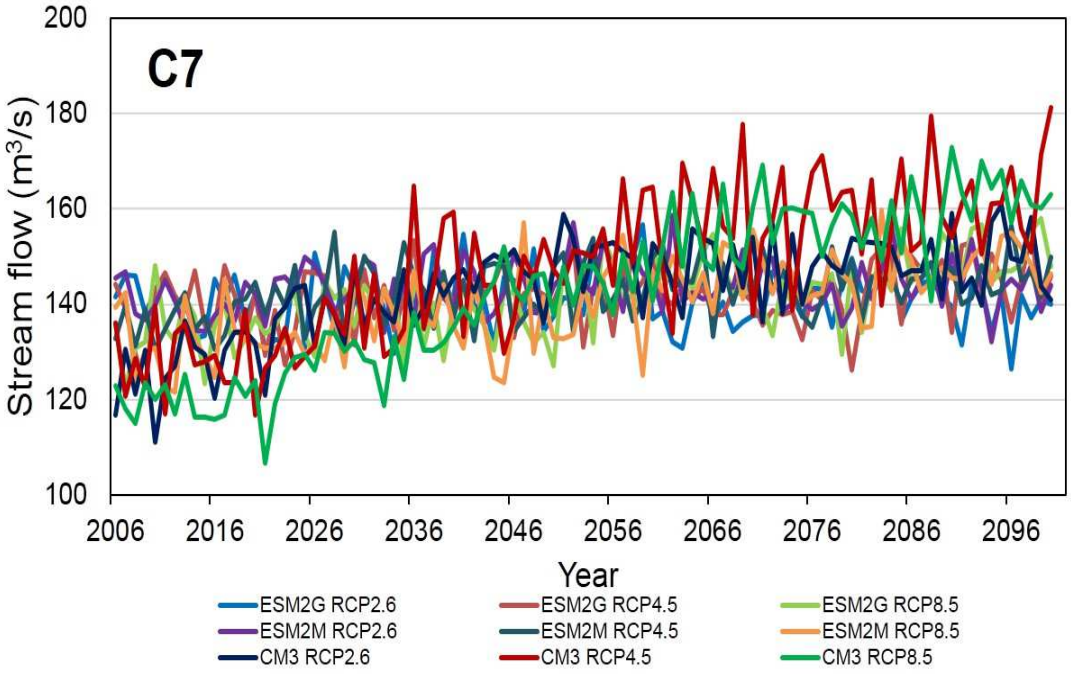

Figure 5.9: Projected streamflow of all scenarios for seventh GCM grid-point combination (C7) at Chugthang.

5.3 Relative Contribution of Climate Variables to Runoff

As per the IPCC AR5, the global air temperature has increased in last 20^{th} century. This warmer climate may lead to less precipitation falling as snow in cold region (Berghuijs et al. 2014). Thus the change in precipitation may exert a great influence in the available water resources, especially in the snowmelt dominated runoff catchments where more than one-sixth of the world's population lives (Barnett et al. 2005). An increasing in temperature and decrease in precipitation as snowfall can alter available water resources as change in runoff for example earlier peak in spring season and decrease in summer-autumn runoff for a total annual precipitation over the region (Zhang et al. 2015). This implies that the change in precipitation due to global warming can alter the temporal distribution of intra-annual runoff, resulting increasing possibility of spring flood disasters and water crises in summer (Allamano et al. 2009; Zhang et al. 2015). The shift in state of precipitation on mean annual runoff are the important factors that controls the available water resources (Zhang et al. 2015). This study focused to understand the relationship between climate variables (snow-ratio, precipitation and evapotranspiration) and mean annual runoff variation induces by climate change.

The main focus of this study is to understand the effect of climate variables (snow-ratio, precipitation and evapotranspiration) on annual runoff using Budyko framework under changing climate. Budyko suggested a framework, which is useful to assess the long term change in annual runoff due to different climate variables (Budyko, 1974). In order the address the problem, historical (1982-2005) and projected CMIP5 GCMs dataset are used. The overall methodology framework of relative contribution of climate variables over the long term annual runoff changes has been shown in Figure 5.10.

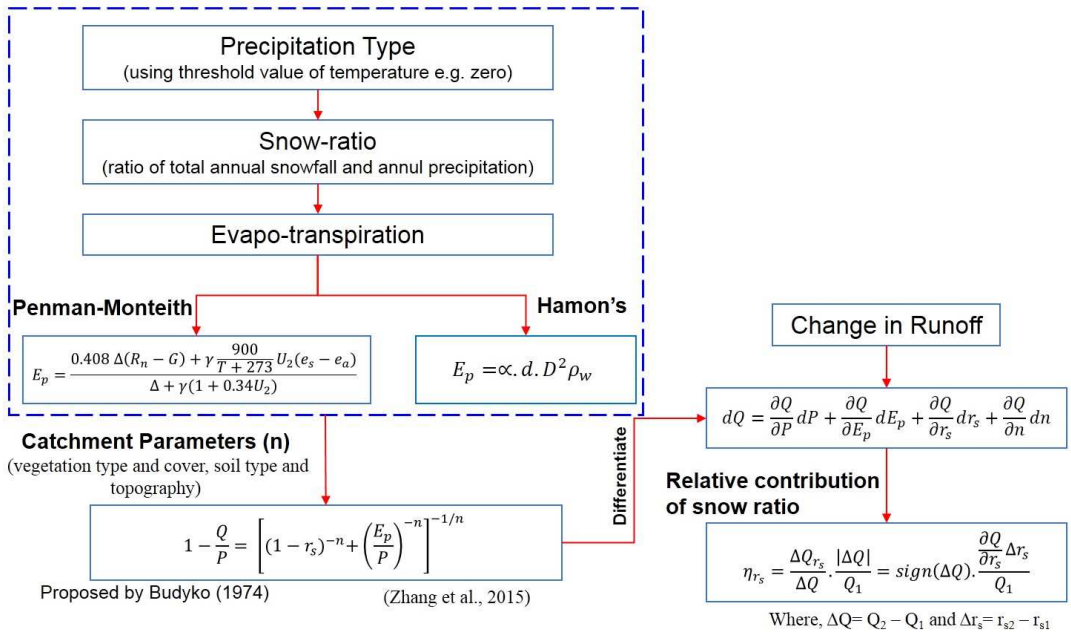

Figure 5.10: Flow chart of relative contribution of climate variables to annual runoff changes.

Due to unavailability of precipitation type at any meteorological stations, the relationship based on the threshold temperature used to categorize the precipitation type e.g. if the temperature for a day is below zero and precipitation occurs that means precipitation occurs as snow else rainfall.

$$\begin{cases} \text{snowfall} & T_d < 0 \\ \text{rainfall,} & T_d > 0 \end{cases} \tag{5.8}$$

Where, T_d is the daily mean temperature

The daily evapotranspiration was estimated based on the Penman-Monteith FAO equation (Allen et al. 1998) and Hamon's equation (Hamon 1960) and compared.

Penman-Monteith Equation

$$\frac{0.408\Delta(R_n - G) + \gamma \frac{900}{T+273} U_z(e_s - e_a)}{\Delta + \gamma(1 + 0.34U_2)} \tag{5.9}$$

Where, ET_o = Reference evapotranspiration $[mm/day]$, R_n = Net radiation at the crop surface $[MJm^{-2}day^{-1}]$, G = Soil heat flux density $[MJm^{-2}day^{-1}]$, T = Mean daily temperature $(^{\circ}C)$, U_2 = Wind speed at $2m$ height $[ms^{-1}]$, e_s and e_a = Saturation and actual vapour pressure $[kPa]$, Δ = Slope vapour pressure curve $[kPa^{\circ}C]$, g = Psychometric constant $[kPa^{\circ}C]$. All these dataset are collected from Food and Agriculture Organization (FAO) and some of them are calculated using FAO equations such as e_s, e_a, Δ, R_n.

Hamon's equation

$$E_p = \alpha.d.D^2\rho_w \tag{5.10}$$

where,α is the adjustment factor, d is the number of days in a month, D is the mean monthly hours of daylight in units of 12 h and ρ_w is a saturation water vapor density, calculate as:

$$\rho_w = 0.0495e^{0.062T} \tag{5.11}$$

where, T is the monthly mean temperature in $^{\circ}C$. The value of α (Hamon's equation) was adjusted, which is calibrated by minimizing the difference between two mean annual E_p values (1982-2005) estimated by Penman–FAO and Hamon's equation for catchment. The future monthly precipitation, temperature and snowfall outputs are extracted from CMIP5 GCM scenarios and future E_p values are calculated using Hamon's equation with adjusted α (adjustment factor).

5.3.1 Snow-Ratio

The snow-ratio (r_s) was calculate as the ratio of mean annual snowfall amount to mean annual precipitation, which can eliminate the influence of phase difference originating

from the snow accumulation and melting in different years (Zhang et al., 2015).

$$snowratio(r_s) = \frac{Totalannualsnowfall}{Totalannualprecipitaiton} \tag{5.12}$$

5.3.2 Inclusion of Snow-Ratio in the Budyko Framework

The assessment of catchment factors such as vegetation type and cover, soil type and topography essential to estimate the mean annual water–energy balance equation under general conditions using mathematical expression. Choudhury's equation provides the theoretical solution to calculate the synthesis parameter (n) which represents the effects of the catchment factors such as vegetation type and cover, soil type and topography (Zhang et al. 2015).

$$1 - \frac{Q}{p} = \left[1^{-n} + \left(\frac{E_p}{p}\right)^{-n}\right]^{-1/n} \tag{5.13}$$

Where n is a synthesis parameter, Q/P is the runoff index and Ep/P is the dryness index.

When snowfall is considered, in the equation 5.13 there may be some differences in energy and water terms. The water–energy balance in form of above equation with consideration of snow can be rewritten as follows:

$$1 - \frac{Q}{p} = \left[(1 - r_s)^{-n} + \left(\frac{E_p}{p}\right)^{-n}\right]^{-1/n} \tag{5.14}$$

Where, r_s is the snow-ratio.

Observed long term discharge (Q), precipitation (P), snow-ratio (r_s) and potential evaporation (E_p) during 1982-2005 are used to calculate the synthesis parameter (n). The value of n can be calculated based on the vegetation type and cover, soil type and topography. Firstly, we have divided past (1982-2005) data in two parts (1982-1993

and 1994-2005) and checked; is there significant change in n value? Result shows the no significant difference in n value. Based on the historical dataset, the n value is chosen as constant for projected scenarios. In this research work we have not project the LULC and topographical changes for future. Thus, the calculated n value is used as constant value for future scenarios because there is no significant change (in n values) in the historical time.

5.3.3 Attribution of runoff change

The Choudhury's equation again used to calculate the projected discharge due to change in climate factors (P, E_p, r_s). Furthermore, this will provide a theoretical tool to attribute the mean annual runoff change to climate variability, especially the snow ratio change. We reorganize Equation 5.14 and differentiate it to calculate change in Q due to changes in climate factors (P, E_p, r_s) and catchment characteristic (n). The first order of equation 5.14.

$$dQ = \frac{\delta Q}{\delta P}dP + \frac{\delta Q}{\delta E_p}dE_p + \frac{\delta Q}{\delta r_s}dr_s + \frac{\delta Q}{\delta n}dn + \tag{5.15}$$

Where,

$$\frac{\delta Q}{\delta P} = 1 - \frac{P-Q}{P}\frac{E_p^n}{[P(1-r_s)]^n + E_p^n} \tag{5.16}$$

$$\frac{\delta Q}{\delta E_p} = -\frac{P-Q}{E_p}\frac{[P(1-r_s)]^n}{[P(1-r_s)]^n + E_p^n} \tag{5.17}$$

$$\frac{\delta Q}{\delta r_s} = \frac{P-Q}{1-r_s}\frac{E_p^n}{[P(1-r_s)]^n + E_p^n} \tag{5.18}$$

$$\frac{\delta Q}{\delta n} = -\frac{P-Q}{n}\left(\frac{ln[P^n(1-r_s)^n + E_p^n]}{n} - \frac{[P(1-r_s)]^n ln[P(1-r_s)] + +E_p^n ln(E_p)}{[P^n(1-r_s)^n + E_p^n]}\right) \tag{5.19}$$

The runoff changes can be estimated between pre and post period due to climatic factors (P, E_p, r_s) and catchment characteristic (n) , respectively. The relative contribution of snow ratio variation to annual runoff change η_{r_s} , is defined as:

$$\eta_{rs} = \frac{\Delta Q r_s}{\Delta Q}.\frac{|\Delta Q|}{Q_1} = sign(\Delta Q).\frac{\frac{\delta Q}{\delta r_s}\Delta r_s}{Q_1} \tag{5.20}$$

Similarly, the relative contribution of precipitation evapotranspiration variation to annual change can be calculated as:

$$\eta_p = \frac{\Delta Q p}{\Delta Q}.\frac{|\Delta Q|}{Q_1} = sign(\Delta Q).\frac{\frac{\delta Q}{\delta P}\Delta P}{Q_1} \tag{5.21}$$

$$\eta_{E_p} = \frac{\Delta Q E_p}{\Delta Q}.\frac{|\Delta Q|}{Q_1} = sign(\Delta Q).\frac{\frac{\delta Q}{\delta E_p}\Delta E_p}{Q_1} \tag{5.22}$$

Where, $\Delta Q = Q_2 - Q_1, \Delta r_s = r_{s2} - r_{s1}, \Delta P = P_2 - P_1 and \Delta E_p = E_{p2} - E_{p1}$ Using equation 5.7, we have calculated the specific catchment parameter n which is about 0.898 for the Teesta River catchment for historical observations. The change in mean annual runoff and precipitation is calculated as the difference between the period of 1982-1993 and 1994-2005, which is decreased about $12.51 m^3/s$ and 6.5 mm, respectively during 1994-2005 with respect to 1982-1993. While, the snow ratio is increased by 0.05 during 1994-2005 with respect to 1982-1993. The estimated specific catchment parameter n = 0.898 is considered for projected scenarios to analyze the discharge using equation 5.7. The change in the snow ratio is also analyzed, which is decreased by 0.038 to 0.096 during 2020-2060 with respect to historical 1982-2005. Figure 5.11 shows the

annual snow-ratio trend for different scenarios and combinations, which indicated that the snow-ratio is continuously decreasing during 21st century. The change in runoff during 2020-2060 is increased by 8 to 18% for RCP2.6, 10 to 15% for RCP4.5 and 2 to 15% of ESM2M, ESM2G and CM3 GCMs respectively, with related to historical (1982-2005) time scale. The precipitation is also increased by 44 to 354 *mm* during 2020-2060 with the baseline period of 1982-2005.

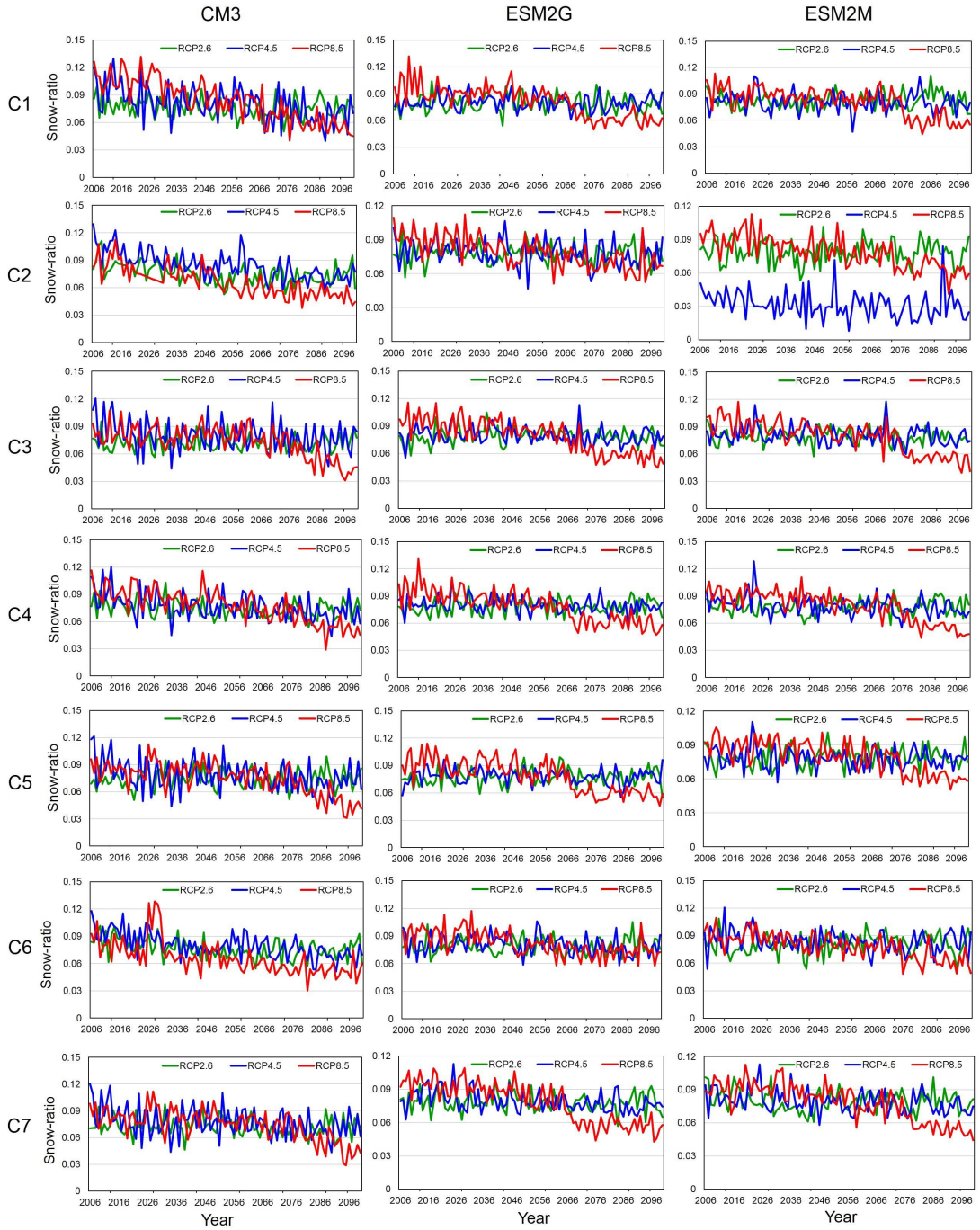

Figure 5.11: Annual projected snow-ratio trends over the study area for three GCMs and their RCP scenarios for all combinations, where C's are combination.

Furthermore, the relative contribution of snow-ratio, precipitation and evapotranspiration to the annual runoff changes for observed and projected scenarios. Table 5.4 shows the percentage relative contribution of climate variables (P, E_p and r_s) to an-

nual runoff changes for different scenarios for different scenarios and all combinations generated from GCM grid-points (see chapter 4).

Table 5.4: Percentage relative contribution of snow ratio, precipitation and evapotranspiration variation to annual runoff change, where C's are GCM grid-point combinations.

Scenarios		Relative change (%) in annual runoff due to climate factors		
		Snow-ratio (rs)	Precipitation (P)	Evapo-transpiration (Ep)
Observed		-0.96	0.33	1.36
C1				
ESM2G	RCP2.6	-1.00	10.24	0.21
	RCP4.5	-0.96	9.56	0.24
	RCP8.5	-0.77	6.94	0.39
ESM2M	RCP2.6	-0.98	11.34	0.18
	RCP4.5	-0.98	8.62	0.24
	RCP8.5	-0.83	6.39	0.37
CM3	RCP2.6	-1.08	8.41	0.08
	RCP4.5	-0.92	9.10	0.20
	RCP8.5	-0.71	4.75	0.31
C2				
ESM2G	RCP2.6	-1.04	17.78	-0.02
	RCP4.5	-1.02	16.23	0.06
	RCP8.5	-0.91	12.35	0.23
ESM2M	RCP2.6	-1.05	19.33	0.00
	RCP4.5	-1.91	17.03	0.13

	RCP8.5	-0.89	15.24	0.24
CM3	RCP2.6	-1.08	9.21	0.16
	RCP4.5	-0.81	11.65	0.25
	RCP8.5	-0.98	2.33	0.30
C3				
ESM2G	RCP2.6	-0.98	8.76	0.12
	RCP4.5	-0.96	8.35	0.15
	RCP8.5	-0.82	6.31	0.30
ESM2M	RCP2.6	-1.00	8.94	0.14
	RCP4.5	-0.98	8.89	0.21
	RCP8.5	-0.88	5.48	0.31
CM3	RCP2.6	-1.16	8.94	0.13
	RCP4.5	-1.02	8.63	0.23
	RCP8.5	-0.98	2.76	0.38
C4				
ESM2G	RCP2.6	-1.04	9.95	0.14
	RCP4.5	-0.96	9.35	0.16
	RCP8.5	-0.84	6.96	0.32
ESM2M	RCP2.6	-1.08	8.74	0.17
	RCP4.5	-1.00	8.68	0.22
	RCP8.5	-0.84	5.12	0.31
CM3	RCP2.6	-1.10	8.86	0.14
	RCP4.5	-1.04	8.85	0.24

	RCP8.5	-0.90	2.85	0.35
C5				
ESM2G	RCP2.6	-1.06	7.57	0.13
	RCP4.5	-1.00	8.57	0.16
	RCP8.5	-0.84	6.28	0.30
ESM2M	RCP2.6	-1.04	8.34	0.12
	RCP4.5	-1.02	7.48	0.20
	RCP8.5	-0.86	4.85	0.28
CM3	RCP2.6	-1.08	8.86	0.13
	RCP4.5	-1.00	8.70	0.24
	RCP8.5	-0.94	2.79	0.40
C6				
ESM2G	RCP2.6	-1.00	16.40	0.02
	RCP4.5	-0.94	14.41	0.11
	RCP8.5	-0.86	8.60	0.28
ESM2M	RCP2.6	-1.04	16.03	0.03
	RCP4.5	-0.88	13.07	0.11
	RCP8.5	-0.92	9.13	0.30
CM3	RCP2.6	-1.08	7.88	0.15
	RCP4.5	-0.96	8.37	0.25
	RCP8.5	-1.15	9.23	0.28
C7				
ESM2G	RCP2.6	-1.02	7.41	0.12

	RCP4.5	-1.00	7.34	0.19
	RCP8.5	-0.82	5.23	0.31
ESM2M	RCP2.6	-1.06	9.71	0.19
	RCP4.5	-0.98	8.19	0.20
	RCP8.5	-0.84	3.65	0.31
CM3	RCP2.6	-1.10	9.21	0.16
	RCP4.5	-1.04	9.11	0.24
	RCP8.5	-0.96	3.05	0.38

From the results, it is clearly showed that snow-ratio and evapotranspiration are not the main factor those affecting the runoff changes, whereas precipitation is the major factor that affects the runoff changes with the ranges of 2 to 19% for different scenarios as shown in Table 5.4. The changes in runoff due to snow-ratio and evapotranspiration are ranged from -0.071 to -1.91% and -0.02 to 0.39% for different scenarios, respectively. The maximum projection changes have been found in 2^{nd} combination. As the possible warming climate quantifies that the change in annual runoff resulting from snow ratio is negative, as the snow ratio decreased during 2020-2060 relative to 1982-2005. This implies that, precipitation is less likely to occur as snowfall. A shift from snowfall towards rainfall over the region is considered not to influence the annual runoff significantly. Similar results found by other researchers for snow-dominated regions (Barnett et al., 2005; Berghuijs et al., 2014). Here, clearly shown that the annual runoff is likely to reduce over the catchment that has significant reduction in precipitation falling as snowfall.

5.4 Summary and Conclusions

This chapter presented the hydrological response over the study area using hydrological modeling and impact on runoff changes due to climate variables. For hydrological modeling MIKE11 NAM model and for relative contribution Budyko framework have been used. The result indicates that the projected streamflow have increased for all scenarios and snow-ratio has decreased over the Teesta River catchment. The streamflow have increased after 2050 with faster rate as compare to before 2050. Precipitation is the major factor for runoff changes, but due to snow-ratio slight decrease in runoff has been observed. In addition, the precipitation is less likely to occur as snow over the catchment.

CHAPTER 6

Glacial Lake Identification and Glacial Lake Outburst Floods Dynamics

6.1 General Overview

This chapter covers the glacial lake identification using remoter sensing application and insights of glacial lake outburst floods (GLOFs) dynamics using hydrodynamic modeling over the Teesta River catchment. To characterize the glacial lake, spatial and temporal LANDSAT remote sensing images are used. There are several limitations in using remote sensing satellite dataset for mapping, therefore the field data is integrated to improve the remote sensing applications. For clear identification of glacial lakes, satellite images should be cloud free and least snow cover (Jain et al., 2012). If cloud cover is present, so removals of clouds from satellite images (atmospheric correction) are essential for glacial lake mapping. Once the corrections are made, the accurate glacial lakes can be mapped.

The global climate change is the one of the important key factor in retreating and shrinking of glaciers all around the world, and Himalayan region is no exception. The

modified glaciated environment can cause the formation of glacial lakes and expansion of their size (Ives et al., 2010). In mountain regions, the glacial lakes are an indicator of hazards in terms of GLOF because of their instability and forming at snow of the retreating glaciers (Gardelle et al., 2011). Therefore, the assessment of GLOF dynamics using hydrodynamic modeling is essential to overcome the hazards from these events. Hydrodynamic modeling can be an important tool to minimize the losses; as it provides the spatial and temporal variation of flow, water depth, velocity and water level etc. In this study, MIKE11 HD hydrodynamic modeling tool was used for GLOF dynamics.

6.2 Inventory of Glacial Lakes

The Teesta River basin covers the snow and glaciers especially at the upstream portion. In the Sikkim Himalaya, a number of glacial lakes at glacier snout are dammed by loose and friable debris. These glacial lakes are an indirect indicator of retreating of glacier and present hazard to downstream locations (Gardelle et al., 2011), but not all glacial lakes are unstable to outburst disastrously. Due to the changing climate, many glaciers are retreating around the world and forming new glacial lakes and increasing existing glacial lakes size. The new formation of moraine-dammed glacial lakes and GLOFs are major concern in the hilly catchments (Kulkarni, 2007). Thus, there is an argent need to carry out a detail glacier lake inventory, to monitor the current status of the glacial lakes, for the sustainable water management and to prevent these region from severe flash flood hazards.

The glacial lake data base is essential to identify the potentially dangerous lakes. The detailed field and remotely senesced survey of individual glacial lake would be useful to quantify parameters (mean depth, potential flood volume in contact with retreating

glacier etc.). But, in the Himalayan region it is not possible to assess all the glacial lakes because some glacial lakes are not reachable/ not assessable for field investigation. Therefore, remote sensing techniques are the best solution to explore each glacial lakes to reduce the hazardous events occurring over the Himalayan region (Worni et al., 2013). Sometimes remote sensing based extraction of glacial lakes sometimes fails, if the glacial lakes are covered by ice, under mountain shadows and cloud contamination. Thus, the cloud free satellite images are selected during melt time periods (during October/November) when the cloud cover is less than 10%. In this study, LANDSAT imageries were obtained for the years 1990, 2000, 2010 and 2014.

6.2.1 Image Rectification

Before extraction of glacial lakes, the remote sensing images should be free from cloud and haze for better interpretation. The top of atmospheric correction is required for removal of cloud and haze. Following are the step for top of atmospheric correction:

1. **Digital Number (DN) to Radiance Conversion:** The following formula is used for converting the DN values into the radiance values.

   For LANDSAT ETM+

   $$L_\lambda = [(LMAX_\lambda - LMIN_\lambda)/255 \times DN_\lambda] + LMIN_\lambda \tag{6.1}$$

   Where, L_λ = radiance in watts/(m^2 * ster * 10^{-6} m), DN = digital number, This formula can used for all bands of LANDSAT with different values of $LMAX_\lambda$ and $LMIN_\lambda$.

   Similarly for LANDSAT 8:

   $$L_\lambda = M_L\, Q_{cal} + A_L \tag{6.2}$$

Where, L_λ is spectral radiance in watts/$(m^2 * srad * \mu$ m), M_L and A_L is Band-specific multiplicative and additive rescaling factor taken from metadata, respectively, Q_{cal} is Quantized and calibrated standard product pixel values (DN).

2. **Radiance to Reflectance Conversion:** the radiance is converted to reflectance using the below given formula:

   For LANDSAT ETM+

$$\rho_P = \frac{(\pi \times L_\lambda \times d^2)}{(ESUN_\lambda \times cos(\theta_s))} \tag{6.3}$$

   Where, ρ_P = Planetary reflectance; L_λ = Spectral band radiance at the sensor's aperture; d = Earth-Sun distance in astronomical units (AU) from nautical handbook or interpolated from values; $ESUN_\lambda$= Mean solar exo-atmospheric irradiances for given wavelength in $watts/m^2/\mu m/ster$ (Markham and Barker, 1987). Use Sun elevation angle as 45.0177078 degrees for Landsat ETM. Sun elevation for Landsat 8 Sun elevation: 61.51233764 and Sun Azimuth as 31.886; θ_s = Solar zenith angle in degrees.

   Similarly for LANDSAT 8

$$\rho\,\lambda' = M_\rho\, Q_{cal} + A_\rho \tag{6.4}$$

   Where, $\rho\lambda^{'}$ = Planetary reflectance without correction for solar angle; M_ρ and A_ρ = Band-specific multiplicative and additive rescaling factor from the metadata, respectively; Q_{cal} = Quantized and calibrated standard product pixel values (DN).

6.2.2 Glacial Lake Extraction

After image rectification, the remote sensing images are used for identification of glacial lakes over the region. The detailed inventory of glacial lakes in North Sikkim Himalaya was prepared using LANDSAT imageries during 1990 to 2014. For detection of glacial lakes, LANDSAT imageries ware used with three indexes namely; Normalized Difference Vegetation Index (NDVI), Normalized Difference Water Index (NDWI) and Normalized Difference Turbidity Index (NDTI) have been applied with visual interpretation. The ERDAS IMAGINE 2014 software was used for different indexes calculation.

$$NDVI = \frac{(Reflectance(NIR) - Reflectance(Red))}{(Reflectance(NIR) + Reflectance(Red))} \tag{6.5}$$

$$NDWI = \frac{(Reflectance(Green) - Reflectance(NIR))}{(Reflectance(Green) + Reflectance(NIR))} \tag{6.6}$$

$$NDTI = \frac{(Reflectance(Red) - Reflectance(Green))}{(Reflectance(Red) + Reflectance(Green))} \tag{6.7}$$

Where, Green, Red and NIR represent green, red and near infrared band, respectively. The NDVI is defined as the identification of vegetation cover. The NDWI is developed to get maximum reflectance of water using green wavelengths and minimum reflectance of NIR. The result shows the water bodies as positive values (McFeeters, 1996; Qiao et al., 2012). The NDTI is defined by (Lacaux et al., 2007) as the identification of turbid water pixel with spectral reflectance characteristics of turbid water. This NDTI is designed to rectify the pure water feature (separate snow and water) (Subramaniam and Saxena, 2011). Figure 6.1 shows the Flow chart of the extraction methodology of glacier lakes over the study area.

Total 203 numbers of glacial lakes are found having area greater than 0.01 km^2, are extracted and most of them are situated in high elevation zones i.e. 78.79% glacial lakes exist in 4500-5500 m elevation and 12.12% glacial lakes exist in more than 5500 m elevation in the year 2014 (Table 6.1). The delineated glacial lakes are mapped over the study are as shown in Figure 6.2.

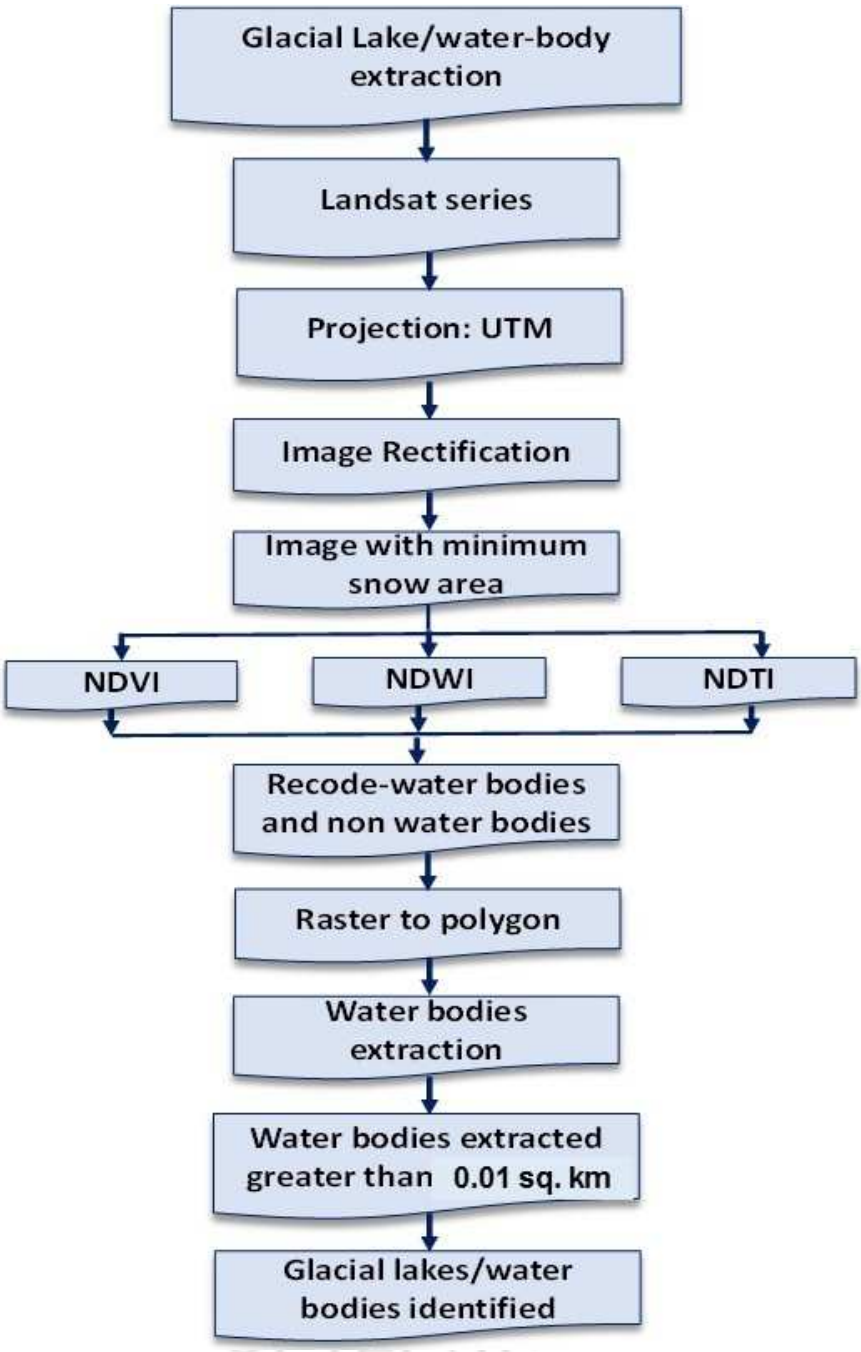

Figure 6.1: Glacial lake extraction methodology flow chart.

Once the glacial lakes mapped as shown in Figure 6.2, the vulnerability of glacial lakes has been analyzed based on the area of lake (>0.05 km^2), lake attached with parental glaciers and/or at the snout of the glacier, steep slope, freeboard, potential flood volume, possible lowering height and change detection using remote sensing

datasets as ICIMOD suggested. Table 6.2 shows the statistics and geographical location of glacial lake delineated from LANDSAT multispectral satellite for the years 1990, 2000, 2010 and 2014. Many glacial lakes are very small over the region so only 73 glacial lakes having area greater than 0.05 km^2 are selected for further analysis (Table 6.2).

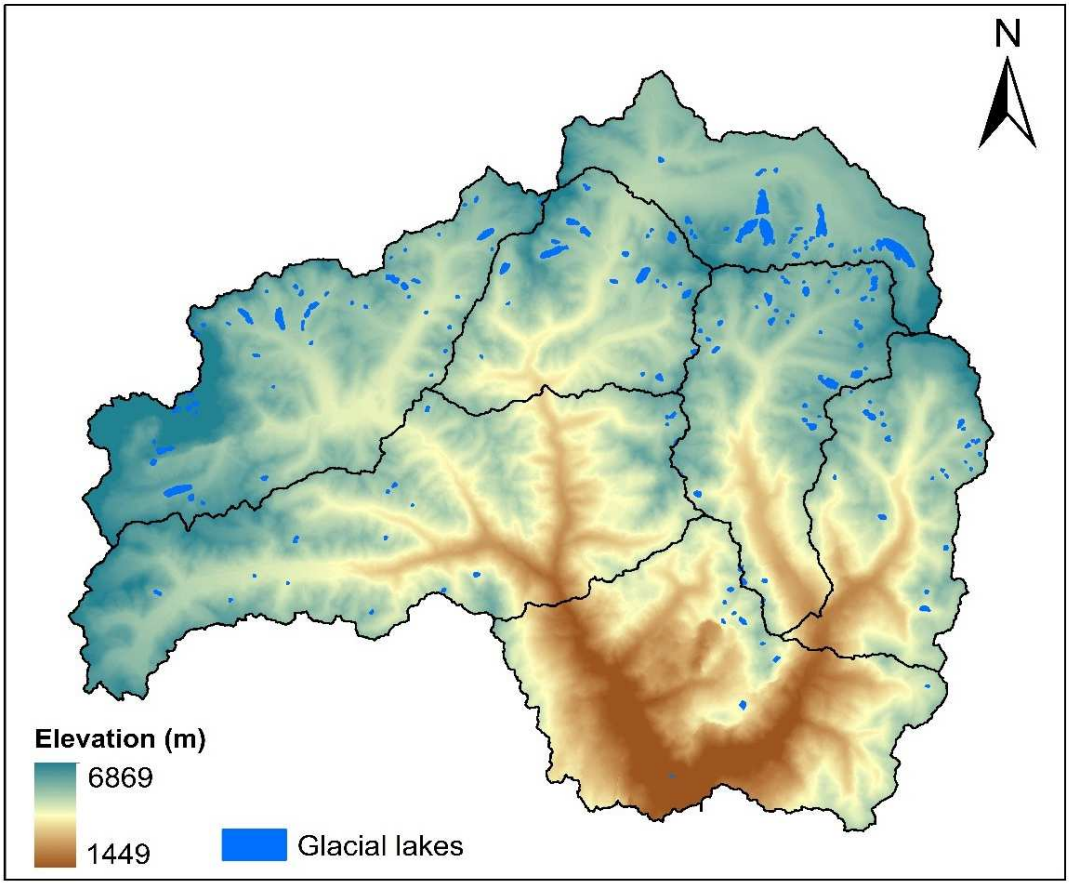

Figure 6.2: Delineated glacial lakes over the study area.

Table 6.1: Proportions of glacial lake counts with elevation in the North Sikkim Himalayas

S. N.	**Elevation Range (m)**	**No. of glacial lakes**	**Glacial lakes (%)**
1.	<3500	0	0
2.	3500-4500	19	9.36
3.	4500-5500	159	78.33
4.	>5500	25	12.32
Total glacial lakes		203	100

Table 6.2: Geographical locations and statistics of glacial lakes during 1990-2014 over the selected study area.

Lake-ID	**Latitude**	**Longitude**	**Area** (km^2)			
			1990	**2000**	**2010**	**2014**
GL-1	27.99	88.81	1.565	1.461	1.512	1.759
GL-2	28.01	88.71	1.325	1.132	1.139	1.152
GL-3	28.01	88.76	1.063	0.999	0.931	1.112
GL-4	28.03	88.71	1.054	1.081	1.091	1.084
GL-5	28.01	88.7	0.765	0.799	0.897	0.927
GL-6	27.9	88.78	0.59	0.286	0.325	0.299
GL-7	27.98	88.62	0.569	0.561	0.563	0.572
GL-8	27.95	88.33	0.574	0.568	0.568	0.622
GL-9	27.99	88.55	0.536	0.533	0.574	0.787
GL-10	27.91	88.2	0.562	0.664	NA	NA
GL-11	28.06	88.63	0.479	0.126	0.121	0.149
GL-12	28	88.64	0.384	0.343	0.316	0.3

GL-13	27.9	88.76	0.335	0.342	0.419	0.389
GL-14	27.94	88.78	0.341	0.119	0.132	0.121
GL-15	28.01	88.49	0.351	0.391	0.448	0.409
GL-16	27.92	88.16	0.311	NA	NA	NA
GL-17	27.67	88.51	0.319	0.231	0.204	0.322
GL-18	27.96	88.74	0.254	0.227	0.214	0.212
GL-19	27.95	88.31	0.24	0.357	0.374	0.332
GL-20	28.01	88.56	0.227	0.255	0.256	0.276
GL-21	28.01	88.57	0.209	0.26	0.243	0.271
GL-22	27.96	88.65	0.184	0.19	0.209	0.136
GL-23	27.96	88.36	0.181	0.166	0.183	0.179
GL-24	27.97	88.8	0.192	0.196	0.188	0.191
GL-25	27.91	88.34	0.192	NA	NA	NA
GL-26	27.73	88.83	0.165	0.185	0.074	0.171
GL-27	27.89	88.24	0.201	0.163	NA	NA
GL-28	27.72	88.45	0.154	0.154	NA	0.149
GL-29	27.83	88.32	0.185	0.092	0.113	0.135
GL-30	28.01	88.65	0.141	0.138	0.115	0.121
GL-31	27.97	88.43	0.154	0.136	0.141	0.145
GL-32	27.76	88.48	0.143	0.087	0.128	0.184
GL-33	27.97	88.44	0.139	0.059	0.087	0.104
GL-34	27.85	88.81	0.133	0.081	0.843	0.084
GL-35	27.82	88.26	0.135	0.06	0.104	0.136

GL-36	27.82	88.66	0.139	0.138	0.145	NA
GL-37	27.72	88.69	0.131	0.116	0.127	0.128
GL-38	27.86	88.86	0.127	0.127	0.139	0.158
GL-39	27.85	88.24	0.127	0.065	0.289	0.308
GL-40	27.84	88.8	0.122	NA	NA	NA
GL-41	27.98	88.79	0.121	0.091	0.097	0.074
GL-42	27.88	88.25	0.12	0.133	0.15	NA
GL-43	27.99	88.74	0.118	0.086	0.118	NA
GL-44	27.92	88.31	0.155	0.106	0.108	0.128
GL-45	27.97	88.42	0.124	0.113	0.13	0.13
GL-46	27.95	88.35	0.132	0.196	0.127	0.211
GL-47	27.97	88.59	0.118	0.119	0.112	0.112
GL-48	27.66	88.69	0.118	0.133	0.145	0.182
GL-49	27.7	88.51	0.1	0.077	NA	NA
GL-50	27.75	88.69	0.125	0.092	0.11	NA
GL-51	27.92	88.67	0.123	0.102	0.107	0.104
GL-52	27.96	88.8	0.114	0.088	0.112	0.122
GL-53	27.67	88.69	0.107	NA	0.125	0.109
GL-54	27.99	88.6	0.106	0.105	NA	0.103
GL-55	27.84	88.23	0.103	0.103	0.127	0.117
GL-56	27.87	88.79	0.099	0.096	0.111	0.112
GL-57	27.82	88.45	0.089	0.076	0.083	0.079
GL-58	27.89	88.27	0.096	0.091	0.093	0.108

GL-59	27.89	88.26	0.121	0.085	NA	0.076
GL-60	27.75	88.68	0.09	0.074	0.072	0.063
GL-61	27.95	88.22	0.092	NA	NA	NA
GL-62	27.87	88.64	0.079	0.079	0.095	NA
GL-63	27.7	88.72	0.09	NA	0.077	NA
GL-64	27.99	88.8	0.08	0.071	0.074	0.078
GL-65	27.88	88.26	0.08	0.091	0.086	0.112
GL-66	28	88.55	0.071	0.101	0.094	0.095
GL-67	27.94	88.27	0.075	0.071	0.063	0.092
GL-68	27.76	88.61	0.065	NA	NA	0.058
GL-69	27.68	88.81	0.074	0.076	0.059	0.057
GL-70	27.77	88.85	0.078	0.062	NA	0.068
GL-71	27.85	88.5	0.081	0.063	NA	0.085
GL-72	27.83	88.42	0.066	NA	NA	NA
GL-73	27.94	88.27	0.064	NA	NA	NA

As per the temporal analysis from 1990-2014, most of the glacial lakes are increasing/decreasing their size, while some of the glacial lakes are disappeared and some are newly formed (Table 6.3). The temporal change of glacial lakes between the years and percentage increase/decrease in 25 years from 1990 to 2014 are shown in Table 6.3.

Table 6.3: Temporal change of glacial lakes area between the years

Lake-ID	**Temporal Change between the years (km^2)**				**Percentage (%)**
	1990-2000	**2000-2010**	**2010-2014**	**1990-2014**	**increase/decrease**
GL-1	-0.104	0.051	0.246	0.193	12.356
GL-2	-0.193	0.007	0.013	-0.173	-13.077
GL-3	-0.064	-0.068	0.181	0.049	4.629
GL-4	0.026	0.01	-0.007	0.03	2.837
GL-5	0.034	0.098	0.029	0.161	21.056
GL-6	-0.304	0.039	-0.026	-0.291	-49.324
GL-7	-0.008	0.002	0.008	0.002	0.418
GL-8	-0.007	0	0.055	0.048	8.381
GL-9	-0.003	0.04	0.213	0.251	46.842
GL-10	0.102	Disappeared	NA	Disappeared	NA
GL-11	-0.353	-0.005	0.028	-0.329	-68.78
GL-12	-0.042	-0.027	-0.016	-0.084	-21.931
GL-13	0.007	0.077	-0.03	0.054	16.114
GL-14	-0.222	0.013	-0.011	-0.22	-64.543
GL-15	0.04	0.057	-0.039	0.058	16.65
GL-16	Disappeared	NA	NA	Disappeared	NA
GL-17	-0.088	-0.028	0.119	0.003	0.996
GL-18	-0.027	-0.012	-0.002	-0.042	-16.497
GL-19	0.117	0.017	-0.042	0.092	38.093
GL-20	0.027	0.001	0.02	0.048	21.29

GL-21	0.05	-0.017	0.028	0.062	29.452
GL-22	0.006	0.019	-0.073	-0.047	-25.816
GL-23	-0.014	0.017	-0.004	-0.002	-1.145
GL-24	0.005	-0.008	0.003	0	-0.056
GL-25	Disappeared	NA	NA	Disappeared	NA
GL-26	0.02	-0.112	0.098	0.006	3.85
GL-27	-0.038	Disappeared	NA	Disappeared	NA
GL-28	-0.001	0	-0.005	-0.006	-3.813
GL-29	-0.093	0.021	0.022	-0.05	-27.092
GL-30	-0.002	-0.023	0.005	-0.02	-14.326
GL-31	-0.018	0.005	0.004	-0.009	-5.838
GL-32	-0.056	0.041	0.056	0.041	28.448
GL-33	-0.08	0.029	0.017	-0.035	-25.005
GL-34	-0.052	0.761	-0.758	-0.049	-36.629
GL-35	-0.075	0.044	0.032	0.001	0.771
GL-36	-0.001	0.007	Disappeared	Disappeared	NA
GL-37	-0.015	0.011	0.002	-0.002	-1.842
GL-38	0	0.011	0.02	0.031	24.78
GL-39	-0.062	0.224	0.019	0.181	142.736
GL-40	Disappeared	NA	NA	Disappeared	NA
GL-41	-0.03	0.006	-0.024	-0.047	-39.032
GL-42	0.013	0.016	Disappeared	Disappeared	NA
GL-43	-0.032	0.033	Disappeared	Disappeared	NA

GL-44	-0.049	0.002	0.02	-0.027	-17.668
GL-45	-0.011	0.017	0	0.006	4.614
GL-46	0.064	-0.069	0.084	0.079	59.463
GL-47	0.001	-0.008	0	-0.006	-5.197
GL-48	0.015	0.013	0.037	0.064	54.414
GL-49	-0.024	Disappeared	NA	Disappeared	NA
GL-50	-0.033	0.018	Disappeared	Disappeared	NA
GL-51	-0.02	0.005	-0.002	-0.018	-14.758
GL-52	-0.026	0.024	0.01	0.008	7.354
GL-53	Disappeared	Formed	-0.016	0.002	2.01
GL-54	-0.001	Disappeared	Formed	-0.002	-2.36
GL-55	0	0.024	-0.01	0.015	14.241
GL-56	-0.003	0.015	0.002	0.014	13.918
GL-57	-0.013	0.007	-0.004	-0.01	-10.902
GL-58	-0.006	0.002	0.015	0.012	12.321
GL-59	-0.036	Disappeared	Formed	-0.045	-37.001
GL-60	-0.016	-0.002	-0.009	-0.027	-29.947
GL-61	Disappeared	NA	NA	Disappeared	NA
GL-62	0	0.016	Disappeared	Disappeared	NA
GL-63	Disappeared	Formed	Disappeared	Disappeared	NA
GL-64	-0.009	0.003	0.004	-0.002	-2.069
GL-65	0.011	-0.005	0.026	0.032	39.836
GL-66	0.03	-0.008	0.001	0.024	34.105

GL-67	-0.003	-0.009	0.029	0.017	22.92
GL-68	Disappeared	NA	Disappeared	-0.008	-11.658
GL-69	0.002	-0.017	-0.002	-0.017	-23.069
GL-70	-0.016	Disappeared	Formed	-0.01	-13.28
GL-71	-0.018	Disappeared	Formed	0.004	5.122
GL-72	Disappeared	NA	NA	Disappeared	NA
GL-73	Disappeared	NA	NA	Disappeared	NA

In Sikkim Himalaya, 50 glacial lakes are having surface area more than 0.1 km^2, 14 glacial lakes are more than 0.3 km2 and 4 glacial lakes are more than 1 km^2. The four glacial lakes (>1 km^2) are GL-1, GL2, GL-3 and GL-4 and their surface area are 1.729, 1.152, 1.112 and 1.084 km^2 as shown in Table 6.2. A significant change in size of glacial lakes is observed last twenty five years from 1990 to 2014 as shown in Table 6.3. Some of the lakes that were present in 1990 have disappeared in 2014, however, formation of new lakes is also noticed in the year 2014. Total 30 out of 73 and 28 out of 73 glacial lakes are increased and decreased their size in last 25 years, respectively. The most of the glacial lakes, with area greater than 0.2 km^2 have increased, while with the area less than 0.2 km^2 have decreased from 1990 to 2014. From the analysis it is observed that the many glacial lakes have been formed and some of them have disappeared too. Figure 6.3 indicates that the newly formed and disappeared glacial lakes over the study area. Based on the areal extension of glacial lakes having area greater than 0.3 km^2 are selected (14 glacial lakes) for calculation of glacial lake parameters such as mean depth and potential flood volume. The temporal change of glacial lakes (area >0.3 km^2) from the year 1990 to 2014 are shown in Figure 6.4. Among the fourteen lakes, some of the

glacial lakes are such as GL-1, GL-3, GL-9 and GL-17 are increased significantly in last five years shown in Table 6.3 and Figure 6.4 with circle.

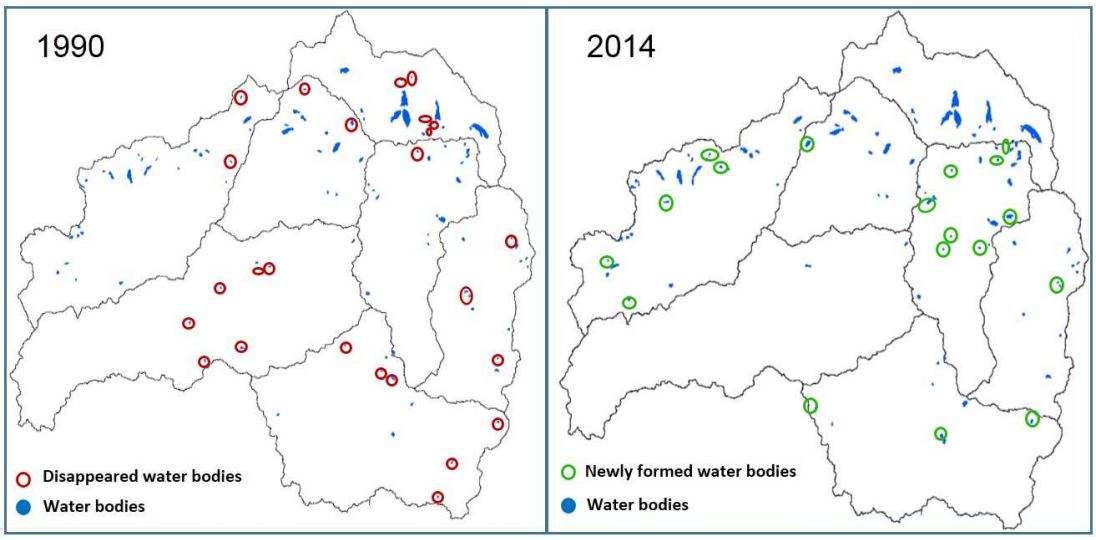

Figure 6.3: Number of lakes, disappeared (at left) and newly formed (at right) over the study area.

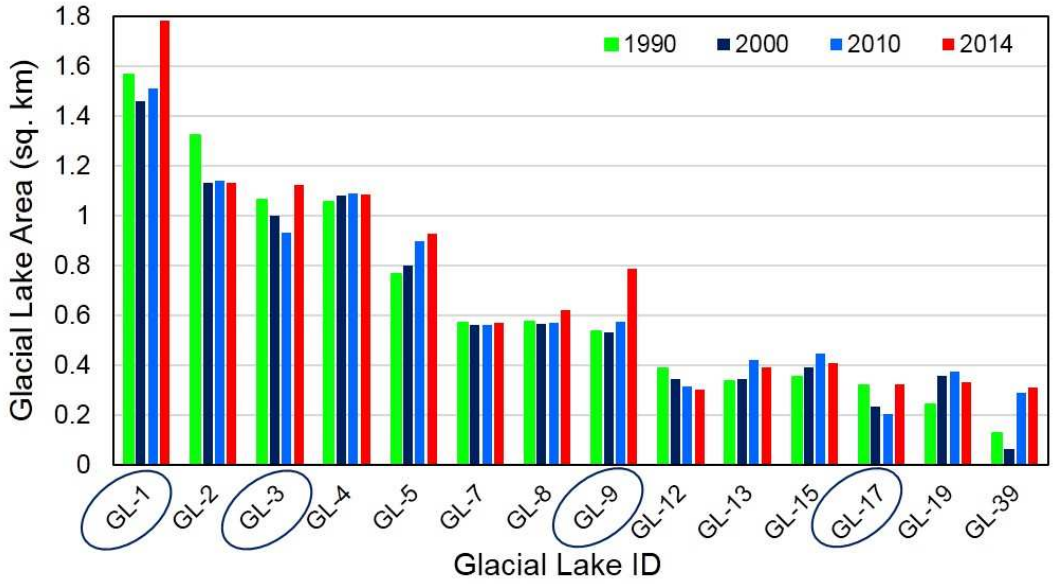

Figure 6.4: Temporal change of glacial lakes (area >0.3 sq. km) from the year 1990 to 2014.

6.3 Glacial Lake Parameters

The estimation of physical glacial lake parameters is important to evaluate the GLOF hazards. But, over the Himalayan region it is very difficult assess all glacial lakes because some of the lakes are situated at a place, those are not reachable/ not assessable for field investigations. Therefore, to evaluate the GLOF hazards an index has been used which is based on the depression angle between the surfaces of glacial lake and surrounding terrain. The depression angle can be calculated from remotely sensed DEM. Although, the depression angle is alternative of width-height ratio of the moraine dam (Clague and Evans, 2000; Huggel et al., 2002; Fujita et al., 2013). This methodology is used to calculate the potential flood volume (PFV) and lowering height (Hp) of glacial lakes using steep lakefront area (SLA) approach, SLA is the profile of moraine inform of glacial lake, which represents the approximate inner profile of glacial lake as suggested by (Fujita et al., 2013) shown in Figure 6.5. The PFV is defined as the minimum possible volume of water that could be released if the glacial lake surface lowered to destroy the embankment of glacial lake. PFV is the multiplication of minimum value of Hp or Dm and surface area of glacial lake (A).

$$PFV = min[H_p \ \ or \ \ D_m].A \tag{6.8}$$

Where, H_p is the possible lowering height during glacial lake outburst (Figure 6.5), A is surface area of glacial lake and

Dm is the mean depth of glacial lake

The mean depth (D_m) is calculated using empirical equation developed by Froehlich

in 1995. This empirical relation is used by many researcher such as Vuichard and Zimmermann (1987); Fujita et al. (2009, 2013), which is mainly obtained from the several Himalayan glacial lakes.

$$D_m = 55.A^{0.25} \tag{6.9}$$

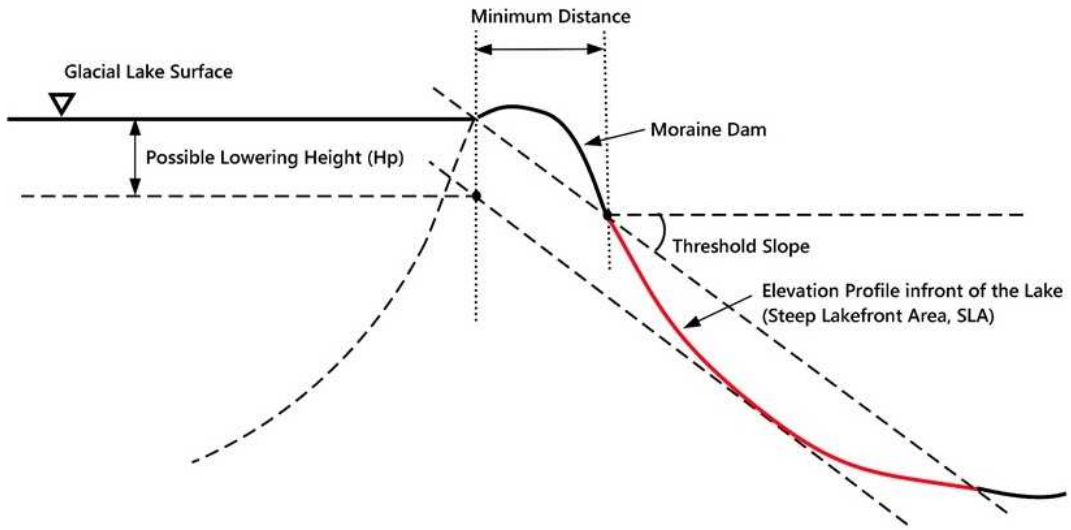

Figure 6.5: The concept of the steep lakefront area (SLA) and glacial lake characteristics

This PFV and mean depth of glacial lakes having area >0.3 km^3 are calculated and listed in Table 6.4. Four glacial lakes having PFVs greater than 10 Mm^3 the lake IDs are GL-1, GL-3, GL-8 and GL-9, the PFV values are 16.271, 19.694, 18.991 and 18.295 Mm^3, respectively. These glacial lakes may vulnerable and pose to outburst. The GL-3 having the maximum PFV and area of the lake is more than 1 km^2, further it is increasing rapidly in last five years from 2010 to 2014. PFV is indicated of potential hazardous glacial lakes over the Himalayan region (Fujita et al., 2013). Major glacial lakes with larger PFV value show the rapid expansion rate, this implies that the PFV will increase over time associated with expansion of lake area.

Table 6.4: Glacial lake parameters and their Characteristics

Lake-ID	**Area (km^2) in 2014**	**Potential lowering height (Hp) (m)**	**Mean depth (Dm) (m)**	**Potential Flood Volume (Mm^3)**
GL-1	1.759	9.25	63.34	16.271
GL-2	1.152	8.5	56.98	9.792
GL-3	1.112	17.71	56.479	19.694
GL-4	1.084	5.3	56.125	5.747
GL-5	0.927	10.5	53.962	9.729
GL-7	0.572	6.5	47.822	3.715
GL-8	0.622	30.51	48.853	18.991
GL-9	0.787	23.25	51.801	18.295
GL-12	0.3	15.11	40.71	4.536
GL-13	0.389	3.6	43.429	1.399
GL-15	0.409	5.47	43.993	2.239
GL-17	0.322	6.25	41.432	2.013
GL-19	0.332	3.01	41.75	0.999
GL-39	0.308	8.2	40.98	2.527

6.3.1 Validation of PFV calculation

The calculated PFV of lakes are validated through Kedarnath flood occurred on 16 and 17 June 2013 due to Chorabari Lake outburst, Uttrakhand, India. Heavy rainfall in the Alaknanda and Bhagirathi catchments was the key reason of the disaster (Durga Rao et al., 2014). Accordingly, pre-GLOF and post-GLOF remote sensing images were

taken. For PFV validation only one lake has been selected (Chorabari glacial lake) because in India only even has been occurred as GLOF. The validation results have clearly shown that, it had an elevation profile steep lakefront area (SLA) in front of lake, but in post GLOF event, no SLA was found. There are some deciding factors of glacial lake outburst such as threshold value ($< 10°$) of steep slope which was higher for Chorabari Lake. It has been found that the streamlines are not same before and after GLOF event. LANDSAT image, CARTO DEM and empirical formula used for surface area (A), potential lowering height (Hp) and mean depth (Dm) of Chorabari glacial lake. The SLA concept applied in the Chorabari Lake to calculate the PFV and obtained PFV was 0.386 Mm^3, which is approximately similar as observed for Chorabari Lake during outburst (estimated about 0.4 Mm^3) (Durga Rao et al., 2014). In addition, the calculate D_m, H_p and PFV of GL-3 are also calculate by Fujita et al., 2013 for the year 2000 and found almost similar results as we got.

6.4 Glacial Lake Outburst Flood (GLOF) Dynamics

In order to evaluate the GLOF dynamics and to identify the triggering events, detailed field investigation is the only way to define the actual condition of moraine dammed structure. Nevertheless, ground-based field survey is not possible for thousands of lakes over the Himalayan glacial lakes, so the SLA concept and PFV technique used to calculate the practical indices using remote sensing imagery and DEM (see section 6.3). For GLOD dynamics, the glacial lake (GL-3) having surface area more than 1 km^2 with maximum PFV value is considered for further assessments.

The flood hydrograph during GLOF has been estimated using some assumptions such as breach width which has been considered as 40, 60 and 80m, Manning's roughness

coefficient 0.04 considered for hilly terrain of Himalayan Rivers and side slope 0.75H: 1V for breach (Jain et al., 2012) calculation. The time of breach formation has been calculated by Froehlich's formula (Froehlich, 1995; Durga Rao et al., 2014; Somos-Valenzuela et al., 2015b).

$$t_f = 0.00254.PFV^{0.53}.H_p^{-0.9} \tag{6.10}$$

Where, PFV is potential flood volume and Hp is potential lowering height.

Based on the assumptions for breach width and side slope, the peak discharge from selected glacial lake are calculated and obtained peak discharges form lake are 4023.456, 5984.128 and 7993.936 m^3/s for 40, 60 and 80m breach widths, respectively. The simulated time of breach formation is about 1.41 hours calculated form equation 6.10 and total amount of water would recede within 81.83, 55.11 and 41.30 min for associated breach widths 40m, 60m and 80m, from selected lake.

After calculation of all glacial lake parameters and peak discharge from lake of selected lake, GLOF simulation has been assessed using hydrodynamic model (MIKE11 HD). The overall methodology of MIKE11 HD for GLOF dynamics as shown in Figure 6.6, where peak discharge from target lake is taken as input parameter (point source).

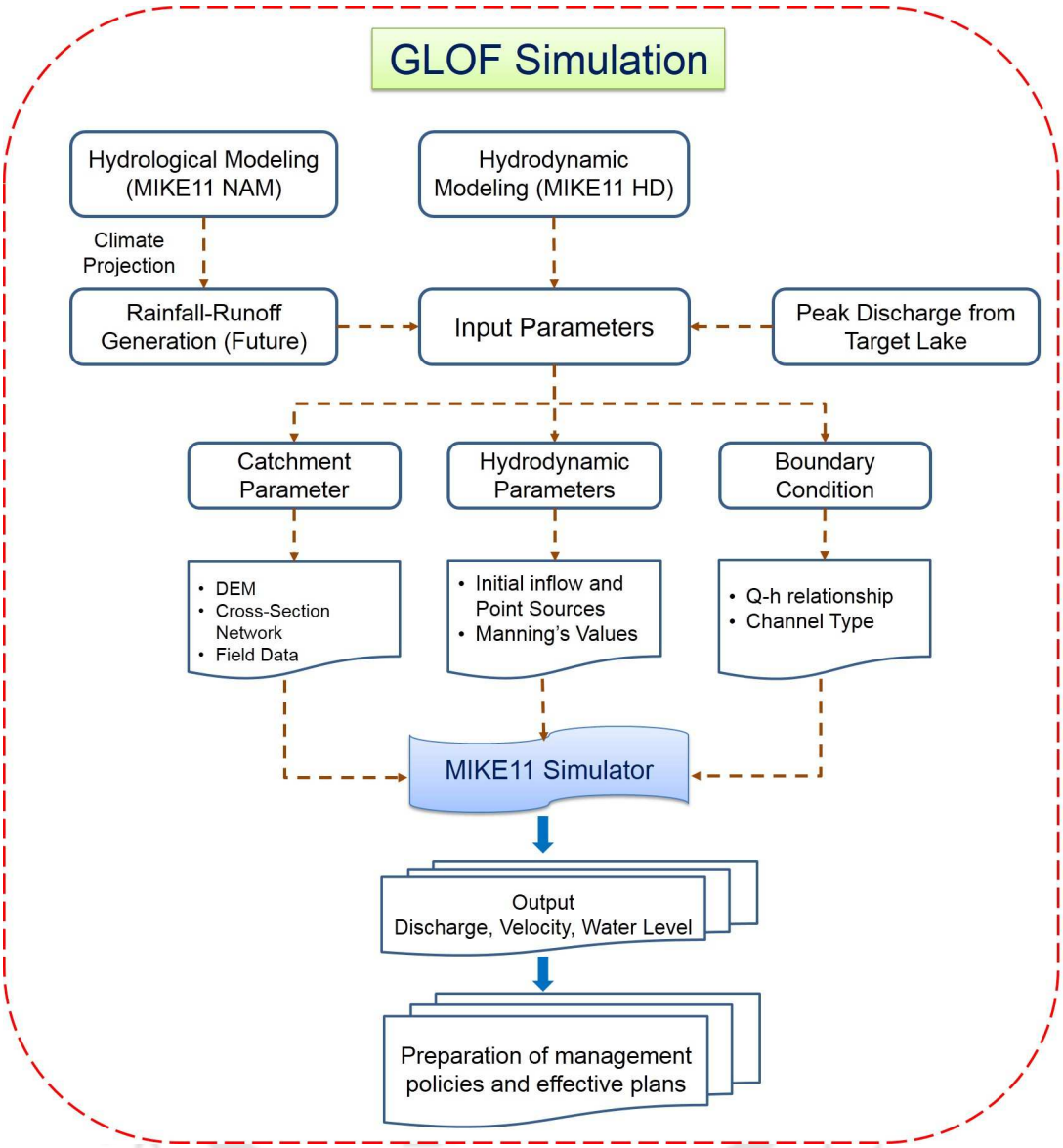

Figure 6.6: Overview of methodology for GLOF dynamics

6.4.1 Hydrodynamic Modeling MIKE 11 HD

The design flood assessment is essential for flood protection measures and its vulnerability in extreme condition. For estimation of hydraulic MIKE11 HD used to generate the water level, velocity and flow velocity during historical (1991-2005) and projected scenarios (2006-2100) over the study area. The MIKE11 is developed by Danish Hydraulic Institute (DHI), which is a 1D user-friendly dynamic modeling tool for the detailed

design, management and operation of both simple and complex river systems. The MIKE11 model is integrated with continuity and momentum equations (Saint-Venant), the solution of these equations is based on an implicit finite difference scheme for one dimensional unsteady flow simulation (Thompson et al., 2004; DHI, 2009). The fully hydrodynamic approach in MIKE 11 system applies for the flood routing and reservoir operation, development of rating curves, water quality and no cohesive sediment transport modules. In this study, MIKE 11 is used for the analysis of discharge, water level and water velocities with GLOF and without GLOF condition at different section of river reach. These are some assumptions associated with MIKE 11 as:

1. Water is incompressible and homogenous.
2. Flow is one-dimensional.
3. Bottom slope of the stream is small.
4. Manning's equation is used to describe resistance effects.
5. Flow everywhere is parallel to the bottom (e.g. wavelengths are large compared with water depths).

In MIKE11 HD setup, several physical and hydro-meteorological datasets such as stream channel network, catchment area boundary and projection parameter details, cross sections (X-Sections) along the river channels, discharge time series at different location, constant or time series water level, hydrodynamic parameters, are necessarily required (Figure 6.6). Additionally, for GLOF simulation, the peak discharges from glacial lake are used as point source for different associated breach widths. Firstly, cross-sections along the river channel have been delineated by utilizing CARTOSAT DEM (30

m spatial resolution) and Google Earth. Furthermore, numbers of cross-sections have been drawn at different location of Teesta River using total station (survey instrument for surface profiling) during field visit. These cross-sections are used to validate the extracted cross-section from DEM and Google Earth. To generate the point source discharge in MIKE 11 NAM (default module) (see chapter 5), a daily precipitation, potential evapotranspiration and temperature datasets are required; those are generated from CMIIP GCMs (see chapter 4). The PFV, lateral inflows, discharge-water level (Q-h) relationship (collected from CWC) and cross-sections are used as input parameters in MIKE11 HD. The other hydrodynamic variables such as manning roughness coefficient, wave approximation etc. are essential to reduce the global assumptions based selection of parameters, which can improve the computation of MIKE 11. The hydrodynamic parameters are listed in Table 6.5. Subsequently, these inputs were used in MIKE11 HD model to simulate flood along the river reach.

The fundamental Saint-Venant equation of MIKE 11 can be written as follows:

$$\frac{\partial Q}{\partial x} + \frac{\partial A}{\partial t} = q \quad ContinuityEquation \tag{6.11}$$

$$\frac{\partial Q}{\partial t} + \frac{\partial}{\partial x}(\propto \frac{Q^2}{A}) + gA\frac{\partial h}{\partial x} + \frac{n^2 gQQ_{abs}}{AR^{4/3}} = 0 \quad MomentumEquation \tag{6.12}$$

where Q is the discharge (m^3/s); A is the cross section flow area (m^2); q is the lateral inflow (m^2/s); h is the water level above a reference datum (m); x is downstream direction (m); t is time (s); n is the Manning resistance coefficient ($s/m^{1/3}$); R is the hydraulic or resistance radius (m); g is the acceleration due to gravity (m^2/s) and a is the momentum distribution coefficient (e).

In momentum equation the terms are defined as:

$\propto \frac{Q^2}{A}$ is fully dynamic wave, $gA\frac{\partial h}{\partial x}$ is Diffusive wave and $\frac{n^2 gQQ_{abs}}{AR^{4/3}}$ is kinematic wave.

The above equation can be transformed to as implicit finite difference equations obtained from Navier-Stokes equation over a computational grid. Using implicit numerical method, the main continuity and momentum equations can be solved using the Lax-Wendroff scheme (Soleymani and Delphi, 2012) as shown in Figure 6.7:

$$Q_1 = \frac{Q_{i-1}^{j} + Q_{i-1}^{j+1} + Q_{i+1}^{j} + Q_{i}^{j+1}}{4} \tag{6.13}$$

$$Q_2 = \frac{Q_{i}^{j} + Q_{i}^{j+1} + Q_{i+1}^{j} + Q_{i+1}^{j+1}}{4} \tag{6.14}$$

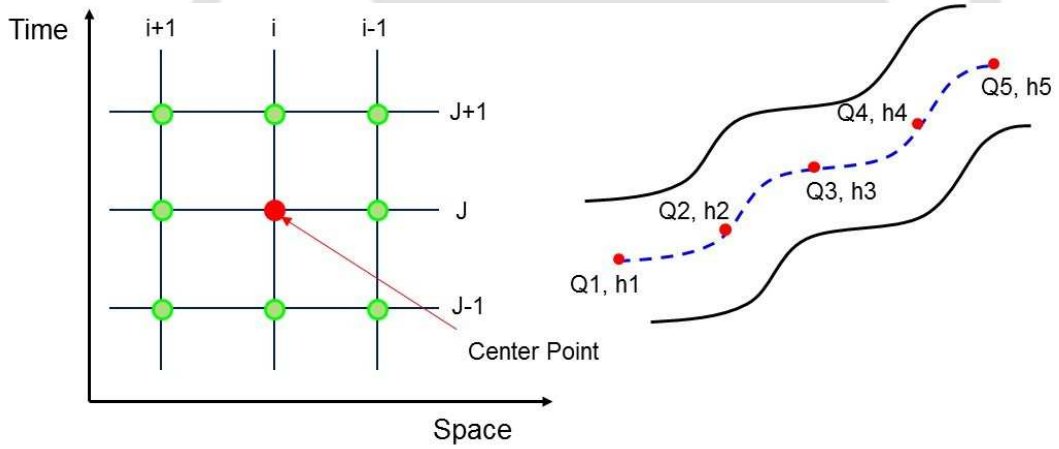

Figure 6.7: Implicit scheme computation grid

Table 6.5: Hydrodynamic parameters for MIKE11 HD setup

Parameter	**Factor**	**Method/Values**	**Description**
Initial Parameters	Initial Discharge	10 cumec	Discharge
	Initial Depth	0.5 cm	Water Level

Wind Factor	Depth	0.0024	Friction parameter value
	Topographical Factor	1	Slopes
Bed Resistant	Resistance Number	15 (10-100)	Manning parameter
	Approach	Uniform Section	
	Resistance Formula	Manning n (0.010 to 0.015s $m^{-1/3}$) / Chezy's Number	
Wave Approximation	Method	High Order Fully Dynamic	Routing method
Coefficient Values	Delta	0.6 (0.5 to 1.0)	Model stabilities parameter
	Delhs	0.01	Minimum allowable water level differences across a weir
	Delh	0.1	Controls the dimensions
	Alpha	1	Velocity distribution coefficient
	Theta	1	Weighting factor for momentum equation

	Eps	0.0001	Water surface slope uses in diffusive wave equation
	Dh Node	0.01	Computational coefficient
	Zeta Min	0.1	Minimum head loss coefficient
	Inter 1 Max	20	Maximum number of iterations
	Nolter	1	No iterations
	Max lter Steady	100	Maximum number of iterations for steady condition
	Froude Exp.	-1	suppression term for convective acceleration

In this study, Teesta River (Lachen and Lachung streams) is routed up to Chugthang. The Teesta River flows approximately 92 km up to Chugthang through the mountainous region of Sikkim Himalaya, which is has been selected for routing. Lachung meets the Lachen River and forms Teesta at Chungthang after travelling around 25 km length. Thus, the cross sections in every 10 km river length have been calculated using field-based survey by using Total Station (survey instrument for surface profiling).

MIKE11 HD Model setup consists various sections such as river network linking (Figure 6.8), river cross section and conveyance definition, boundary condition, HD parameter setup and simulation time step. The model stability depends on the several hydrodynamic parameters; those are used as inputs in hydrodynamic parameter

setup file in MIKE11 HD model. Bed and flood resistance of Teesta River is defined as the Manning's (M) value; the resistance factor is input from one chainage to another chainage along the river flow path. The Manning's value is taken from the literature review. Many hydrodynamic parameter are taken as global values as suggested in MIKE11 documentation. The Delta and Delhs coefficients are the very sensible parameters for model stability; the optimized value of Delta (0.6) is selected after several trial and error computations. Model run time is chosen as in minutes (1 min) because of very steep slope of Teesta River (Figure 6.9) in which model was stable condition. Figure 6.9 shows the longitudinal profile of Teesta River at different chainage points along the flow path.

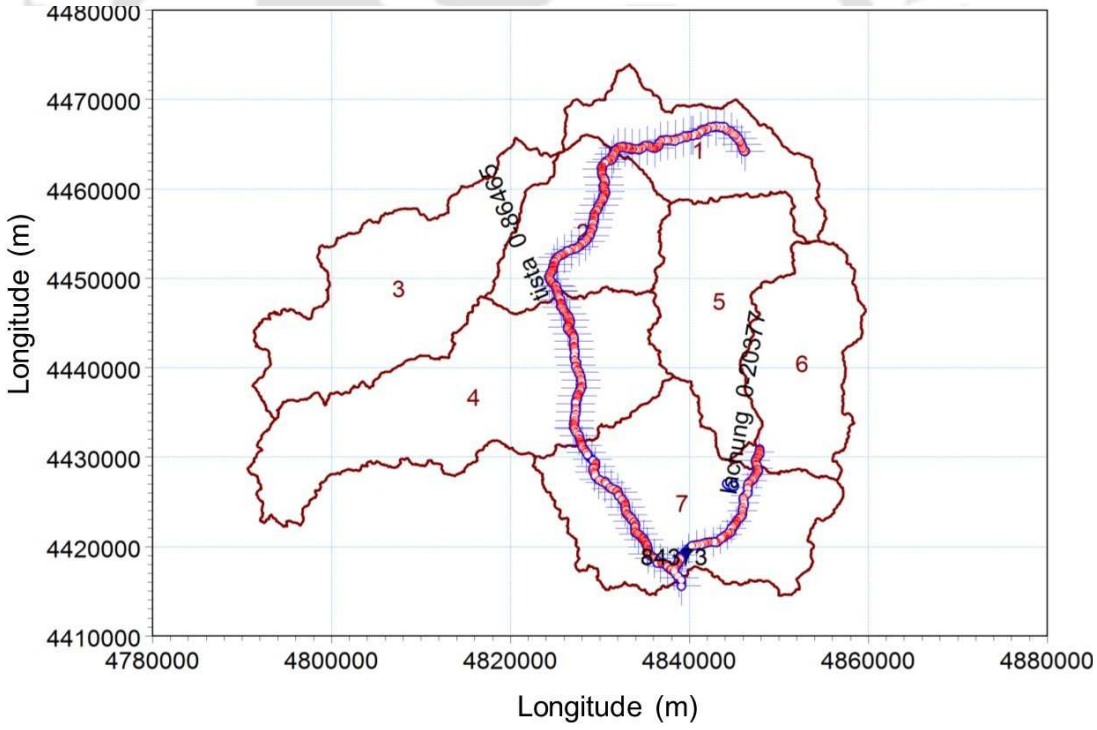

Figure 6.8: Teesta River stream network and cross-section details.

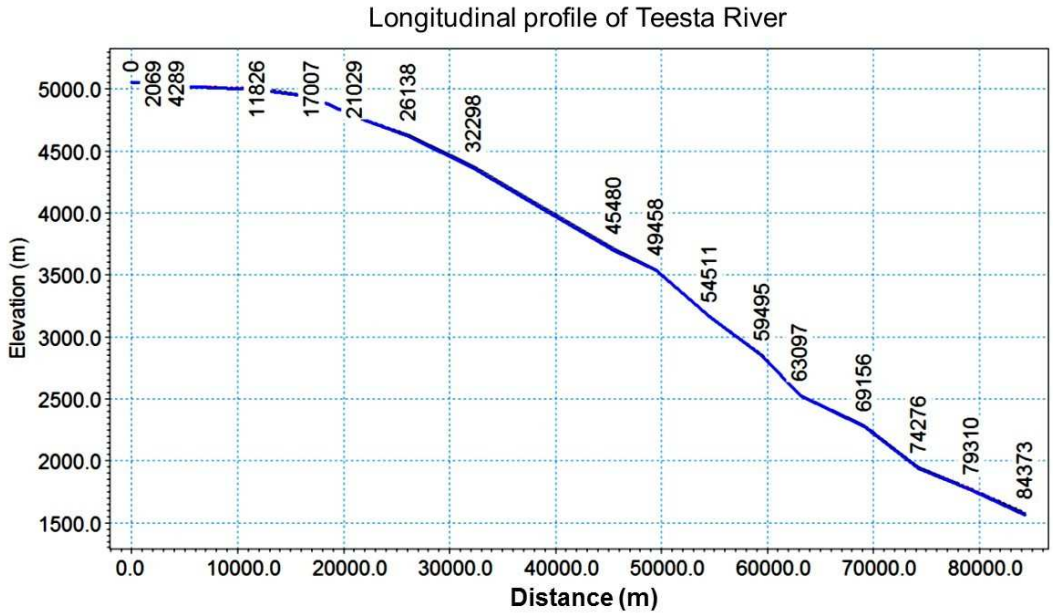

Figure 6.9: Longitudinal profile of Teesta River stream at each cross sections.

MIKE11 has been calibrated with historical dataset during 1991-2005 at the outlet of the catchment. The generated discharge from MIKE11 is compared at the gauge location Chugthang. Based on the computed discharge and water level, discharge-depth (Q-H) relationships are produced at the different chainage point of the river. Q-H relations for the different chainage points are shown in Figure 6.10.

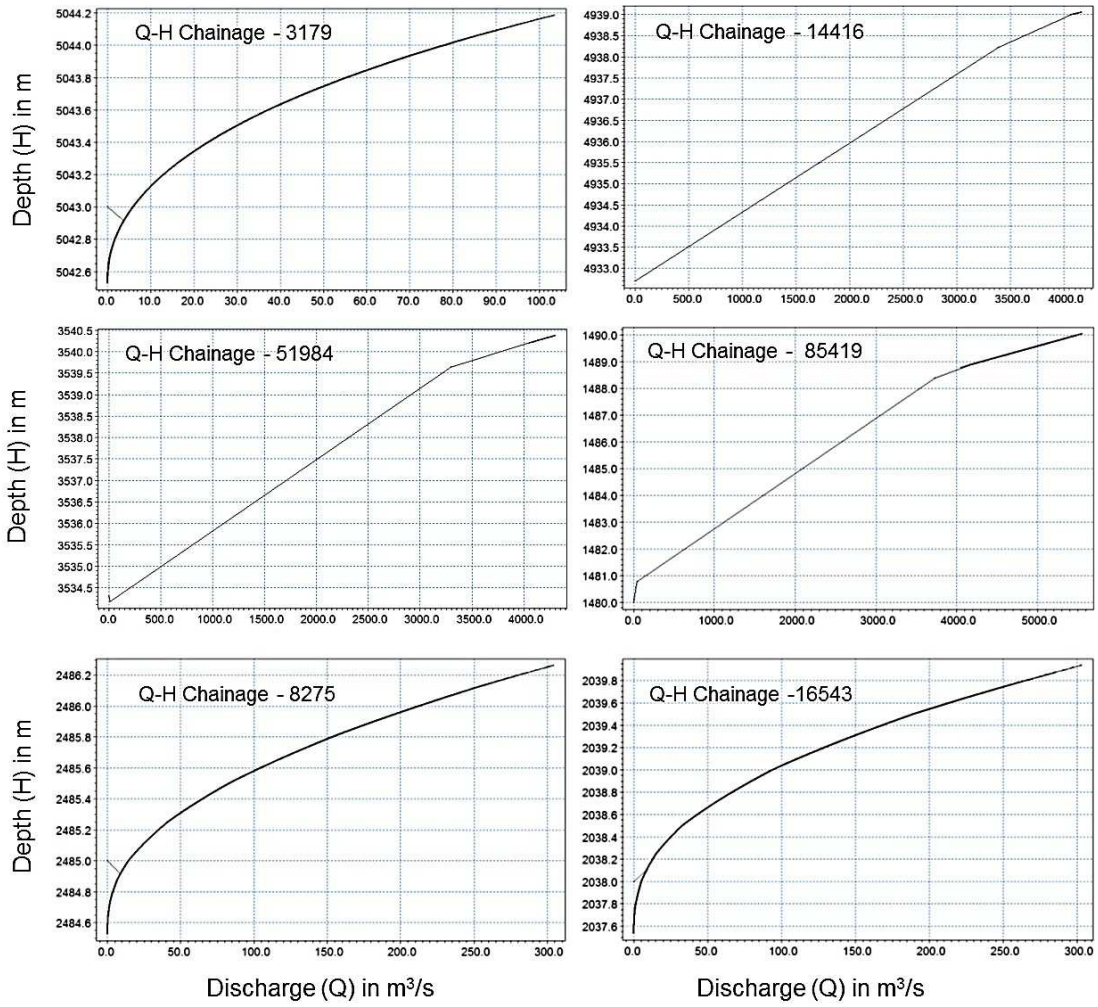

Figure 6.10: Discharge-depth (Q-H) relationship of Teesta River at different chainage points.

For GLOF simulation the estimated peak discharges from glacial lakes from associated breach widths are taken as point source in MIKE11 input. The selected lake has surface area 1.112 km^2, PFV 19.694 Mm^3 and potential lowering height 17.71 m (Figure 6.11, Table 6.4). Model rout the flood discharge along the river reach for GLOF and no GLOF conditions. Figure 6.11 shows the flow path of Teesta River and Chugthang habitat area where the outburst flood will strike. During GLOF and no GLOF (NC) the hydrodynamic parameters such as discharge, velocity and flow depth are assessed along the river length at different chainage points as shown in Figures 6.12, 6.13, 6.14,

respectively. The flood peak discharges at the glacial lake site is 4023.76 m^3/s for 40 m, 5984.13 m^3/s for 60 m and 7993.94 m^3/s for 80 m and at the catchment outlet are 5488.40 m^3/s for 40 m, 7455.27 m^3/s for 60 m and 9469.36 m^3/s for 80 m, breach widths from the chainage where lake outburst flood strikes to outlet of catchment. Whereas, the peaks discharge at the catchment outlet is about 1438.49 m^3/s for no GLOF condition. This implies that the flood peak discharge during GLOF would be much higher as compare to no GLOF condition over the region. The peak discharge during GLOF increases about 3 to 6 times with reference to no GLOF (Figure 6.12), which create huge disaster at the surrounding areas. Similarly, during GLOF, the flowing velocity varies from 5.73 to 13.34 m/s for 40 m, 6.42 to 14.61 m/s for 60 m and 6.99 to 15.38 m/s for 80 m beach widths (Figure 6.13). However, at no GLOF condition the flowing velocity varies from 0.92 to 8.07 m/s. Due to steep slopes over the region and huge discharge (during GLOF), the velocity increases about 100% as compare to no GLOF condition. Simulation of peak discharge from the lake has revealed that the water flow would take 1.5-2.5 hours to reach the Chungthang habitat in the region (Figure 6.11), in case of GLOF event.

In addition, depth of the flowing water at the outlet of the catchment during normal condition is about 5.89 m but after outburst, it could be about 10.09 m for 40 m, 11.96 m for 60 m and 13.28 m for 80 m beach widths. This implies that the flow depth would increase more than 100% at the outlet of the catchment. This high velocities and flow depths, it can erode banks of river and causes land slide and can intense damage as flow with debris cover to mountain communities. This flow with debris can be extremely destructive because they can increase in magnitude.

Figures 6.12, 6.13 and 6.14 represent the discharge, velocity and water depth at

each chainage for a day with maximum projected discharge found for different moraine dam breach conditions. The result presents, the discharge could increase up to 3-6 times and velocity and water depth increase more than 100% as compare to without GLOF condition at each section of Teesta River up to Chugthang. Flowing debris cover with high velocity and water depth can accelerate the undesirable impacts. As there is no flat terrain for water spread (inundation), so increasing water depth will directly affect the Teesta hydropower project near Chugthang. From this comprehensive study; discharge, flowing velocity and water depth are the important parameters which would provide some valuable insights into GLOF awareness, encouraging government policy and effective plan in response to socioeconomic consequences, future climate and flash flood scenarios. Proper management and policy is required to handle the huge amount of water for outburst condition. At the catchment outlet, GLOF events can adversely affect to the hydropower project located at the Chugthang (outlet) in near future. Furthermore, the maximum velocity occurred due to GLOF could cause significant scouring of bed as well as river banks resulting in landslides and flow carries debris cover. The hydrodynamic modeling provides the reasonable results of GLOF events, which bolsters up for further risk assessment.

Figure 6.11: Flow path of Teesta River and Chugthang habitat area.

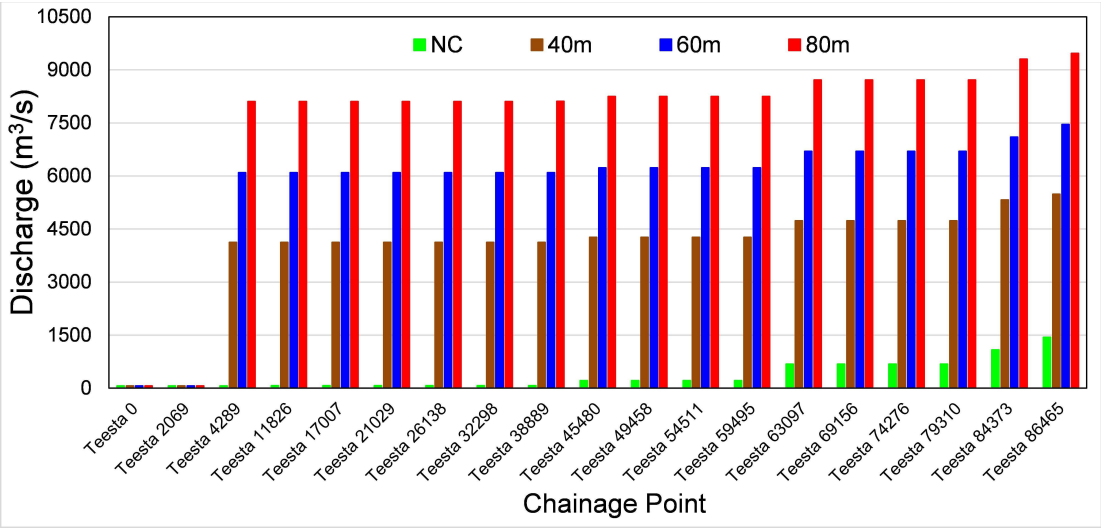

Figure 6.12: Variation of discharges along the river reach considering GLOF for 40m, 60m and 80m breach widths and no GLOF (Normal condition, NC).

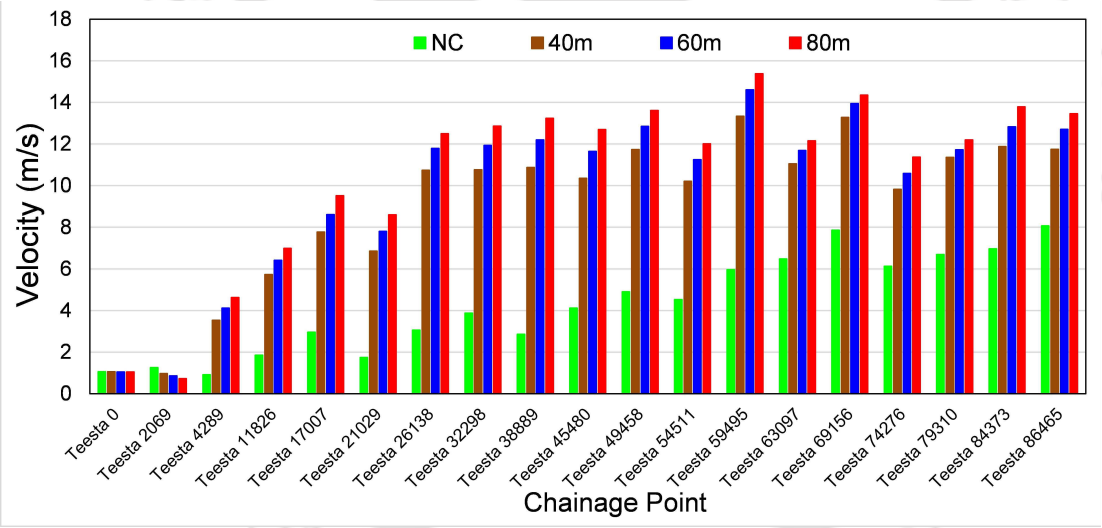

Figure 6.13: Variation of flow velocities along the river reach considering GLOF for 40m, 60m and 80m breach widths and no GLOF (Normal condition, NC).

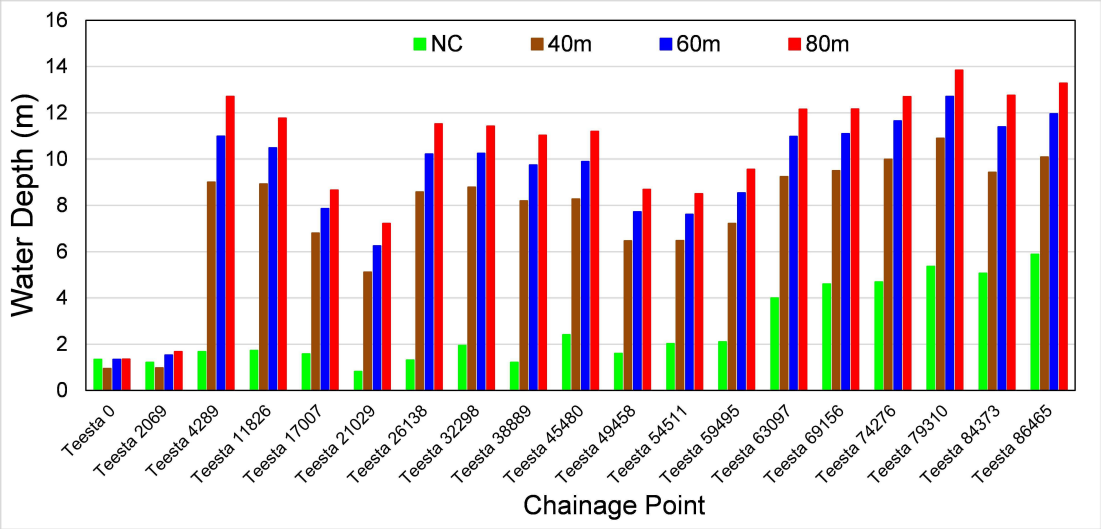

Figure 6.14: Variation of water depths along the river reach considering GLOF for 40m, 60m and 80m breach widths and no GLOF (Normal condition, NC).

6.4.2 GLOF Hazard Consequences

Two glacier-fed rivers (Lachen and Lachung) meeting at Chugthang and forms the Teesta River. At this junction point, the Teesta stage-III power project is located and Chugthang is the full of habitat. In case of outburst, the area could be at risk. At the downstream of the Teesta stage-III power project, a number of hydropower projects are going on and some are being planned. Accordingly, proper management of huge discharge, high velocity and depth is needed otherwise it can create deadly disaster not only for power project but also for surrounding settlement. Also high velocity and depth can erode banks of rivers and causes land slide and can intense damage to mountain communities. For example - the designed reservoir level is just five meter below at the crossing bridge near the Chugthang, during outburst, water will overflow from this bridge and thereby it may collapse. In Teesta River catchment up to Chugthang, no flat terrain for inundation, so the flood will directly affect to the hydropower project and its functioning.

6.5 Summary and Conclusions

This chapter highlights the glacier hazards in terms of glacial lakes and glacial lake outburst flood (GLOF). The glacial lakes are delineated from the remote sensing applications and hydrodynamic modeling (MIKE11 HD) for GLOF dynamics. Total 203 >0.01 km^2 glacial lakes are identified, some glacial lakes are increasing and some are decreasing and disappeared as well. Over the study area most of the glacial lakes situated at the high elevation zone (>4500 m). The glacial lake having area more than 1 km^2 and maximum PFV is selected for GLOF dynamics. The result highlights that, during GLOF the peak discharge could increase about 4-6 time and flow velocity and water depth would increase about 100% as compare to no GLOF condition. This implies, it can create huge disaster at the downstream of Teesta River catchment.

CHAPTER 7

Conclusions and Recommendations for Future Work

This study presents the assessment of climate extremes and glacier hazards over the upper Teesta River basin induced by climate change. To accomplish the above objectives, first, the impact of climate change was analyzed by predicting the meteorological variables (precipitation and temperature) using CMIP5 GCMs with their RCP scenarios; then the joint probabilistic behaviors of climate extremes were investigated using parametric copula; the hydrologic modeling was then carried out to assess the present and future change in river discharge; glacial lakes identification and temporal change detection with its vulnerability was evaluated and finally, the hydrodynamic modeling (MIKE11 HD) was used to assess the impact of GLOF dynamics at the downstream of Teesta River.

7.1 Projection of Precipitation and Temperature and their Extremes

Firstly, precipitation and temperature datasets are downscaled using SDSM over the study area. The projected precipitation is consistently increasing and their extremes

are changing with time such as heavy and very heavy precipitation days are increased, while number of wet days and CWD are decreased with less dry spell (CDD). The precipitation are showing upward trends for all projected scenarios, but CM3 model projecting much higher range as compare to ESM2G and ESM2M. The higher projection in CM3 model may be due to consideration of only atmospheric component of land and ocean, while ESMs consists both atmospheric and human activities component during construction of models. This indicates the climate model having large projection than earth system models over the Eastern Himalaya. The RCP8.5 of all three GCMs has significant large positive change in 21st century time series as well as in monsoon and non-monsoon time series for all combinations. The SDII, WD, R10 and R20 are showing increasing trend in different scenarios. From the quantification, it is observed that the heavy and very heavy precipitation days are increased, while number of wet days and CWD are decreased with less dry spell (CDD). These increasing or decreasing trends are dominant for high extreme events.

The temperature result exhibits that the widespread and significant warming trend has been observed related to extreme indices especially, indices calculated from daily temperatures. Monthly maximum temperature shows the increasing trends during winter months, whereas monsoon month shows decreasing trends over the region. Similarly, the monthly minimum temperature shows the increasing trends for all months except for some of the combinations (2nd and 6th) of January month. Extreme indices of maximum temperature, Ice-day, cooler day and warmer day are decreasing continuously, the maximum decrease in day are 2.9 days, 7.22 days and 43.71 days, respectively. Although, warmest days (TXx) has increased by 1.83°C and coldest days (TXn) decreased by 4.83°C. Similarly, minimum temperature extreme indices; frost days, cool nights and

warmer nights are decreased, whereas the temperature of warmer nights has increased and temperature of cool nights have increased. The reductions in FD0 is 11.07days, in TN10p is 9.68 days and in TN90p 20.7 days, while, TNx increased by 1.41°C and TNn decreased by 3.61°C. The result implies that the minimum temperature indices are more pronounced than maximum temperature indices. Form the analysis, it is clearly shown that the intensity of warming and cooling have been increased over the North Sikkim region.

7.2 Bivariate Analysis of Precipitation and Temperature Extremes

The precipitation and temperature extremes are analyzed spatially and temporally using bivariate copulas. Firstly, three copulas belonging to different families such as Frank copula belongs to Archimedean family, Plackett copula belongs to Plackett family and Gaussian copula belongs to Elliptical family are used to select best fit copula. These three copulas are suitable for both positively and negatively correlated variables, thus, in this study three copulas from different families have been chosen. The changes in joint return period of extreme combinations are analyzed for the projected scenarios during 2021-2100.

The spatial distribution of joint return period of precipitation extreme combinations for 5-year, 10-year and 20-year are almost similar during 1979-2005. The joint return period of $T_{[CWD,CDD]}$, is decreased for all projected scenarios, indicating the co-occurrence of floods and droughts are more frequent in same year over the region. The $T_{[WD,SD]}$ is also decreased and other extreme combinations had no significant changes. The decrease in joint return period of $T_{[WD,SD]}$, indicating the frequent co-occurrence

of number of wet days with high precipitation intensity in the same year in future. These changes may be due to change in marginal distributions and bivariate relations of extremes. Under the RCP8.5 scenario, the co-occurrence of floods and droughts are more frequent within the same year in future.

The 5 and 10-year joint return periods of temperature extremes are also spatially similar over the region during 1979-2005. The joint return period of [TN10, TN90] is decreased but other extreme combinations are increased for all scenarios. The decreased value indicates the frequent co-occurrence extremes, whereas the increased value indicates the less frequent co-occurrence of extremes. Under the RCP8.5 scenario, joint return periods of some of the extreme combinations are decreased in upper part of the region, which indicates that the cooling is more frequent in future.

From the analysis, it is observed that there are various response mechanism in the climate system that can either be positive or negative, these effects are forcing to change the climatic conditions e.g. glaciers and snow begin to melt due to increasing the concentration of greenhouse gases and warm Earth's climate. Due to warming trend, snowmelt rate and runoff rate could be change and can alter the water resources system over the study area.

7.3 Remote Sensing Applicability for Inventory of Glacial Lakes

The areal expansions of glacial lake are most indispensable evidence to identify the potential sources of GLOF risk and vulnerability. The study found a total 203 glacial lakes having area more than 0.01 km^2 and about 73 glacial lakes having are more than 0.05 km^2 over the catchment. Among of the glacial lakes about 90% of glacial lakes are

situated above the 4500 m altitude. Some glacial lakes are found to be increasing in their areal extent and some are newly formed during 1990 to 2014. Further, some lakes are decreasing and some are getting extinct also. The reason behind these decreasing or extinction may be climate change, glacier retreating, loss of connection from the parent glaciers, etc. Melting of glaciers and decrease in the supply of fresh water in these water bodies can lead to shortage of water in the main river channel. The Himalayas are one among the young folded mountains, they are fragile. The upper Teesta River catchment falls under the Zone- IV of the Indian seismic chart. Any high magnitude scale of earthquake in this area and resultant avalanches or ice/glacier blocks from parent glacier fall into the lakes can trigger the event of GLOF.

7.4 Hydrological and Hydrodynamic Modeling with GLOF Simulation

The MIKE11 NAM rainfall runoff model was found suitable for hilly catchments e.g. Teesta River to simulate the hydrological response of the basin to the rainfall and generating daily runoff with high degree of accuracy. The model performed well to simulate daily runoff in good agreement with observed runoff in terms of timing, rate, volume and shape of hydrograph. The model was automatically calibrated with nine important parameters. The projected precipitation and temperature scenarios generated from CMIP5 GCMs with their RCPs are used to generate the projected streamflow. The elevation band approach used to formulate the snowmelt component of streamflow. The projected scenarios of streamflow showed significant increase over the study area during the 21st century. The monthly observation of streamflow showed significant increase in all months except July month.

From the Budyko framework analysis, it is clearly found that the precipitation is the major factor that affects the runoff changes, the ranged from 2 to 19% for different scenarios. As the possible warming climate quantifies that the change in annual runoff resulting from snow-ratio is negative, as the snow-ratio decreased during 2020-2060 relative to 1982-2005. This implies that, precipitation is less likely to occur as snowfall. A shift from snowfall towards rainfall over the region is considered not to influence the annual runoff significantly as compare to precipitation.

Additionally for GLOF simulation a glacial lake having surface area more than 1 km^2 with maximum PFV (19.92 Mm^3) is considered for Hydrodynamic modeling (MIKE11 HD). The hydrodynamic parameters such as discharge, velocity and water depth have been observed at each cross-section along the river reach. The discharge could increase up to 4-6 times as compare to without GLOF condition at each section of Teesta River up to Chugthang. Further the flowing velocity and water depth could be almost double during outburst as compared to no GLOF situation. In case of GLOF, the simulated peak discharge from the glacial lake would take 1.5-2.5 hours to reach the Chugthang habitat region. The increased high velocity and water depth can accelerate the undesirable impacts such as erosion of river banks, land slide and can intense damage as flow with debris cover to mountain communities. Over the catchment up to Chugthang, there is no flat terrain for water spread, so increasing water depth will directly affect the Teesta hydropower project near Chugthang. From this comprehensive study; discharge, flowing velocity and water depth are the important parameters which would provide some valuable insights into GLOF awareness, encouraging government policy and effective plan in response to socioeconomic consequences, future climate and flash flood scenarios.

7.5 Recommendations for Future Scope

- In this study, only three GCMs datasets have been used, but a large set of GCM can be useful to assess the uncertainty associated with GCMs.
- Impact of non-linear dependency on joint probability behavior of climate extreme events can also be assess using copula.
- Bivariate dependency of precipitation extremes over temperature extreme can be assessed used copula.
- The glacial lake parameters such as depth, area and breach condition can be estimate by field observation instead of empirical formulas for better interpretation of vulnerability.
- Using GLOF results, the development of early flood warning system would be more useful to reduce the hazards over the North Sikkim Himalaya.

References

Abbaspour, K. C., Yang, J., Maximov, I., Siber, R., Bogner, K., Mieleitner, J., Zobrist, J., and Srinivasan, R. (2007). Modelling hydrology and water quality in the pre-alpine / alpine Thur watershed using SWAT. *Journal of Hydrology*, 333:413–430.

Akaike, H. (1974). A new look at the statistical model identification. *IEEE Transactionson Automatic Control*, 19(6):716–723.

Alexander, L. V., Zhang, X., Peterson, T. C., Caesar, J., Gleason, B., Klein Tank, A. M. G., Haylock, M., Collins, D., Trewin, B., Rahimzadeh, F., Tagipour, A., Rupa Kumar, K., Revadekar, J., Griffiths, G., Vincent, L., Stephenson, D. B., Burn, J., Aguilar, E., Brunet, M., Taylor, M., New, M., Zhai, P., Rusticucci, M., and Vazquez-Aguirre, J. L. (2006). Global observed changes in daily climate extremes of temperature and precipitation. *Journal of Geophysical Research Atmospheres*, 111:D05109.

Allamano, P., Claps, P., and Laio, F. (2009). Global warming increases flood risk in mountainous areas. *Geophysical Research Letters*, 36:L24404.

Amir, M., Khan, M., Rasul, M., Sharma, R., and Akram, F. (2015). Hydrologic and hydrodynamic modelling of extreme flood events to assess the impact of climate change in a large basin with limited data. *Journal of Flood Risk Management*.

Anacona, P. I., Mackintosh, A., and Norton, K. (2015a). Reconstruction of a glacial lake outburst flood (glof) in the engaño valley, chilean patagonia: Lessons for glof risk management. *Science of the Total Environment*, 527:1–11.

Anacona, P. I., Norton, K., and Mackintosh, A. (2015b). Reconstruction and modelling of the 1977 GLOF of the Engano Lake Chilean Patagonia. *Geophysical Research Abstracts*, 17:8305.

Austin, J., Zhang, L., Jones, R. N., Durack, P., Dawes, W., and Hairsine, P. (2010). Climate change impact on water and salt balances: An assessment of the impact of climate change on catchment salt and water balances in the Murray-Darling Basin, Australia. *Climatic Change*, 100(3):607–631.

Baban, S. J. (1993). The evaluation of different algorithms for bathymetric charting of lakes using Landsat imagery. *International Journal of Remote Sensing*, 14(12):2263–2273.

Babu Govindha Raj, K., Remya, S. N., and Vinod Kumar, K. (2013). Remote sensing-based hazard assessment of glacial lakes in sikkim himalaya. *Current Science*, 104(3):359–364.

Bajracharya, B., Shrestha, A. B., and Rajbhandari, L. (2007a). Glacial Lake Outburst Floods in the Sagarmatha Region. *Mountain Research and Development*, 27(4):336–344.

Bajracharya, S. R. and Mool, P. (2009). Glaciers, glacial lakes and glacial lake outburst floods in the Mount Everest region, Nepal. *Annals of Glaciology*, 50(53):81–86.

Bajracharya, S. R., Mool, P. K., and Shrestha, B. R. (2007b). Impact of climate change on Himalayan glaciers and glacial lakes: Case studies on GLOF and associated hazards in Nepal and Bhutan. Technical report, ICIMOD.

Bannerjee, B. (2013). *GLOF study Using Remote Sensing and Ground Based Measurement Techniques*. PhD thesis, Master's Thesis, Indian Institute of Remote Sensing, Indian Space Research Organisation.

Barnett, T. P., Adam, J. C., and Lettenmaier, D. P. (2005). Potential impacts of a warming climate on water availability in snow-dominated regions. *Nature*, 438(17):303–309.

Berghuijs, W. R., Woods, R. a., and Hrachowitz, M. (2014). A precipitation shift from snow towards rain leads to a decrease in streamflow-supplement. *Nature Climate Change*, 4(7):583–586.

Bolch, T., Kulkarni, a., Kaab, a., Huggel, C., Paul, F., Cogley, J. G., Frey, H., Kargel,

J. S., Fujita, K., Scheel, M., Bajracharya, S., and Stoffel, M. (2012). The State and Fate of Himalayan Glaciers. *Science*, 336(6079):310–314.

Boo, K.-O., Kwon, W.-T., and Baek, H.-J. (2006). Change of extreme events of temperature and precipitation over korea using regional projection of future climate change. *Geophysical Research Letters*, 33(1).

Breien, H., De Blasio, F. V., Elverhoi, A., and Hoeg, K. (2008). Erosion and morphology of a debris flow caused by a glacial lake outburst flood, Western Norway. *Landslides*, 5:271–280.

Budhathoki, K. P., Bajracharya, O. R., Pokharel, K., Budhathoki, K. P., and Pokharel, B. K. (2010). Assessment of Imja Glacier Lake outburst Flood (GLOF) Risk in Dudh Koshi River Basin using Remote Sensing Techniques. *Journal of Hydrology and Meteorology*, 7(1):75–91.

Budyko, M. I. (1974). Climate and life. *Academic Press, New York*, page 508.

Burn, D. H. and Hag Elnur, M. A. (2002). Detection of hydrologic trends and variability. *Journal of Hydrology*, 255(1-4):107–122.

Chattopadhyay, N. (2010). Climate change and food security in india. In *Climate change and food security in South Asia*, pages 229–250. Springer.

Chen, J., Brissette, F. P., and Leconte, R. (2011). Uncertainty of downscaling method in quantifying the impact of climate change on hydrology. *Journal of Hydrology*, 401:190–202.

Chen, Y., Li, W., Fang, G., and Li, Z. (2017). Hydrological modeling in glacierized catchments of Central Asia: status and challenges. *Hydrology and Earth System Sciences Discussions*, 21(July):669–684.

Chen, Y. D., Zhang, Q., Xiao, M., Singh, V. P., and Zhang, S. (2016). Probabilistic forecasting of seasonal droughts in the Pearl River basin, China. *Stochastic Environmental Research and Risk Assessment*, 30(7):2031–2040.

Clague, J. J. and Evans, S. G. (2000). A review of catastrophic drainage of moraine-dammed lakes in British Columbia. *Quaternary Science Reviews*, 19:1763–1783.

Colombo, A. F., Etkin, D., and Karney, B. W. (1999). Climate variability and the frequency of extreme temperature events for nine sites across Canada: Implications for power usage. *Journal of Climate*, 12(8):2490–2502.

Cook, S. J. and Quincey, D. J. (2015). Estimating the volume of Alpine glacial lakes. *Earth Surface Dynamics*, 3:559–575.

Crosbie, R. S., Dawes, W. R., Charles, S. P., Mpelasoka, F. S., Aryal, S., Barron, O., and Summerell, G. K. (2011). Differences in future recharge estimates due to GCMs, downscaling methods and hydrological models. *Geophysical Research Letters*, 28(L11406).

Crosbie, R. S., McCallum, J. L., Walker, G. R., and Chiew, F. H. S. (2010). Modelling climate-change impacts on groundwater recharge in the Murray-Darling Basin, Australia. *Hydrogeology Journal*, 18(7):1639–1656.

Dai, A. (2011). Drought under global warming: a review. *Wiley Interdisciplinary Reviews: Climate Change*, 2(1):45–65.

Dai, A., Qian, T., Trenberth, K., and Milliman, J. D. (2009). Changes in Continental Freshwater Discharge from 1948 to 2004. *Journal of Climate*, 22(10):2773–2792.

Das, S., Kar, N. S., and Bandyopadhyay, S. (2015). Glacial lake outburst flood at Kedarnath, Indian Himalaya: a study using digital elevation models and satellite images. *Natural Hazards*, 77(2):769–786.

De, U., Dube, R., and Rao, G. P. (2005). Extreme weather events over india in the last 100 years. *J. Ind. Geophys. Union*, 9(3):173–187.

De Paiva, R. C. D., Buarque, D. C., Collischonn, W., Bonnet, M. P., Frappart, F., Calmant, S., and Bulhoes Mendes, C. A. (2013). Large-scale hydrologic and hydrodynamic modeling of the Amazon River basin. *Water Resources Research*, 49:1226–1243.

DHI (2009). MIKE 11: A modelling system for rivers and Channels. Reference manual. Denmark: Danish Hydraulic Institute. Technical report, DHI.

Donat, M. G., Alexander, L. V., Yang, H., Durre, I., Vose, R., Dunn, R. J. H., Willett, K. M., Aguilar, E., Brunet, M., Caesar, J., Hewitson, B., Jack, C., Klein Tank, A. M. G., Kruger, A. C., Marengo, J., Peterson, T. C., Renom, M., Rojas, C. O., Rusticucci, M., and Salinger, J. (2013). Updated analyses of temperature and precipitation extreme indices since the beginning of the twentieth century: The HadEX2 dataset. *Jounal of Geophysical Research Atmospheres*, 118:2098–2118.

DPR (2005). Carrying capicity study of teesta basin in sikkim. volume-i introductory volume. Technical report, Ministry of Environmetal and Forest, University of Delhi.

Duhan, D. and Pandey, A. (2015). Statistical downscaling of temperature using three techniques in the Tons River basin in Central India. *Theoretical and Applied Climatology*, 121(3-4):605–622.

Durga Rao, K. H. V., Venkateshwar Rao, V., Dadhwal, V. K., and Diwakar, P. G. (2014). Kedarnath flash floods: A hydrological and hydraulic simulation study. *Current Science*, 106(4):598–603.

Dutta, D., Herath, S., and Musiake, K. (2000). Flood inundation simulation in a river basin using a physically based distributed hydrologic model. *Hydrological Pro*, 14(3):497–519.

Easterling, D. R., Meehl, G. A., Parmesan, C., Changnon, S. A., Karl, T. R., and Mearns, L. O. (2000). Climate extremes: observations, modeling, and impacts. *science*, 289(5487):2068–2074.

Favre, A. C., Adlouni, S. E., Perreault, L., Thiemonge, N., and Bobee, B. (2004). Multivariate hydrological frequency analysis using copulas. *Water Resources Research*, 40:1–12.

Findell, H. L., Shevliakova, E., Milly, P., and Stouffer, R. J. (2007). Modeled Impact of Anthropogenic Land Cover Change on Climate. *Americal Meteorological Society*, 20:3621–3634.

Frich, P., Alexander, L. V., Della-Marta, P., Gleason, B., Haylock, M., Tank, A. K., and Peterson, T. (2002). Observed coherent changes in climatic extremes during the second half of the twentieth century. *Climate research*, 19(3):193–212.

Froehlich, D. C. (1995). Peak outburst from Breached Embankment dam. *Journal of Water Resources Planning and Management*, 121(1):90–97.

Fujita, K., Saka, A., Nuimura, T., Yamaguch, S., and Sharma, R. R. (2009). Recent changes in Imja Glacial Lake and its damming moraine in the Nepal Himalaya revealed by in situ surveys and multi-temporal ASTER imagery. *Environment Research Letter*, 4:1–7.

Fujita, K., Sakai, A., Takenaka, S., Nuimura, T., Surazakov, A. B., Sawagaki, T., and Yamanokuchi, T. (2013). Potential flood volume of Himalayan glacial lakes. *Natural Hazards and Earth System Sciences*, 13:1827–1939.

Gagnon, S., Singh, B., Rousselle, J., and Roy, L. (2005). An Application of the Statistical DownScaling Model (SDSM) to Simulate Climatic Data for Streamfl ow Modelling in Québec. *Canadian Water Resources Journal*, 30(4):297–314.

Gao, G., Fu, B., Wang, S., Liang, W., and Jiang, X. (2016). Determining the hydrological responses to climate variability and land use / cover change in the Loess Plateau with the Budyko framework. *Science of the Total Environment*, 557-558:331–342.

Gardelle, J., Arnaud, Y., and Berthier, E. (2011). Contrasted evolution of glacial lakes along the Hindu Kush Himalaya mountain range between 1990 and 2009. *Global and Planetary Change*, 75(1-2):47–55.

Genest, C. and Favre, A.-C. (2007). Everything You Always Wanted to Know about Copula Modeling but Were Afraid to Ask. *Journal of Hydrologic Engineering*, 12(4):347–368.

Ghosh, S. and Dutta, S. (2012). Impact of climate change on flood characteristics in Brahmaputra basin using a macro-scale distributed hydrological model. *Journal of Earth System Science*, 121(3):637–657.

Gleeson, T., Wada, Y., Bierkens, M. F. P., and Beek, L. P. H. V. (2012). Water balance of global aquifers revealed by groundwater footprint. *Nature*, 488:197–200.

Gomez, M., Concepción Ausín, M., and Carmen Domínguez, M. (2016). Seasonal copula models for the analysis of glacier discharge at King George Island, Antarctica. *Stochastic Environmental Research and Risk Assessment*, pages 1–15.

Gottardi, G. and Venutelli, M. (2004). Central scheme for two-dimensional dam-break flow simulation. *Advances in Water Resources*, 27:259–268.

Greve, P., Gudmundsson, L., Orlowsky, B., and Seneviratne, S. I. (2015). Introducing a probabilistic Budyko framework. *Geophysical Research Letters*, 42:2261–2269.

Griggs, D. J. and Noguer, M. (2002). Climate change 2001: the scientific basis. contribution of working group i to the third assessment report of the intergovernmental panel on climate change. *Weather*, 57(8):267–269.

Grimaldi, S., Petroselli, A., Salvadori, G., and De Michele, C. (2016). Catchment compatibility via copulas: A non-parametric study of the dependence structures of hydrological responses. *Advances in Water Resources*, 90:116–133.

Grimaldi, S. and Serinaldi, F. (2006). Asymmetric copula in multivariate flood frequency analysis. *Advances in Water Resources*, 29(8):1155–1167.

Huggel, C., Haeberli, W., Kaab, A., Bieri, D., and Richardson, S. (2004). An assessment procedure for glacial hazards in the Swiss Alps. *Canadian Geotechnical Journal*, 41:1068–1083.

Huggel, C., Kääb, A., Haeberli, W., Teysseire, P., and Paul, F. (2002). Remote sensing based assessment of hazards from glacier lake outbursts: a case study in the Swiss Alps. *Can. Geotech. J*, 39:316–330.

Immerzeel, W. W. and Bierkens, M. F. P. (2012). Asia's water balance. *Nature Geoscience*, 5(12):841–842.

India-WRIS (2012). River basin atlas of india. rrsc-west, nrsc, isro, jodhpur, india. Technical report, NRSC, ISRO.

IPCC (2007). Synthesis report. contribution of working groups i, ii and iii to the fourth assessment report of the intergovernmental panel on climate change.

IPCC (2014). *Climate change 2014: Synthesis report. Contribution of working groups I, II and III to the Fifth Assessment Report of the Intergovernmental Panel on Climate Change*. IPCC.

Ives, J. D., Shrestha, R. B., Mool, P. K., et al. (2010). *Formation of glacial lakes in the Hindu Kush-Himalayas and GLOF risk assessment.* ICIMOD Kathmandu, Technical Report.

Jain, S. K., Lohani, A. K., Singh, R. D., Chaudhary, A., and Thakural, L. N. (2012). Glacial lakes and glacial lake outburst flood in a Himalayan basin using remote sensing and GIS. *Natural Hazards*, 62(3):887–899.

Jiang, C., Xiong, L., Wang, D., Liu, P., Guo, S., and Xu, C.-y. (2015). Separating the impacts of climate change and human activities on runoff using the Budyko-type equations with time-varying parameters. *Journal of Hydrology*, 522:326–338.

Kääb, A., Berthier, E., Nuth, C., Gardelle, J., and Arnaud, Y. (2012). Contrasting patterns of early twenty-first-century glacier mass change in the Himalayas. *Nature*, 488(7412):495–498.

Kang, H., An, K. H., Park, C. K., Solis, A. L. S., and Stitthichivapak, K. (2007). Multimodel output statistical downscaling prediction of precipitation in the Philippines and Thailand. *Geophysical Research Letters*, 34(15):1–5.

Kao, S. C. and Govindaraju, R. S. (2010). A copula-based joint deficit index for droughts. *Journal of Hydrology*, 380(1-2):121–134.

Katz, R. W. and Brown, B. G. (1992). Extreme events in a changing climate: variability is more important than averages. *Climatic change*, 21(3):289–302.

Kendall, M. G. (1948). *Rank Correlation Methods.* Griffin.

Klein Tank, A. M. G., Peterson, T. C., Quadir, D. A., Dorji, S., Zou, X., Tang, H., Santhosh, K., Joshi, U. R., Jaswal, A. K., Kolli, R. K., Sikder, A. B., Deshpande, N. R., Revadekar, J. V., Yeleuova, K., Vandasheva, S., Faleyeva, M., Gomboluudev, P., Budhathoki, K. P., Hussain, A., Afzaal, M., Chandrapala, L., Anvar, H., Amanmurad, D., Asanova, V. S., Jones, P. D., New, M. G., and Spektorman, T. (2006). Changes in daily temperature and precipitation extremes in central and south Asia. *Journal of Geophysical Research*, 111:D16105.

Krishna, A. P. (2005). Snow and glacier cover assessment in the high mountains of Sikkim Himalaya. *Hydrological Processes*, 19(12):2375–2383.

Kulkarni, A. V. (2007). Effect of global Warming on the Himalayan cryosphere. *Jalvigyan Sameeksha*, 22:93–108.

Kumar, N., Jaswal, A. K., Mohapatra, M., and Kore, P. A. (2016). Spatial and temporal variation in daily temperature indices in summer and winter seasons over India (1969–2012). *Theoretical and Applied Climatology*.

Kumar, R., Singh, R. D., and Sharma, K. D. (2005). Water resources of India. *Current Science*, 89(5):794–811.

Lacaux, J., Tourre, Y., Vignolles, C., Ndione, J., and Lafaye, M. (2007). Classification of ponds from high-spatial resolution remote sensing: Application to rift valley fever epidemics in senegal. *Remote Sensing of Environment*, 106(1):66–74.

Lesk, C., Rowhani, P., and Ramankutty, N. (2016). Influence of extreme weather disasters on global crop production. *Nature*, 529(7584):84–87.

Li, J., Zhang, Q., Chen, Y. D., and Singh, V. P. (2015). Future joint probability behaviors of precipitation extremes across China: Spatiotemporal patterns and implications for flood and drought hazards. *Global and Planetary Change*, 124:107–122.

Li, Y., Chen, B.-M., Wang, Z.-G., and Peng, S.-L. (2011). Effects of temperature change on water discharge, and sediment and nutrient loading in the lower Pearl River basin based on SWAT modelling. *Hydrological Sciences Journal*, 56(1):68–83.

Lu, G. Y. and Wong, D. W. (2008). An adaptive inverse-distance weighting spatial interpolation technique. *Computers and Geosciences*, 34:1044–1055.

Lutz, A. F., Immerzeel, W. W., Kraaijenbrink, P. D. A., Shrestha, A. B., and Bierkens, M. F. P. (2016). Climate change impacts on the upper indus hydrology: Sources, shifts and extremes. *PLoS ONE*, 11(11):1–33.

Madsen, H. (2000). Automatic calibration of a conceptual rainfall–runoff model using multiple objectives. *Journal of Hydrology*, 235:276–288.

Mahmood, R. and Babel, M. S. (2013). Evaluation of SDSM developed by annual and monthly sub-models for downscaling temperature and precipitation in the Jhelum basin, Pakistan and India. *Theoretical and Applied Climatology*, 113:27.44.

Mann, H. B. (1945). Nonparametric tests against trend. *Econometrica: Journal of the Econometric Society*, pages (245–259).

Manton, M., Della-Marta, P., Haylock, M. R., Hennessy, K., Nicholls, N., Chambers, L., Collins, D., Daw, G., Finet, A., Gunawan, D., et al. (2001). Trends in extreme daily rainfall and temperature in southeast asia and the south pacific: 1961–1998. *International Journal of Climatology*, 21(3):269–284.

Markham, B. and Barker, J. (1987). Thematic mapper bandpass solar exoatmospheric irradiances. *International Journal of remote sensing*, 8(3):517–523.

Marti, G., Andler, S., Nielsen, F., and Donnat, P. (2016). Optimal transport vs. Fisher-Rao distance between copulas for clustering multivariate time series. *IEEE Workshop on Statistical Signal Processing Proceedings*, 2016-Augus(2):2–6.

McFeeters, S. K. (1996). The use of the normalized difference water index (ndwi) in the delineation of open water features. *International journal of remote sensing*, 17(7):1425–1432.

Mckillop, R. J. and Clague, J. J. (2007). A procedure for making objective preliminary assessments of outburst flood hazard from moraine- dammed lakes in southwestern British Columbia. *Natural Hazards*, 41:131–157.

Mearns, L. O., Katz, R. W., and Schneider, S. H. (1984). Extreme High-Temperature Events: Changes in their probabilities with Changes in Mean Temperature.

Meehl, G. A., Covey, C., Delworth, T., Latif, M., McAvaney, B., Mitchell, J. F. B., Stouffer, R. J., and Taylor, K. E. (2007). The WCRP CMIP3 Multimodel Dataset; A new era in climate change research. *Americal Meteorological Society*, 88:1383–1394.

Meetei, L. I., Pattanayak, S. K., Bhaskar, A., Pandit, M. K., and Tandon, S. K. (2007). Climatic imprints in Quaternary valley fill deposits of the middle Teesta valley, Sikkim Himalaya. *Quaternary International*, 159:32–49.

Mergili, M., Schneider, D., Worni, R., and Schneider, J. F. (2011). Glacial lake outburst floods in the Pamir of Tajikistan: Challenges in prediction and modeling. *Italian Journal of Engineering Geology*, 3:973–982.

Mileham, L., Taylor, R. G., Todd, M., Tindimugaya, C., and Thompson, J. (2009). The impact of climate change on groundwater recharge and runoff in a humid, equatorial catchment: sensitivity of projections to rainfall intensity. *Hydrological Sciences Journal*, 54(4):727–738.

Mishra, S. K., Chaudhary, A., Shrestha, R. K., Pandey, A., and Lal, M. (2014). Experimental Verification of the Effect of Slope and Land Use on SCS Runoff Curve Number. *Water Resources Management*, 28:3407–3416.

Moberg, A., Jones, P. D., Lister, D., Walther, A., Brunet, M., Jacobeit, J., Alexander, L. V., Della-Marta, P. M., Luterbacher, J., Yiou, P., Chen, D., Tank, A. M. G. K., Saladié, O., Sigró, J., Aguilar, E., Alexandersson, H., Almarza, C., Auer, I., Barriendos, M., Begert, M., Bergström, H., Böhm, R., Butler, C. J., Caesar, J., Drebs, A., Founda, D., Gerstengarbe, F. W., Micela, G., Maugeri, M., Österle, H., Pandzic, K., Petrakis, M., Srnec, L., Tolasz, R., Tuomenvirta, H., Werner, P. C., Linderholm, H., Philipp, A., Wanner, H., and Xoplaki, E. (2006). Indices for daily temperature and precipitation extremes in Europe analyzed for the period 1901-2000. *Journal of Geophysical Research Atmospheres*, 111:D22106.

Mondal, A. and Mujumdar, P. P. (2015). Regional hydrological impacts of climate change: implications for water management in India. *Proc Int Assoc Hydrol Sci*, 366:34–43.

Mool, P. K., Maskey, P. R., Koirala, A., Joshi, S. P., Wu, L., Shrestha, A. B., Eriksson, M., Gurung, B., Pokharel, B., Khanal, N. R., Panthi, S., Adhikari, T., Kayastha, R. B., Ghimire, P., Thapa, R., Shrestha, B., Shrestha, S., and Shrestha, R. B. (2011). Glacial Lakes and Glacial Lake Outburst Floods in Nepal. *ICIMOD*, pages 1–109.

Mujumdar, P. P. and Ghosh, S. (2008). Modeling GCM and scenario uncertainty using a possibilistic approach: Application to the Mahanadi River, India. *Water Resources Research*, 44.

Nash, J. and Sutcliffe, J. (1970). River flow forecasting through conceptual model: Part I - A discussion and principles. *Journal of Hydrology*, 10:280–290.

Nayak, P. C., Venkatesh, B., Krishna, B., and Jain, S. K. (2013). Rainfall-runoff

modeling using conceptual , data driven , and wavelet based computing approach. *Journal of Hydrology*, 493:57–67.

Nelson, R. B. (2006). An Introduction to Copulas. *Springer science & Business media*, 137(7):2143–2150.

Osti, R. and Egashira, S. (2009). Hydrodynamic characteristics of the Tam Pokhari Glacial Lake outburst flood in the Mt. Everest region, Nepal. *Hydrological Processes*, 23:2943–2955.

Pramanik, N., Panda, R. K., and Sen, D. (2010). One Dimensional Hydrodynamic Modeling of River Flow Using DEM Extracted River Cross-sections. *Water Resources Management*, 24:835–852.

Qiao, C., Luo, J., Sheng, Y., Shen, Z., Zhu, Z., and Ming, D. (2012). An Adaptive Water Extraction Method from Remote Sensing Image Based on NDWI. *Indian Society of Remote Sensing*, 40(3):421–433.

Rai, P. K. and Mishra, V. N. (2017). Changes of Glacier Lakes Using Multi-Temporal Remote Sensing Data : A Case Study from India. *Geographica Pannonica*, 21(3):132–141.

Raina, V. and Srivastava, D. (2014). Glacier atlas of india. *GSI Publications*, 7(1).

Renard, B. and Lang, M. (2007). Use of a Gaussian copula for multivariate extreme value analysis: Some case studies in hydrology. *Advances in Water Resources*, 30(4):897–912.

Richardson, S. D. and Reynolds, J. M. (2000). An overview of glacial hazards in the Himalayas. *Quaternary International*, 65-66:31–47.

Rosegrant, M. W. and Cline, S. A. (2003). Global food security: challenges and policies. *Science*, 302(5652):1917–1919.

Rounce, D. R., Watson, C. S., and McKinney, D. C. (2017). Identification of Hazard and Risk for Glacial Lakes in the Nepal Himalaya Using Satellite Imagery from 2000 – 2015. *Remote Sensing*, 9(654):1–19.

Sachindra, D., Huang, F., Barton, A., and Perera, B. (2014). Statistical downscaling of general circulation model outputs to precipitation—part 1: calibration and validation. *International Journal of Climatology*, 34(11):3264–3281.

Salvadori, G. and De Michele, C. (2004). Frequency analysis via copulas: Theoretical aspects and applications to hydrological events. *Water Resources Research*, 40(12):1–17.

Schneider, D., Huggel, C., Cochachin, A., Guillén, S., and García, J. (2014). Mapping hazards from glacier lake outburst floods based on modelling of process cascades at Lake 513, Carhuaz, Peru. *Advances in Geosciences*, 35(April 2010):145–155.

Shamsudin, S. and Hashim, N. (2002). Rainfall runoff simulation using MIKE11 NAM. *Journal of Civil Engineering*, 15(2).

Sheffield, J., Wood, E. F., and Roderick, M. L. (2012). Little change in global drought over the past 60 years. *Nature*, 491(7424):435–438.

Shrestha, A., Eriksson, M., Mool, P., Ghimire, P., Mishra, B., and Khanal, N. (2010). Glacial lake outburst flood risk assessment of sun koshi basin, nepal. *Geomatics, Natural Hazards and Risk*, 1(2):157–169.

Shrestha, F., Xiao, G., Khanal, N. R., Maharjan, S. B., Shrestha, R. B., Li-zong, W., Mool, P. K., and Bajracharya, S. R. (2017). Decadal glacial lake changes in the Koshi basin , central Himalaya , from 1977 to 2010 , derived from Landsat satellite images. *Journal of Mountain Science*, 14(10):1969–1984.

Sillmann, J., Kharin, V. V., Zhang, X., Zwiers, F. W., and Bronaugh, D. (2013a). Climate extremes indices in the CMIP5 multimodel ensemble: Part 1. Model evaluation in the present climate. *Journal of Geophysical Research Atmospheres*, 118:1716–1733.

Sillmann, J., Kharin, V. V., Zwiers, F. W., Zhang, X., and Bronaugh, D. (2013b). Climate extremes indices in the CMIP5 multimodel ensemble: Part 2. Future climate projections. *Journal of Geophysical Research Atmospheres*, 118:2473–2493.

Singh, V., Bera, A. K., and Sharma, J. R. (2013). Hydrological stream flow modeling on Tungabhadra catchment : Parameterization and uncertainty analysis using SWAT

CUP Hydrological stream flow modelling on Tungabhadra catchment : parameterization and uncertainty analysis using SWAT CUP. *Current Science*, 104(9):1187–1199.

Singh, V. and Goyal, M. K. (2016). Analysis and trends of precipitation lapse rate and extreme indices over north Sikkim eastern Himalayas under CMIP5ESM-2M RCPs experiments. *Atmospheric Research*, 167:34–60.

Singh, V., Goyal, M. K., and Chu, X. (2016). Multicriteria Evaluation Approach for Assessing Parametric Uncertainty during Extreme Peak and Low Flow Conditions over Snow Glaciated and Inland Catchments. *Journal of Hydrologic Engineering*, 21(1):04015044.

Singh, V. P. and Woolhiser, D. A. (2002). Mathematical Modeling of Watershed Hydrology. *Journal of Hydrologic Engineering*, 7(4):270–292.

Sklar, A. (1959). Fonctions de reprtition a n dimensions et leursmarges. *Publ. Inst. Statist. Univ. Paris*, 8:229–231.

Snyder, W. M. (1962). Some possibilities for multivariate analysis in hydrologic studies. *Journal of geophysical research*, 67(2):721–729.

Soleymani, M. and Delphi, M. (2012). Comparison of flood routing models (Case study : Maroon River, Iran). *World Applied Sciences Journal*, 16(5):769–775.

Somos-Valenzuela, M. A., McKinney, D. C., Byers, A. C., Rounce, D. R., Portocarrero, C., and Lamsal, D. (2015a). Assessing downstream flood impacts due to a potential GLOF from Imja Tsho in Nepal. *Hydrology and Earth System Sciences*, 19:1401–1412.

Somos-Valenzuela, M. A., McKinney, D. C., Byers, A. C., Rounce, D. R., Portocarrero, C., and Lamsal, D. (2015b). Assessing downstream flood impacts due to a potential GLOF from Imja Tsho in Nepal. *Hydrology and Earth System Sciences*, 19(3):1401–1412.

Subash, N. and Sikka, A. (2014). Trend analysis of rainfall and temperature and its relationship over india. *Theoretical and applied climatology*, 117(3-4):449–462.

Subramaniam, S. and Saxena, M. (2011). Automated algorothm for extraction of wetlands from IRS resourcesat LISS III data. *International Archives of the Photogrammetry, Remote Sensing and Spatial Information Sciences*, XXXVIII:193–198.

Taylor, K. E., Stouffer, R. J., and Meehl, G. A. (2012). An overview of CMIP5 and the experiment design. *Bulletin of the American Meteorological Society*, 93(4):485–498.

Thakur, P. K., Aggarwal, S., Aggarwal, S. P., and Jain, S. (2016). One-dimensional hydrodynamic modeling of GLOF and impact on hydropower projects in Dhauliganga River using remote sensing and GIS applications. *Natural Hazards*, 83(2):1057–1075.

Thompson, J. R., Sørenson, H. R., Gavin, H., and Refsgaard, A. (2004). Application of the coupled MIKE SHE/MIKE 11 modelling system to a lowland wet grassland in southeast England. *Journal of Hydrology*, 293:151–179.

Thornton, P. K., Ericksen, P. J., Herrero, M., and Challinor, A. J. (2014). Climate variability and vulnerability to climate change : a review. *Global Change Biology*, 20:3313–3328.

Trenberth, K. E., Dai, A., van der Schrier, G., Jones, P. D., Barichivich, J., Briffa, K. R., and Sheffield, J. (2014). Global warming and changes in drought. *Nature Clim. Change*, 4(1):17–22.

Van Roosmalen, L., Sonnenborg, T. O., and Jensen, K. H. (2009). Impact of climate and land use change on the hydrology of a large-scale agricultural catchment. *Water Resources Research*, 45(7):1–18.

Vilimek, V., Klimes, J., Emmer, A., and Benesova, M. (2015). Geomorphologic impacts of the glacial lake outburst flood from Lake No. 513 (Peru). *Environmental Earth Sciences*, 73:5233–5244.

Vorosmarty, C. J., Green, P., Salisbury, J., and Lammers, R. B. (2000). Global Water Resources : Vulnerability from Climate Change and Population Growth. *Science*, 289(5477):284–288.

Vu, M. T., Aribarg, T., Supratid, S., Raghavan, S. V., and Liong, S.-Y. (2015). Statistical downscaling rainfall using artificial neural network: significantly wetter Bangkok? *Theoretical and Applied Climatology*, 126(3):453–467.

Vuichard, D. and Zimmermann, M. (1987). The 1985 catastrophic drainage of a moraine-dammed lake, khumbu himal, nepal: cause and consequences. *Mountain Research and Development*, pages 91–110.

Wang, D. and Tang, T. (2014). A one-parameter Budyko model for water balance captures emergent behavior in darwinian hydrologic models. *Geophysical Research Letters*, 41:4569–4577.

Wang, G., Yao, C., Okoren, C., and Chen, S. (2006). 4-Point FDF of Muskingum method based on the complete St Venant equations. *Journal of Hydrology*, 324:339–349.

Wang, J., Hong, Y., Li, L., Gourley, J. J., Khan, S. I., Yilmaz, K. K., Adler, R. F., Policelli, F. S., Habib, S., Irwn, D., Limaye, A. S., Korme, T., and Okello, L. (2011). The coupled routing and excess storage (CREST) distributed hydrological model. *Hydrological Sciences Journal*, 56(1):84–98.

Wang, J. S., Ni, H. G., and He, Y. S. (2000). Finite-difference TVD scheme for computation of dam-break problems. *Journal of Hydraulic Engineering*, 126(4):253–262.

Wang, X., Gebremichael, M., and Yan, J. (2010). Weighted likelihood copula modeling of extreme rainfall events in Connecticut. *Journal of Hydrology*, 390(1-2):108–115.

Wang, Y., Mukherjee, M., Wu, D., and Wu, X. (2016). Combating river pollution in China and India: policy measures and governance challenges. *Water Policy*, 18(5):122–137.

Watanabe, T., Lamsal, D., and Ives, J. D. (2009). Evaluating the growth characteristics of a glacial lake and its degree of danger of outburst flooding, Nepal. *Norwegian Journal of Geography*, 63:255–267.

Watanbe, T. and Rothacher, D. (1996). The 1994 lugge tsho glacial lake outburst flood, bhutan himalaya. *Mountain Research and Development*, 16(1):77–81.

Westoby, M. J., Brasington, J., Glasser, N. F., Hambrey, M. J., Reynolds, J. M., Hassan, M. A. A. M., and Lowe, A. (2015). Numerical modelling of glacial lake outburst floods using physically based dam-breach models. *Earth Surf. Dynam*, 3:171–199.

Westra, S., Brown, C., Lall, U., and Sharma, A. (2007). Modeling multivariable hydrological series: Principal component analysis or independent component analysis? *Water Resources Research*, 43(6).

Wilby, R. L., Dawson, C. W., and Barrow, E. M. (2002). SDSM - A decision support tool for the assessment of regional climate change impacts. *Environmental Modelling and Software*, 17:147–159.

Wilby, R. L., Wigley, T. M. L., Conway, D., Jones, P. D., Hewitson, B. C., Main, J., and Wilks, D. S. (1998). Statistical downscaling of general circulation model output: A comparison of methods. *Water Resources Research*, 34(11):2995–3008.

Williams, C. A., Reichstein, M., Buchmann, N., Baldocchi, D., Beer, C., Schwalm, C., Wohlfahrt, G., Hasler, N., Foken, T., Papale, D., Schymanski, S., and Schaefer, K. (2012). Climate and vegetation controls on the surface water balance : Synthesis of evapotranspiration measured across a global network of flux towers. *Water Resource Research*, 48:1–13.

Worni, R., Huggel, C., and Stoffel, M. (2013). Glacial lakes in the indian himalayas—from an area-wide glacial lake inventory to on-site and modeling based risk assessment of critical glacial lakes. *Science of the Total Environment*, 468:S71–S84.

Worni, R., Stoffel, M., Huggel, C., Volz, C., Casteller, A., and Luckman, B. (2012). Analysis and dynamic modeling of a moraine failure and glacier lake outburst flood at Ventisquero Negro, Patagonian Andes (Argentina). *Journal of Hydrology*, 444-445:134–145.

Wu, J., Miao, C., Wang, Y., Duan, Q., and Zhang, X. (2017). Contribution analysis of the long-term changes in seasonal runoff on the Loess Plateau , China , using eight Budyko-based methods. *Journal of Hydrology*, 545:263–275.

Xu, X., Liu, W., Scanlon, B. R., Zhang, L., and Pan, M. (2013). Local and global factors controlling water-energy balances within the Budyko framework. *Geophysical Research Letters*, 40:6123–6129.

Yang, D., Sun, F., Liu, Z., Cong, Z., Ni, G., and Lei, Z. (2007). Analyzing spatial and temporal variability of annual water-energy balance in nonhumid regions of China using the Budyko hypothesis. *Water Resource Research*, 43:1–12.

Yue, S. (2001). The Gumbel logistic model for representing a multivariate storm event. *Advance in Water Resources*, 24:179–185.

Zhan, C. S., Jiang, S. S., Sun, F. B., Jia, Y. W., Niu, C. W., and Yue, W. F. (2014). Quantitative contribution of climate change and human activities to runoff changes in the Wei River basin , China. *Hydrology and Earth System Sciences*, 18:3069–3077.

Zhang, D., Cong, Z., Ni, G., Yang, D., and Hu, S. (2015). Effects of snow ratio on annual runoff within the Budyko framework. *Hydrology and Earth System Sciences*, 19(4):1977–1992.

Zhang, L., Hickel, K., Dawes, W. R., Chiew, F., Western, A., and Briggs, P. (2004). A rational function approach for estimating mean annual evapotranspiration. *Water Resource Research*, 40:1–14.

Zhang, L. and Singh, V. P. (2006). Bivariate flood frequency analysis using the copula method. *Journal of Hydrologic Engineering*, 11(2):150–164.

Zhang, L. and Singh, V. P. (2007). Bivariate rainfall frequency distributions using Archimedean copulas. *Journal of Hydrology*, 332:93–109.

Zhang, Q., Li, J., Singh, V. P., and Xu, C. Y. (2013). Copula-based spatio-temporal patterns of precipitation extremes in China. *International Journal of Climatology*, 33(5):1140–1152.

Zhang, Q., Singh, V. P., Li, J., Jiang, F., and Bai, Y. (2012). Spatio-temporal variations of precipitation extremes in Xinjiang, China. *Journal of Hydrology*, 434-435:7–18.

Zhao, N., Xun, C. F. C., and Yue, Z. T. X. (2015). A comparison of two downscaling methods for precipitation in China. *Environmental Earth Sciences*, 74:6563–6569.

List of Publications

- Goswami U. P., Hazra B. and Goyal M. K. (2018), Copula-based probabilistic characterization of precipitation extremes over North Sikkim Himalaya. Atmospheric Research, Elsevier, doi:10.1016/j.atmosres.2018.05.019. (Published, Impact Factor:3.778)

- Goswami U. P., Bhargav K., Hazra B. and Goyal M. K. (2017), Spatiotemporal and joint probability behavior of temperature extremes over the Himalayan region under changing climate. Theoretical and Applied Climatology, Springer, doi.org/10.1007/s00704-017-2288-1. (Published, Impact Factor:2.64)

- Goyal M. K. and Goswami U. P. (2017), "Teesta River and its Ecosystem." Chapter in The Indian Rivers: Scientific and socioeconomic aspect, Editor: D S Singh, Springer (Published).

- Goswami U. P. and Goyal M. K., Assessment of glacial lake development and downstream flood impacts of critical glacial lake. Journal of Hydrologic Engineering, ASCE, (Revision submitted).

- Goswami U. P. and Goyal M. K., Relative contribution of climate variable on annual runoff using Budyko framework over the Eastern Himalaya. (Under Preparation).

- Goswami U. P. and Goyal M. K., Bivariate dependency of precipitation extremes over temperature extremes in the North Sikkim Himalaya (Under Preparation).